

Studying the interaction of ultrashort, intense laser pulses with solid targets

DISSERTATION

zur Erlangung des akademischen Grades

Doctor rerum naturalium

Dr. rer. nat.

vorgelegt der

**Fakultät Mathematik und Naturwissenschaften
der Technischen Universität Dresden**

von

Dipl.-Phys. (Medizinphysik) Josefine Metzkes

geboren am 09.10.1983 in Berlin-Mitte

eingereicht am 17.08.2015

verteidigt am 04.12.2015

Die Dissertation wurde in der Zeit von 12/2009 bis 08/2015
am Helmholtz-Zentrum Dresden-Rossendorf
im Institut für Strahlenphysik angefertigt

1. Gutachter: *Prof. Thomas E. Cowan, PhD*
2. Gutachter: *Prof. Dr. Jörg Schreiber*

Abstract

This thesis experimentally investigates laser-driven proton acceleration in the regime of target normal sheath acceleration (TNSA) using ultrashort (pulse duration $\tau_L = 30$ fs), high power (~ 100 TW) laser pulses. The work focuses on how the temporal intensity profile of the ultrashort laser pulse influences the plasma formation during the laser-target interaction and the subsequent acceleration process. The corresponding experiments are performed at the Draco laser facility at the Helmholtz-Zentrum Dresden – Rossendorf.

The main result of the thesis is the experimental observation of transverse spatial modulations in the laser-driven proton distribution. The onset of the modulations occurs above a target-dependent laser energy threshold and is found to correlate with parasitic laser emission preceding the ultrashort laser pulse.

The analysis of the underlying plasma dynamics by using numerical simulations indicates that plasma instabilities lead to the filamentation of the laser-accelerated electron distribution. The resulting spatial pattern in the electron distribution is then transferred to the proton distribution during the acceleration process. The plasma instabilities, which the electron current is subjected to, are a surface-ripple-seeded Rayleigh-Taylor or a Weibel instability. Regarding their occurrence, both instabilities show a strong dependence on the initial plasma conditions at the target. This supports the experimentally observed connection between the temporal intensity profile of the laser pulse and the development of spatial modulations in the proton distribution.

The study is considered the first observation of (regular) proton beam modulations for TNSA in the regime of ultrashort laser pulses and micrometer thick target foils. The experiments emphasize the requirement for TNSA laser power scaling studies under the consideration of realistic laser-plasma interaction conditions. In that way, the potential of the upcoming generation of Petawatt power lasers for laser-driven proton acceleration can be assessed and fully exploited.

In the second part of the thesis, experimental pump-probe techniques are investigated. With an imaging method termed *high depth-of-field time-resolved microscopy* in a reflective probing setup, micrometer-size *local* features of the near-critical density plasma as well as the *global* topography of the plasma can be resolved. The spatio-temporal resolution of the target ionization and heating dynamics is achieved by probing the target reflectivity, whereas the angular distribution of the reflected probe beam carries signatures of the plasma expansion. The presented probing technique avails to correlate the temporal intensity profile of a laser pulse with the spatio-temporal plasma evolution triggered upon laser-target interaction.

Zusammenfassung

Die vorliegende Dissertation beschäftigt sich experimentell mit der lasergetriebenen Protonenbeschleunigung im Regime der sogenannten *target normal sheath acceleration*¹ (TNSA). Dabei werden ultra-kurze ($\tau_L = 30$ fs) Laserpulse hoher Spitzenleistung (~ 100 TW) genutzt, die am Draco-Laser am Helmholtz-Zentrum Dresden – Rossendorf erzeugt werden können. Die zentrale Fragestellung der Experimente ist der Einfluss des zeitlichen Intensitätsprofils des Laserpulses auf die Plasmaerzeugung bei der Laser-Target-Wechselwirkung und auf die anschließende Teilchenbeschleunigung.

Das wesentliche Ergebnis der Arbeit ist die experimentelle Beobachtung räumlich transversaler Modulationen in den Strahlprofilen der beschleunigten Protonenverteilungen. Diese Modulationen werden oberhalb einer von der Targetgeometrie abhängigen Laserenergie gemessen und sind mit dem Auftreten von parasitärer Laserstrahlung korreliert, die den ultra-kurzen Laserpuls begleitet.

Durch die Analyse der zugrundeliegenden Plasmadynamik mit Hilfe numerischer Simulationen lassen sich die räumlichen Modulationen in der Protonenverteilung auf Plasmainstabilitäten zurückführen, die zur Filamentierung der laserbeschleunigten Elektronenverteilung führen. Die Plasmainstabilitäten - von Oberflächenmodulationen angeregte Rayleigh-Taylor oder Weibel-Instabilitäten - weisen bezüglich ihrer Ausprägung eine starke Abhängigkeit von den initialen Plasmabedingungen auf. Das stützt die experimentelle Beobachtung, dass das zeitliche Intensitätsprofil des Laserpulses das Auftreten der räumlichen Modulationen in der Protonenverteilung beeinflusst.

Die vorgestellte Studie kann als erste experimentelle Beobachtung einer regelmäßigen räumlichen Modulation der Protonenverteilungen im TNSA-Regime unter der Verwendung von ultra-kurzen Laserpulsen und Targetfolien mit Dicken im Mikrometerbereich betrachtet werden. Die Daten stellen heraus, dass experimentelle Skalierungsstudien unter realistischen Laser-Plasma-Wechselwirkungsbedingungen die Voraussetzung dafür sind, das Potential von Lasern mit Petawatt-Spitzenleistungen für die lasergetriebene Protonenbeschleunigung realistisch einzuschätzen und optimal zu nutzen.

Im zweiten Teil der Arbeit werden experimentelle Anrege-Abfrage-Techniken untersucht, die eine Korrelation des zeitlichen Intensitätsprofils des Laserpulses mit der räumlich-zeitlichen Plasmadynamik erlauben. Indem die Methode der *high depth-of-field time-resolved microscopy*² in einem reflektiven Anrege-Abfrage-Aufbau verwendet wird, können einerseits *lokale* räumliche Signaturen auf der Mikrometerskala in der nah-kritischen reflektierenden Plasmaoberfläche vermessen werden. Darüber hinaus kann die *globale* Topographie der reflektierenden Oberfläche aufgelöst werden. Die räumlich-zeitliche Untersuchung der Targetionisation und -heizung wird durch die Messung der Targetreflektivität erreicht, während die Expansion des Plasmas in der Winkelverteilung des reflektierten Abfragestrahls sichtbar wird.

¹ein Mechanismus zur lasergetriebenen Ionenbeschleunigung, bei dem Ionen in einem Raumladungsfeld entlang der Targetnormalenrichtung Energie gewinnen

²zeitaufgelöste Mikroskopie mit hoher Tiefenschärfe

List of Publications by the Author

1. T. Kluge, **J. Metzkes**, K. Zeil, M. Bussmann, U. Schramm, T. E. Cowan. Two surface plasmon decay of plasma oscillations. *Physics of Plasmas* 22 (6064502), 2015
2. K. Zeil, **J. Metzkes**, T. Kluge, M. Bussmann, T. E. Cowan, S. D. Kraft, R. Sauerbrey, B. Schmidt, M. Zier, U. Schramm. Robust energy enhancement of ultrashort pulse laser accelerated protons from reduced mass targets. *Plasma Physics and Controlled Fusion* 56 (084004), 2014
3. T. Kluge, C. Gutt, L. G. Huang, **J. Metzkes**, U. Schramm, M. Bussmann, T. E. Cowan. Using X-ray free-electron lasers for probing of complex interaction dynamics of ultra-intense lasers with solid matter. *Physics of Plasmas* 21 (033110), 2014
4. **J. Metzkes**, T. Kluge, K. Zeil, M. Bussmann, S. D. Kraft, T. E. Cowan, U. Schramm. Experimental observation of transverse modulations in laser-driven proton beams. *New Journal of Physics* 16 (23008), 2014
5. K. Zeil, M. Baumann, E. Beyreuther, T. Burris-Mog, T. E. Cowan, W. Enghardt, L. Karsch, S. D. Kraft, L. Laschinsky, **J. Metzkes**, D. Naumburger, M. Oppelt, C. Richter, R. Sauerbrey, M. Schürer, U. Schramm, J. Pawelke. Dose-controlled irradiation of cancer cells with laser-accelerated proton pulses. *Applied Physics B - Lasers and Optics* 110 (437), 2013
6. **J. Metzkes**, L. Karsch, S. D. Kraft, J. Pawelke, C. Richter, M. Schürer, M. Sobiella, N. Stiller, K. Zeil, U. Schramm. A scintillator-based online detector for the angularly resolved measurement of laser-accelerated proton spectra. *Review of Scientific Instruments* 83 (123301), 2012
7. K. Zeil, **J. Metzkes**, T. Kluge, M. Bussmann, T. E. Cowan, S. D. Kraft, R. Sauerbrey, U. Schramm. Direct observation of prompt pre-thermal laser ion sheath acceleration. *Nature Communications* 3 (874), 2012.
8. T. Kluge, S. A. Gaillard, K. A. Flippo, T. Burris-Mog, W. Enghardt, B. Gall, M. Geissel, A. Helm, S. D. Kraft, T. Lockard, **J. Metzkes**, D. T. Offermann, M. Schollmeier, U. Schramm, K. Zeil, M. Bussmann, T. E. Cowan. High proton energies from cone targets: electron acceleration mechanisms. *New Journal of Physics* 14 (023038), 2012
9. **J. Metzkes**, T. E. Cowan, L. Karsch, S. D. Kraft, J. Pawelke, C. Richter, T. Richter, K. Zeil, U. Schramm. Preparation of laser-accelerated proton beams for radiobiological applications. *Nuclear Instruments and Methods in Physics Research A* 653 (172), 2011
10. C. Richter, L. Karsch, Y. Dammene, S. D. Kraft, **J. Metzkes**, U. Schramm, M. Schürer, M. Sobiella, A. Weber, K. Zeil, J. Pawelke. A dosimetric system for quantitative cell irradiation experiments with laser-accelerated protons. *Physics in Medicine and Biology* 56 (1529), 2011

11. S. D. Kraft, C. Richter, K. Zeil, M. Baumann, E. Beyreuther, S. Bock, M. Bussmann, T. E. Cowan, Y. Dammene, W. Enghardt, U. Helbig, L. Karsch, T. Kluge, L. Laschinsky, E. Lessmann, **J. Metzkes**, D. Naumburger, R. Sauerbrey, M. Schürer, M. Sobiella, J. Woithe, U. Schramm, J. Pawelke. Dose-dependent biological damage of tumour cells by laser-accelerated proton beams. *New Journal of Physics* 12 (085003), 2010
12. K. Zeil, S. D. Kraft, S. Bock, M. Bussmann, T. E. Cowan, T. Kluge, **J. Metzkes**, T. Richter, R. Sauerbrey, U. Schramm. The scaling of proton energies in ultrashort pulse laser plasma acceleration. *New Journal of Physics* 12 (045015), 2010

Contents

| | |
|---|------------|
| Abstract | iii |
| Zusammenfassung | v |
| List of Publications by the Author | vii |
| 1. Introduction | 1 |
| 1.1. Motivation | 1 |
| 1.2. Content of the Thesis | 5 |
| 2. Theory of Relativistic Laser Pulses Interacting with Solid Targets | 7 |
| 2.1. Plasma Formation | 7 |
| 2.1.1. Ionization | 7 |
| 2.1.2. Non-Ionizing Target Modification Processes | 9 |
| 2.2. Plasma Properties and Their Modeling | 10 |
| 2.2.1. The Plasma Fluid Model | 11 |
| 2.2.2. Plasma Expansion into Vacuum | 12 |
| 2.3. Propagation of Non-Relativistic Electromagnetic Waves in Plasmas | 13 |
| 2.3.1. General Properties | 13 |
| 2.3.2. The Role of Plasma Gradients | 14 |
| 2.4. Relativistic Laser-Plasma Interaction | 16 |
| 2.4.1. Single Electron Dynamics in a Relativistic Laser Field | 16 |
| 2.4.2. Relativistic Plasma Optics | 18 |
| 2.5. Electron Acceleration and Propagation in Overdense Plasmas | 19 |
| 2.5.1. Electron Acceleration at Overdense Plasma Surfaces | 19 |
| 2.5.2. Propagation of Dense Electron Currents Through the Plasma | 20 |
| 2.5.3. Instabilities in Plasmas | 21 |
| 2.6. Laser-Driven Ion Acceleration | 23 |
| 2.6.1. The Physical Picture of TNSA | 23 |
| 2.6.2. Scaling Models for TNSA | 25 |
| 2.6.3. Experimental Overview | 26 |
| 3. Transverse Modulations in Laser-Driven Proton Beams | 29 |
| 3.1. Motivation | 29 |
| 3.1.1. The Scalability of TNSA to Increasing Laser Powers | 29 |
| 3.1.2. Complex-Physics Phenomena in TNSA | 30 |
| 3.1.3. TNSA Scaling Study at Draco I | 31 |
| 3.2. Experimental Setup | 31 |
| 3.2.1. The Draco I Laser System | 31 |
| 3.2.2. Target Chamber Setup | 36 |
| 3.3. Experimental Results | 38 |
| 3.3.1. Proton Data | 38 |
| 3.3.2. Electron Data | 42 |

| | | |
|---------------------|---|------------|
| 3.3.3. | Summary and Correlation of the Experimental Signatures | 43 |
| 3.3.4. | Target Surface Characterization | 44 |
| 3.4. | Numerical Analysis of the Transverse Spatial Fine-Scale Modulations | 45 |
| 3.4.1. | Simulation Setup | 46 |
| 3.4.2. | Simulation Results | 47 |
| 3.5. | Comparison of the Experimental and PIC Simulation Results | 50 |
| 3.5.1. | Estimation of the Preplasma Conditions | 50 |
| 3.5.2. | Discussion of the Experimental Signatures | 52 |
| 3.5.3. | Consideration of Signatures Beyond Target Rear Surface TNSA | 54 |
| 3.6. | Conclusion | 57 |
| 4. | Reflective Optical Probing of Laser-Driven Plasmas at Solid Targets | 59 |
| 4.1. | Motivation | 59 |
| 4.2. | Plasma Probing Via the Specularly Reflected Pump Pulse | 61 |
| 4.2.1. | Experiment | 61 |
| 4.2.2. | Modeling of the Experiment | 64 |
| 4.2.3. | High Depth-of-Field Time-Resolved Microscopy | 66 |
| 4.3. | Setup of the Reflective Pump-Probe Experiments | 68 |
| 4.4. | Rear Surface Probing | 72 |
| 4.4.1. | Experimental Results | 72 |
| 4.4.2. | Modeling of the Experiment | 74 |
| 4.4.3. | Data Analysis and Comparison with Plasma Simulations | 78 |
| 4.5. | Rear Surface Probing of Reduced-Mass Targets | 84 |
| 4.5.1. | Analysis of the Experimental Data | 84 |
| 4.5.2. | Discussion | 88 |
| 4.6. | Front Surface Probing | 89 |
| 4.6.1. | Experiment | 89 |
| 4.6.2. | Analysis of the Signal Formation | 91 |
| 4.7. | Conclusion | 95 |
| 5. | Summary and Outlook | 97 |
| A. | Appendix | 101 |
| A.1. | Raw Data for the Laser Proton Beam Filamentation | 101 |
| A.2. | Online Detectors for Laser-Driven Proton Beams | 105 |
| A.3. | Additional Data for the Specularly Reflected Pump Pulse Probing | 121 |
| A.4. | Modeling of the Reflective Pump-Probe Experiment | 122 |
| A.5. | Raw Data from the Front Surface Probing | 129 |
| A.6. | Modeling the Target Reflectivity Using Fresnel's Equations | 131 |
| Bibliography | | i |

1. Introduction

1.1. Motivation

Laser-Driven Ion Sources for Medical Applications

Methods of physics have been applied in medical research and care over centuries but what is nowadays known as translational medicine or research - i.e. the translation of laboratory methods to clinical methods [1] - gained its momentum in the late 19th century with the discovery of xrays (1895), radioactivity (1896) and radium (1898) [2]. The transfer of these fundamental physics discoveries from the laboratory into established clinical applications in the form of imaging or radiation therapy devices only took 15 years [2]. Since then, translational research has made available the findings of fundamental physics research for patient care in terms of ultrasound, computed tomography and magnetic resonance imaging as well as radiation therapy with photons, electrons, protons and ions, to only name a few examples. The benefits from the relation of physics and medicine as established by translational research are however reciprocal. The high standards set by medical devices regarding reproducibility, stability and uptime of machines have considerably stimulated the advancement of physics-based technologies.

In the field of radiation therapy with hard xrays (megaelectronvolt energy photons), for example, the corresponding linear accelerators have matured to commercial turnkey machines in over 60 years of research and development, which can be operated by trained medical personnel. In the case of ion therapy [3], on the other hand, the size and cost of according accelerators still limits their application to only 30 facilities world wide [4]. Ion therapy can however be favorable for sensitive tumor entities because the inverse depth dose profile of ions allows for an optimized dose distribution.

One approach to miniaturize ion accelerators are laser-driven ion sources (LDIS), which exploit the extremely high electric fields (\sim TV/m) that can be supported in laser-produced plasmas [5, 6, 7, 8, 9, 10]. These extreme fields, which exceed the capabilities of conventional ion accelerators by six orders of magnitude, allow for a considerable reduction of the necessary accelerator length. In that way, *compact* LDIS-based ion accelerators are made possible.

The most matured physical mechanism underlying LDIS is target normal sheath acceleration (TNSA) [11, 12, 13]. In TNSA, an ultra-intense ($I_L \sim 10^{18} - 10^{21}$ W/cm²) laser pulse ($\tau_L \sim 10 - 100$ fs or $\tau_L \sim 1 - 10$ ps) irradiates the surface of a micrometer thick solid target, which leads to a rapid ionization of the material and the formation of a plasma. Electrons are driven to relativistic energies by the laser field and set up quasi-static electric space-charge fields at the target surfaces as they leave the target volume. These fields serve the acceleration of ions. The mechanism is depicted in Figure 1.1.

LDIS can hence simultaneously produce a large variety of particles and radiation, including ~ 60 MeV/nucleon protons and ions, megaelectronvolt electron pulses and xray pulses [11, 12, 13, 14]. Laser-driven ion pulses feature a high flux ($10^{11} - 10^{13}$ particles per pulse), a pulse duration in the order of picoseconds at the source and a high laminarity [15]. Due these favorable particle properties they deliver - in combination with the short acceleration length - LDIS have potential for numerous applications [16].

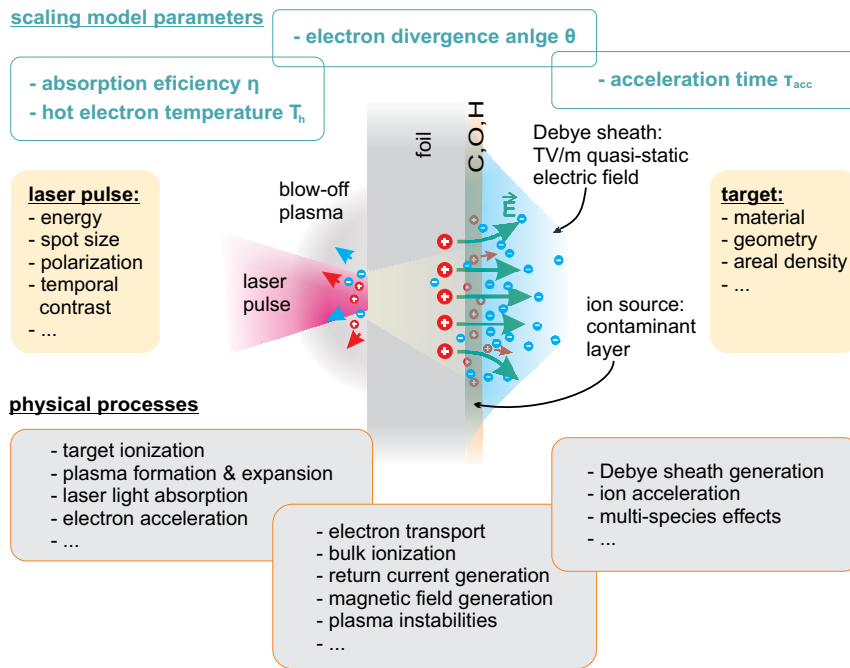


Figure 1.1: Overview of the target normal sheath acceleration mechanism (TNSA). The central part of the figure shows a sketch of the TNSA process. At the bottom part, the according underlying physical processes occurring at the target front surface, inside the target volume and at the target rear surface are summarized. In the top part of the figure, the parameters used in TNSA scaling models for the representation of the target front, bulk and target rear processes are given. The adjusting knobs for the acceleration process are the laser pulse and target parameters, listed at the left and right of the TNSA sketch, respectively.

Currently pursued fields of application encompass proton radiography of high energy density matter and transient electric fields in plasmas [17], compact neutron sources [18], fast ignition in inertial confinement fusion [19], isotope production [20] and, as introduced, LDIS-based particles sources for radiation therapy of cancer. The envisioned benefits from LDIS for ion therapy generally focus on a potential cost reduction due to the reduced accelerator size, including a reduction in costly radiation protection shielding [5]. In the best scenario, all-optical setups without a gantry or the simultaneous generation of radiation for imaging will be made possible with LDIS [8, 9].

Challenges Regarding Laser-Based Accelerators in Medical Applications

The presented thesis is embedded in the multi-disciplinary onCOOPtics project in Dresden (Germany), which aims at translating LDIS into clinically applicable machines for radiation therapy. As a cooperation of clinical-based institutions (OncoRay - National Center for Radiation Research in Oncology, Technische Universität Dresden) as well as groups focused on laser-plasma research (Helmholtz-Zentrum Dresden – Rossendorf, HZDR), the project encompasses the entire task area from developing the laser-driven accelerator, designing beam delivery systems based on pulsed magnets [21, 22, 23], developing dosimetry for pulsed sources [24] and studying the *in vitro* and *in vivo* radiobiological effectiveness of laser-accelerated protons [25, 26].

The road map for the development of medical LDIS-based accelerators is determined by the requirements for and capabilities of synchrotron- or cyclotron-based ion accelerators operated for cancer treatment [4]. Regarding the particle output - here protons - a medical ac-

celerator for radiation therapy of cancer firstly has to provide approximately 200 - 225 MeV protons to treat deep-seated (up to 30 cm depth) tumors [4]. Secondly, the accelerated proton distribution has to be fully on-demand controllable and reproducible concerning the particle number, energy, spectrum (depth dose distribution) and spatial distribution (transverse dose distribution). Only in that way, the required maximum allowable deviation of $\pm 5\%$ between the prescribed and delivered dose in an irradiated voxel can be achieved [4]. These requirements characterize a matured accelerator for which a set of machine input parameters unambiguously determines the particle output parameters.

The Status of Laser-Based Accelerators

LDIS, on the contrary, cannot be considered a mature accelerator *technology* yet. However, considerable progress has been made since the first observation of directed, energetic proton emission (maximum kinetic energies of 55 MeV) at high energy, long pulse (picosecond pulse duration) laser systems [11, 12, 13]. These developments firstly include the fact that high power but ultrashort pulse (~ 10 -100 fs) laser systems have proven to be as capable as drivers for LDIS in the TNSA regime as high energy glass laser systems [27]. In contrast to glass laser systems, which deliver only about one laser pulse and hence particle pulse per hour, Ti-Sapphire-based ultrashort pulse laser systems feature 1-10 Hz repetition rates. In that way, LDIS can provide the particle flux of 10^{10} protons per second, as required for medical particle accelerators [4].

Maximum proton energies of 40 MeV in the TNSA regime have been reported from an ultrashort pulse laser system using simple micrometer thick metal foils as targets [28]. Novel target designs have been shown to yield higher proton energies by optimizing the acceleration conditions and these targets can potentially push the energy limit of LDIS (e.g. [29, 30, 31], [32] and therein). Moreover, in addition to TNSA, several advanced acceleration mechanisms, which can (potentially) provide increased particle energies, have been identified and tested. A strong emphasis in research is on radiation pressure acceleration (RPA), relativistic transparency and/or breakout-afterburner acceleration ([33] and therein). Apart from increased particle energies, RPA is also predicted to deliver narrow-band energy spectra under optimal laser-target interaction conditions. This feature closely resembles the spectral properties of synchrotrons or cyclotrons. However, the thermal (exponential) spectra of TNSA might be applicable and even favorable for the deposition of a prescribed depth dose distribution in tissue, when an adapted beam shaping system is applied [23].

The first testbed for application experiments with LDIS - and at the same time the first step in translational research [1] - are *in vitro* radiobiological studies aiming to determine the biological effectiveness of laser-accelerated protons [34, 25, 35, 36, 37, 26]. The studies are performed under a large variety of conditions (target type, energy filter, single- or multi-shot irradiation mode). This illustrates the breadth of possible approaches in establishing LDIS-based accelerators with an applicable particle output. In the study by Zeil *et al.* performed at the HZDR, an average dose uncertainty comparable to irradiations with a conventional proton source ($< 10\%$) is achieved for the delivery of a prescribed dose to each cell sample with multiple proton pulses [26]. These results indicate that LDIS can in principle provide reproducible particle output.

Laser-Based Accelerator Research at the HZDR

Comparison of the requirements for medical accelerators on the one hand and the status of LDIS on the other hand clearly indicates two major challenges for laser-driven sources:

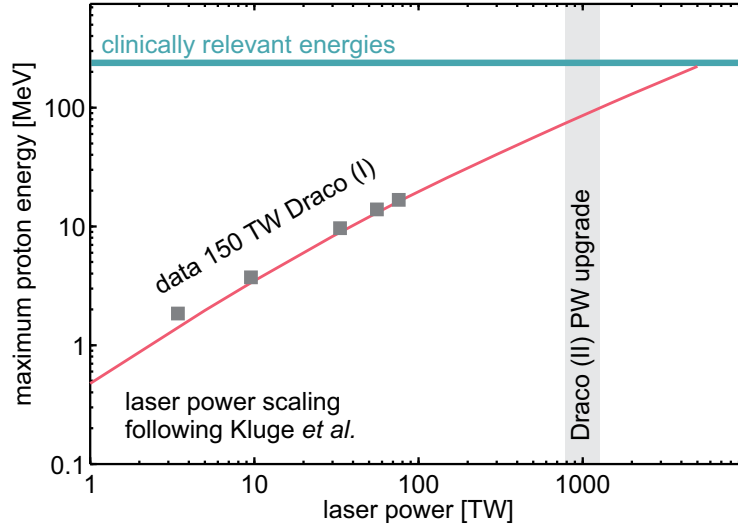


Figure 1.2.: Laser power scaling of the maximum proton energy in the TNSA regime. The laser power scaling is based on the model by Kluge *et al.* [43], which agrees well with experimental data measured at the Draco I laser system. The scaling predicts an approximately fivefold increase of the maximum proton energies for the Draco PW upgrade.

the provision of sufficient particle energies and the stability and tunability of the laser-accelerated proton distribution.

The respective accelerator research of the LDIS program in Dresden is performed at the Institute of Radiation Physics at the Helmholtz-Zentrum Dresden – Rossendorf (HZDR). The HZDR operates the 150 TW, high repetition rate (10 Hz), ultrashort pulse ($\tau_L = 30$ fs) Ti:Sapphire laser system Draco (I), which is based on the chirped pulse amplification (CPA) technique [38].

Significant advancement of LDIS towards applicable (medical) accelerators is to be expected from the new generation of ultrashort pulse, high repetition rate (\sim Hz) laser systems providing Petawatt (PW) laser power [39]. At the HZDR, the 150 TW Draco I laser system is currently upgraded (Draco II) and will deliver two independent laser pulses at 150 TW and 1 PW, which can be synchronized at the interaction point in the final setup. Laser power scalings for the robust TNSA mechanism predict that protons with kinetic energies approaching 100 MeV will be achievable with PW-class ultrashort pulse laser systems [40, 41, 42, 43]. This corresponds to a fivefold increase in available proton energies compared to Draco I [27] (Figure 1.2). Whether the large potential of ultrashort pulse PW laser sources for LDIS can be exploited in an *experimental* setting is a crucial topic for investigations. This question will considerably influence the chance of successful realization of LDIS-based accelerators as future drivers in radiation therapy facilities. The relevant studies, however, do not have to wait for the availability of PW laser sources. The scaling behavior of TNSA under different interaction conditions can already give an indication of effects that might arise for PW laser powers. Thereby, the scaling characteristics of all parameters of the accelerated proton distribution relevant for an application (e.g. particle energy, spectrum and spatial distribution) need to be taken into account.

1.2. Content of the Thesis

TNSA and the Role of the Temporal Intensity Contrast

Scaling models as applied for the above-mentioned predictions represent LDIS based on the TNSA process via a small set of input and output parameters. From a physics point of view however, the LDIS consists of the laser pulse, the target and all complex, nonlinear and in some aspects extreme phenomena underlying the light-matter interaction and the acceleration process. In detail, the LDIS firstly comprises the primary laser-target interaction including the target ionization and plasma generation. These processes are governed by nonlinear to relativistic optics, high-field atomic physics and plasma physics. Secondly, the LDIS includes the main pulse interaction with the preformed plasma, which is responsible for the generation of the hot electron distribution and the electron transport properties through the target. Both steps are very likely subjected to plasma instabilities. The final step of the LDIS is the proton acceleration itself. Here, the hot electron distribution transfers energy but possibly other characteristics (e.g. its spatial distribution), which it has acquired in the acceleration or transport process, to the proton distribution. In Figure 1.1, the complexity of TNSA is illustrated.

Precondition for a controlled accelerator based on LDIS is the understanding of and control over all sub-processes, which are determined by the laser pulse properties (energy, pulse duration, spatio-temporal intensity distribution, polarization, etc.) and the target characteristics (e.g thickness, material, shape, areal density). These are in turn also the adjusting knobs to be tuned for LDIS to meet the requirements for applicable accelerators.

One central laser pulse parameter influencing all stages of the acceleration process and hence its dynamics and performance is the temporal intensity contrast. The temporal intensity contrast is defined as the ratio of the background laser intensity normalized to the peak intensity of the ultrashort pulse. Even in the case of a ~ 10 fs long main pulse, the background intensity can span over nanosecond timescales. The temporal intensity contrast therefore determines the temporal window relevant for the laser-target interaction, starting with the target ionization and plasma formation. In combination with the plasma expansion, the temporal intensity contrast strongly influences the plasma conditions at main pulse arrival. These then influence the laser light absorption efficiency (e.g. [44]) as well as the hot electron generation and transport (e.g. [43]). At the same time, plasma expansion at the target rear surface, which is often triggered by background laser intensity preceding the ultrashort laser pulse, directly affects the ion/proton acceleration process (e.g. [45]).

From a laser-technological standpoint, the temporal intensity contrast is crucial because it is determined by the performance of the entire laser chain. Moreover, unambiguous characterization for the final/fully amplified laser pulse is challenging. Finally, the increased laser peak powers available from the upcoming PW-class lasers will likely lead to increased absolute background laser intensities unless filter techniques for background radiation suppression are developed.

Thesis Outline

The research of the presented thesis focuses on two aspects of the laser pulse's temporal intensity contrast in relation to the TNSA acceleration process. The corresponding experimental work is performed at the Draco I laser system at the HZDR.

TNSA Scaling - Experimental Observation of Transverse Modulations in Laser-Driven Proton Beams Firstly, an experimental laser energy scaling study in the TNSA regime is presented. It focuses on the effect of a non-ideal (i.e. prepulses present) temporal intensity contrast on the laser-target interaction conditions, and subsequently the acceleration physics. The experiment investigates the laser energy dependent characteristics of the proton distribution emitted at the target rear surface. Thereby, the spectral (maximum proton energy, spectral modulations) as well as spatial (beam modulations, beam divergence) properties are considered. As the main result, the scaling study reveals the transition from homogeneous to transversely strongly modulated proton beam profiles as a function of the laser energy applied on target and the target parameters. This study, published in [46], is considered the first observation of (regular) proton beam modulations for TNSA within the regime of ultrashort laser pulses and micrometer thick interaction targets.

The data analysis based on numerical plasma simulations indicates that instabilities in the laser-produced plasma at the target front surface lead to an electron beam filamentation. The spatially modulated electron distribution then represents the source of the observed proton beam modulations. The specific filamentation processes (surface-ripple-seeded Rayleigh-Taylor or Weibel instability) in the electron distribution are observed to be strongly influenced by the preplasma conditions at the target. These are determined by the temporal intensity contrast of the laser pulse. The proton beam distribution hence serves as a sensitive probe for changes in the laser-target interaction conditions and the acceleration process.

Reflective Optical Probing of Laser-Driven Plasmas at Solid Targets The analysis of the presented TNSA scaling study is supported by numerical plasma simulations. Limited by the computational capabilities, the plasma distribution cannot be calculated self-consistently based on the temporal intensity contrast of the laser pulse. Instead, the plasma distribution that the ultrashort main pulse is interacting with is pre-set. This approximation is particularly critical when investigating effects which crucially depend on the specific plasma conditions, e.g. plasma instabilities. Experimental techniques which allow for the measurement of the temporal evolution of the plasma formation are hence crucial. These can provide realistic input parameters for PIC simulations.

The second part of this thesis is therefore concerned with the development, testing and application of optical pump-probe techniques, which give access to the spatio-temporal plasma evolution resulting from laser irradiation. The presented pump-probe experiments are performed in a reflective mode in which the specularly reflected portion of the probe pulse is imaged onto a camera using a long-distance large-aperture microscope objective. Reflective probing allows to investigate near-critical densities, which is the region relevant for the conversion of laser into particle energy and the triggering of plasma instabilities. The particular setup provides spatial resolution of surface features on the micrometer-scale, where the image contrast can either be due to a target surface structure or can be caused by a spatial variation of the target reflectivity. Moreover, using the depth-of-field (DOF) of the imaging system, signatures of the global topography of the reflecting plasma surface are studied. The target shape imprints into the angular distribution of the reflected probe beam. The imaging technique is termed *high depth-of-field time-resolved microscopy*. By applying the technique to the target's front as well as rear surface, the topography and temporal dynamics of near-critical density surfaces are investigated and related to the temporal intensity contrast of the laser system.

2. Theory of Relativistic Laser Pulses Interacting with Solid Targets

Relativistic laser pulses - brought into interaction with matter in laser-driven plasma acceleration - feature peak intensities above 10^{18} W/cm², a factor $\sim 10^8$ times higher than the threshold intensity for material ionization. Considering ultrashort laser pulses with a pulse duration of $\tau_L \sim 10 - 100$ fs, the rising pulse edge hence quickly ionizes the target, so that the main portion of the pulse interacts with a plasma. With the focus on laser-driven ion acceleration, the central aspects of the laser-plasma interaction are the transfer of the laser pulse energy to fast electrons in an overdense plasma, the electron propagation through the target bulk and the energy transfer to ions in quasi-static field structures set up in the plasma.

This chapter gives an introduction to these processes with the emphasis on plasma formation and the resulting optical plasma properties. Both aspects relate to the pump-probe experiments presented in this thesis. A second point relevant for this thesis are the transport of intense electron currents and plasma instabilities. The chapter closes with a section on laser-driven proton acceleration in the target normal sheath acceleration (TNSA) scheme.

2.1. Plasma Formation

Due to the extreme peak intensities of relativistic laser pulses, the interaction with matter is not only determined by the ultrashort pulse itself but also by the inherently present background radiation. The present background radiation expands the temporal window relevant for the interaction from the femto- to the picosecond timescale - e.g. with target ionization by prepulses - up to the nanosecond timescale (Figure 2.1). All subsequent plasma processes following the initial interaction up to the acceleration of ions are influenced by the initial laser-target interaction conditions and hence the spatio-temporal intensity distribution of the incoming laser pulse.

2.1.1. Ionization

Depending on the instantaneous laser intensity, different field ionization mechanisms play a role in the plasma formation (Figure 2.2). These mechanisms can approximately be distinguished by comparing the incoming laser intensity I_L with the atomic field strength E_{at} and the derived atomic intensity I_{at} . For the hydrogen atom ground state for instance holds [47]:

$$E_{at} = \frac{e}{4\pi\epsilon_0 a_B^2} \approx 5 \cdot 10^{11} \text{ V/m} \quad \Rightarrow \quad I_{at} = \frac{\epsilon_0 c}{2} \cdot E_{at}^2 \approx 4 \cdot 10^{16} \text{ W/cm}^2 \quad . \quad (2.1)$$

Here e is the elementary charge, ϵ_0 the permittivity of free space, a_B the Bohr radius and c the speed of light in vacuum.

If $I_{at}/I_L \gg 1$, the laser intensity is small compared to the atomic binding strength and

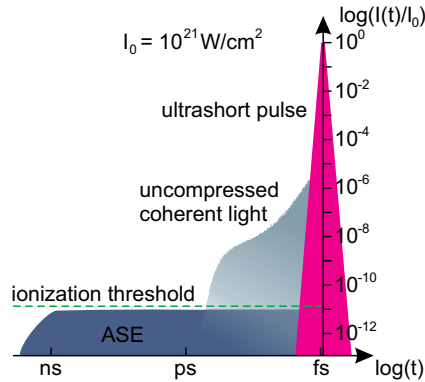


Figure 2.1.: Schematic temporal contrast curve of a high-intensity laser system. The temporal contrast $I_L(t)/I_0$ is defined as the ratio of the laser intensity at time t normalized to the peak intensity of the ultrashort pulse at $t=0$, I_0 . The origin of the different background components is discussed in Section 3.2.1. Whereas the nanosecond amplified spontaneous emission (ASE) background mainly causes non-ionizing target modification, ionization starts on the picosecond timescale during the background of uncompressed pulse parts.

can be treated as a time-dependent perturbation to the atomic potential. Multi-photon ionization (MPI) is observed, in which an atom simultaneously absorbs n photons at the frequency ω_L from the laser field in order to yield the atomic binding energy: $E_b = n \cdot \hbar\omega_L$ [48]. The threshold intensity of 10^{10} W/cm² for MPI [49] is reached during the early part of the laser pulse's rising edge in modern high-intensity laser systems (Figure 3.3).

For a laser intensity above 10^{13} W/cm², above-threshold ionization (ATI) occurs. In that case, the atom absorbs s more photons than the n photons required for ionization, the excess energy being transferred to the photoelectron as kinetic energy ($E_{kin} = (n + s) \cdot \hbar\omega_L - E_b$) [48]. ATI is attributed to an interplay of the AC-Stark effect, which shifts the ionization level when coupled to an intense laser field, and the ponderomotive potential of the focused laser pulse (Section 2.4) [47].

The perturbative approach of MPI breaks down when the atomic Coulomb potential V_C for an ion with charge state Z is severely deformed by the laser field potential V_L . For the combined potential $V(x, t)$ then holds

$$V(x, t) = V_C + V_L = -\frac{Ze^2}{4\pi\epsilon_0 x} - exE(t) \quad (2.2)$$

in the case of a laser field E polarized in x-direction. As Equation (2.2) shows, the external laser field lowers the Coulomb barrier so that electrons can leave their bound state via tunneling (tunneling ionization Figure 2.2). The oscillations of E on the femtosecond timescale (electric field and envelope) can be omitted [50].

Instantaneous ionization occurs when the Coulomb barrier is suppressed below a bound state level at even higher laser field strengths (barrier-suppression ionization, BSI). The corresponding appearance intensity I_{app} can be estimated by equating the combined potential $V(x, t)$ at x_{max} (Figure 2.2) with the binding energy E_b of a particular atomic state [48]:

$$I_{app}[\text{W/cm}^2] \sim 4 \cdot 10^9 \cdot \frac{E_b^4 [\text{eV}^4]}{Z^2} \quad (2.3)$$

Exemplary values for I_{app} for aluminum are $5.2 \cdot 10^{12}$ W/cm², $2.9 \cdot 10^{14}$ W/cm² and $8.9 \cdot 10^{16}$ W/cm² for Al¹⁺, Al³⁺ and Al⁵⁺, respectively.

These data confirm that the rising edge of a relativistic laser pulse can efficiently create a plasma at the interaction target. As to which of the ionization mechanisms dominates the ionization process in a specific laser intensity range strongly depends on the pulse duration and exact time structure of the laser pulse, e.g. the steepness of the rising pulse edge [50]. Once a sufficient number of free electrons has been created, they collisionally ionize the target bulk which is, even in the case of a transparent material, shielded from the laser field by overdense plasma (Section 2.3.1). Collisional ionization and field ionization in the Debye sheath (Section 2.6) are responsible for the plasma formation at the target rear surface.

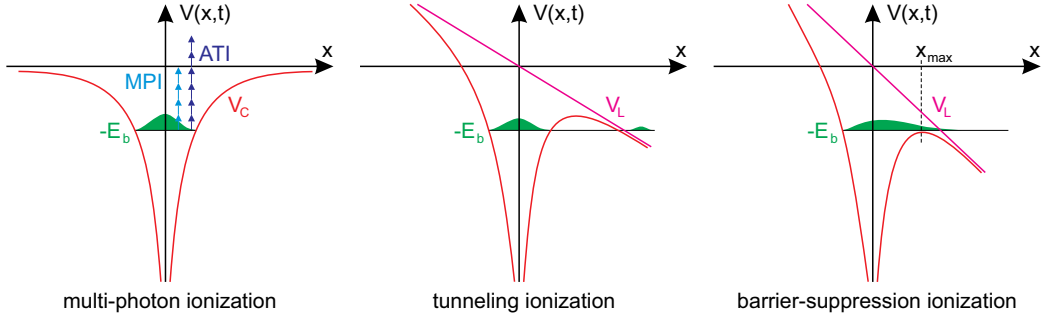


Figure 2.2.: Field ionization mechanisms in plasma formation.

2.1.2. Non-Ionizing Target Modification Processes

The rising edge of the main laser pulse and potentially present ultrashort prepulses on the picosecond timescale mainly contribute to the plasma formation by target ionization (Section 2.1.1). In addition, several experiments have shown that the often nanoseconds long pedestal of amplified spontaneous emission (ASE) preceding the pulse (Figure 2.1) can modify the target material even though its intensity is below or just at the ionization threshold [51, 45, 52, 53, 54]. Regarding laser-driven proton acceleration, the intensity level and duration of the ASE have for instance been shown to affect the maximum proton energies attainable with thin targets [45]. Moreover, an influence on the angular proton emission pattern by ASE-driven shocks has been observed [52, 53, 54]. ASE can also contribute to the amount of preplasma at the target front surface when initially neutral ablated target material is ionized by prepulses or the rising pulse edge [51].

Hereafter, the interaction of a nanosecond long ASE pedestal with a metal target material will be sketched in order to derive the threshold fluence for ablation. Ablation here refers to ion emission from the target surface due to target evaporation.

The physical picture can be summarized as follows [55]: Laser light below the ionization threshold penetrates the target up to the skin depth $l_s = c/\omega_p$, where ω_p is the plasma frequency (Section 2.2) [48]. Within this depth, laser energy is absorbed by the free electrons of the target material via inverse bremsstrahlung. The equilibrium temperature and heat capacity of the electronic system are T_e and C_e . Equilibration with the lattice of the target material (T_i , C_i) occurs on the timescale of picoseconds via collisions and is described by the collision frequency ν . Moreover, energy is transported out of the skin depth region by diffusion. The laser-to-target heat transfer and energy transport in the

target is described by the one-dimensional two-temperature diffusion model [55]:

$$\begin{aligned}
C_e \frac{\partial T_e}{\partial t} &= \frac{\partial Q(z)}{\partial z} - \nu(T_e - T_i) + S(z, t) && \text{electronic subsystem} \\
C_i \frac{\partial T_i}{\partial t} &= \nu(T_e - T_i) && \text{lattice subsystem} \\
Q(z) &= -k_e \frac{\partial T_e}{\partial z} && \text{heat flux} \\
S(z, t) &= I_L(t) \cdot A \frac{2}{l_s} e^{-\frac{2z}{l_s}} && \text{laser source term} \quad .
\end{aligned} \tag{2.4}$$

The parameters k_e and A are the electron thermal conductivity and the material absorption coefficient and $I_L(t)$ is the laser intensity at the target surface. The z -direction is oriented normal to the target surface.

If ASE is considered, which is present for timescales a factor 10^3 longer than the equilibration time, Equation (2.4) reduces to

$$C_i \frac{\partial T}{\partial t} = \frac{\partial}{\partial z} \left(k_0 \frac{\partial T}{\partial z} \right) + S(z, t) \quad . \tag{2.5}$$

It holds $T_e = T_i =: T$ and $k_0(T)$ is the equilibrium thermal conductivity of the material [55]. Hence, the target temperature T is determined by the absorption of laser energy and the heat transport within the target.

Based on the energy absorbed per surface volume (E_{surf}), it can be estimated whether the target surface will undergo evaporation due to the ASE of duration τ_{ASE} . Equating E_{surf} and the heat of evaporation per volume Q_e provides the evaporation/ablation threshold fluence F_{abl} [55, 51]. The heat of fusion and heat capacity are neglected in comparison to Q_e :

$$E_{surf} [\text{J/cm}^3] = \frac{A \bar{I}_L \cdot \tau_{ASE}}{l_d} = A \bar{I}_L \cdot \sqrt{\frac{\tau_{ASE}}{\alpha}} \quad \rightarrow \quad F_{abl} [\text{J/cm}^2] = \frac{Q_e}{A} \cdot \sqrt{\alpha \cdot \tau_{ASE}} \quad . \tag{2.6}$$

Here, the time-dependent intensity $I_L(t)$ has been replaced by the average absorbed intensity $A \bar{I}_L$. $l_d = \sqrt{\alpha \cdot \tau_{ASE}}$ is the time-dependent diffusion depth with the thermal diffusivity $\alpha = k_0/C_i$. For a state-of-the-art Ti:Sapphire laser system with a peak laser intensity of $10^{20} - 10^{21} \text{ W/cm}^2$ and an ASE contrast level of $\lesssim 10^{-10}$ (Figure 3.3), a value of $\bar{I}_L \sim 10^{10} \text{ W/cm}^2$ is expected. With $\tau_{ASE} = 5 \text{ ns}$, the laser fluence on the target surface is $\approx 50 \text{ J/cm}^2$. This value is above the ablation threshold for aluminum (Al) but below F_{abl} for gold (Au) according to the data summarized in Table 2.1. For Al, the ablation condition $E_{surf} = Q_e$ - i.e. the absorbed energy equals the heat of evaporation - is already reached after $\tau_{ASE} = 240 \text{ ps}$ of ASE irradiation. Note that this simple model neglects the temperature-dependence of the material properties ρ , C_i and α .

2.2. Plasma Properties and Their Modeling

The plasma produced in the interaction of an intense laser pulse with a solid target can in principle be described as a quasi-neutral system of N particles, electrons and ions, mutually coupled by their self-consistent electric and magnetic fields. Since the consideration of only the electric fields (Coulomb force) already gives a system of $6N$ coupled equations, analytic modeling of plasmas requires simplifying assumptions.

| material | ρ [g/cm ³] | A | α [cm ² /s] | Q_e [kJ/cm ³] | F_{abl} [J/cm ²] |
|-----------------------|-----------------------------|------|-------------------------------|-----------------------------|--------------------------------|
| Al | 2.7 | 0.13 | 0.5 [51] | 28.4 | 11 |
| Au | 19.3 | 0.03 | 1.3 [56] | 33.5 | 90 |
| H₂O | 1.0 | 0.98 | $1.4 \cdot 10^{-3}$ | 2.3 | $6.2 \cdot 10^{-3}$ |

Table 2.1.: Material parameters for aluminum, gold and water at room temperature. The ablation threshold F_{abl} is given for $\tau_{ASE} = 5$ ns. The ablation threshold for water is considerably lower than the ablation threshold for the target bulk materials Al and Au. Hence, the hydro-carbon contaminant layer present at the target surface is removed quickly when laser-irradiated.

In the two-fluid plasma model, electrons and ions are described as separate fluids, each - at least locally - in thermodynamic equilibrium. The velocity distribution is hence Maxwellian and can be characterized by temperatures T_e (electrons) and T_i (positive ions). Plasma phenomena related to non-Maxwellian particle velocity distributions can be treated in kinetic plasma models. In that case, the independent variables space \vec{r} and time t are complemented by the velocity \vec{v} .

2.2.1. The Plasma Fluid Model

General Properties

The plasma fluid describes plasma dynamics, which are governed by *collective* effects. Those are mediated by fields arising from local deviations from charge neutrality on spatial scales of at least the Debye length λ_D . λ_D is the characteristic length over which the electric potential of a discrete charge is screened by the plasma, here for a positive charge:

$$\lambda_D = \sqrt{\frac{\epsilon_0 k_B T_e}{n_e e^2}} \quad . \quad (2.7)$$

k_B is the Boltzmann constant and T_e and n_e are the electron temperature and density. The short-scale plasma dynamics ($|\vec{r}| < \lambda_D$) are determined by collisions between ions and electrons, which occur at a frequency [48]

$$\nu_{ei} [s^{-1}] \sim 2.91 \cdot 10^{-6} \cdot \frac{Z n_e [\text{cm}^{-3}]}{T_e^{3/2} [\text{eV}^{3/2}]} \cdot \ln \Lambda \quad \Lambda = \frac{12\pi}{Z} \cdot \lambda_D^3 n_e \quad . \quad (2.8)$$

$\ln \Lambda$ is the Coulomb logarithm and Z the ionic charge state. For a plasma as produced by an ultrashort, intense laser pulse with $Z = 6$, $n_e = 10^{23} \text{ cm}^{-3}$ and $T_e = 1 \text{ keV}$ follows a collision frequency of $\nu_{ei} \approx 10^{14} \text{ s}^{-1}$ and a mean collision time $\tau_{ei} = 1/\nu_{ei}$ of ≈ 8 fs.

The collisionality of the plasma is characterized by the ratio ν_{ei}/ω_p with the plasma frequency ω_p [57]:

$$\omega_p = \sqrt{\frac{e^2 n_e}{\epsilon_0 m_e}} \quad . \quad (2.9)$$

ω_p is the density-dependent characteristic eigenfrequency of electron plasma waves excited by plasma density fluctuations. For the given plasma parameters ($Z = 6$, $n_e = 10^{23} \text{ cm}^{-3}$, $T_e = 1 \text{ keV}$) holds $\nu_{ei}/\omega_p \approx 10^{-2} \ll 1$ and the plasma can hence be describe as collisionless.

Fluid Equations

The temporal evolution of the phase space distribution $f_j(\vec{r}(t), \vec{v}(t), t)$ in the self-consistent collective electric and magnetic fields for each plasma species j (charge q_j , mass m_j) is described by the Vlasov equation [57]:

$$\frac{\partial f_j}{\partial t} + \vec{v} \cdot \frac{\partial f_j}{\partial \vec{r}} + \frac{q_j}{m_j} \left(\vec{E} + \vec{v} \times \vec{B} \right) \cdot \frac{\partial f_j}{\partial \vec{v}} = 0 \quad (SI) \quad . \quad (2.10)$$

Equation (2.10) follows from the continuity equation for $f_j(\vec{r}, \vec{v}, t)$, as the particle number is conserved, and the equation of motion with the Lorentz force. Moreover, the fields \vec{E} and \vec{B} have to fulfill Maxwell's equations.

A set of equations for the plasma parameters density n_j , mean velocity \vec{u}_j and pressure p_j without a direct velocity-dependence results from the velocity moments of the Vlasov equation (Equation (2.10)) [57]:

$$\begin{aligned} \frac{\partial n_j}{\partial t} + \frac{\partial}{\partial \vec{r}} \cdot (n_j \vec{u}_j) &= 0 && \text{continuity equation} \\ n_j \left(\frac{\partial \vec{u}_j}{\partial t} + \vec{u}_j \cdot \frac{\partial \vec{u}_j}{\partial \vec{r}} \right) &= \frac{n_j q_j}{m_j} \left(\vec{E} + \vec{u}_j \times \vec{B} \right) - \frac{1}{m_j} \frac{\partial p_j}{\partial \vec{r}} && \text{force equation} \\ p_j &= n_j \theta_j \quad \theta_j = k_B T_j && \text{isothermal EOS} \\ \frac{p_j}{n_j^\gamma} &= \text{const} \quad \gamma = \frac{N+2}{N} && \text{adiabatic EOS} \quad . \end{aligned} \quad (2.11)$$

The equations of state (EOS) relate density and pressure of the plasma and the assumption underlying the isothermal EOS is a heat flow fast enough to keep the fluid at a constant temperature. It is valid when the thermal particle velocity is larger than the phase velocity v_{ph} of a plasma process under consideration ($v_t \gg \omega/k = v_{ph}$). In the opposite limit $v_t \ll \omega/k = v_{ph}$, the heat flow is neglected, which leads to the adiabatic EOS.

The full set of equations for the fluid model includes Maxwell's equations:

$$\begin{aligned} \nabla \cdot \vec{E} &= \frac{\rho}{\epsilon_0} & \nabla \times \vec{E} &= -\frac{\partial \vec{B}}{\partial t} & \rho &= \sum_j n_j q_j \\ \nabla \cdot \vec{B} &= 0 & \nabla \times \vec{B} &= \mu_0 \vec{j} + \mu_0 \epsilon_0 \frac{\partial \vec{E}}{\partial t} & \vec{j} &= \sum_j n_j q_j \vec{u}_j \quad . \end{aligned} \quad (2.12)$$

2.2.2. Plasma Expansion into Vacuum

The fluid equations (Equation (2.11) to Equation (2.12)) will be applied to characterize essential plasma dynamics, focusing on the interaction with external electromagnetic fields, e.g. laser pulses. To that end, the spatial profile of a one-dimensional (z-direction), isothermal plasma slab freely expanding into vacuum is calculated, as it sets the interaction conditions for the plasma and the laser pulse.

The plasma is assumed to consist of ions with density n , mass M , charge Z , mean velocity u and pressure p_i , as well as electrons (mass m , pressure p_e , temperature T_e). Neglecting magnetic fields and the electron inertia, for the electron and ion fluid follows from

Equation (2.11):

$$\left. \begin{aligned} n_e e E &= -\nabla p_e \\ \frac{\partial u}{\partial t} + u \frac{\partial u}{\partial z} &= \frac{Z e E}{M} - \frac{\nabla p_i}{n M} \end{aligned} \right\} \quad \frac{\partial u}{\partial t} + u \frac{\partial u}{\partial z} = -c_s^2 \frac{1}{n} \frac{\partial n}{\partial z} \quad . \quad (2.13)$$

The electric field here serves as the transmitter of the electron pressure to the ions.

To get to the combined equation in Equation (2.13), the isothermal EOS for the electron fluid (Equation (2.11)) is applied and the following assumptions are made: $p_e \gg p_i$ and $n_e \sim Z n$. The latter holds true for spatial scales $|\vec{r}| \gg \lambda_D$. c_s is the ion sound velocity and defined as $c_s = \sqrt{Z k_B T_e / M}$.

A self-similar solution for the plasma expansion of the form $n = f(z/t)$ and $u = g(z/t)$ to Equation (2.13) and the continuity equation for the ion fluid (Equation (2.11)) is:

$$u = c_s + \frac{x}{t} \quad \text{and} \quad n = n_0 \cdot e^{-\frac{x}{c_s t}} \quad \text{with} \quad n_0 := n(z=0) \quad . \quad (2.14)$$

During the expansion, the plasma acquires an exponential density profile with a scale length L_p defined as

$$L_p = \frac{n}{|\partial n / \partial z|} = c_s t \quad . \quad (2.15)$$

At $z = L_p$, the plasma density has decreased to n_0/e . L_p itself is time-dependent and increases at the rate of the ion sound speed c_s .

The precondition for steep plasma gradients, as favorable for the interaction with ultrashort laser pulses, are hence a minimal pre-heating of the target (T_e low) and a short plasma expansion time, i.e. the target ionization occurs only during the rising pulse edge.

2.3. Propagation of Non-Relativistic Electromagnetic Waves in Plasmas

The propagation of an external electromagnetic wave in a plasma and the resulting physical effects - the energy absorption as well as the optical plasma properties - strongly depend on interaction parameters such as the wave's angle of incidence onto the plasma, its polarization or the plasma scale length L_p . In this section, central results for different interaction parameters will be discussed, following the treatment by Krueer and Gibbon [57, 48].

2.3.1. General Properties

Starting point are the fluid equations (Equation (2.11)) and Maxwell's equations (Equation (2.12)) under the influence of an external harmonic (frequency ω_L) electric field: $\vec{E} = \vec{E}_0(\vec{r}) \cdot \exp(-i\omega_L t)$. For high-frequency light waves, the ion plasma can be treated as stationary and for the linearized force equation for the electrons follows:

$$\frac{\partial \vec{j}}{\partial t} = \frac{n_e e^2}{m_e} \vec{E}_0 e^{-i\omega_L t} \quad \longrightarrow \quad \vec{j} = i \cdot \frac{\omega_p^2 \epsilon_0}{\omega_L} \vec{E} =: \sigma \vec{E} \quad . \quad (2.16)$$

Here, the definition of the current $\vec{j} = -n_e e \vec{v}_e$ and of the electron plasma frequency (Equation (2.9)) are used and σ is the plasma conductivity. The optical plasma properties, such as the dielectric function ϵ and the index of refraction n_r , are connected to σ via

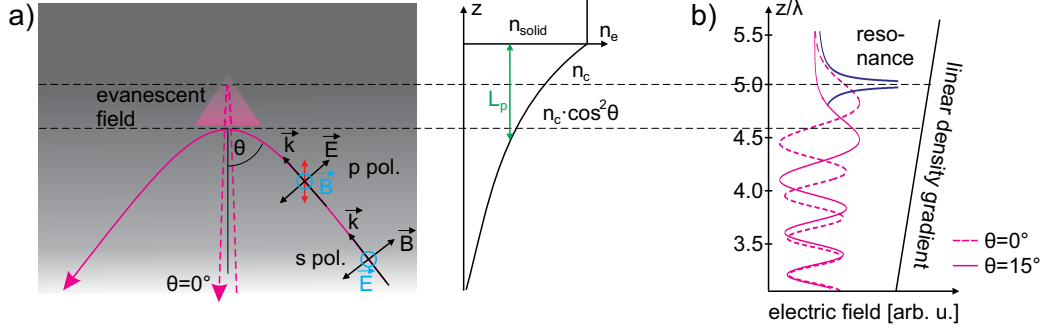


Figure 2.3.: Propagation of electromagnetic waves in a plasma gradient. a) An electromagnetic wave propagating into a density gradient under an angle θ is reflected at the density $n_c \cdot \cos^2 \theta$. For $\theta \geq 0^\circ$, an evanescent field tunnels up to the critical density n_c . For p-polarization, the electric field \vec{E} has a component along the density gradient (red arrow), allowing for resonance absorption. b) The electric field in a smooth linear gradient with $n_e = n_c \cdot z/L$ and $L = 5\lambda$ has the form of the Airy function A_i (dashed line). In the case of p-polarization and oblique incidence ($\theta = 15^\circ$), the evanescent field resonantly excites electron plasma waves at the critical density n_c (solid purple lines).

Ampere's law (Equation (2.12)):

$$\epsilon = 1 + i \cdot \frac{\sigma}{\omega_L \epsilon_0} \quad \longrightarrow \quad \epsilon = n_r^2 = 1 - \left(\frac{\omega_p}{\omega_L} \right)^2 \quad \longrightarrow \quad n_r = \sqrt{1 - \left(\frac{\omega_p}{\omega_L} \right)^2} . \quad (2.17)$$

Light propagation in a plasma is only possible for real values of n_r , i.e. $\omega_L > \omega_p$. For lower frequencies, the electron plasma response time $1/\omega_p$ is fast enough to shield the plasma. With Equation (2.9) and Equation (2.17), the propagation condition for waves in a plasma can also be formulated as a density constraint with the critical plasma density n_c . Densities that allow for propagation are termed under-critical:

$$n_{prop} < n_c = \frac{\epsilon_0 m_e \omega_L^2}{e^2} . \quad (2.18)$$

2.3.2. The Role of Plasma Gradients

Smooth Plasma Gradients

Following Equation (2.18), an electromagnetic wave that impinges normally onto a plasma gradient with under- and over-critical regions can propagate up to n_c . Around the reflection point, an enhancement of the electric field is expected, as a standing wave forms. Furthermore, a part of the field decays exponentially into the overdense plasma region (evanescent wave). For a quantitative analysis, the wave equation for the transverse electric field $E(x, y)$ is solved under the consideration of a spatially varying dielectric function $\epsilon(\omega_L, z)$ in z -direction [57]:

$$\frac{d^2 E(x, y)}{dz^2} + \frac{\omega_L^2}{c^2} \cdot \epsilon(\omega_L, z) \cdot E(x, y) = 0 \quad \text{with} \quad \epsilon = 1 - \frac{z}{L} . \quad (2.19)$$

The density here increases linearly from 0 to n_c over the distance L starting at $z = 0$ and a smooth gradient is assumed, i.e. $L/\lambda \gg 1/2\pi$. The solution to Equation (2.19) has the

form of the Airy¹ function A_i : $E(\eta) \propto Ai(\eta)$ with $\eta = (\omega_L^2 L/c^2)^{1/3} \cdot (z - L)$ [57]. $Ai(z)$ is plotted in Figure 2.3b for $L = 5\lambda$, showing that the field maximum is reached at $\eta = -1$ ($z \approx 4.8\lambda$) with a field enhancement factor of $\approx 1.9 \cdot (\omega_L L/c)^{1/6}$. The field decays to $1/e$ of the maximum value at $\eta \approx 0.75$ ($z \approx 5.1\lambda$), i.e. over a distance $\Delta z \approx \lambda/3$ relative to the peak position.

Oblique Incidence at p-polarization - Resonance Absorption

In the case of oblique incidence onto a plasma gradient, s- and p-polarized waves (out-of- and in-plane polarization) have entirely different absorption properties (Figure 2.3a). In the case of an s-polarized wave impinging under an angle θ , the discussion from above remains valid, only the reflection point being shifted to a lower density $n = n_c \cdot \cos^2\theta$. The electric field for $\theta = 15^\circ$ is plotted in Figure 2.3b.

p-polarized waves, on the other hand, can couple to the plasma via electron plasma waves, thereby providing an absorption mechanism for laser light termed resonance absorption [57]. The mechanism is sketched in Figure 2.3: The p-polarized wave obliquely impinging onto the plasma gradient possesses an electrical field component E_z along the plasma gradient and drives plasma charge density oscillations, since the electron density varies along the z-direction ($n_e = f(z)$). The oscillation amplitude is [57]

$$z_{os} = \frac{eE_z}{m_e\omega_L^2} = \frac{v_{os}}{\omega_L} \quad \text{or} \quad z_{os}[\text{m}] = 1.4 \cdot 10^{-7} \cdot \lambda^2[\mu\text{m}^2] \cdot \sqrt{\frac{I_L[\text{W}/\text{cm}^2]}{10^{18}}} \quad , \quad (2.20)$$

with the laser intensity I_L . At the critical density ($\omega_p = \omega_L$ at $z = L$), these fluctuations resonantly excite electron plasma waves and the corresponding electrical field E_z is strongly enhanced: $E_z \propto E_{res}/\epsilon(z)$ [57], $\epsilon(z) \rightarrow 0$ for $z \rightarrow L$ (Equation (2.19)). The qualitative behavior of E_z in the resonance region is shown in Figure 2.3b. The amplitude E_{res} is given by the exponentially decaying evanescent field, that tunnels into the resonance region, when the incoming wave is reflected at a distance $L \cdot (1 - \cos^2\theta)$ from the critical density (Figure 2.3) [57]:

$$E_{res} = \frac{E_{vac}}{\sqrt{\frac{2\pi\omega_L L}{c}}} \cdot \phi(\tau) \quad \text{with} \quad \phi(\tau) \sim 2.3\tau \cdot e^{-\frac{2\tau^3}{3}} \quad . \quad (2.21)$$

E_{vac} is the field strength in the plasma-free space and $\tau = (\omega_L L/c)^{1/3} \cdot \sin\theta$. The field energy locally available in the electrostatic wave in the resonance region is hence known.

To describe its dissipation into the plasma, the so far applied collisionless model is extended by a damping factor ν in the dielectric function [57]:

$$\epsilon(\omega_L) = 1 - \frac{\omega_p^2}{\omega_L(\omega_L + i\nu)} = 1 - \frac{\left(\frac{\omega_p}{\omega_L}\right)^2}{1 + \left(\frac{\nu}{\omega_L}\right)^2} + i \cdot \left(\frac{\nu}{\omega_L}\right) \cdot \frac{\left(\frac{\omega_p}{\omega_L}\right)^2}{1 + \left(\frac{\nu}{\omega_L}\right)^2} \quad . \quad (2.22)$$

Equation (2.22) also follows when a collisional term $-\nu\vec{j}$ is considered on the right-hand side of the linearized force equation in Equation (2.16). ν is not specific to a damping mechanism and can describe energy loss due to electron-ion collisions or wave-particle interaction [57]. Note, that the consideration of damping in the dielectric function automatically leads to a universal absorption mechanism (polarization-independent), termed

¹not to be confused with the Airy *pattern* resulting from refraction at a circular aperture

collisional absorption.

Integration of $|E_{res}|^2$ with $\epsilon(z)$ from Equation (2.22) over the plasma gradient then results in an absorption fraction $f_A \sim \phi^2(\tau)/2$ with $\phi(\tau)$ from Equation (2.21). Optimal absorption is achieved for $\tau_{opt} = 0.8$, corresponding to $\theta_{opt} \approx 15^\circ$ for $L = 5\lambda$. In a physical picture, θ_{opt} optimizes the electric field E_z along the plasma gradient driving the plasma waves (large θ optimal) and E_{res} , which decreases with a growing distance between the reflection point and n_c (small θ optimal). The model for resonance absorption (a solution for θ at τ_{opt}) breaks down at $L/\lambda = 0.08$, which is however the preplasma regime reached with ultrashort laser pulses. The case of steep gradients will therefore be treated in the following.

Step Plasma Gradients

Brunel Heating For an electromagnetic p-polarized wave obliquely impinging onto a steep ($L_p/\lambda \ll 1$), highly overdense ($n_e/n_c \gg 1$) plasma gradient, the evanescent field in the overdense plasma decays over the skin depth $l_s = c/\omega_p$ or $l_s/\lambda = (1/2\pi) \cdot \sqrt{n_c/n_e}$ [48]. This is the standard interaction scenario for ultrashort, relativistic laser pulses with solid targets. Exemplarily, for an overdense plasma with $L_p/\lambda = 0.1$ and $n_e/n_c = 100$ follows $l_s/\lambda \approx 0.02$. In comparison, for the oscillation amplitude of an electron in the laser field hold $z_{os} = 0.1 \mu\text{m} = \lambda/10$ for a laser wavelength of $1 \mu\text{m}$ and an intensity of 10^{18} W/cm^2 (Equation (2.20)). Hence, the excursion length of the electrons is in the order of L_p and resonance absorption fails as the plasma region around n_c is too narrow to support plasma waves. On the other hand, $z_{os} \gg l_s$, so that electrons from the skin depth region are pulled out into the plasma-free space in front of the target surface by the electric field. When accelerated back into the target in the next half-cycle of the laser field, the electrons propagate freely into the target bulk with a velocity v_{os} (Equation (2.20)) as the laser can only penetrate up to l_s . This absorption mechanisms is the Brunel or vacuum heating mechanism [58], in which electrons gain energy directly in the oscillating laser field instead of an electrostatic plasma mode (resonance absorption, Section 2.3.2).

Brunel heating, as resonance absorption, leads to a supra-thermal or *hot* electron distribution in the plasma. The according mean energy of the hot electrons is generally characterized by a hot electron temperature $k_B T_h$, or short T_h . For Brunel heating, T_h scales with the laser intensity I_L as $T_h \propto (I_L \cdot \lambda^2)^a$ with $1/3 \leq a \leq 1/2$ [59]. The role of hot electrons for laser-driven proton acceleration will be discussed in Section 2.6.

2.4. Relativistic Laser-Plasma Interaction

The laser-plasma interaction processes discussed so far, e.g. resonance absorption and Brunel heating, are relevant for a broad laser intensity range starting at $\sim 10^{14} \text{ W/cm}^2$. Access to a new class of interaction phenomena is given at $I_L \sim 10^{18} \text{ W/cm}^2$ (for $\lambda = 800 \text{ nm}$), at so-called *relativistic* laser intensities.

2.4.1. Single Electron Dynamics in a Relativistic Laser Field

The linearized force equation (Equation (2.16)), starting point for the treatment of wave propagation in a plasma, neglects the magnetic field contribution (Equation (2.11)). This assumption is valid until the oscillation velocity v_{os} (Equation (2.20)) approaches c , the speed of light, and the relativistic laser-plasma interaction regime is reached. In that case, the transverse oscillatory electron motion along the electric field direction is superposed by a longitudinal drift motion in the wave propagation direction. Representative electron trajectories are plotted in Figure 2.4.

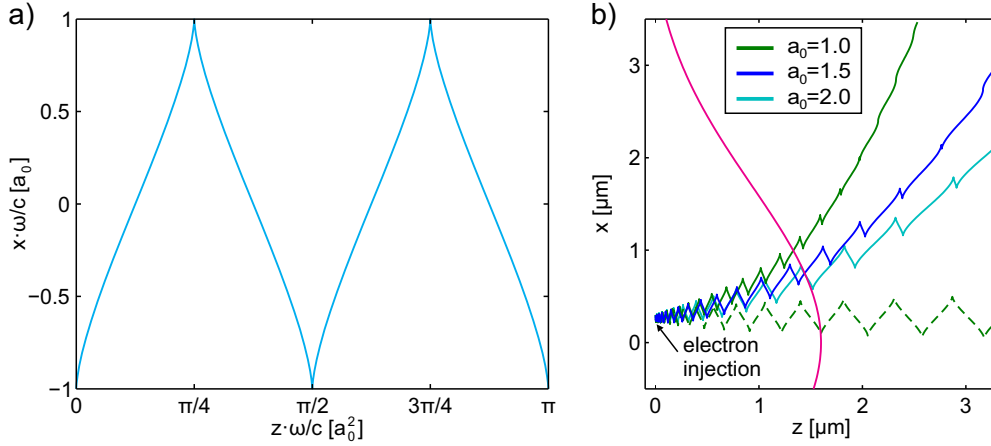


Figure 2.4.: Single electron dynamics in a relativistic laser field. a) Laboratory-frame trajectory of an initially resting electron in an electromagnetic field linearly polarized in x-direction (electric field) and propagating in z-direction. For the trajectory holds [48]: $x \cdot \omega_L/c a_0 = -\cos \phi$ and $z \cdot \omega_L/c a_0^2 = 1/4 \cdot (\phi - 1/2 \cdot \sin(2\phi))$ with $\phi = \omega_L(t - z/c)$. b) Comparison of the electron trajectories in a spatially homogeneous and spatially inhomogeneous laser pulse. The magenta line represents the spatially (full width at half maximum FWHM = 4 μm) and temporally (FWHM $\tau_L = 20$ fs) Gaussian intensity profile of the laser pulse at $\lambda = 800$ nm. The pulse propagation is along the z-direction and the pulse maximum reaches $z = 0$ at 50 fs. The electron in the homogeneous laser field (dashed line) rests again after the pulse has passed, whereas the consideration of the spatial profile (solid lines) leads to ponderomotive scattering and a net energy gain. The scattering angle decreases with increasing a_0 .

The non-relativistic and the relativistic laser-plasma interaction regime are separated by the condition $a_0 \sim 1$ ($I_L \sim 10^{18}$ W/cm² at $\lambda = 800$ nm), where a_0 is termed the normalized vector potential. a_0 equals the ratio of the momentum of the electron oscillation $m_e v_{os}$ and $m_e c$:

$$a_0 = \frac{eE}{m_e c \omega_L} = \sqrt{\frac{I_L [\text{W/cm}^2] \cdot \lambda_L^2 [\mu\text{m}^2]}{1.37 \cdot 10^{18}}} \quad (2.23)$$

The Ponderomotive Force

The high oscillation velocities at relativistic intensities automatically involve large oscillation amplitudes l_{os} in the micrometer-range in the electric field of the laser (Equation (2.20)). l_{os} is hence comparable to the micrometer-size focal spots generally applied in experiments for solid-target laser-driven particle acceleration (Section 2.6). In that case, an initially resting electron samples the intensity gradient of the laser pulse during the first half-cycle of the field oscillation: Starting in the center of the focal spot, it is accelerated towards the low-intensity edge region of the focal spot during the first half-cycle of the field oscillation. Now subjected to a reduced field strength, the electron cannot return to its starting point and finally leaves the focal spot region with a finite velocity (Figure 2.4). This process is termed ponderomotive scattering and the electron is ejected from the focal spot region under an angle $\cos \alpha_{ps} = \sqrt{\gamma^{-1}/\gamma+1}$ relative to the laser pulse's propagation direction [48]. α_{ps} decreases from 90° for the non-relativistic case, i.e. transverse emission, as the Lorentz factor γ increases.

In the non-relativistic case ($a_0 \ll 1$), the corresponding ponderomotive force, which an electron is subjected to in a harmonic electric field with a spatially varying amplitude

$\vec{E}_0(\vec{r})$, is given by [48]

$$\vec{F}_p^{non-rel} = -\frac{e^2}{4m_e\omega_L^2} \cdot \vec{\nabla} \vec{E}_0^2(\vec{r}) \quad . \quad (2.24)$$

This expression can be derived from the force equation (Equation (2.11)) for the electron fluid, taking into consideration a first-order expansion (gradient) of the spatially varying laser field and averaging over the high temporal frequencies [57].

The (ponderomotive) energy U_p gained during ponderomotive scattering by a free electron initially at rest is given by $U_p = m_e c^2 \cdot (\bar{\gamma} - 1)$ with $\bar{\gamma}$ being the Lorentz factor averaged over a laser cycle. In the limiting case of $a_0 \ll 1$ holds

$$U_p^{non-rel} = m_e c^2 \cdot \left(\sqrt{1 + \frac{a_0^2}{2}} - 1 \right) \quad . \quad (2.25)$$

A similar expression for the Lorentz factor can be derived in the case of electron acceleration at a steep interface between vacuum and an overdense plasma, where the ponderomotive force can be balanced by an electric field set up at the interface: $\gamma = \sqrt{1 + a_0^2 \sin^2 \omega_L t}$ (e.g. [60]). The role of this mechanism for electron acceleration in the relativistic regime will be discussed in Section 2.5.1.

2.4.2. Relativistic Plasma Optics

At relativistic laser intensities, when $v_{os} \rightarrow c$, the optical plasma properties are influenced by three mechanisms, firstly ponderomotive scattering, secondly the relativistic mass of the oscillating electron and thirdly the nonlinear electron motion in the laser field. The latter effect results in nonlinear Thomson scattering [61].

The relativistic mass $m^{rel} = \gamma \cdot m_e$ affects the plasma frequency ω_p (Equation (2.9)) and hence the plasma's index of refraction n_r^{rel} . It becomes a function of the laser intensity I_L and as γ increases monotonically with I_L , hence does n_r^{rel} . In first order holds:

$$n_r^{rel} = \sqrt{1 - \left(\frac{\omega_p / \sqrt{\bar{\gamma}}}{\omega_L} \right)^2} = \sqrt{1 - \frac{n_e}{n_c \cdot \bar{\gamma}}} \quad . \quad (2.26)$$

For a relativistic, finite-width (spatially) laser pulse propagating in an underdense plasma, relativistic self-focusing following from Equation (2.26) can hence compensate for the beam diffraction and facilitate collimated beam propagation over a long distance (relativistic self-channeling, [48]). The focusing effect is enhanced by electrons being ponderomotively scattered from the high-intensity region, so that n_r^{rel} further increases in the central part of the pulse as n_e decreases.

For an overdense target, relativistic transparency occurs, an effect that plays a significant role in advanced laser-ion acceleration schemes [16, 33]. In the non-relativistic intensity case, the critical density n_c , up to which a laser pulse can propagate, is defined by Equation (2.18). If the laser pulse intensity increases to $a_0 \sim 1$, e.g. during the rising pulse edge, the relativistic electron mass m^{rel} replaces m_e and hence n_c increases. That results in a larger penetration depth of the laser into the plasma and hence an increased interaction volume [62].

2.5. Electron Acceleration and Propagation in Overdense Plasmas

At laser intensities of maximal 10^{21} W/cm², laser-driven proton and ion acceleration - due to the comparatively large ion inertia - depends on quasi-static electric fields, e.g. at the target surfaces (TNSA, Section 2.6). These fields are set up by a distribution of *hot* electrons, i.e. electrons accelerated to megaelectronvolt energies in the laser field or connected electrostatic fields (e.g. resonance absorption, Section 2.3.2). Hot electrons, in contrast to the *cold* electrons restricted to the target bulk, can propagate and hence transport energy through the target (Section 2.5.2). The hot electron temperature T_h and density n_h determine the achievable accelerating gradients in the quasi-static electric fields (Section 2.6), making scaling models for T_h and n_h important. According scaling models for T_h will be discussed in the first part of this section, focusing on laser-driven electron acceleration at overdense plasma surfaces and relativistic intensities. Secondly, key features of the propagation of the megaelectronvolt electron distribution through the target bulk will be summarized, including instabilities the electron transport can be subjected to.

2.5.1. Electron Acceleration at Overdense Plasma Surfaces

The collisionless absorption mechanisms resonance absorption and Brunel heating depend on oblique laser incidence onto the target surface in order to be operational. On the other hand, the discussion in Section 2.4 shows that for relativistic laser intensities and the presence of a field gradient, the transverse oscillatory motion of electrons in the laser field can be translated into a net energy gain in longitudinal direction. At overdense plasma surfaces, this electron acceleration mechanism is termed $v \times B$ heating [63]. It results in electron bunches being injected into the target bulk at twice the laser frequency (Figure 2.4, [63]). The $v \times B$ mechanism has therefore been identified experimentally via the second harmonic coherent transition radiation emitted from the target rear surface originating from the $2\omega_L$ -electron bunches [64]. More indirect indications for the relevance of $v \times B$ heating at relativistic laser intensities is given by data in [27], where the maximum proton energy was shown to be independent from the angle of incidence (normal vs. oblique). First experimental data in the range of $I_L \lesssim 10^{19}$ W/cm² for the hot electron temperature T_h as a function of the laser intensity by Malka *et al.* [65] followed the scaling

$$T_h = m_e c^2 \cdot \left(\sqrt{1 + a_0^2} - 1 \right) \quad , \quad (2.27)$$

which is in agreement with [66] and corresponds to the ponderomotive potential of the laser pulse (Equation (2.25)) for the non-relativistic case². Experimental data from Chen *et al.* for higher laser intensities up to $I_L \lesssim 10^{21}$ W/cm² however indicate that the ponderomotive scaling overestimates T_h ([67], see Figure 2.5 for $a_0 \gtrsim 5$). Instead, they apply an empirical scaling proposed by Beg *et al.*: T_h [MeV] = 0.215 · (I_L [10¹⁸ W/cm²] · λ^2 [μm²])^{1/3} [68, 69].

A relativistic analytic scaling model for the mean kinetic energy $T_h(I_L)$ for the hot electron distribution has however only been presented recently by Kluge *et al.* [43]. Independent from a specific acceleration mechanism, T_h follows as the weighted ensemble average of the kinetic energy. Since the laboratory time is not Lorentz invariant, the ensemble average over time is replaced by the average over the laser field's phase ϕ , over which the electron

²In Equation (2.25), a_0^2 is replaced by $a_0^2/2$ in order to account for the cycle average of the harmonically oscillating laser field. This scaling is for instance used in [13].

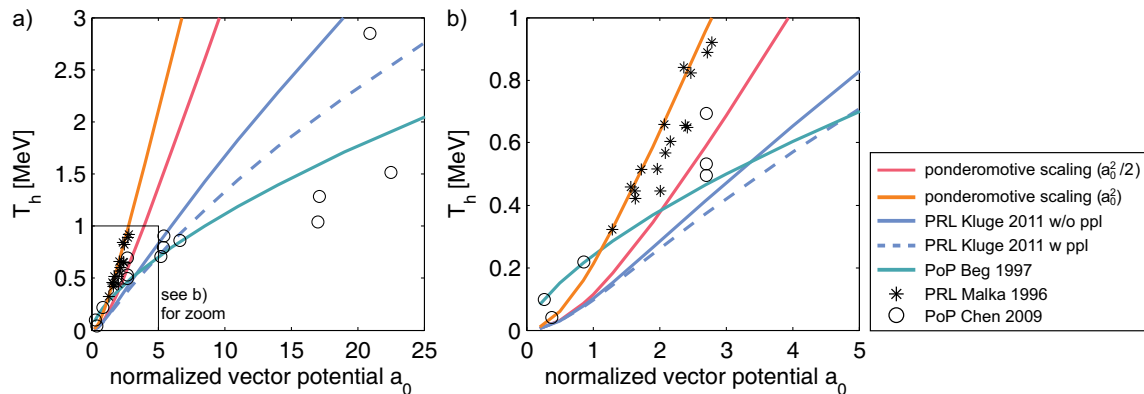


Figure 2.5.: Scaling of the hot electron temperature at overdense plasma surfaces. The hot electron temperature T_h as a function of a_0 is plotted for the ponderomotive scaling with a_0^2 and $a_0^2/2$, the relativistic scaling by Kluge *et al.* with and without preplasma (Equation (2.28), [43]) and the scaling by Beg *et al.* [68]. Additionally, three experimental data sets are shown, recorded at the Ti:Sapphire Callisto laser system (up to 10 J laser energy, $\tau_L = 100$ fs, $\lambda = 800$ nm) and the RAL Vulcan laser system (up to 400 J laser energy, $\tau_L = 400$ fs, $\lambda = 1053$ nm) by Chen *et al.* [67] and CEA/LV laser system (up to 40 J laser energy, $\tau_L = 300$ - 500 fs, $\lambda = 1056$ nm) by Malka *et al.* [65].

distribution $dN/d\phi$ is constant. This treatment results in

$$T_h = m_e c^2 \cdot \left(\frac{\pi}{2K(-a_0^2)} - 1 \right) , \quad (2.28)$$

where K is the complete elliptical integral of the first kind for a steep plasma gradient [43]. For $a_0 \ll 1$, Equation (2.28) converges to Equation (2.27) with $a_0^2 \rightarrow a_0^2/2$ (Equation (2.25)) [43]. All scaling models and representative data points are summarized in Figure 2.5.

2.5.2. Propagation of Dense Electron Currents Through the Plasma

The megaelectronvolt energy electron bunches produced in the laser-plasma interaction and injected into the target over the laser pulse duration τ_L form a dense current J_h . It can reach the megaampere level, as a simple estimation shows:

$$J_h = \frac{-e}{\tau_L} \cdot N_h = \frac{-e}{\tau_L} \cdot \frac{\eta E_L}{k_B T_h} = \frac{-e}{30 \text{ fs}} \cdot \frac{0.25 \cdot 2.9 \text{ J}}{2.5 \text{ MeV}} \approx -10 \text{ MA} . \quad (2.29)$$

Here, a laser intensity of $5 \cdot 10^{20} \text{ W/cm}^2$ is assumed, from which follows $k_B T_h = 2.5 \text{ MeV}$ (Equation (2.28)). N_h is the hot electron number, E_L the laser energy and $\eta = 0.25$ the absorption efficiency or ratio of laser energy into hot electrons [43].

For an electron with $E_{kin} = 2.5 \text{ MeV}$, calculations based on the collisional stopping power following the Bethe-Bloch treatment give a stopping range of $R_{BB} = 570 \mu\text{m}$ in aluminum [70]. Megaampere currents, however, interact more strongly with the comparably cold (mean electron energies of ~ 10 - 100 eV [71]) electron distribution that constitutes the target bulk and are subjected to so-called non-collisional inhibition effects.

The concept of non-collisional inhibition or ohmic stopping was introduced by Bell *et al.* [72], who showed that an intense hot electron current density \vec{j}_h propagating through a solid density plasma has to draw a return current density \vec{j}_c from the cold plasma electrons with $\vec{j}_h + \vec{j}_c \approx 0$. If uncompensated, the magnetic field generated by \vec{j}_h would otherwise violate energy conservation, exceeding the input energy E_L by orders of magnitude. Re-

sulting from \vec{j}_c and the finite resistivity ρ_c of the cold background plasma is an electric field $\vec{E}_c = \rho_c \vec{j}_c$, which determines the hot electron propagation in the target [48].

The influence of the target resistivity on the propagation of hot electron is confirmed experimentally, indicating a strong connection to the spatial distribution of protons accelerated in the TNSA regime. These are hence often used as a diagnostic tool to study the electron transport. Fuchs *et al.* [73], for instance, have investigated the electron transport in insulators and conductors, yielding disrupted versus smooth proton beam profiles in the two cases, respectively. In an insulator, establishment of a return current firstly requires the allocation of free electrons through ionization, whereas a conductor can provide them immediately [74]. But even the material of a conducting metal foil can influence the spatial distribution of the hot electron current inside the bulk (smooth vs. filamented) via resistive magnetic fields generated by the return current [75, 76]:

$$\frac{\partial B_R}{\partial t} = -\nabla \times (\rho_c \vec{j}_c) = -(\rho_c \nabla \times \vec{j}_c + \nabla \rho_c \times \vec{j}_c) \quad . \quad (2.30)$$

The second term describes gradients in the resistivity, which due to $\rho_c \sim Z/T^{3/2}$ are dependent on the material's ionization state and heat capacity and hence become element-specific. For thin targets, the reflux current of hot electrons between the space-charge fields at both target surfaces has to be taken into account as well, which further complicates the treatment of electron transport [71]. Moreover, as for instance shown in three-dimensional simulations of an overdense plasma irradiated with a laser intensity of $2 \cdot 10^{19}$ W/cm² by Sentoku *et al.*, the hot electron transport is generally subjected to plasma instabilities [77]. A brief overview of plasma instabilities will hence be given in the following Section 2.5.3.

2.5.3. Instabilities in Plasmas

Excitations in plasmas (e.g. plasma waves) can oscillate (electron plasma waves, Section 2.3), be damped or grow due to a positive feedback loop. The latter case leads to plasma instabilities. Even when restricting the discussion to the small subtopic of laser-driven ion acceleration at solid density targets, the abundance and significant role of instabilities in plasma physics can be illustrated. Whereas the enhancement in ion acceleration in the break-out afterburner (BOA) regime [78] was attributed to a Buneman-type instability [79], in experiments in the radiation pressure acceleration (RPA) regime a Rayleigh-Taylor instability was shown to be detrimental for the performance [80]. The experimental characterization of the instability onset and growth in the case of micro- to nanometer thick solid targets is challenging but methods such as proton radiography/deflectometry [81] and high harmonic generation have been employed successfully [82]. Otherwise, spatially modulated proton beam profiles often serve as a diagnostic tool for instability/filamentation during the hot electron transport in the target volume [80, 46]. Instabilities can for instance be classified according to their excitation or driving mechanism [83], as summarized in Table 2.2.

Exemplary Instability Analysis - Weibel Instability

In order to discuss the basic elements of instability analysis, the case of the Weibel instability will be discussed following the original work by Weibel [85]. The Weibel instability is a growing mode solely in the electron fluid of the plasma, that occurs for a sufficiently anisotropic velocity distribution [85]. Starting point is the Vlasov equation (Equation (2.10)) with f_j being anisotropic. Furthermore, the Lorentz-force term is treated as a perturbation ($(\vec{E}_{pt} + \vec{v} \times \vec{B}_{pt}) \cdot \partial f_{pt} / \partial \vec{v}$), where \vec{E}_{pt} , \vec{B}_{pt} and f_{pt} denote perturbation terms

| | |
|------------------------|---|
| Streaming | driven by relative drifts of different species in the plasma, e.g. energetic particles streaming through a plasma ex.: Buneman instability [84, 79] |
| Rayleigh-Taylor | driven by an external force on a plasma boundary (sharp or with gradient) ex.: radiation pressure driven RT instabilities [66, 80] |
| Universal | driven by the plasma pressure in confined plasmas |
| Kinetic | driven by an anisotropy in the velocity distribution of a plasma species (deviation from the equilibrium Maxwellian distribution) ex.: Weibel instability [85] |

Table 2.2.: Classification of instabilities. Classification of instabilities according to their driving mechanisms, including exemplary instabilities relevant in the field of laser-driven ion acceleration. After [83].

to the electric and magnetic field and the distribution function. Assuming a harmonic space- and time-dependence for all first-order perturbation terms ($\sim \exp(i\omega_L t + i\vec{k} \cdot \vec{r})$) and with further assumptions³, a dispersion relation for the transverse electromagnetic waves can be derived [85]:

$$\Omega^4 - \left(1 + \left(\frac{K}{u_0}\right)^2\right) \cdot \Omega^2 - K^2 = 0 \quad \text{for} \quad \Omega = \frac{\omega_L}{\omega_p} \quad \text{and} \quad K = \frac{u_0 k}{\omega_p} \quad . \quad (2.31)$$

ω_L and ω_p are the laser and plasma frequency (Equation (2.9)) and u_0 a scaling factor in the distribution function f_j (see footnote). The function $D(\Omega, K, u_0 = 1) = \Omega^4 - (1 + K^2) \cdot \Omega^2 - K^2$ is plotted for $K = \{1, 2, 3, 4\}$ in Figure 2.6 as a function of Ω , showing that for $K \neq 0$ two of the four roots of Equation (2.31) are real. Of the two imaginary roots, one is negative

$$\Omega = - \sqrt{\frac{1}{2} \left\{ \left(1 + \left(\frac{K}{u_0}\right)^2\right) - \sqrt{\left(1 + \left(\frac{K}{u_0}\right)^2\right)^2 + 4K^2} \right\}} \quad , \quad (2.32)$$

and leads to a growing mode or instability with $\sim \exp(\gamma t)$ following from the ansatz $\sim \exp(i\omega_L t)$ for the perturbative parameters. The dispersion relation (Equation (2.31)) and the growth rate $\gamma = |\Im(\Omega)| \cdot \omega_p$ (Equation (2.32)) are central parameters in describing and identifying instabilities e.g. in numerical simulations.

A physical picture of the Weibel instability was given by Fried [86] (see [83]), together with an extension of Weibel's theory to instability modes perpendicular to the direction of the anisotropy. This scenario is now generally referred to as a Weibel instability [87]. Moreover, the term *Weibel-like* instability is used to summarize the filamentation and the Weibel instability, which both give rise to magnetic fields in plasma [88]. The origin of the instability is however different and whereas the Weibel instability occurs due to a temperature anisotropy, the filamentation instability is triggered in plasmas with counter-

³1. For the distribution function holds $f_j(\vec{v}) = F(\sqrt{v_x^2 + v_y^2}, v_z)$ and $f_j \sim \exp(-v_0^2/2u_0^2 - v_3^2/2u_3^2)$ is Gaussian. The width of the distribution function in radial (x -/ y -direction) and z -direction are u_0 and u_3 . , 2. $\omega_L k / u_3 \gg 1$ or equivalently $u_0 \gg u_3$

streaming electron currents [88]. A common scenario in laser-driven plasmas giving rise to a filamentation instability are the counter-streaming hot electrons accelerated at the target front surface, and the cold return generated in the target bulk [89]. In the context of this thesis, the term *Weibel instability* (WI) will be used to denote all Weibel as well as Weibel-like instabilities.

Experimental studies on the Weibel instability are generally performed in connection with laser-driven fusion experiments, in which the occurrence of a WI can prohibit efficient heating of the fusion material by laser-accelerated electrons [90]. Hence, the majority of experimental studies considers picosecond-long laser pulses with ~ 10 -100 J of laser energy, which are brought into interaction with at least several $10\ \mu\text{m}$ thick targets (e.g. Al-coated glass substrate [91], dielectric targets [92], metal foils [93], foam targets [94], conducting wires [81]). For the case of ~ 10 fs long laser pulses, a WI has been observed in plasmas from metal-coated dielectric targets using magneto-optical imaging [95]. Neither study investigates the translation of the filamentation pattern in the laser-driven electron distribution into the TNSA-accelerated protons from the target rear surface.

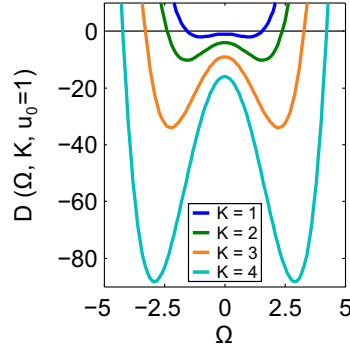


Figure 2.6.: Dispersion relation of the Weibel instability. Plot of $D(\Omega, K, u_0 = 1) = \Omega^4 - (1 + K^2) \cdot \Omega^2 - K^2$ for $K = \{1, 2, 3, 4\}$. The dispersion relation is given by solutions to the equation $D(\Omega, K, u_0) = 0$. The real roots correspond to the intersections with the black line in the plot.

2.6. Laser-Driven Ion Acceleration

As the final point in this chapter, it will be sketched how the distribution of hot ($T_h \sim \text{MeV}$) electrons (Section 2.5.1) accelerated in the laser field transfers parts of its energy to ions in a quasi-static electric fields. The focus is on laser-driven ion acceleration at overdense targets, i.e. the target normal sheath acceleration (TNSA) mechanism and the according scaling models.

2.6.1. The Physical Picture of TNSA

TNSA was the first acceleration scheme to yield intense beams of protons with energies of several 10 MeV [11, 12, 13] at PW long-pulse ($\tau_L = 500$ fs to the order of picoseconds) lasers. Figure 2.7 summarizes the three stages of the TNSA process [13], of which the hot electron generation and propagation (Figure 2.7a) is discussed in Section 2.5. The hot electron distribution, refluxing through the target, exits at the rear surface and establishes a space-charge electric field, which is quasi-static during the pulse duration. Along the target normal direction, the field has a spatial extend of a Debye length (Equation (2.7))

and is termed Debye sheath. The according electric field strength is determined by the hot electron temperature T_h and density n_h and can be estimated to TV/m [13]:

$$E_{TNSA} \sim \frac{k_B T_h}{e \lambda_D} \propto \sqrt{n_h k_B T_h} \sim \frac{\text{TV}}{\text{m}} . \quad (2.33)$$

Hydrocarbon contaminants, naturally present on the target surface, but bulk material as well, are ionized in the Debye sheath field and the resulting ions gain kinetic energies of $\sim \text{MeV}/\mu\text{m}$ per nucleon. Due to their charge-to-mass ratio, protons are accelerated most efficiently. The accelerated pulse of multiple ion species (e.g. protons, carbon, oxygen) propagates into vacuum, quasi-charge-neutralized by copropagating electrons from the Debye sheath. The Debye sheath field is predominantly oriented along the target normal direction, hence the *target normal* in TNSA. A sheath field is also established at the target front surface, but several experiments confirmed that the highest energy ions originate from the non-irradiated target rear surface [96, 97].

Apart from the accelerating fields, which exceed those of conventional accelerators by a factor $\sim 10^6$, TNSA also provides short (picosecond range, [16]) and intense ion pulses ($\sim 10^{13}$ protons above 10 MeV energy [12]) with an ultra-low emittance [15]. It is only limited by the collision rate with the Debye sheath hot electrons [15]. The particle spectra yielded in TNSA are exponential with a well-defined maximum or cut-off energy (e.g. [12]). Apart from screening effects in the accelerated particle distribution, the spectral shape is attributed to the lateral (parallel to the target surface) structure of the accelerating field E_{TNSA} , which yields a locally varying cut-off energy. The lateral field structure - caused by a laterally Gaussian-shaped sheath density n_h [98] - is also responsible for the decrease in angular beam divergence ($\sim 40^\circ - 5^\circ$, [99]) and decrease in source size ($\lesssim 100 \mu\text{m}$, [100, 99]) with increasing ion energies [15].

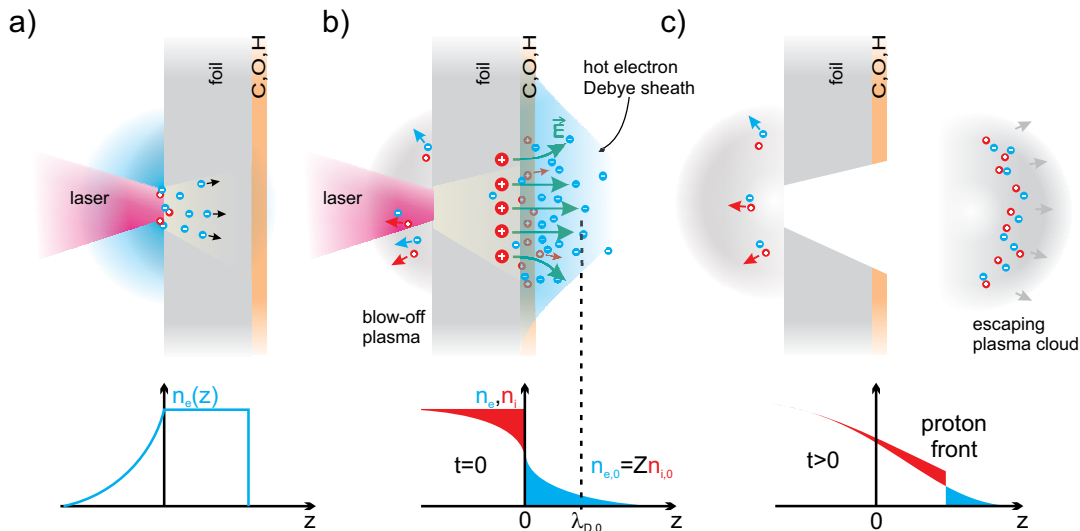


Figure 2.7.: Target normal sheath acceleration - TNSA. The three stages of the acceleration process. a) Laser absorption and electron acceleration. b) Hot electron transport through the target and setting-up of the Debye sheath. Ionization of the contaminant layer (C, H, O). c) Expansion and propagation of the charge-neutral electron-ion plasma into vacuum. n_e is the electron, n_i the ion density and Z the ion charge state.

2.6.2. Scaling Models for TNSA

Since numerical simulations under realistic laser-target interaction conditions are time-consuming, scaling models are developed as a means to study the parameter space in TNSA. An overview over the corresponding scaling models is given in [101]. A recent model, that is benchmarked using data from the Draco I laser facility [54], is published in [102]. Here, the electrostatic model by Schreiber *et al.* [41] and the isothermal expansion model by Mora [40] will be presented.

Electrostatic Scaling Model

Schreiber *et al.* [41] model the TNSA acceleration mechanism (Section 2.6) as driven by a positive surface charge at the target rear that is induced by the hot electron Debye sheath (Figure 2.7). The sheath and hence the surface charge are confined to an area with radius $B = r_L + d \cdot \tan \theta$, derived from the laser focal spot radius r_L and its projection onto the rear surface for a target thickness d and a hot electron divergence angle θ . From the N_h hot electrons accelerated at the target front surface, a ratio $Q/N_h = 2\lambda_D/\tau_L \cdot c$ contributes to the Debye sheath. Here λ_D is the Debye length⁴ and τ_L the laser pulse duration. Q is in agreement with the self-consistently induced surface potential for a thermal electron spectrum with a mean energy $k_B T_h$.

A proton, described as a test particle in the potential of the induced surface charge density $Q \cdot e/\pi \cdot B^2$, can gain a maximum energy E_∞^p for an infinite acceleration time [41]:

$$E_\infty^p = k_B T_h \cdot \frac{B}{\lambda_D} = 2m_e c^2 \cdot \sqrt{\frac{\eta P_L}{P_R}} \quad . \quad (2.34)$$

η is the absorption efficiency of laser energy into hot electron energy, P_L the laser power and $P_R = 8.71$ GW the relativistic power unit. Considering the TNSA dynamics, the acceleration process terminates when the electron population of the Debye sheath leaves the target surface. That is accounted for in a correction factor X for E_∞^p to yield the maximum proton energy E_{max}^p for a finite acceleration time [41, 103]:

$$E_{max}^p = X^2 \cdot E_\infty^p \quad \text{with} \quad X = \tanh\left(\frac{\tau_L}{2\tau_0}\right) \quad \text{and} \quad \tau_0 = \frac{B}{\sqrt{\frac{2E_\infty^p}{m_p}}} \quad . \quad (2.35)$$

With m_p being the proton mass, it takes τ_0 for a proton with energy E_∞^p to propagate the distance B away from the target surface, which corresponds to the region of an approximately constant electric field [104].

The electrostatic model has specific relevance for the case of ultrashort laser pulses, because the assumption of a quasi-static field matches the experimentally confirmed acceleration conditions during the intra-pulse phase of TNSA for ultrashort laser pulses [27].

Plasma Expansion Scaling Model

A second approach to model TNSA is an isothermal [40] or adiabatic [105] plasma expansion into vacuum, i.e. a fluid approach. In the former case, the one-dimensional expansion of cold protons, initially resting in the negative half-space ($z \leq 0$), is described. It is driven by the electrostatic potential Φ of a thermal electron distribution with mean energy $k_B T_h$.

⁴defined with an additional factor 2 in the numerator compared to Equation (2.7)

$k_B T_h$ is assumed constant, hence an isothermal model. The expansion dynamics are described by Poisson's equation for Φ and the according electron density distribution, as well as the continuity equation and equation of motion for the ions in the potential Φ [40]. Most relevant for the scaling of the proton energy with the input laser parameters is the behavior of the proton front, i.e. the protons originating from $z=0$. Numerical solution of the set of equations describing the plasma expansion results in an expression for the proton front velocity and hence the maximum proton energy [40]:

$$v_{front}^p \sim 2c_s \cdot \ln \left(\tau + \sqrt{\tau^2 + 1} \right) \quad \longrightarrow \quad E_{max}^p \sim 2k_B T_h \left[\ln \left(\tau + \sqrt{\tau^2 + 1} \right) \right]^2 \quad . \quad (2.36)$$

It holds $\tau = \omega_{pp} t / \sqrt{2e^1}$, and $c_s = \sqrt{k_B T_h / m_p}$ is the ion sound velocity, $\omega_{pp} = \sqrt{n_h e^2 / \epsilon_0 m_p}$ the proton plasma frequency, m_p the proton mass, n_h the hot electron density and e^1 is Euler's number. Moreover, the expansion model predicts the thermal proton (ion) spectrum observed experimentally for TNSA [12].

As in the electrostatic model [41], the assumption of an isothermal plasma, i.e. an infinite energy reservoir, demands the artificial truncation of the acceleration process by setting t in Equation (2.36) to a finite value. Fuchs *et al.* [42] found $t^{long} = 1.3 \tau_L$ for $\tau_L = 0.15 - 10$ ps by fitting Equation (2.36) to experimental data. For the case of ultrashort laser pulses with $\tau_L \sim 10$ fs, an energy transfer time between electrons and ions has to be taken into account, estimated to 60 fs: $t^{short} = 1.3 \cdot (\tau_L + 60 \text{ fs})$ [106].

2.6.3. Experimental Overview

In the following, experimental results considered central for the understanding and improvement of TNSA will be presented. Moreover, experimental studies are discussed, which show signatures of the complex plasma physics underlying TNSA, e.g. plasma instabilities. As a last point, the role of the plasma conditions for the TNS-accelerated proton distribution is highlighted.

Tailoring TNSA

Efforts to improve the TNSA performance are concerned with increasing the particle yield [107, 108, 109, 110, 111, 32], performing species-specific acceleration ($\sim 10 \mu\text{m}$ thick foils e.g. [112], $\sim 10 \text{ nm}$ thick foil [113]), influencing the ion beam divergence [114, 115, 108, 116, 117, 118, 119], increasing the cut-off energy [16, 33] and tailoring of the particle spectrum [120, 121, 122, 123]. The two latter points are discussed in more detail.

Avenues to Higher Particle Energies Avenues to increased ion and particularly proton energies are directly suggested by Equation (2.33), showing that the hot electron parameters T_h and n_h at the target rear surface control the accelerating field strength. Ways to actively manipulate either parameters from the past 15 years are extensively reviewed in [16, 33], including e.g. optical preplasma manipulation and special target designs. Most successfully have conical-shaped targets and reduced-mass targets (RMTs) proven to yield increased proton energies, the former having set a new record of a maximum proton energy of 67.5 MeV at the Trident laser facility in 2009 [30]. The enhancement is attributed to an increase in T_h through a continuous electron acceleration along the inner cone wall [31]. In reduced-mass targets, i.e. targets with a finite transverse size, refluxing of the hot electrons within the target volume leads to a time-averaged increased electron density (n_h), temperature (T_h), homogeneity and particle source size in the accelerating Debye

sheath [108, 32]. Both experiments by Buffechoux *et al.* and Zeil *et al.* show a doubling of the proton cut-off energy and an increase in the particle yield when comparing large foils and the optimal RMT size. The successful experimental realizations of RMTs range from freestanding droplet targets [124, 125, 126, 127] to metal foils supported by wires [108, 128, 129], to micromachined RMTs [32].

Spectral Shaping In an expanding multi-species plasma (e.g. from hydrocarbon contaminants), the different ion species spatially separate in expansion direction, leading for the lightest ions to an accelerating field structure that is influenced by the expansion fronts of the heavier ions [33]. Those multi-species effects cause spectral modulations up to narrow-band peaks and they can alternatively be grown by accelerating a light species from a heavy target substrate [120, 121, 122, 123]. The effect is enhanced by artificially restricting the lateral source size to the central and hence homogeneous part of the Debye sheath [120]. Another approach to spectral modification are double-pulse or staged acceleration schemes [130].

Experimental Signatures of Complex-Physics Phenomena in TNSA

The discussion mainly focuses on experiments where a large foil target with a thickness in the range of micrometers to ~ 100 nm is irradiated with laser pulses of ~ 10 -100 fs pulse duration. The arising complex-physics phenomena observed are hence either correlated to specific laser pulse properties (temporal intensity contrast, polarization, etc.) or the target material, but not e.g. the target shape.

Modulated Proton Beams The most apparent observation in the TNSA regime, which indicates the complex physical processes underlying the acceleration mechanism, are spatial modulations in the proton beam profiles. These can originate from different stages of the acceleration process, i.e. the electron transport through the target bulk or the ion acceleration at the target rear. In the latter case, either the inherent target surface roughness [131] or engineered surface structures [15] have been observed to be imprinted into the proton beam profiles during the laminar plasma expansion at the target rear. Regarding the electron transport, the target bulk conductivity has a significant influence. Whereas foils from conducting material yield smooth beam profiles, insulating targets often feature modulated or filamented beam profiles, as measured by Fuchs *et al.* [73]. Analysis of the optical radiation generated by the laser-accelerated electron distribution by Mancossi *et al.* has shown that in the case of insulating targets, the electron current is subjected to an instability (ionization front instability) in the target bulk and hence filaments [132]. Gremillet *et al.* have used transverse shadowgraphy in transparent targets to detect electron filamentation in overdense plasmas [91]. Different degrees of filamentation or collimation of the laser-driven hot electron current inside the target bulk have also been observed for metal and hence conducting targets, which is attributed to the generation of resistive magnetic fields from the interplay of the material-specific bulk temperature and ionization (Equation (2.30), [133, 76]). Gizzi *et al.* have shown that a difference in electron current transport through the target bulk caused by resistive magnetic fields can as well be triggered by coating the rear surface of a metal target with a dielectric layer [134]. Experiments comparing diamond versus amorphous carbon targets indicated that the target lattice structure can influence the electron transport [135]. The studies by Antici, Sentoku, Gizzi and McKenna *et al.* [133, 76, 134, 135] use proton beam profiles recorded on radiochromic film to diagnose the electron transport. In some experiments,

the source of the proton beam structure is not traceable [136, 137].

Influence of the Plasma Conditions Whereas the transport characteristics are strongly dependent on the target bulk properties, the acceleration performance regarding the maximum proton energy is strongly correlated with the plasma conditions at the target surfaces. In the according experimental studies, the plasma conditions are either improved by laser pulse cleaning via a plasma mirror [138, 139] or deteriorated by prolongation of the ASE pedestal [45] or application of a second laser pulse at the target front surface [140]. The resulting plasma conditions at main pulse arrival can either be derived from numerical simulations [45, 140] or qualitatively estimated from the change in temporal intensity contrast [138, 139]. In all cases, the maximum proton energy decreases when the plasma conditions are worsened, which is attributed to a pre-heating and -expansion of the target rear surface plasma [45].

Indirectly, the target rear plasma conditions can also be altered by changing the target thickness, as the rear surface pre-expansion is caused by electrons laser-accelerated at the target front surface, which reflux through the target. This leads to a saturation or break-up of the otherwise observed proton cut-off energy increase with decreasing target thickness [45, 138, 139, 123].

Besides pre-heating of the target rear surface, the ASE pedestal of the laser pulse has also been interpreted to launch shocks at the target front surface, which leads to a target-thickness dependent deformation of the rear surface of the target. The experimental signature is an angular deflection of the proton distribution from the expected target normal direction in TNSA [52, 53, 54].

Dollar *et al.* have shown that an artificially created 30 fs long prepulse on the picosecond timescale can trigger a preplasma expansion that - via multi-species effects - allows to manipulate the shape of the energy spectrum of the proton distribution [123].

More challenging to access experimentally is the influence of the preplasma conditions on the initial laser energy absorption at the target front surface. For a 1 ps long laser pulse ($E_L = 115$ J) and preplasma gradients in the range of ~ 10 -100 μm , McKenna *et al.* have shown that self-focusing of laser pulses in the preplasma can increase the absorption efficiency of laser light [107]. In the ultrashort pulse regime and using plane foil targets, two experiments by Ceccotti *et al.* ($I_L^{max} 5 \cdot 10^{18}$ W/cm², [139]) and Zeil *et al.* ($I_L^{max} = 8 \cdot 10^{20}$ W/cm², [27]) have been performed. In the latter case, the presence of a preplasma with a scale length of $L_P \approx 100$ nm (estimated from particle-in-cell simulations) leads to a dominance of $j \times B$ heating [63] and results in a maximum proton energy that is almost independent from the angle of incidence or polarization of the laser pulse [27]. In the experiment of Ceccotti *et al.*, performed at an intensity a factor $\sim 10^2$ lower, the ultra-high pulse contrast from a plasma mirror suppresses preplasma expansion and hence $j \times B$ heating. Efficient coupling of the laser pulse is therefore only given for p-polarization [139]. The collection of data shows the rich effects in TNSA triggered by different plasma conditions.

3. Transverse Modulations in Laser-Driven Proton Beams

In this chapter, an experiment on the laser energy scaling of proton acceleration in the TNSA regime is presented. The study focuses on the effect of non-ideal temporal intensity contrast conditions on the beam profiles of the accelerated proton distribution. These are observed to be a sensitive indicator for changes in the laser-target interaction conditions. Following an introduction, the experimental setup including the Draco I laser system and the experimental results are presented. The data analysis is supported by numerical simulations, which allow for modeling of the plasma dynamics underlying TNSA for different interaction conditions.

3.1. Motivation

3.1.1. The Scalability of TNSA to Increasing Laser Powers

A medical application of laser-driven ion sources (LDIS) as pursued in the Dresden cooperation for laser-driven medical accelerators (Chapter 1) foremostly depends on the accelerator's ability to reliably and tunably provide applicable particle distributions at sufficiently high particle energies of ~ 200 MeV [4]. *Applicable* here refers to a proton distribution with a sufficient particle flux and a smooth beam profile. The latter is the precondition for homogeneous dose distributions [4, 25]. TNSA has shown to provide applicable proton distributions for radiobiological studies using ~ 4000 laser-driven proton pulses at an accuracy level comparable to the conditions at a conventional proton accelerator ([26], A.2). The LDIS research at the HZDR hence currently focuses on the robust TNSA mechanism (Section 2.6).

An increase of the particle energies for a given input laser power can be yielded by optimizing the laser-target interaction conditions via the target design (Section 2.6). Moreover, an equally important access to higher particle energies is the scaling of acceleration mechanisms to higher laser powers. This approach gains particular relevance in view of the increasing availability of PW laser systems [39], such as Draco II at the HZDR.

The laser power or intensity scaling for the maximum proton energy is thereby predicted by analytic models for the acceleration process. Two established models [40, 41] are summarized in Section 2.6.2. The validity of both models has been investigated in several experimental studies, covering the laser powers in the 100 TW-class range at ultrashort pulse ($\tau_L \sim 10$ -100 fs) and long pulse ($\tau_L \sim 1$ -10 ps) laser systems [41, 42, 141, 54]. For the class of ultrashort pulse CPA laser systems with repetition rates of ~ 1 -10 Hz, which are relevant as potential drivers of medical accelerators, the (future) PW laser sources correspond to an approximately sevenfold increase in available laser power on target. A reliable scaling prediction therefore requires experimental studies, particularly due to the fact that the scaling models necessarily represent a simplified and idealized case of the complex laser-target interaction conditions and acceleration process in TNSA.

In the conceptually useful but in itself simplified physical picture of TNSA, proton or ion acceleration using relativistic laser pulses and (relativistically) overcritical targets is

divided in three sub-processes: 1. laser absorption and electron acceleration, 2. electron transport and electric field generation and 3. ion acceleration and propagation into vacuum (Section 2.6.1, Figure 2.7). In the scaling models [40, 41], the first sub-process is considered in the model input parameters T_h and n_h ¹, which are the temperature and density of the hot electron distribution driving the acceleration (Section 2.6.2). The electron transport through the solid density target (Section 2.5.2) is either neglected [40] or modeled as a smoothly diverging electron distribution inside the target with a variable divergence angle θ [41]. The final acceleration process is in both models represented by an acceleration time τ_{acc} , which accounts for the lifetime of the electric field at the target rear and/or the protons' transit time through the field structure [40, 41, 42]. Figure 1.1 in Chapter 1 graphically summarizes these relations.

The above-mentioned successful experimental verification of both scaling models indicates that the parameter set $\{T_h, n_h, \theta, \tau_{acc}\}$ can constitute a valuable description of the TNSA process regarding the prediction of maximum proton energies. On the other hand, each parameter is a representation of the complex light-matter interaction and plasma physics of the acceleration process, e.g. the ionization and plasma formation dynamics (Section 2.1), or the complex effects (e.g. instabilities) of the electron transport through the target bulk (Section 2.5.2). All these depend on the particular laser-target interaction conditions. As a result, the derivation of generalized theoretical models for the parameter set $\{T_h, n_h, \theta, \tau_{acc}\}$ is rendered challenging because the parameters are themselves sensitively influenced by the laser pulse (e.g. energy, duration, polarization, temporal intensity contrast) and target properties (e.g. thickness, material, shape, areal density). This fact is for example reflected in the multitude of scaling models for T_h or the lack of reliable models for the conversion efficiency of laser energy into (hot) electron energy [142].

The scalability of TNSA to the PW laser level hence depends on whether the behavior of the underlying complex processes (ionization, plasma expansion, plasma instabilities, etc.) can be understood and controlled for increasing laser pulse powers interacting with the target. This point is particularly relevant for the case of laser-driven medical accelerators, where an applicable proton distribution has to be generated besides the provision of sufficient proton energies. TNSA has been shown to fulfill these requirements on the ~ 100 TW laser power level for ultrashort pulse lasers and at moderate proton energies [26], but the scaling behavior of the beam properties such as the spatial distribution of particles needs to be verified in experimental scaling studies.

3.1.2. Complex-Physics Phenomena in TNSA

The corresponding experimental studies however do not necessarily depend on the availability of PW laser sources because the physical processes such as ionization, plasma formation, electron acceleration and transport underlying the TNSA process are not solely governed by the laser pulse energy. In fact, an investigation of the TNSA scaling behavior under different laser-target interaction conditions, as given by a variation of e.g. the pulse duration, polarization or target properties, can indicate effects that might likewise arise at the PW laser power level.

A parameter of particular relevance for the laser-target interaction conditions and hence acceleration process is the temporal intensity contrast. For the laser-target interaction with the laser pulse, the temporal intensity contrast defines the starting time, which can

¹In the model by Schreiber *et al.* [41], the absorption efficiency into hot electrons is used instead of n_h , where n_h and η are related as $\eta E_L \approx n_h V_h \cdot k_B T_h$ with the hot electron volume V_h and laser energy E_L .

be shifted to nanoseconds before the ultrashort ($\tau_L \sim 10$ fs) main pulse due to the commonly present background radiation. In combination with the effects of plasma expansion and plasma gradient steepening via the radiation pressure of the main pulse, the temporal intensity contrast sets the plasma conditions, which determine the laser absorption and electron acceleration (e.g. [44, 43]). Moreover, the temporal intensity contrast contributes to the ion acceleration conditions at the target rear surface by potentially triggering and driving a pre-expansion of the rear surface plasma gradient (Section 2.6). In summary, the temporal intensity contrast of the laser pulse affects all stages of the TNSA process. Regarding the PW laser technology, the temporal intensity contrast is going to be a crucial parameter: When peak laser power is increased without a simultaneous improvement of the normalized temporal intensity contrast of the laser systems, the absolute background intensity on target will increase compared to levels achieved at ~ 100 TW systems today. These properties render the temporal intensity contrast a key parameter for TNSA scaling studies, which aim at an extrapolation of the underlying physics to more extreme interaction conditions, as relevant for PW laser pulse powers.

A selection of experimental results, which illustrate the complex physics phenomena underlying TNSA and the role of different plasma conditions, are presented in Section 2.6.3. These studied effects can be beneficial as well as detrimental when aiming at proton distributions with the highest achievable energies, controlled spectra and homogeneous proton beam profiles. One of the most apparent observations, which indicate the complexity of the plasma physics underlying TNSA, are spatial modulations in the proton beam profiles.

3.1.3. TNSA Scaling Study at Draco I

An experimental laser energy scaling study in the TNSA regime for a non-ideal (i.e. including prepulses) temporal intensity contrast is performed at the Draco I laser system. By varying the plasma conditions by a change of the laser energy as well the the target type for the given temporal intensity contrast, regimes of TNSA are reached where complex phenomena of the electron transport become relevant and measurable. As the main result, the scaling study reveals the transition from homogeneous to transversely strongly filamented proton beam profiles as a function of the laser energy applied on the target and the target parameters. Whereas proton beam modulations have been observed for a number of laser and target conditions recently [73, 133, 76, 143, 81, 80], this result is considered the first observation for micrometer-thick target foils irradiated with ~ 30 fs long laser pulses.

3.2. Experimental Setup

The experimental scaling study is conducted at the ultrashort pulse, high power laser system Draco laser system at the HZDR. The Draco system - the *Dresden Laser Acceleration Source* - was installed in its original version (Draco I) in 2007/2008 and delivers a peak power of 150 TW.

3.2.1. The Draco I Laser System

General Setup

The Draco I laser system is based on the PULSAR² system and delivers 30 fs pulses at a central wavelength of 800 nm with an energy of 4-5 J (compressed) using the technique

²Amplitude Technologies, Evry, France

of chirped pulse amplification (CPA) [38]. Ti:Sapphire crystals serve as the gain medium, where the broad amplification bandwidth between 650 nm and 1050 nm and its high thermal damage threshold make this material very suitable for the use in high repetition rate (10 Hz), intense, ultrashort pulse lasers.

An outline of the laser chain of Draco I is presented in Figure 3.1. As the pulse source, a Ti:Sapphire oscillator at 800 nm central wavelength and a spectral width of 95 nm provides 10 fs pulses at the nanojoule level. The oscillator operates at a repetition rate of 78 MHz, of which a Pockels cell selects a 10 Hz pulse train. After amplification in the Booster amplifier, the pulses are dispersively stretched to a duration of 500 ps in the grating stretcher module.

In the cavity of a regenerative amplifier (RA), the stretched pulse is amplified to a pulse energy of 1 mJ in 12 passes. Following the RA, the pulse passes three multipass amplifiers with Ti:Sapphire crystals as gain media, pumped by flashlamp-pumped, frequency-doubled Nd YAG lasers. In five, four and four passes, respectively, the pulse is amplified to 20 mJ, 500 mJ and finally 6 J. Due to the high heat load in the third amplifier (9 pump lasers with a total of 18 J of pump energy) the final Ti:Sapphire crystal is cryogenically cooled to 140 K to increase the thermal conductivity. Cryogenic cooling thus allows for a laser operation at various (e.g. 10 Hz or single shot) repetition rates without thermal lensing in the crystal.

After the last amplification stage, the final laser energy on target can be passively adjusted via a variable attenuator. This element, consisting of a motorized wave plate and a set of thin film polarizers, is crucial for laser energy scaling studies because it allows for a laser energy variation without changing the pump laser configuration. It is followed by a large aperture Pockels cell (75 mm diameter) which protects the laser system from light back-reflected into the laser system from the experiment and enables the irradiation of solid targets under normal incidence. Two telescopes expand the beam to its final diameter of 100 mm before compression to reduce the fluence on the optics in the beamlines. Starting at the compressor chamber, the pulse is transported in vacuum in order to prevent e.g. filamentation of the intense beam in air and the onset of nonlinear optical effects in general. The pulse compression in the grating compressor and the transport between the final amplifier and the target point have an overall efficiency of about 65%, i.e. 65% of the laser energy in the fully amplified but stretched laser pulse are transferred to the compressed 30 fs long pulse.

Optimization and Diagnostics of the Pulse Parameters

Designed for experiments on laser-driven ion acceleration, the intensity and the temporal intensity contrast of the final pulse are optimized. Both parameters crucially influence the laser-target interaction dynamics. Highest pulse intensities - resulting from an optimal pulse compression in the temporal and spatial domain - are achieved via an active management of the spectral (dispersion) and spatial (wave front) phase in the laser chain. To achieve a high temporal intensity contrast, i.e. the ratio of the background intensity $I_L(t)$ to the peak intensity I_0 , the lasers pulses are cleaned from parasitic background radiation (e.g. ASE) throughout the amplification process.

Focal Spot Optimization The compressed pulse is either sent to the experimental setup in a second vacuum chamber or transported to the diagnostics setup in air after beam attenuation at a wedged glass substrate. A deformable mirror consisting of 31 separate piezo-driven electrodes manipulates the spatial phase of the beam and flattens the wave

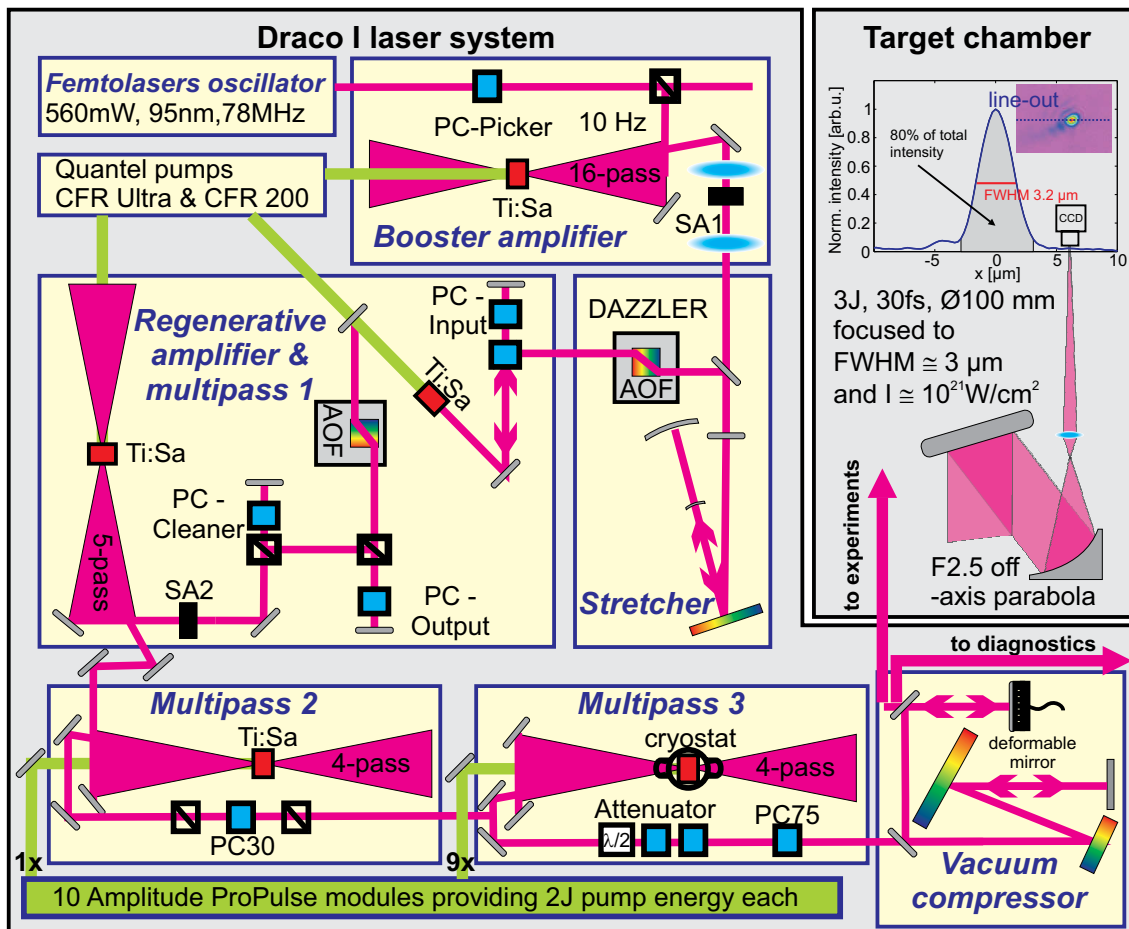


Figure 3.1.: Setup of the Draco I laser system including the focal spot characterization in the target chamber. The used abbreviations are: PC for Pockels cell and SA1/2 for saturable absorber. After [104].

front for an optimal focusability. For setting up, the mirror is operated in a closed loop with a grating-based wave front sensor SID4 (Phasics).

After optimization of the adaptive optics, the Draco beam can be focused to an almost diffraction-limited spot (FWHM $\approx 3 \mu\text{m}$) with a 250 mm focal length parabolic mirror at the laser-target interaction point inside the target chamber (Figure 3.1, Section 3.2.2, Figure 3.4). 80% of the laser energy are contained in the focal spot (diameter of $2 \cdot \text{FWHM}$, Figure 3.1). Optimization and imaging of the focal spot at the millijoule level is performed with a dedicated long-distance microscope objective³ (focal length $f = 100 \text{mm}$). The objective is corrected for spherical and chromatic aberrations and features a physical resolution of $3 \mu\text{m}$. From the working distance of 81 mm and a free aperture of 50 mm results $F/\# = 1.6$. Hence, the complete laser beam ($F/\# = 2.5$) is captured and imaged onto a CCD camera with a magnification of ≈ 30 .

Pulse front tilts, which originate from a detuning of the compressor grating angles and result in a spatial chirp in the focal spot, are diagnosed with an inverted field autocorrelator.

³TSO Thalheim Spezialoptik GmbH, Pulsnitz, Germany

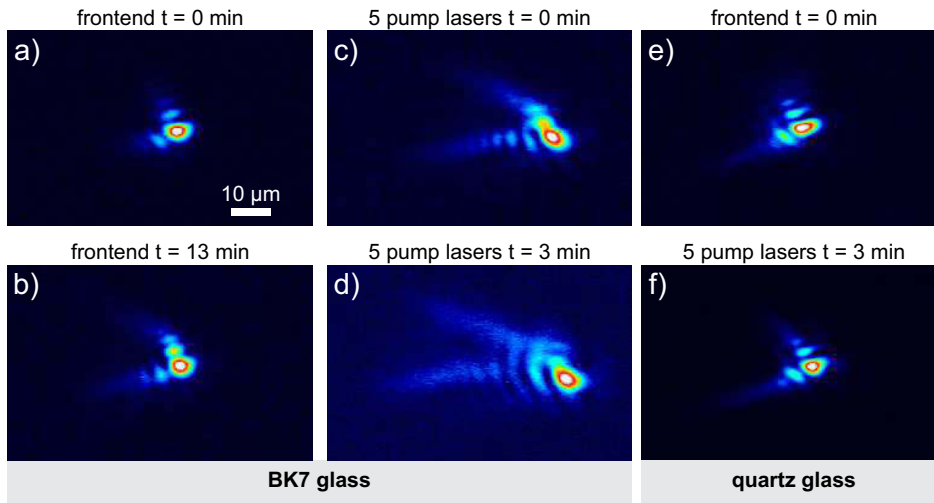


Figure 3.2.: Thermal lensing in the multipass 3 amplifier. Focal spot of the Draco I laser system for different window materials in the cryostat, which cools the Ti:Sapphire crystal, and different laser amplification configurations. The given times indicate how long the laser system has been running in the given configuration before data acquisition. All images are scaled to their maximum individual value, hence the brighter background in d) signifies a lower peak intensity, in that case due to defocusing. a- d) BK7 windows with thermal lensing. e- f) Quartz windows without thermal lensing.

Thermal Lensing Since the focal spot characterization and optimization is performed at the millijoule level with the multipass 3 amplifier unpumped, the focal spot characteristics of the fully amplified laser pulse are examined for a potential influence of thermal lensing in the transmission elements of the laser chain. To that end, the focal spot of the amplified laser pulse is validated in the same imaging system described above. Therefore, it is attenuated with two glass wedges inserted in between the last amplifier and the vacuum compressor⁴. The resulting focal spot images for two different cryostat window materials and various amplifier settings are shown in Figure 3.2. In the *frontend* setting (Figure 3.2a, b, e), all amplifiers up to the multipass 2 are pumped. In the other setting, the multipass 3 amplifier is pumped with five ProPulse pump laser at 10 Hz as well (Figure 3.2c, d, f). The BK7 windows feature strong thermal lensing, leading to a defocusing of the laser pulse in the focal plane of the imaging system (Figure 3.2c- d). Replacement of the windows by quartz windows resolves the issue, as Figure 3.2e- f show⁵. This window configuration is applied for the experimental scaling study and excludes a laser energy dependence of the focal spot characteristics.

Pulse Duration Characterization An ultrashort compressed pulse of minimally 25 fs (30 fs on a daily basis) is achieved by controlling dispersion effects and gain-narrowing during the amplification process. Dispersion of the pulse occurring during amplification in the gain medium itself and through transmissive optical elements is precompensated by an

⁴With the attenuator being placed in front of the vacuum compressor, a potential influence of the compressor gratings onto the focal spot characteristics cannot be evaluated. The gratings have been observed to heat up under irradiation with the fully amplified 800 nm seed pulse under 10 Hz irradiation but all proton acceleration experiments are performed with a shot-to-shot interval of several 10s. Hence, an influence is not expected.

⁵The reason why quartz windows feature less thermal lensing is a combination of the optical (absorption), thermo-physical (heat capacity, heat conductivity) and mechanical stability properties.

acousto-optic programmable dispersive filter (AOF) DAZZLER⁶ situated at the stretcher output. A second AOF (MAZZLER⁷) compensates for the gain-narrowing associated with the high gain amplification in the regenerative amplifier. The AOF introduces spectrally selective losses and ensures an identical overall gain for all wavelengths in the pulse. A bandwidth of 60 nm can hence be transported through the amplification chain.

The pulse length is characterized interferometrically with an FC SPIDER⁸ device [144]. In order to compensate higher order dispersion, the SPIDER also provides the spectral phase measurement for the AOF DAZZLER programming and generates the phase correction terms the DAZZLER applies to the stretched pulse.

Temporal Intensity Contrast Conditions To provide for a high temporal pulse contrast on the nanosecond and up to the ~ 100 ps range, the amplified spontaneous emission (ASE) from the oscillator and the regenerative amplifier (RA) is suppressed by saturable absorbers (SA1 and SA2 in Figure 3.1). The ASE background or potential nanosecond prepulses produced in the RA are furthermore suppressed with two Pockels cells in combination with thin film polarizers. This technique provides a temporal intensity contrast $I_L(t)/I_0 \lesssim 10^{-10}$ (Figure 3.3, ASE section).

To rule out prepulses from the RA and determine the level of ASE, the temporal contrast on the nanosecond timescale is measured with a fast photodiode in combination with calibrated neutral density filters. This measurement covers > 10 orders of magnitude in dynamic range. For contrast measurements in the time window of 500 ps before the pulse peak, a scanning third order autocorrelator SEQUOIA⁹ is used. It features a dynamic range of 12 orders of magnitude and a temporal resolution of about 100 fs. Representative data for the normalized temporal intensity contrast are shown in Figure 3.3. At times shorter than 100 ps before the pulse peak up to the ultrashort main pulse itself, uncompressed coherent pulse parts determine the temporal contrast e.g. by limiting the steepness of the rising pulse edge. The influence from uncompensated higher order spectral phase on the pulse's rising edge is visible from the side lobes at 1 ps and 3 ps before the pulse. Optimization of the temporal contrast around the pulse peak (picosecond range) is achieved through an optimized spectral phase correction procedure. Therefore, a WIZZLER¹⁰ instead of an FC SPIDER is used for the spectral phase characterization in feedback with the DAZZLER. The WIZZLER is based on self-referenced spectral interferometry (SRSI) and features a higher dynamic range of up to five orders of magnitude, hence providing a more sensitive phase measurement [145, 146]. The prominent side lobes in the contrast curve are eliminated in this way (Figure 3.3, former contrast/red curve).

Prepulses on the Picosecond Timescale In contrast to the setup (Figure 3.3, red curve, *former* setup) employed for the experiments published in [25, 27, 26], the temporal contrast curve for the scaling measurement features a series of prepulses on the timescale of -10 ps to -4 ps. With regards to the prepulse source, note that each prepulse (Figure 3.3, blue trace) corresponds to a postpulse (Figure 3.3, green trace). Furthermore, the picosecond delay times of the postpulses suggest multiple reflections from millimeter thick reflective

⁶Fastlite, Valbonne Sophia Antipolis, France

⁷Fastlite, Valbonne Sophia Antipolis, France

⁸acronym for: few-cycle spectral phase interferometry for direct electric field reconstruction, A·P·E Angewandte Physik & Elektronik GmbH, Berlin, Germany

⁹Amplitude Technologies, Evry, France

¹⁰Fastlite, Valbonne Sophia Antipolis, France

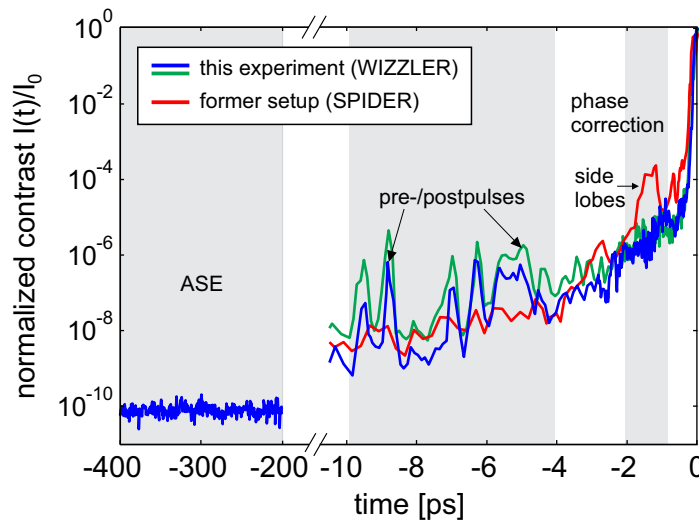


Figure 3.3.: Temporal intensity contrast on different timescales for two different setups. For the temporal range ≥ -10 ps, two sets of spectral phase correction are compared. For the setup employed in the presented experiment, prepulses occur in the range of -10 ps to -4 ps (blue curve). For comparison, the temporal contrast *after* the main pulse is overlaid (green curve), indicating that each prepulse has a corresponding symmetric postpulse with respect to the main pulse.

optical elements as their origin¹¹. As reported in [147, 148], nonlinear phase generation (B integral) in the laser chain can lead to the translation of post- to prepulses. The process of nonlinear/intensity-dependent phase generation acts on the intensity-modulated combined field of the post- and main pulse. Both pulses overlap and interfere after stretching and due to the correlation of wavelength and time in the stretched pulse, this overlap results in a spectral phase modulation and in the occurrence of satellite pulses (prepulses) after compression. The pulse duration of the prepulse is comparable to the post- or main pulse it is derived from [148].

The possibility of the prepulses being artifacts from the SEQUOIA measurement is ruled out by analyzing the spatio-temporal reflectivity and expansion dynamics at the target surfaces. In that way, the third order autocorrelation measurement of the temporal intensity contrast curve is verified independently at the target point (Chapter 4).

3.2.2. Target Chamber Setup

For the experiment, the compressed p-polarized pulses provided by Draco I with a maximum laser energy E_L of 2.9 J are focused ($I_L \approx 5 \cdot 10^{20}$ W/cm²) under normal incidence onto micrometer-thick solid target. The laser-target interaction setup as presented in Figure 3.4 is housed in a dedicated vacuum chamber evacuated to about $3 \cdot 10^{-6}$ mbar. It is composed of three units: 1. laser beam focusing, 2. mechano-optical target alignment and 3. particle diagnostics. Transport and interaction of the laser beam take place in vacuum to prevent both nonlinear interaction in air and the absorption and scattering of protons when propagating between source and detector.

¹¹The prepulses started to occur with the insertion of an optical isolator (Faraday rotator) in the beam path before the stretcher. The isolator was used to prevent back-reflected light in the laser chain from coupling back into the oscillator. However, the optical isolator is neither the source of the postpulses, nor is the pulse sufficiently stretched in the device to create a sufficient pulse overlap between the main and the postpulses.

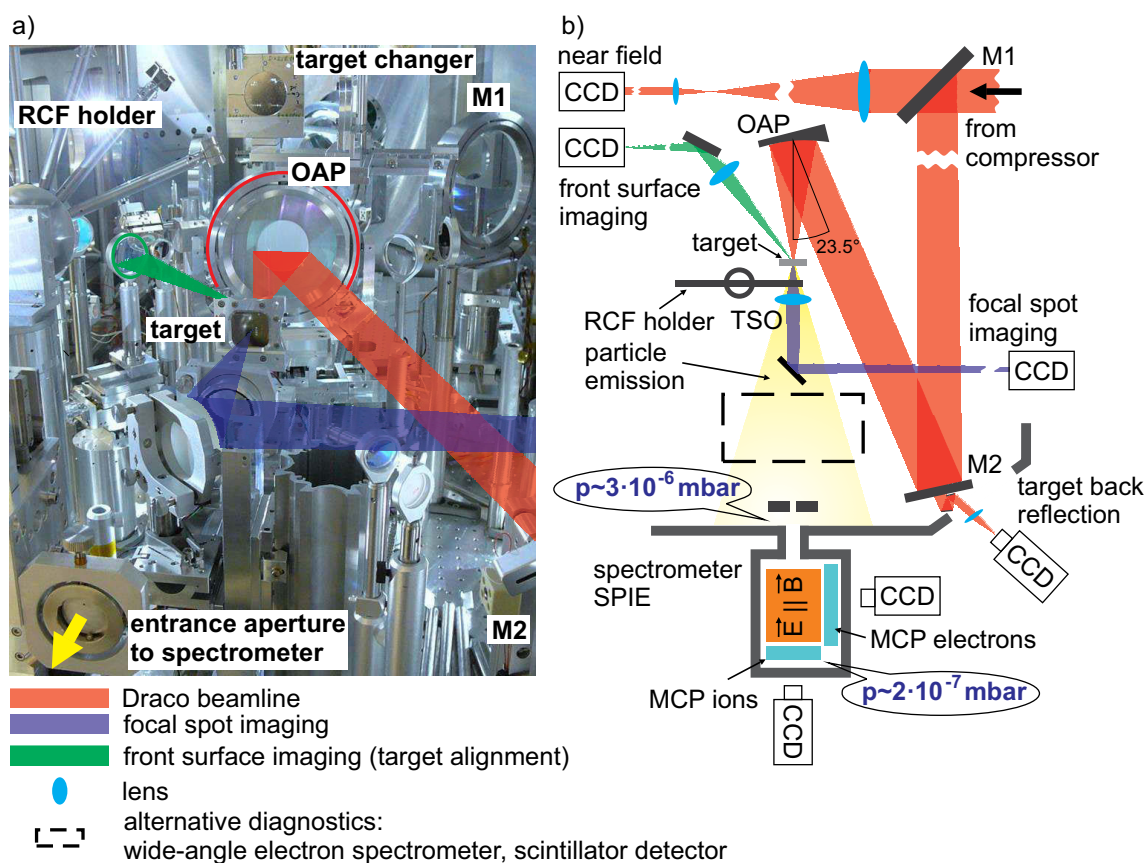


Figure 3.4.: Experimental setup for laser-driven proton acceleration at the Draco I laser system. a) Photographic view of the interaction area including the main optical beamlines. The target changer system can store up to four target holders and allows fresh targets to set up under vacuum conditions by using an electromagnet manipulator. b) Schematic view of the target chamber and spectrometer chamber, the latter housing the combined spectrometer for ion and electron detection, SPIE. Differential pumping maintains the pressure in the spectrometer chamber in the low 10^{-7} mbar range to minimize the background signal on the MCP detectors.

Laser Beam Focusing and Target Alignment

The optical beamline providing the compressed pulse to the interaction point consists of two folding mirrors (M1, M2) and an off-axis parabolic mirror (AOP) with a 23.5° off-axis angle. The parabola's focal length is 250 mm and it has a free aperture of 152 mm ($F/\# = 1.6$) to handle the beam diameter of 100 mm ($F/\# = 2.5$) (Figure 3.4). The resulting focal spot is shown in Figure 3.1. The focal spot imaging system (Figure 3.4, Section 3.2.1) also sets and preserves the position of the interaction point for target alignment. In lateral direction, this is realized via a reference point on the CCD camera chip and in focal/longitudinal direction via the object plane of the lens. The alignment accuracy in focal direction amounts to $10 \mu\text{m}$ and is below the Rayleigh range of the focused laser beam. For the alignment of the frequently used large foil targets (diameter up to 50 mm), a second optical reference setup is available because the foils cover the complete field of view of the microscope objective. The foil alignment system images the focal spot of an alignment laser co-propagating with the Draco beam on the target's front surface under an angle. In that way, a change in the longitudinal (focal) position of the target translates into a shift of the focus position on the camera chip. The resolution of $10 \mu\text{m}$ in focal direction achieved with the microscope objective is maintained. Motorized stages

allow for target positioning in all three spatial directions, rotation about the vertical axis and target tilting with a resolution in the micrometer-range.

Particle Diagnostics

The energy-resolved spatial distribution of the accelerated proton beam is measured with stacks of radiochromic film (RCF, Gafchromic HD-810/EBT2¹²) placed 45 mm behind the non-irradiated target rear side. RCF are used to record the fine-scale transverse modulations in the proton beam profiles. Through a hole in the RCF stack, the central part of the particle distribution propagates into the spectrometer SPIE 60 cm downstream from the target (Figure 3.4). It consists of a Thomson parabola spectrometer for ion detection with a parallel magnetic (560 mT) and electric (370 kV/m) field perpendicular to the particle propagation axis. In the magnetic field, the spectral dispersion of the electron distribution in an energy range from 0.5-7.5 MeV is obtained as well. The spectrometer is hence used for the online measurement of high resolution spectra of all ion species and the electron distribution produced in the laser-target interaction. The particle signals are amplified and recorded at the spectrometer's rear (ions) and side (electrons) exit using image-resolving microchannel plate (MCP) detectors. The MCPs are coupled to fluorescence screens that are read out with CCD cameras. Detailed information about the spectrometer as well as radiochromic film can be found in Appendix A.2.

3.3. Experimental Results

This section presents the experimental results for the TNSA scaling study at Draco I performed for the temporal intensity contrast conditions discussed above. As targets, large titanium foils with thicknesses of 2 and 3 μm are used, which are referred to as 2 μm Ti and 3 μm Ti in the following. Additionally, 2 μm thick titanium foils are spin-coated with a layer of photo-resist (PR, thicknesses of $\approx 0.8 \mu\text{m}$ and $\approx 3.5 \mu\text{m}$) at the rear side. These targets are referred to as 0.8 μm PR and 3.5 μm PR. The laser pulse energy on target is varied from 0.6 J to 2.9 J.

3.3.1. Proton Data

Scaling of the Maximum Proton Energies

Data for the maximum proton energy as a function of the laser energy on target for the three different target types are summarized in Figure 3.5 (a) 2 μm Ti, b) 3 μm Ti, c) 0.8 μm PR). The data are recorded using RCF and the maximum proton energies correspond to the last layer in the RCF stack which shows a proton signal, i.e. dose. This method gives a lower limit for the maximum proton energy. Details about the respective uncertainties are discussed in the caption of Figure 3.5.

For the 3 μm Ti and 0.8 μm PR target, the maximum proton energy increases monotonously and features an almost linear relation between the laser energy on target and the maximum proton energy. This behavior agrees with the prediction of the electrostatic scaling model by Schreiber *et al.* ([41], Section 2.6.2) for the case of ultrashort laser pulses [54]. For the 2 μm Ti target, the data indicate a saturation of the maximum proton energy for laser energies $E_L \geq 2.1 \text{ J}$. Moreover, the RCF dose values plotted in the background of Figure 3.5a indicate a dose decrease for the laser energy of 2.9 J in comparison to the case

¹²ISP International Specialty Products, Wayne, New Jersey, USA

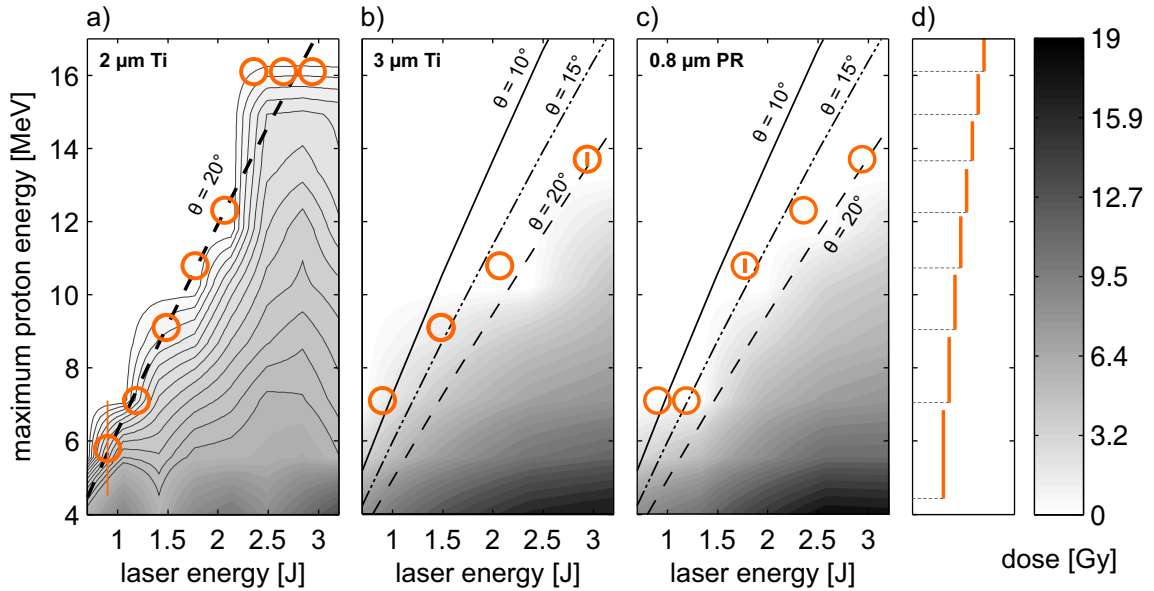


Figure 3.5.: Laser energy dependence of the maximum proton energies and proton dose. Maximum proton energies derived from RCF data for a) 2 μm titanium target, b) 3 μm titanium target, c) 2 μm titanium target coated with 0.8 μm of photo-resist. The statistical error for each maximum proton energy data point is indicated in the plots a-c). Markers without error bars correspond to a single shot result and small vertical bars within the marker represent averaging over multiple shots yielding the same maximum proton energy. d) Systematic errors for the maximum proton energies. The asymmetric systematic errors represent the fact that the given maximum proton energies, derived from the last RCF stack layer in the stack showing a dose signal from protons, are lower limits. The systematic uncertainty corresponds to the difference in proton energy of consecutive RCF sensitive layers in the stack.

The black lines in a-c) are predictions by the electrostatic scaling model ([41], Section 2.6.2) for the following parameter set: focal spot radius $r_L = 1.7 \mu\text{m}$, target thickness $d = 2/3 \mu\text{m}$, electron divergence angle $\theta = 10/15/20^\circ$, absorption efficiency into hot electrons $\eta = 0.25$ [43], pulse duration $\tau_L = 30 \text{ fs}$. Depending on the choice of the electron divergence angle θ , the model can fit the measured maximum proton energies for specific laser energy ranges in b-c). The model cannot fit the data with a unique θ , as it is the case for the data in a) for $E_L \leq 2.1 \text{ J}$.

In the background, the dose for each RCF layer in the evaluated stacks is plotted, which is averaged over an area of 18 mm^2 and a background dose of 0.5 Gy is subtracted. Each RCF layer is evaluated at the position where the beam spot of the highest energy protons is situated for the respective RCF stack. The dose values are interpolated for the missing laser and proton energy values. Note that each RCF layer represents the accumulated dose of all protons with a kinetic energy at or above its respective Bragg peak energy, which depends on the depth in the stack.

of $E_L = 2.7$ J. Below the laser energy of 2.1 J, the scaling of the maximum proton energy agrees with the electrostatic scaling model for the 2 μm Ti target.

Proton Beam Profiles

Apart from the indication of a saturation in the maximum proton energy and a decrease in dose for the 2 μm Ti target, the energy scaling behavior does not hint at a change in interaction conditions for increasing laser energies. On the other hand, the proton beam profiles indicate a change in the acceleration process by the occurrence of transverse modulations.

Representative data for the observed transverse spatial modulations in the proton beam profiles are summarized in Figure 3.6b. The data set shows proton beam profiles measured with RCF for laser energies in the range from 0.9 J to 2.9 J for the 3 μm Ti target. The Bragg peak energies E_{BP} for the different laser energies are chosen to yield comparable proton beam diameters. The chosen RCF layers hence represent similar *relative* proton energy ranges compared to the maximum proton energy achieved for each shot (see Figure 3.5).

Whereas the beam profiles carry only some random inhomogeneities for lower laser energies, they are modulated with a net-like fine-scale pattern for the highest laser energy. Within a proton pulse, the modulations persist up to the highest proton energies without major changes of the pattern. The RCF layers shown are hence representative for the proton beam (Figure 3.6a).

Comparing the characteristics of the different targets used (Figure 3.9), two major observations are made: Firstly, all targets featuring spatially modulated beam profiles consistently display the same net-like fine-scale pattern above a target-dependent laser energy threshold¹³. Comparison of the proton beam profiles for the 2 μm Ti at 1.5 J of laser energy (Figure 3.9a) and the 3 μm Ti target at 2.9 J (Figure 3.9b) demonstrates that for a thicker target the onset of the net-like fine-scale pattern is only achieved for an increased laser energy. In accordance with these observations, for the 3.5 μm PR target tested (Figure 3.9d), a smooth beam profile is observed even for the highest laser energy on target.

Secondly, in terms of target properties, the proton beam modulations are predominantly a function of the target thickness, particularly with regards to the spatial characteristics of the pattern. The target composition seems to play no significant role. Accordingly, the ≈ 3 μm thick 0.8 μm PR target consisting of a 2 μm thick titanium foil and 0.8 μm of PR features almost the same laser energy dependence of the transverse beam profile modulation as the 3 μm Ti target. The only difference is the reduced dose contrast of the pattern (signal-to-background ratio for the net-like features) in the case of the 0.8 μm PR target.

Spectral Shape and Proton Beam Divergence

The comparison of the spatially resolved beam profiles with the simultaneously measured proton spectra (SPIE diagnostic) indicates that the transverse spatial modulations coincide with a modulation of the energy spectrum. As Figure 3.6g shows, an exponential energy distribution is observed for a laser energy of 0.9 J and the spectra for the intermediate laser energies (1.5 J and 2.1 J) feature a multi-temperature energy distribution. Both are in accordance with other experimental observations for TNSA [45, 54]. For a

¹³For the thinnest target (2 μm Ti), the spatial scale of the transverse net-like modulation pattern increases for $E_L > 2.1$ J (Figure A.2).

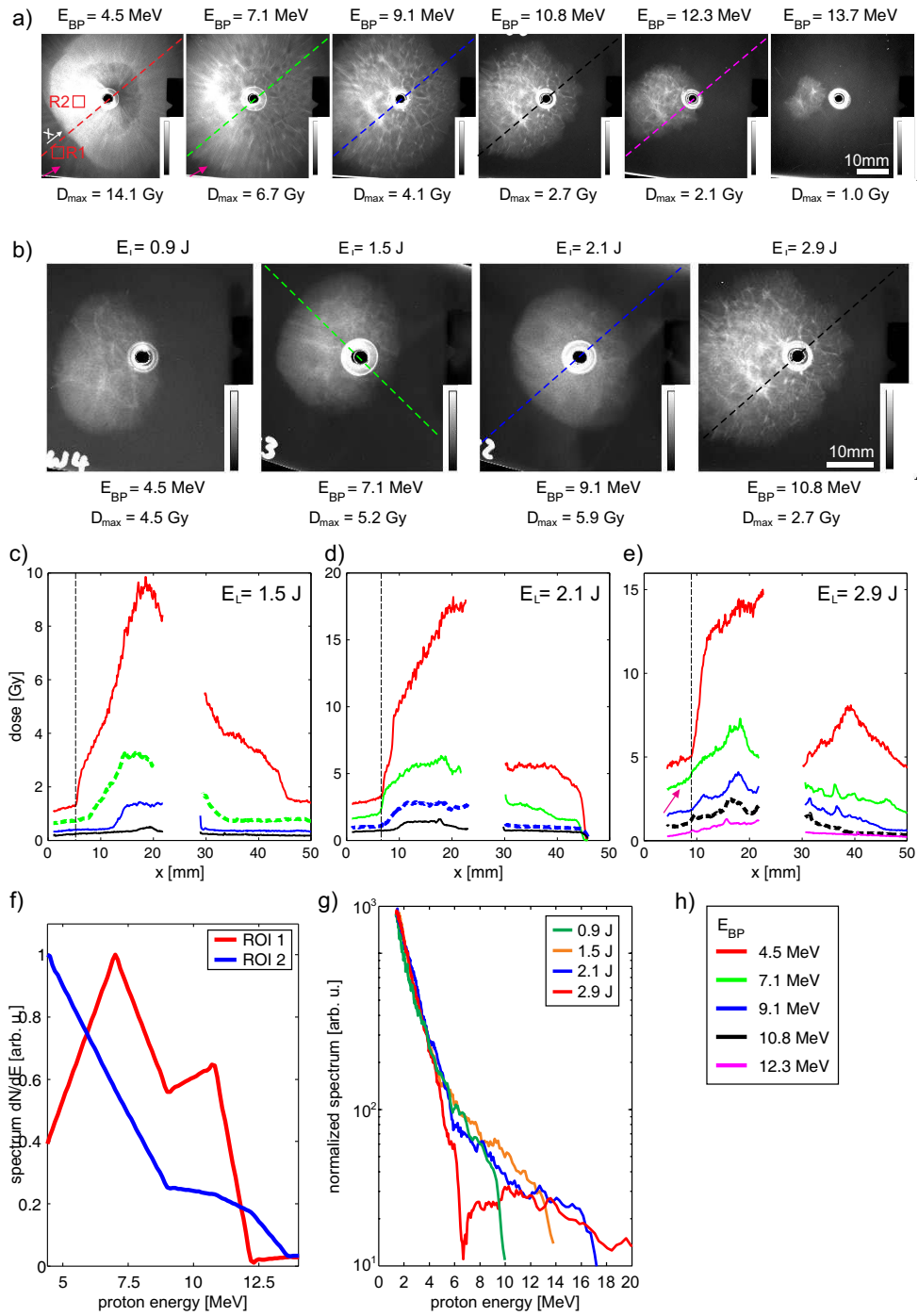


Figure 3.6.: Proton data for the $3\ \mu\text{m}$ Ti target. a) Spatially resolved dose profiles (single shot) measured with RCF for a laser energy of 2.9J on target. Each layer represents protons with energies at or above the respective Bragg peak energy E_{BP} . The dose in each layer ranges from $D_{min} = 0\text{Gy}$ to D_{max} (see colorbar). b) Dose profiles showing the laser energy dependence ($E_L = 0.9\text{-}2.9\text{J}$) of the occurrence of the spatial beam modulations. c-e) Lineouts of the dose profiles along the lines indicated in a) and b). Apart from $E_L = 2.9\text{J}$, the lineouts are chosen to cross the proton beam spot for the last irradiated RCF layer (corresponds to the maximum proton energy, Figure 3.5). The dashed lineouts correspond to the RCF layers shown in b). The hole region in the RCF is left out in the plots. f) Linear, normalized proton spectra derived from the RCF data in a) for ROI1 and ROI2 (R1/2 in a). For details on the spectral deconvolution see Appendix A.2. g) Normalized (to the same maximum value) proton spectra measured with the Thomson parabola comparing the spectral shape for different E_L (see legend). h) Legend for c-e).

laser energy of 2.9 J however, the spectrum is modulated and the proton distribution features a spectrally separated broad shoulder for the high particle energies in addition to an exponentially decreasing low energy part.

Proton spectra for the same target (3 μm Ti) and laser energy parameters ($E_L = 2.9$ J) but a position off-center in the proton distribution are derived by deconvolving the corresponding RCF depth dose profile at the positions $R1/2$ marked in Figure 3.6a. In the spectrum at position $R1$ (Figure 3.6f, red curve), the proton number per energy bin dN/dE decreases for < 7.5 MeV. This signature is comparable to the high energy shoulder measured in the central part of the beam (SPIE diagnostic) for $E_L = 2.9$ J (Figure 3.6g), as discussed above. The low energy part of the spectrum is not measured at $R1$, since the RCF stacks can only detect protons with energies ≥ 4.5 MeV. On the other hand, the deconvolved spectrum at position $R2$ (Figure 3.6f, blue curve) features a monotonous increase of dN/dE with decreasing proton energy.

The spectral feature of a dose decrease in the spectral range of ~ 6 MeV observed in the beam center and at the position $R1$ is consistent with the depth dose profile in the RCF. With regards to the spectrum at the beam center, the RCF layer at $E_{BP} = 4.5$ MeV shows a reduced dose in the central part of the beam. This is visible in Figure 3.6a as well as in the respective lineout in Figure 3.6e, in which the dose decreases between 30-40 mm for $E_{BP} = 4.5$ MeV.

At position $R1$ in the proton beam profile for $E_{BP} = 4.5$ MeV, an additional weaker background (pink arrows in Figure 3.6a, $x \leq 10$ mm in Figure 3.6e) is present in addition to the central beam profile ($x > 10$ mm in Figure 3.6e). Taking into account the observed decreasing proton number for proton energies < 7.5 MeV, this background must be attributed to dose deposition by protons with energies > 4.5 MeV, i.e. energies above the Bragg peak energy of the respective RCF layer. Consequently, the proton beam diameter increases from $E_{BP} = 4.5$ MeV compared to $E_{BP} = 7.1$ MeV. This is equivalent to an increase in the proton beam divergence with increasing proton energy and contradicts the characteristics of laser-driven ions generally reported, e.g. in [15, 149]. Both features - the reduced dose in the central part of the beam and the proton beam divergence increase with increasing proton energy - uniquely occur for the highest laser energy on target.

3.3.2. Electron Data

In addition to the proton spectra, electron spectra are recorded using the SPIE spectrometer. Figure 3.7a shows evaluated spectra (interpolated and smoothed) for the 0.8 μm PR target for three laser energies. The data are fitted by a two-temperature exponential decay model of the form $dN/dE = A_1 \cdot e^{-E/T_1} + A_2 \cdot e^{-E/T_2}$ [150, 151]. E is the electron energy and T_1 and T_2 correspond respectively to the temperature of the low and high electron energy parts¹⁴. Figure 3.7b-c summarizes laser-energy dependent data for T_1 and T_2 for three different target types. For the 3 μm Ti and the 0.8 μm PR target, the temperature T_2 features an interesting behavior: T_2 is almost constant for laser energies $E_L < 2$ J with values $T_2 = 3-5$ MeV but increases by almost a factor of 2 for $E_L > 2$ J. The increase of the electron temperature coincides with the onset of transverse modulations in the proton beam profiles (Figure 3.6). On the other hand, the 2 μm Ti target features $T_2 = 3$ MeV for a laser energy of 2.9 J. The data point is the average over seven evaluated spectra so that a shot-to-shot fluctuation can be ruled out. For comparison, the electron tempera-

¹⁴To ensure that the microchannel plate (MCP) used to record and amplify the electron signal does not saturate, the amplification voltage is varied by ± 50 V in an otherwise identical setup [152]. For electron energies above 1 MeV, i.e. the range relevant for a determination of T_2 , no sign of a signal saturation is found.

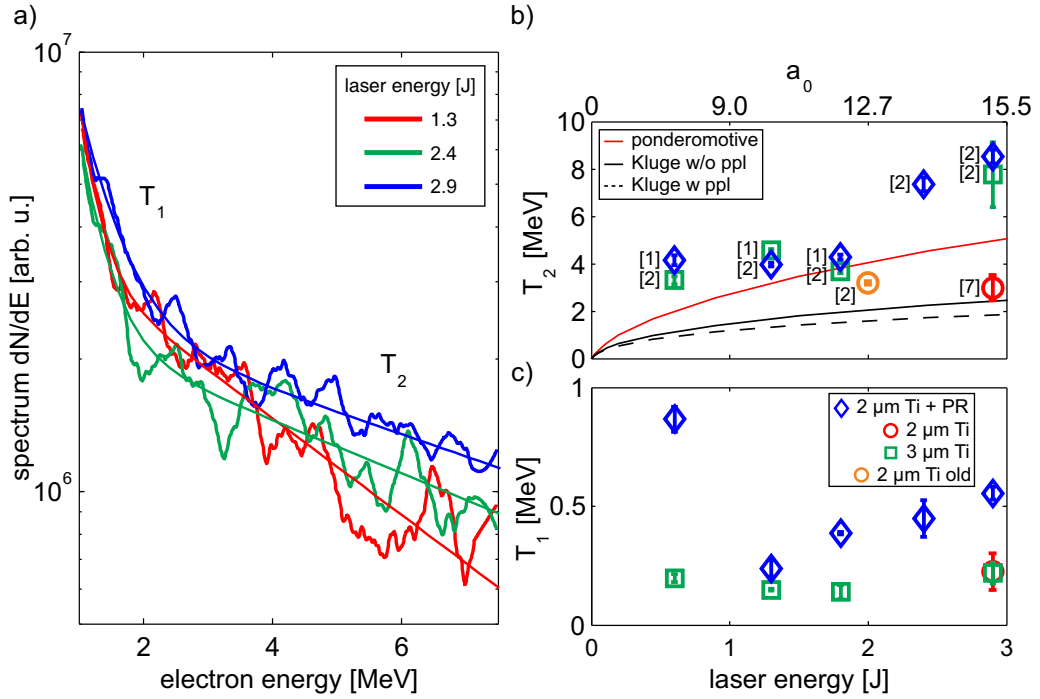


Figure 3.7.: Electron data recorded behind the target rear surface. a) Electron spectra (interpolated and smoothed) for the 0.8 μm PR target for three laser energies. The data are fitted with a two-temperature exponential decay functions with T_1 for the low energy part and T_2 for the high energy part of the spectrum. The fluctuations in the spectra are due to fluctuations in the raw data, which are emphasized in the logarithmic plot. b) Laser energy dependence of the electron temperature T_2 for three different target types. The error bars correspond to the uncertainty of the exponential fit and the uncertainty of the mean when several data points are averaged. The numbers in brackets next to the data points correspond to the number of data averaged. The measured electron temperatures are compared to three of the common scaling models for laser-driven electrons, i.e. the ponderomotive scaling (Equation (2.25)) and the two scalings without and with preplasma presented by Kluge *et al.* in [43] (Section 2.5.1). In particular the measured high electron temperatures (e.g. 3 μm Ti, $E_L = 2.9$ J) exceed even the ponderomotive scaling model, which predicts the highest electron temperatures. c) Laser energy dependence of the electron temperature T_1 .

ture measured for a 2 μm Ti target and the temporal intensity contrast applied in former experimental campaigns (compare *former setup* in Figure 3.3) is plotted in Figure 3.7b (*old* in the common legend to both plots, shown in Figure 3.7c). T_2 is found comparable to the other values plotted for $E_L \sim 2$ J. Values for higher laser energies and the *former* temporal contrast setup are unfortunately not available.

The data for T_1 feature no clear trend for the laser energy dependence. This behavior is in agreement with the results by Link *et al.* regarding the correlation of the low energy component of electron spectra and the primary electron distribution generated at the target front surface [151].

3.3.3. Summary and Correlation of the Experimental Signatures

To summarize the experimental data, the trends observed in the proton beam profiles regarding the fine-scale modulations (Figure 3.6, Figure 3.9) are quantified and correlated with the following experimental signatures in the proton and electron data:

- a spectral modulation correlated with an energy-dependent dose reduction in the central part of the proton beam (Figure 3.6a, g)
- an increase in proton beam divergence with increasing proton energies in the proton energy range of ≈ 4.5 -7.1 MeV (Figure 3.6a, f)
- an increase in the electron temperature for the 3 μm Ti and 0.8 μm PR target (Figure 3.7) .

The proton beam modulations for different laser energies and target types (Section 3.3.1) are quantified using two features which contribute to the visual impression of the pattern. These features are derived from the evaluation of three beam profile lineouts per data set (i.e. RCFs for different targets and laser energies E_L). Details on the data analysis are summarized in the caption of Figure 3.8. The first feature is the average modulation depth ΔD_p of the peaks in the profile lineouts, i.e. the dose difference between the raw and a smoothed reference lineout. The second feature is the integrated number of peaks in the three lineouts evaluated per data set. ΔD_p measures the visibility of the modulations and $\#peaks$ differentiates the fine-scale from random modulations. The former by trend exhibit peaks consistently over the entire beam profile.

The results of the quantification are summarized in Figure 3.8. Data sets featuring the transverse fine-scale modulations are characterized by $\Delta D_p \geq 0.05$ and $\#peaks \geq 10$ (shaded area). The small numbers inside the markers indicate the laser energy on target for each data point. The two main trends in the data derived from the visual impression are well reproduced: Firstly, the transition from homogeneous to modulated beam profiles for increasing laser energy and secondly the observation that the transition occurs at lower laser energies for thinner targets (i.e. 2 μm Ti). However, for the 0.8 PR target at $E_L = 2.9$ J, the automatic characterization of the fine-scale modulations fails because the pattern is less pronounced (lower dose contrast) as indicated above and evident in Figure 3.9c.

The experimental observations listed above are - by a color code - integrated into the same plot. All data points featuring the reported transverse fine-scale modulations lie in the overlap region of the shaded areas. In summary, Figure 3.8 hence indicates the coincidence of the proton beam modulations and the proton distribution's spectral modulation, the increased proton beam divergence and the increased electron temperatures. The origin of these features, which hint at a change in the laser-target interaction and/or the acceleration conditions, will be studied in the following sections.

3.3.4. Target Surface Characterization

The occurrence of spatially modulated proton beams can hint at various effects in the laser-target interaction. Based on the fact that the presented data show a laser energy dependent evolution of the proton beam profiles for a fixed target type, the possibility of the modulations being imprinted into the proton beam from a surface structure at the target rear side [131, 15] can very likely be excluded. To further confirm this hypothesis, the target rear surfaces are characterized with scanning electron microscopy (SEM) and atomic force microscopy (AFM) techniques. The results are summarized in Figure 3.9e-g. Whereas the 2 and 3 μm Ti foils appear smooth in the SEM (Figure 3.9e-f), a strong surface structure with a transverse frequency of roughly 1 μm and an amplitude ~ 100 nm is visible in the SEM picture for the 0.8 μm PR target (Figure 3.9g). It is assumed that this surface structure stems from the target preparation process in which the foil is cooled while fixed in an aluminum frame using liquid nitrogen so that it stretches

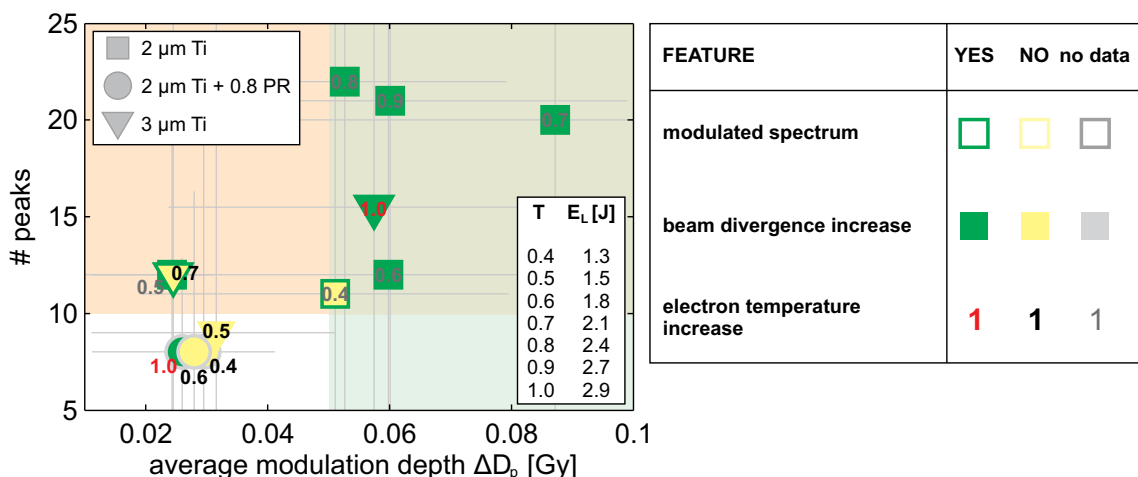


Figure 3.8.: RCF data analysis. Quantification of the modulations observed in the RCF data (dose). The small numbers inside the markers indicate the laser energy on target for each data point (see legend). To derive the data (x- and y-axis of the plot), three lineouts per data set are evaluated. The RCF stack layers are chosen to yield similar proton beam diameters for all data sets (compare Figure 3.6b). For the average modulation depth ΔD_p , the peaks in the three lineouts (smoothed with a moving average filter of 0.8 mm width) are detected and the corresponding dose values of a reference lineout (smoothed with a moving average filter of 2 mm width) at the peak position are subtracted. ΔD_p is the average over all peaks of a data set. $\#peaks$ is the integrated number of peak in the three lineouts. The large error bars plotted in grey indicate the noise level in the data. The shaded areas indicate for which data sets the transverse fine-scale modulations are observed. The experimental observations regarding the proton and electron data are represented in the plot via a color code (see legend). The plot indicates the coincidence of these observations with the fine-scale modulation feature.

during warming. This apparently causes tension and disruption in the formerly smooth PR layer. The AFM characterization of the pure $2\ \mu\text{m}$ Ti target reveals surface structures with a spatial frequency below 200 nm and a modulation amplitude below 10 nm peak-to-valley. The surface roughness is hence orders of magnitude smaller than in the case of the coated target. In conclusion, the fact that uncoated as well as coated Ti targets show a comparable behavior regarding the proton beam modulation despite the very different surface topography at the target rear, indicates that the transverse modulations observed cannot be traced back to a target rear surface structure.

3.4. Numerical Analysis of the Transverse Spatial Fine-Scale Modulations

Having ruled out the target surface structure as the source of the observed fine-scale modulations, changes in the hot electron generation at the target front surface or the electron transport through the target bulk are two other likely sources for spatial modulations (Section 2.6.3). Particle-in-cell (PIC) simulations are performed to study dynamic processes in the high-intensity laser-target interaction, which can result in spatial modulations of the proton beam qualitatively comparable to the experimental findings. The simulation study focuses on the influence of the preplasma conditions at the target front surface on the electron and proton dynamics, because the experiment is performed with a temporal intensity contrast differing from a formerly employed setup at Draco I (Figure 3.3). This *former* setup yielded spatially smooth megaelectronvolt proton distributions [54, 27].

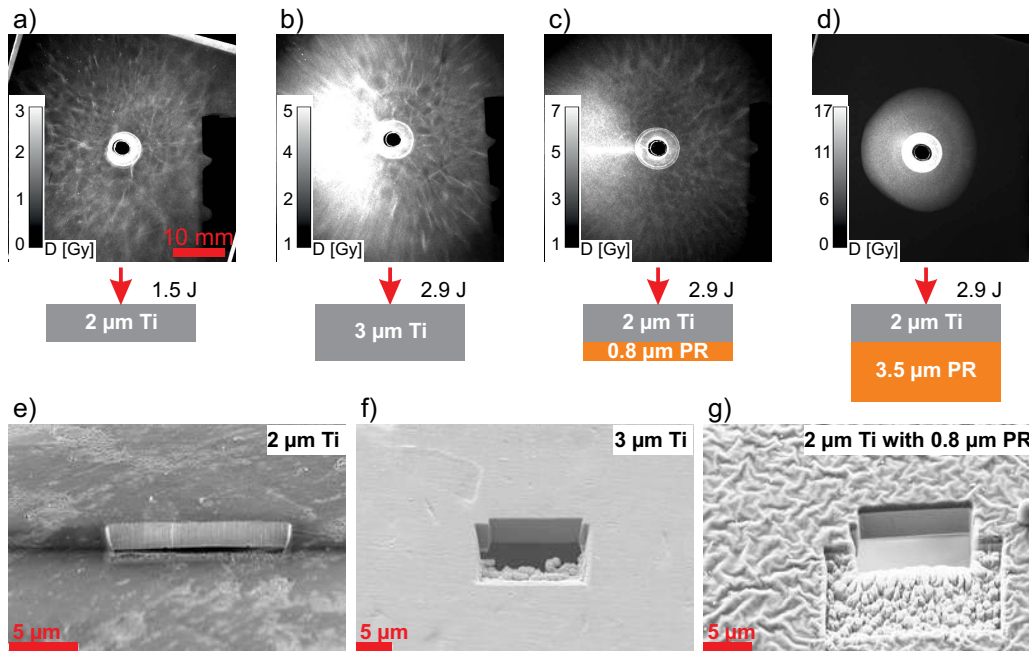


Figure 3.9.: Comparison of different targets and target characterization. a - d) The proton beam dose profiles for different targets at a Bragg peak energy of 7.1 MeV are compared. The red arrows point at the laser-irradiated side of the targets. e - g) Scanning electron microscopy images of the targets' surface topography. The holes visible in the surfaces are drilled for target thickness measurements using a focused ion beam. For the 0.8 μm PR target, the PR-coated rear surface is characterized.

3.4.1. Simulation Setup

The simulations are carried out with the collisional 2D3V¹⁵ iPICLS code [153] using a simulation box of a $10\lambda \times 10\lambda$ size with 192 cells per wavelength λ and 192 time steps per laser period. For the purpose of analysis, the laser pulse is modeled as a plane wave with periodic boundary conditions. Tests for the influence of focusing however yield equal transverse filamentation patterns in the electron energy density (Figure 3.10). The laser intensity or normalized field strength and the pulse duration are set to approximately match the parameters of the Draco I laser system with $I_L = 2 \cdot 10^{20} \text{ W/cm}^2$ ($a_0 = 10$) and $\tau_L = 50 \text{ fs}$ (FWHM). The pulse has a Gaussian rising edge and a 40 fs wide flat top to provide a long period of constant intensity for analysis.

The interaction targets are modeled with ions preionized to $q/A = 1/2$ or $q/A = 1/6$ with a resulting electron density of $100 n_c$. n_c is the critical density. This density is lower than that of a fully ionized solid foil, which is $716 n_c$ for titanium. Yet, test simulations for different electron densities show qualitatively comparable electron dynamics once the electron density is large enough to constitute an opaque foil. In order to model different preplasma conditions as resulting from a variation of the temporal pulse contrast, the laser-irradiated target front side is either composed of a step-like or an exponentially decreasing density gradient with a variable scale length L_p . The target rear side is covered with a 0.5λ thick layer of ions preionized to $q/A = 1/2$ for both preionization cases in order to allow for a direct analysis of the dynamics of ions accelerated from the target rear side. Excluding the preplasma gradient, the total target thickness is set to 2λ .

¹⁵spatial coordinates considered in two dimensions, particle momenta considered in three dimensions

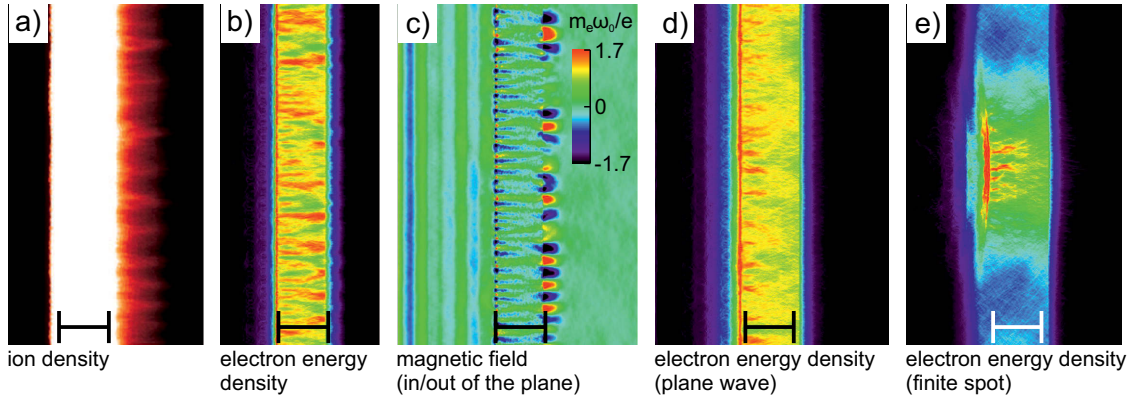


Figure 3.10.: PIC simulation results studying transverse modulations in laser-driven protons distributions. Data for $a_0 = 10$, $n_e = 100 n_c$, $q/A = 1/6$ at 80 fs (a) and 33 fs (b - e) after the pulse has reached its maximum. a) Spatially modulated ion density at the target rear surface for the laser pulse modeled as a plane wave and a preplasma scale length of $L_p = 0.1 \lambda$. b) The corresponding electron energy density. c) The corresponding magnetic field in y-direction (perpendicular to the plane shown) averaged over one laser cycle. d - e) The electron energy density for a plane wave (d) and focused (e) laser pulse for $L_p = 0.3 \lambda$. The lines at the bottom of each subfigure mark a width of 2λ . The electron energy densities are measured in $m_e c^2 n_e$ and scaled to $2/3$ (b, d) and $1/2$ (e) of the respective maximum value. The corresponding color bar is given in Figure 3.11.

3.4.2. Simulation Results

The simulation results summarized in Figure 3.10 show that in the parameter range studied, transverse spatial modulations of the rear side accelerated ions (Figure 3.10a) can indeed be observed. They originate from a filamentation of the electron distribution accelerated at the target front side (Figure 3.10b), the electrons being subjected to different plasma instabilities depending on the initial plasma conditions.

Steep Gradient Case

In the first set of simulations, the influence of the laser intensity for targets with a step-like density gradient is studied. The chosen preionization of $q/A = 1/2$ matches the case of light target ions (e.g. titanium), which are ionized almost completely at the given laser intensities. Snapshots of the electron energy densities for the normalized field strengths $a_0 = 5/10/25$ at 33 fs after the pulse has reached its maximum are presented in Figure 3.11a - c. Whereas the electron energy density is almost homogeneous for $a_0 = 5$, transverse filaments reach throughout the target for $a_0 = 10$ and $a_0 = 25$. Lineouts parallel to the target surface of the snapshots taken at 1.5λ inside the target (Figure 3.11d) indicate an increased modulation strength (peak-to-valley ratio) with increasing laser intensity. Translation of the spatial modulation into the ion density is confirmed by the lineouts in Figure 3.11e. The graphs correspond to the spatial distribution of ions at the target rear side with at least 50% of the maximum ion energy in the simulation. The data are averaged in z-direction at 80 fs after the pulse has reached its maximum and the ion density fluctuation around the lineout average are plotted (solid line in the plot).

The analysis of the electron dynamics shows that the spatial modulation within the electron distribution originates directly from the target front surface, which itself develops a lateral rippling (inset Figure 3.11b). The electron jets injected into the target by the $v \times B$ force are hence spatially bunched in lateral direction similar to [154]. They propagate ballistically within the target after being driven beyond the critical density and

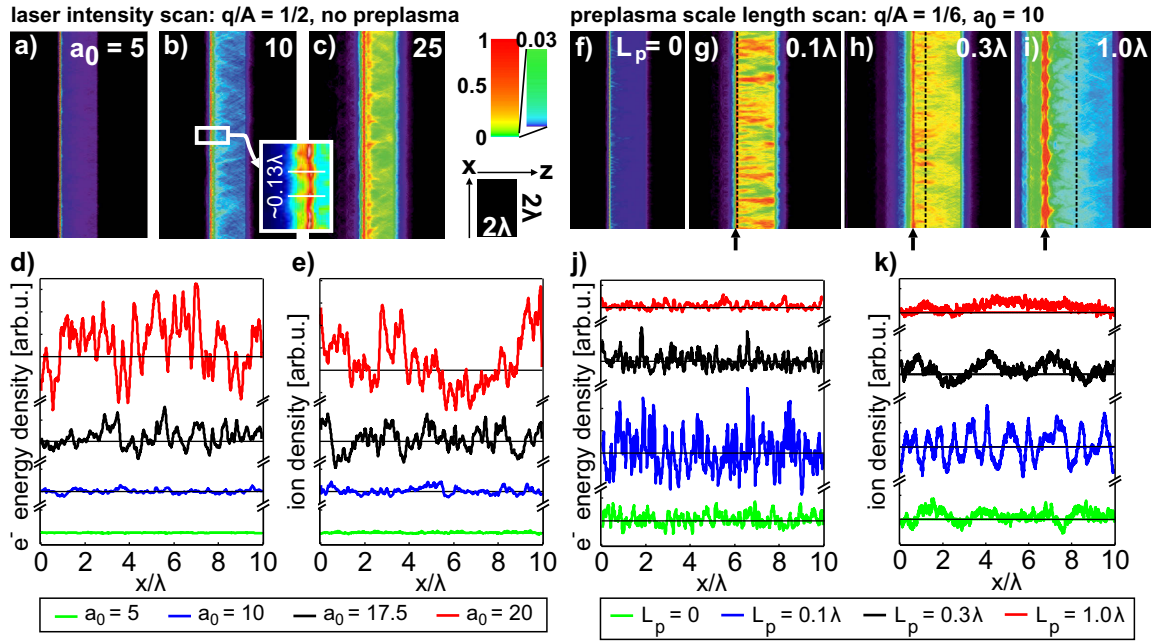


Figure 3.11.: PIC simulation results for the steep and finite gradient case. a - c) and f - i) Snapshots of the electron energy density 33 fs after the pulse has reached its maximum for different laser intensities and preplasma scale lengths. In contrast to the electron density, the electron energy density allows for the distinction of the energetic electrons accelerated at the target front surface from the background electrons within the volume of the target. In that way, the visibility of spatial modulations is increased. Each snapshot is normalized to $2/3$ of its individual maximum value. The inset in b) illustrates the observed surface rippling. The black arrows below g - i) mark the position where the energy density is maximal and the dashed lines correspond to the position of the target surface without the preplasma gradient. d) and j) Lineouts parallel to the target surface of the electron energy density taken at 1.5λ inside the target. e) and k) Lineouts of ions at the rear surface with at least 50% of the maximum ion energy in the simulation, averaged in z -direction. The point in time is 80 fs after the pulse has reached its maximum. The vertical scales in all lineout plots are linear and consistent within each plot. The lineouts represent the (energy) density fluctuation around the respective mean value for the lineout, which is shown as a solid line in the plots.

thereby preserve the lateral modulation. For illustration, Figure 3.12 shows the contrast of the electron energy density ($\max - \min / (\max + \min)$) sampled during copropagation with an injected electron bunch.

A study presented by Kluge *et al.* [155, 156] connects the surface ripple formation with the decay of a plasma oscillation at the plasma frequency into electron surface waves. The surface waves then form a standing wave pattern and when the results from [157] are applied, a node spacing of $\approx \lambda/10$ is yielded. This value is in accordance with the simulations (Figure 3.11b). The surface structure then supposedly seeds a Rayleigh-Taylor (or Rayleigh-Taylor-like instability as in used in [80]) instability, which would otherwise have a much slower growth rate [158].

Finite Preplasma Gradient

In a second set of simulations, the influence of a preplasma gradient is investigated for the parameters $a_0 = 10$ and $q/A = 1/6$ (preionization of the target). This choice suppresses the aforementioned rippling mechanism because the heavier target ions (low charge

state) now inhibit surface acceleration and reduce the instability growth rate. For the plasma scale lengths, the parameter range relevant at Draco I (see Section 3.5.1) is tested: $L_p = 0/0.1/0.3/1.0 \lambda$.

Figure 3.11f-i and Figure 3.11j present the electron energy densities at 33 fs after the pulse has reached its maximum for different preplasma scale lengths. For the case of $L_p = 0$, a weak lateral spatial modulation of the electrons energy density can be observed at the target front side. The comparison with the plasma dynamics for the case of lighter ions ($q/A = 1/2$) shows that the front surface plasma stays much flatter during the laser-target interaction due to the suppression of the surface rippling. With the introduction of preplasma at the target front surface, a considerable change in the plasma dynamics is observed: Whereas the directionality of the electron filaments is diffuse for a steep density gradient (Figure 3.11b), for $L_p = 0.1 \lambda$ and 0.3λ the electron filaments are strongly directed in laser direction (Figure 3.10b) and accompanied by surrounding magnetic fields (Figure 3.10c). As shown in Figure 3.12, the contrast of an injected electron bunch (electron energy density) with respect to the background increases during propagation, i.e. the bunches acquire their transverse modulation as they travel through the bulk of the target. It is therefore concluded that the thin preplasma shelf allows for more efficient electron acceleration and hence strong electron currents. These currents then drive a Weibel instability (WI) ([89, 77], Section 2.5.3).

As the simulations show, the WI critically depends on the preplasma scale length with the modulation depth being maximized for $L_p \approx 0.1 \lambda$. Figure 3.11f-i illustrates this aspect: The energy density peak (marked by black arrow) is localized close to the target surface ($n_e = 100 n_c$, black dashed line) for $L_p = 0.1 \lambda$, hence, this is a setup, in which efficient transport of front side accelerated electrons into the target is possible. On the other hand, the energy density peak lies far out in the preplasma region for the larger scale lengths. Moreover, the spatial structure in the electron current is washed out during propagation in the target bulk for $L_p \geq 0.3 \lambda$. Hence, translation of the lateral spatial modulation in the electron distribution into the target rear side accelerated ions is also strongest for the optimum preplasma scale length of 0.1λ , as the electron filaments reach furthest into the target in this case. Filament merging yields different spatial modulation frequencies for the electron energy density (Figure 3.11j) as compared to the ion distribution (Figure 3.11k). For instance, in the case of $L_p = 0.1 \lambda$, the distance of neighboring electron filaments is $\lambda_{\perp} \approx 0.2 \lambda$ for the electron energy density at the target front surface (Figure 3.10b) and $\lambda_{\perp} \approx \lambda$ for the ion density (Figure 3.10a).

Summary

In summary, two instabilities are identified which can trigger a break-up of the electrons at or close to the target front surface. This process results in a modulated ion distribution at the target rear side. The investigated simulation sets are limiting cases and feature two distinct break-up processes for the hot electrons: a surface-ripple-seeded Rayleigh-Taylor and a Weibel instability. The intermediate case (e.g. targets preionized to $q/A = 1/2$ with a preplasma gradient present) leads to a simultaneous occurrence of both instabilities [155]. The PIC simulation results emphasize the role of the preplasma conditions in the formation of specific instabilities.

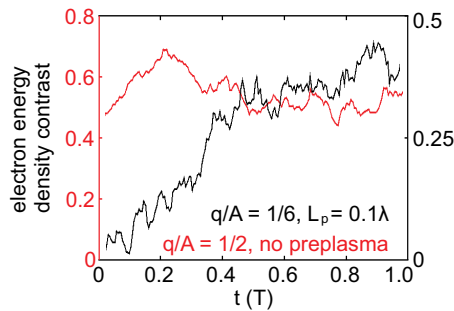


Figure 3.12.: Evolution of the contrast of the electron energy density. Contrast of the electron energy density ($\max - \min / (\max + \min)$), which is sampled during copropagation with an injected electron bunch for two different target parameter sets. $t(T) = 0$ corresponds to the point in time when the electron bunch reaches the target front surface but excludes the preplasma gradient. In the case of a steep preplasma gradient, the electron bunches already feature a transverse modulation when injected into the target volume. On the other hand, in the case of a small preplasma gradient, the transverse modulation develops during propagation through a Weibel instability. The propagation time of $t = 1 T$ corresponds to a propagation distance of 1λ for relativistic electrons. Note that the growth in the contrast of the electron energy density at the target front surface for the case of $q/A = 1/6$ and $L_p = 0.1 \lambda$ is masked in Figure 3.11 by the highly nonlinear color scale, which is optimized to yield a high visibility of the filaments. The plot is taken from the publication [156].

3.5. Comparison of the Experimental and PIC Simulation Results

In order to establish a link between the simulation results and the experimental data, the preplasma conditions resulting from the specific temporal intensity contrast applied in the experimental campaign (Figure 3.3) are analyzed based on dedicated PIC simulations. The analysis of these simulation data is followed by a discussion of the experimental observations in the framework of the laser-target interaction dynamics derived from the PIC simulations. Section 3.5.2 closes with a summary of the hypotheses regarding the experimental observations by taking into account effects which are not considered in the PIC simulations presented in Section 3.4. Possible test experiments are suggested.

3.5.1. Estimation of the Preplasma Conditions

Simulation Setup

The PIC simulations are performed with the collisional 2D3V iPICLS code [153]. The simulation box has a size of $18.75 \lambda \times 37.5 \lambda$ with 48 cells per laser wavelength $\lambda = 800 \text{ nm}$. The temporal resolution is set to 48 time steps per laser period. The spatial intensity profile of the laser pulse is defined as Gaussian with an FWHM of $3.5 \mu\text{m}$ and a peak intensity ($I_L(t = 0)$) of $5 \cdot 10^{20} \text{ W/cm}^2$. The target is a $2 \mu\text{m}$ thick Ti foil with a layer of 10 nm of PMMA as hydrocarbon contamination. The target density is set to $714 n_c$ (critical density) and the simulation is initialized with a cold, singly ionized target. Direct impact (collisional) and field ionization are included in the code. The temporal profile of the p-polarized laser pulse, which impinges normally onto the target, is modeled after the measured temporal intensity contrast starting at -9.3 ps (Figure 3.3, Figure 3.13k). For comparison, the plasma distribution resulting from the temporal intensity contrast in the former setup (Figure 3.3) is simulated.

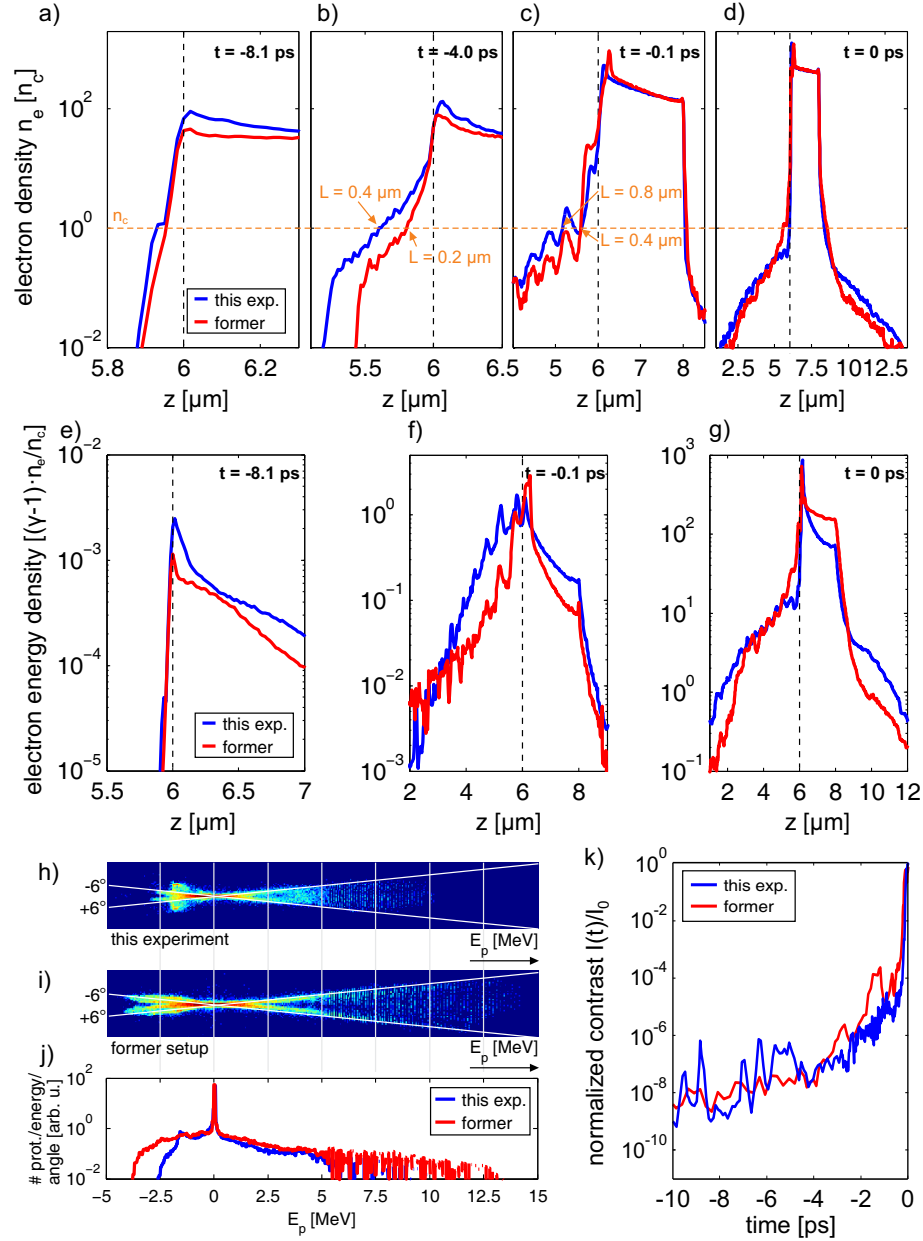


Figure 3.13.: PIC simulation results for the preplasma conditions. a-d) Electron density averaged over $2T$ (laser period) and normalized to the critical density n_c at 800nm at different temporal delays with respect to the peak pulse arrival at $t = 0$. The blue and red lines correspond to the results for the temporal intensity contrast from this and the former experimental setup (k). In c), the standing wave of the laser field imprints into the plasma density. e-f) Electron energy density. All plots show lineouts through the target center at $x = (15 \pm 0.4) \mu\text{m}$ along the laser propagation direction (averaged over a region of $\pm 0.4 \mu\text{m}$). The laser irradiates from the left and the original position of the (cold) target front surface at $z = 6 \mu\text{m}$ is marked with a dashed line. h-i) Polar plot of the proton energy distribution for both temporal intensity contrast settings at 200 fs after peak pulse arrival. The color scale gives the proton number/energy/angle in arbitrary units and is the same in both plots. Protons at positive energies move in laser propagation direction (left to right) and vice versa. j) Proton spectra, derived via spatial averaging (vertical axis) in h) and i). k) Temporal intensity contrast applied in the simulations starting at $t = -9.3$ ps.

Simulation Results

Figure 3.13 summarizes the simulation results on the temporal evolution of the electron density n_e and the electron energy density. The plasma expansion and energy deposition caused by prepulses are both clearly visible and at $t = -4$ ps, the critical density surface has expanded by $L = 0.4 \mu\text{m}$ for this experiment (blue trace in Figure 3.13b, f). The pre-expanded plasma is then steepened and compressed (n_e increases) by the rising edge of the peak pulse for times $t > -2$ ps and the longitudinal (z -direction) spatial preplasma distribution features a complex shape with a two-step exponential decay for $n_e > n_c$ and $n_e < n_c$, respectively¹⁶. Shortly before the peak of the main pulse interacts with the target, the critical density surface is positioned a length $L \geq 0.4 \mu\text{m}$ in front of the initial target surface position ($z = 6 \mu\text{m}$, Figure 3.13c), a pre-expansion caused by the prepulses at -10 ps to -4 ps prior to peak pulse arrival.

Hence - based on the PIC simulation results for the plasma instability analysis in Section 3.4 regarding the influence of the preplasma conditions - a Weibel instability in the electron distribution accelerated at the target front surface is considered the source for the experimentally observed transverse modulations in the proton beam profiles.

A comparison of the two temporal intensity contrast settings (Figure 3.13k) indicates differences in the expansion behavior for early times ($t < -2$ ps) during which the specific temporal pulse structure determines the plasma dynamics. Nonetheless, both setups feature comparable longitudinal density distributions once pulse steepening sets in¹⁷. The local energy densities however show differences of up to a factor of 10 at $t \approx 0$. The differences in preplasma conditions created by both temporal intensity contrast setups translate into the angular and spectral distribution of protons accelerated in the plasma (Figure 3.13h-j) with the *former* setup delivering higher proton energies¹⁸.

3.5.2. Discussion of the Experimental Signatures

In the following, the experimental signatures analyzed in Section 3.3 will be discussed in the framework of a Weibel instability.

Evaluation of the Spatial Scale of the Modulations

The spatial scale of modulation patterns originating from plasma instabilities can be characteristic for the respective filamentation mechanism. Here, the transverse spatial modulation scale is derived based on the quantitative analysis results (Section 3.3.1) using the distance of neighboring peaks as a measure. Included in the analysis are data sets with a proton beam diameter of $\approx 50 \mu\text{m}$ on the RCF layer at a Bragg peak energy of 7.1 MeV,

¹⁶Therefore, L does not correspond to a scale length as defined for an exponential preplasma gradient (Section 2.2.2) but corresponds to the distance of the critical density surface from the original cold target surface.

¹⁷Not considered in the PIC simulations is the contribution from the amplified spontaneous emission background (Section 3.2.1, Figure 3.3), which according to the simulated data presented in Figure 4.12e can cause preplasma expansion as well. The ASE level can be expected to be similar in both temporal intensity contrast settings.

¹⁸Besides delivering an estimate of the preplasma conditions for the experimental setup, the simulations also indicate that the interplay of plasma expansion and steepening on the picosecond timescale before peak pulse arrival renders the definition of a unique preplasma scale length characterizing the plasma conditions difficult. It is however beyond the scope of this thesis to define the parameter set (e.g. plasma scale length, electron temperature, ionization degree) which governs the plasma dynamics and particle acceleration (e.g. protons) and which should hence be used for the initialization of the plasma distribution resulting from a realistic temporal laser pulse profile in a PIC simulation when only the interaction with the ultrashort main pulse is considered in PIC (e.g. as in Section 3.4).

which clearly feature the net-like fine-scale modulations (i.e. $2\ \mu\text{m}$ Ti for 0.6 and $0.7 E_L$, $3\ \mu\text{m}$ Ti for $1.0 E_L$ and $0.8\ \mu\text{m}$ PR for $1.0 E_L$). The evaluation gives (3.2 ± 1.6) mm for the peak-to-peak distance measured on an RCF 45 mm behind the laser-irradiated target. Under the assumptions that the modulations observed in the proton distribution originate from the foil surface and that the proton distribution expands lamarily [15], the RCF image is projected back onto the focal spot region with a diameter of $d_L = 3.4\ \mu\text{m}$. That results in a lateral scale of $\lambda_\perp = (0.2 \pm 0.1)\ \mu\text{m} \approx (0.25 \pm 0.1)\ \lambda$. The uncertainty corresponds to the statistical error of the RCF analysis. The largest contribution to the *systematic* error is the source size chosen for the back-projection of the RCF image. The focal spot ($d_L = 3.4\ \mu\text{m}$) is chosen because the occurrence of the beam modulations is correlated to high laser intensities on target. However, the actual spot size which generates hot electrons is unknown and a doubling of the source size in the back-projection leads to an increase in λ_\perp by 100%. This systematic error could be reduced by the application of targets with a machined rear surface structure, which serves as a spatial gauge when imaged onto the RCF by the expanding proton distribution [15].

λ_\perp conforms with the λ_\perp -value derived from the PIC simulation results for $L_p = 0.1\ \lambda$ (Figure 3.11g, j). In this setup, the occurrence of the electron filamentation due to the WI is most pronounced. Parameters such as the exact preplasma scale length, the bulk temperature profile, transverse density gradients or the target surface roughness may however influence the transverse spatial modulation scale [156].

For a WI, Sentoku *et al.* predict a maximum growth rate for a transverse wave vector $k_\perp = \omega_p/c$ (or $\lambda_\perp = 2\pi \cdot c/\omega_p$), which is the inverse of the skin depth ([89], Section 2.3.2). This result is confirmed in simulations [159] and experiments [93]. Since $\omega_p \propto \sqrt{n_e}$ (Equation (2.9)), the skin depth is related to the density of the filamenting Weibel-unstable electron distribution. The value for λ_\perp derived from the data corresponds to a density of $n_e = 2.8 \cdot 10^{22}\ \text{cm}^{-3}$ or $\approx 10 n_c$ at $\lambda = 800\ \text{nm}$. This value approximately agrees with the estimated beam density n_b for a laser energy of $E_L \approx 3\ \text{J}$ ¹⁹.

Laser Energy Dependence

The experimental data show that the transverse spatial modulations in the proton beam profiles occur above a (target thickness-dependent) threshold laser energy (3.3.1). This trend can be analyzed in the framework of an analytic model by Silva *et al.*, which provides a threshold condition for a purely transverse Weibel instability for the case of a cold, relativistic beam in a cold plasma [159]:

$$\alpha := \frac{n_b}{n_e} > \gamma_b \cdot \left(\frac{p_\perp}{p_\parallel} \right)^2 . \quad (3.1)$$

Here, α is the ratio of the beam to bulk electron density, γ_b is the Lorentz factor of the laser-driven electron beam and p_\perp and p_\parallel are the electron (beam) momenta perpendicular and parallel to the beam propagation direction. Under the assumption that the background density n_e as well as the ratio of the electron beam parameters p_\perp and p_\parallel are independent from the laser energy [160], the threshold condition for a WI reduces to $\gamma_b/n_b < 1/n_e$.

¹⁹For the laser energy $E_L = 2.9\ \text{J}$, an absorption efficiency $\eta = 0.25$ and a mean electron temperature $k_B T_e = 2.5\ \text{MeV}$ follows for the number of electrons in the accelerated distribution: $N_e = \eta \cdot E_L / k_B T_e = 1.8 \cdot 10^{12}$. For the electron volume holds $V_e = (\pi/4) \cdot d_f^2 \cdot \tau_L \cdot c = 8.2 \cdot 10^{-11}\ \text{cm}^3$. τ_L is the laser pulse duration. See Section 2.5.2 for details.

$(p_{\parallel}/p_{\perp})^2 =: C_1$. Taking into account the laser energy dependence²⁰ of n_b and γ_b , for the threshold condition follows it $\gamma_b/n_b = 1/(C_3 \cdot \sqrt{E_L}) + C_4/C_3 < C_1$, where all C_i are real constant values. This corresponds to a scenario in which the threshold condition can start to be fulfilled when the laser energy increases, as observed in the experiment.

A laser energy dependent change in plasma conditions is also indicated by the increase of the hot electron temperature (Figure 3.7) for $E_L > 2$ J in the case of the 3 μm Ti and 0.8 μm PR target. An increase in electron temperature can firstly be related to a change in the electron acceleration conditions or mechanism at the target front surface (e.g. [43]). Moreover, apart from a change in the source term, Link *et al.* discuss that the electron distribution escaping from the target and measured in a spectrometer is influenced by the self-consistent electric fields generated along the target surfaces [151]. In addition, space-charge electric fields generated in the bulk of the target can alter the electron propagation ([72], Section 2.5.2). Both effects - a change in the electron acceleration and/or propagation - can be correlated to changes in the plasma conditions. The claim of the plasma conditions changing as a function of the laser energy, as established based on the spectral and spatial characteristics of the proton distribution, is hence supported.

Target Thickness-Dependence

The threshold laser energy for the occurrence of the transverse proton beam modulations is observed to increase with increasing target thickness (Figure 3.9). Two potential contributions can be considered. The first is the coalescence of the electron current filaments in the bulk of the target, e.g. driven by guiding global magnetic field structures surrounding the electron beam [77, 161]. Indications of filament merging (Figure 3.11g) as well as a wash-out of the transverse structure in the electron distribution during propagation (Figure 3.11h) are visible in the numerical data. Both filament merging and wash-out can result in a target thickness-dependence for the degree of filamentation present in the electron distribution at the target rear surface. The relevance which the propagation through the target bulk has for the thickness dependence is indicated when comparing the transverse modulation patterns measured for the two ≈ 3 μm thick target types (3 μm Ti and 2 μm Ti with 0.8 μm of photo-resist at the target rear): Whereas the spatial scales of the fine-scale pattern are in agreement, the pattern features a lower dose contrast with respect to the background for the 0.8 μm PR target (Figure 3.9).

A second scenario is that the dependence on target thickness arises from a change of the laser-target/plasma interaction conditions (plasma density distribution, electron temperatures, etc.) due to different electron refluxing, hole boring and/or relativistic transparency dynamics for thinner and thicker targets, respectively (see e.g. Figure 3.14).

A quantitative estimate of the contribution of each effect could be performed based on a data set including a larger variety of materials for the targets, sandwich targets (also varying the target front surface material) and target thicknesses.

3.5.3. Consideration of Signatures Beyond Target Rear Surface TNSA

Up to this point, the experimental observations are discussed in the framework of conventional TNSA, where the proton acceleration occurs at the target rear surface of a (metal)

²⁰For the laser energy dependence of n_b and γ_b thereby holds $n_b = C_2 \cdot E_L/k_B T_h = C_3 \cdot \sqrt{E_L}$ (see Equation (2.29) and explanation) and $\gamma_b = (1 + k_B T_h/0.511 \text{keV}) \propto (1 + C_4 \cdot \sqrt{E_L})$, where the C_i are constants. Here, the mean hot electron energy $k_B T_h$ is approximated as $k_B T_h \propto a_0 \propto \sqrt{E_L}$ (see Figure 2.5 and Equation (2.23)). For the WI threshold hence follows $\gamma_b/n_b = 1/(C_3 \cdot \sqrt{E_L}) + C_4/C_3 < C_1$.

foil target. The proton distribution then acquires its transverse modulations from a spatially modulated Debye sheath, as observed in the PIC simulations (Section 3.4). The modulated energy spectra, which are observed to coincide with the spatial modulation however do not fit into the framework of TNSA at the target rear surface. In the following, potential explanations indicating approaches for consecutive (experimental) studies will be discussed.

Proton Beam Divergence

As discussed in Figure 3.6, the proton energy-dependence of the proton beam divergence changes in conjunction with the occurrence of the transverse fine-scale modulations follows a trend in disagreement with the behavior generally observed in TNSA (Section 2.6.1). In particular the comparison of the RCF layers for the Bragg peak energies 4.5 MeV and 7.1 MeV indicates that the diameter of the beam profile is increased when the proton energy increases.

Several theoretical and simulation studies have discussed a correlation of a WI and the hot electron beam divergence driving TNSA [162, 163, 164]. Adam *et al.* and Debayle *et al.* both attribute the electron beam divergence mainly to the formation of a thin WI-filamented magnetic field layer located close to the laser-plasma interaction surface. This layer is seen to scatter the fast electrons. A more indirect effect is discussed by Debayle *et al.*. They show that an increase of the preplasma scale length at the target front surface leads to an increase of the electron beam divergence because the WI is enhanced by the decrease in surrounding plasma density for the hot electron beam (compare Equation (3.1), [163]). Additionally, an increase in the preplasma scale length increases the volume in which hot electrons are generated and the non-planarity of the electron source is observed to add to the beam divergence as well [163, 164].

Alternative Acceleration Scenarios

Up to this point, the discussion has focused on the strongly modulated high energy part of the proton beam profiles (RCF for $E_{BP} = 7.1$ MeV in Figure 3.6). However, the proton beam profiles also exhibit a smoother, less diverging lower energy part (RCF for $E_{BP} = 4.5$ MeV). This observation - supported by the measured modulated proton spectra (Figure 3.6g) - indicates the existence of two distinct proton distributions. Consequently, acceleration mechanisms with an accelerating structure that can deliver two proton distribution need to be considered. Two distinct proton sources can be provided when proton acceleration at the target front surface is taken into consideration in addition to rear surface TNSA. Several experimental studies have shown that the protons emitted at the target rear surface gain higher energies and feature a smaller beam divergence and higher conversion efficiency in TNSA [96, 97]. On the other hand, protons accelerated at the target front surface in laser propagation direction (i.e. towards the target rear surface) have been observed experimentally and are reported to feature a larger angular divergence but a reduced maximum energy compared to protons from the target rear surface [97].

The increased beam divergence agrees with the properties of the proton species featuring the transverse spatial modulations. The maximum particle energies of this species are however considerably larger than the energies of the less diverging proton distribution, whose maximum energy is < 7.1 MeV according to the experimental data (Section 3.3.1). On the other hand, PIC simulations performed for the Draco I laser parameters show that the energy gain of protons originating from the target front surface, which are accelerated towards the target rear surface, can change considerably with the target thickness

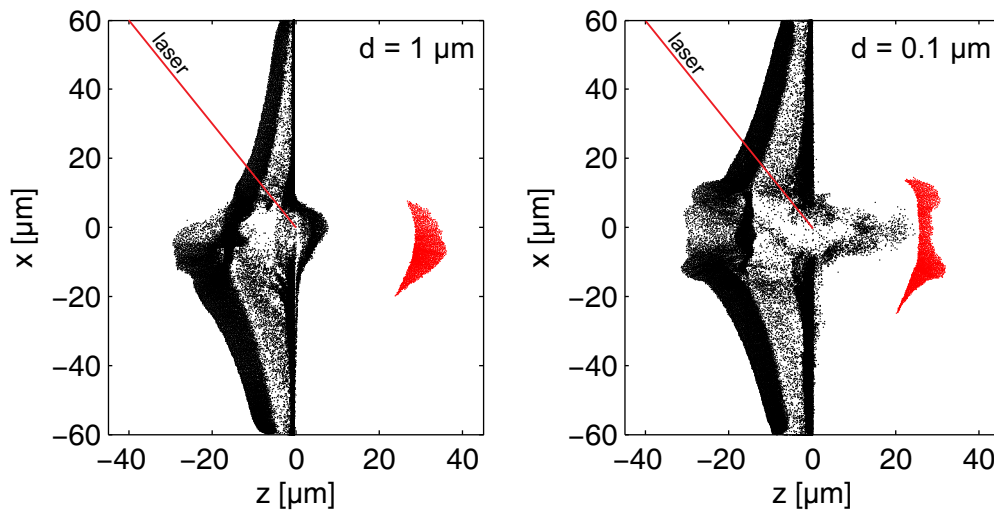


Figure 3.14.: PIC simulation results indicating the role of protons accelerated at the target front surface. Spatially resolved proton distributions for two different target thicknesses at 500 fs after main pulse arrival derived from PIC simulations (2D3V PICLS) for laser-target interaction conditions comparable to Draco I. The black distributions represent protons originating from the target front surface with energies below 50% of the maximum proton energy in the simulation (E_{max}). Protons at positions $z > 0$ are accelerated towards the target rear surface. The red distributions are protons with energies $> 0.5 E_{max}$ from the target rear surface. Whereas the target rear surface proton energies are comparable, protons from the target front surface gain higher energies for the case of the thinner target. Note that the z -coordinate approximately correlates with the proton energy. Simulation setup: Ti targets of $120 \mu\text{m}$ width, covered with 30 nm of hydrocarbons at the surfaces, are irradiated under 45° with linearly polarized light ($\lambda = 800 \text{ nm}$) at a peak intensity of 10^{21} W/cm^2 . The focal spot diameter is $5 \mu\text{m}$. The simulation box has a size of 19440×8330 cells, with 55 cells per wavelength and 55 time steps per laser period. The electron density is $122 n_c$ at full ionization. Prepulses are considered by modeling a 3.5 ps long pedestal in addition to the 30 fs long main pulse. The intensity level of the pedestal is stepwise increased from 10^{13} W/cm^2 to the peak intensity [27]. Ionization and collisions are included.

(Figure 3.14). Whereas the energies of protons originating from the target rear surface (red distribution) are comparable in both cases, protons from the target front surface gain higher energies for the thinner target (black distribution). Note that the z -coordinate approximately correlates with the proton energy.

The feasibility of (experimental) preplasma conditions under which TNSA at the target rear surface is suppressed (low energy proton species), whereas front surface accelerated protons gain high energies ($> 10 \text{ MeV}$), is an open question. The contribution of proton acceleration from the target front and rear surface can be discriminated experimentally by selectively removing the proton source (i.e. hydrocarbon contaminants, Section 2.6.1) via ablation (e.g. [120]). The plasma conditions and hence interaction conditions for the laser pulse can either be varied via the thickness of the target (e.g. [45]) or via a tailored preplasma gradient produced with a second independent laser pulse (e.g. [93]).

Additional Filamentation Mechanisms

Apart from a Weibel instability, further mechanisms can potentially contribute to the filamentation of the laser-accelerated electron distribution. The PIC simulation study in Section 3.4 indicates that a surface-ripple-seeded Rayleigh-Taylor instability can be relevant for laser-target/plasma interaction conditions including a steep density gradient

and high ion mobility. An experimental approach for the detection of surface rippling is suggested by An der Brügge *et al.*, who show that the spatial distribution of high order harmonics changes when emitted from a target surface that is affected by a plasmon decay instability and hence features a regular ripple structure [82].

Not included in the simulations are potential filamentation processes due to resistive magnetic fields, as discussed by Sentoku *et al.* and Leblanc *et al.* ([76, 161], Section 2.5.2). Since the presented simulations (Section 3.4) are initialized with uniformly pre-ionized targets excluding ionization, the resistivity gradients necessary for the magnetic field generation cannot form [76]. The same holds true for the global resistive magnetic field structures forming around the - in reality - finite-width hot electron beam propagating through the bulk of the target [77, 165, 76, 161]. These are suppressed due to the plane wave setup in the PIC simulations (Section 3.4.1).

Moreover, a contribution from the target rear surface plasma is suggested by an experimental study of Wei *et al.* in the regime of longer laser pulses (Vulcan laser, $\tau_L \approx 1$ ps, $E_L = 20 - 40$ J) [93]. The study correlates the observation of a WI in the laser-accelerated electron distribution to the existence of an ≈ 10 μm long plasma gradient (created with a second laser pulse) at the rear surface of the 20 μm thick Au target [93]. Corresponding numerical simulations indicate that the WI is seeded at the target front surface, suppressed in the target bulk [76] and then enhanced again when the plasma gradient at the target rear provides the conditions for Equation (3.1) to be fulfilled. The relevance of the target rear plasma distribution for WI in addition to the target front surface plasma conditions can be investigated by seeding plasma expansion solely at the target rear surface with a second, independent laser pulse.

3.6. Conclusion

The presented experiment investigates laser-driven proton acceleration in the TNSA regime with a prepulse-accompanied temporal intensity contrast of the laser pulse. This setup aims at the provision of non-optimal laser-target interaction conditions. In that way, plasma instabilities are triggered, which potentially become relevant when scaling the available laser power for laser-driven ion sources (LDIS) to the PW level.

The experimental study performed with the ultrashort pulse Draco I laser system results in the observation of spatially modulated proton beams emitted from micrometer thick metal foils irradiated with laser pulses of $\sim 10^{20}$ W/cm² peak intensity. The transverse fine-scale modulations feature a clear dependence on the laser energy and the target thickness for their onset. They are interpreted as a signature of a Weibel instability in the laser-accelerated hot electron distribution which drives TNSA. The study hence reaches a regime in which *controlled* TNSA - characterized by smooth beam profiles and exponential energy spectra - merges into more complex interaction conditions. A similar observation, i.e. the onset of plasma instabilities (Rayleigh-Taylor instability), was recently reported by Palmer *et al.* for radiation pressure acceleration of protons using nanometer thick foils [80]. It indicates that the issue of scalability for laser-driven proton acceleration mechanisms, which motivates the presented experimental study, is not restricted to TNSA. Note that *scalability* here encompasses the scaling behavior of all particle properties relevant to yield an applicable proton distribution. Depending on the envisioned application, these properties may include the particle yield and/or the spatial dose distribution in addition to the achievable particle energies.

The presented experimental data and analysis indicate that the interaction conditions have to be tuned carefully to avoid that growing modes of plasma perturbations are triggered.

In particular, when aiming for e.g. the highest achievable particle energy and a homogeneous dose distribution, the set of parameters (laser pulse length, temporal intensity contrast, target material, etc.) determining the interaction conditions might have to be adapted independently for each laser energy value. As seen in the presented experiment, an exclusive increase of the laser energy can change the laser-target/plasma interaction conditions in an uncontrolled manner.

Another approach is the application of sandwich targets. This target type features a defined near-critical density layer in front of the overdense target, the latter providing the quasi-static electric field for the proton acceleration. In the near-critical density plasma, the laser pulse can shape self-consistently, which has yielded increased proton energies in several experimental studies [166, 167, 168].

A second central result of the work is that changes in the plasma dynamics are probed more sensitively by the proton beam profile homogeneity than by the maximum proton energy, because the latter shows signs of saturation only for the highest laser energies and thinnest target type tested. The maximum proton energy is however the key observable in most experiments on LDIS. This is partly due to the fact that the maximum proton energy is most accessible via Thomson parabola spectrometers operable in real-time. The development of *online* detector systems, that provide spatially resolved proton spectra - comparable to an RCF stack - is therefore a central task in furthering LDIS. Two scintillator-based online detectors developed as a part of this thesis are presented in Appendix A.2. These detectors are optimized to deliver key parameters of the accelerated proton distribution, such as the maximum proton energy, the particle yield and the global beam shape.

Finally, the presented study emphasizes the requirement for experimental techniques which can resolve - in space and time - firstly the laser-target/plasma interaction conditions resulting from the temporal intensity contrast of the laser pulse and secondly the plasma parameters signifying changes in the plasma dynamics, e.g. the electron density inside the overdense target. The former will be addressed in Chapter 4 by reflective pump-probe experiments.

4. Reflective Optical Probing of Laser-Driven Plasmas at Solid Targets

In this chapter, reflective optical probing techniques applied to laser-driven plasmas at solid density target surfaces are presented. The experimental studies aim to spatio-temporally resolve the plasma formation and expansion at the target front and rear surface. Both points are relevant for laser-driven ion acceleration experiments. Analytic and numerical models of the experimental setup as well as particle-in-cell simulations of the plasma formation support the analysis of the experimental results. The relevance and potential of optical plasma probing is highlighted by the application to targets of different geometries. The respective results help to understand the differences in the performance of the ion acceleration, which are related to the shape of the target.

4.1. Motivation

Relevance of the Spatio-Temporal Plasma Conditions

In laser ion acceleration, an (ultra)short, high-power laser pulse is focused onto a thin solid target and produces a plasma that supports quasi-static electric fields of TV/m. Here, ions gain megaelectronvolt energies in micrometer-scale distances. The filamentation of these laser-accelerated proton beams due to plasma instabilities is studied as the main topic of this thesis in Chapter 3. The experimental diagnostic tool applied to analyze the onset of plasma instabilities are spectrally resolved beam profiles of the accelerated proton distribution. Via the comparison of the experimental data with particle-in-cell (PIC) simulation results, conclusions regarding the plasma dynamics can be indirectly drawn. However, to match of the PIC simulation setup with the real experimental conditions is challenging. Among other contributions, the severe influence of the spatio-temporal laser pulse intensity contrast (Section 3.2.1) on the interaction dynamics between laser and target is often either only approximated by pre-set plasma density distributions or neglected. This approximation becomes particularly critical when investigating plasma instabilities, which considerably depend on the specific plasma conditions at the main pulse arrival, e.g. the preplasma scale length around the critical density surface [156]. In order to provide more realistic input parameters for PIC simulations, experimental techniques that allow for the measurement of the spatio-temporal evolution of the target ionization and plasma formation are desirable. Moreover, plasma probing data make it possible to relate the temporal intensity contrast of the laser system with the spatio-temporal *on-target contrast*, i.e. the plasma conditions at the target. This correlation is a relevant input to an understanding of the ion acceleration performance based on the performance of the driving laser.

Pump-Probe Experiments

The ultra-fast dynamics of laser-driven plasmas on timescales of the laser pulse duration and the temporal intensity contrast, i.e. in the femto- to picosecond range, make pump-

probe experiments an ideal diagnostic tool. In a pump-probe experiment, a short, low intensity laser pulse is used to probe the plasma conditions generated by the pump laser pulse at different temporal delays. The formation of plasma at the initially sharp target-vacuum interfaces is - for the laser-irradiated target front surface - either triggered by prepulses preceding the main (pump) laser pulse or, in the case of a negligible prepulses, by the rising pulse edge. Energetic electrons accelerated in the laser-target interaction at the front surface in turn heat the target rear surface, likewise creating a plasma that expands into vacuum behind the target. The probe pulse illuminating the target surface propagates through the underdense portion of the plasma up to the laser frequency- and incidence-angle-dependent critical density surface.

Depending on the particular experimental setup, a vast variety of plasma parameters can be investigated using pump-probe experiments. This encompasses for instance ionization dynamics, plasma expansion, target heating, shock formation or electron transport effects. Using interferometric techniques, the electron density of the underdense plasma region can be determined, which gives access to related parameters such as the electron temperature [169, 170]. Shadowgraphy measurements of the plasma parallel to the target surface can provide information about filament formation in the electron transport when using transparent, solid density targets [91]. Effects at the critical density are usually studied via the analysis of a probe beam that is reflected off the critical density surface. One example is the analysis of the time-dependent Doppler shift within a reflected probe [171, 172]. Moreover, complex plasma features, such as the magnetic field strength and the magnetic field topography at the target rear surface are investigated using reflective probing techniques [173]. Probing of the reflectivity of the target can be used as a diagnostic tool of the fast electron transport in the target bulk [174] and along the surface [175].

Apart from those examples concerning the regime of relativistic laser intensities, pump-probe experiments of laser-irradiated surfaces have also been performed at lower laser intensities in connection with absorption studies [176] and ultra-fast material heating, melting and target ablation [177]. These studies give relevant input for an understanding of the effects of low intensity prepulses generally accompanying the pump laser pulse.

Optical Probing at Near-Critical Densities

For experiments on laser-driven ion acceleration, the investigation of the (near-)critical densities of the plasma is most relevant. In this region, the highest plasma densities accessible to the laser pulse occur and hence the conversion of laser into particle energy as well as a potential triggering of plasma instabilities take place (Chapter 2).

The pump-probe experiments presented in this thesis are performed in a reflective mode, in which the specularly reflected portion of the probe pulse is imaged onto a camera using a long-distance large-aperture microscope objective - a technique here termed *high depth-of-field time-resolved microscopy*. This setup makes it possible to spatially resolve surface features on the micrometer scale, where the image contrast can either be due to an initial cold target surface structure or be caused by a spatial variation of the target's reflectivity. Moreover, using the depth-of-field (DOF) of the imaging system, signatures of the global topography of the reflecting plasma surface can be recorded, because the global shape imprints into the angular distribution of the reflected probe. This technique borrows from the numerically tested scheme of Schumacher *et al.* [178], who proposed analyzing the critical density topography at the laser-irradiated target surface via the change in divergence induced in the reflected main (pump) laser beam.

Apart from plasma probing, a similar technique termed e.g. photothermal displacement

spectroscopy [179], has long been applied for the characterization of thermally induced (i.e. by laser irradiation) deformations and damages on optical surfaces. Fundamentally, the method exploits the fact that the reflection angle of a low power laser beam, which probes the surface under investigation, changes when a thermal bump forms. The main difference compared to the reflective plasma probing technique presented are the deformation amplitudes and hence probe beam deflection angles. For photothermal displacement spectroscopy, a surface expansion of \ll nm is expected for a thermal bump with a width in the $\sim 100 \mu\text{m}$ range [179]. For plasma expansion, on the other hand, ~ 100 nm up to $\sim 10 \mu\text{m}$ expansion amplitudes for similar bump widths are likely to occur. Assuming a Gaussian shape for the surface bump (either thermal or in the plasma) and probe beam reflection at the inflection point, the former case yields reflection angles of $\sim (10^{-6})^\circ$, whereas in the plasma case, the angles can become as large as $\sim 1^\circ$. Hence, for the plasma case, probe beam detection is only possible via a large screen at a distance from the probe (Section 4.2) or close to the probed surface, e.g. with a lens imaging the surface (*high depth-of-field time-resolved microscopy*).

In the following sections, the technique of *high depth-of-field time-resolved microscopy* is firstly applied to investigate the critical or reflecting surface topography and its temporal dynamics at the target rear surface (Section 4.4). Secondly, by probing the target front surface, it is sought to measure the spatio-temporal on-target intensity contrast, i.e. to witness the spatio-temporal reflectivity changes at the target due to laser interaction (Section 4.6). With this method, the laser's spatio-temporal intensity contrast can be verified.

4.2. Plasma Probing Via the Specularly Reflected Pump Pulse

Apart from measurements with a separate probe pulse, the condition of the target at main pulse arrival can already be inferred from the analysis of the reflected portion of the pump pulse itself [180, 181]. Pirozkhov *et al.* [180] have for instance shown that the laser intensity dependent (specular) reflection properties of the target for the laser pulse itself correlate with the temporal intensity contrast. Furthermore, the content of second harmonic radiation in the specular reflection has been identified as a method to estimate the plasma density gradient at the target front surface [182]. The same has been observed for the generation of high harmonics at laser-irradiated solid density target surfaces [183]. In this section, an experiment is presented which shows that the specularly reflected pump pulse can be analyzed for changes in the spatial pattern in addition to its energy and spectral content. The spatial/angular distribution of reflected light can contain information about the topography of the reflecting surface and hence its expansion.

4.2.1. Experiment

The setup and results of the experiment performed at the Draco I laser system are presented in Figure 4.1. Irradiating the target under an angle of 45° , the specularly reflected light is captured on a large-aperture (96 mm diameter) energy meter. The reflected energy as well as the beam profile are recorded as the detector surface is imaged onto a CCD camera. Positioned 120 mm behind the target, the full acceptance angle of the energy meter is 44° , whereas the full opening angle of the laser beam is only 23° . The target is a several millimeter thick gold-coated glass substrate, which provides a reflecting surface of optical quality. The laser energy on target is set to 187 mJ and the intensity is varied by changing the distance between the focal spot position and the target surface. Data for

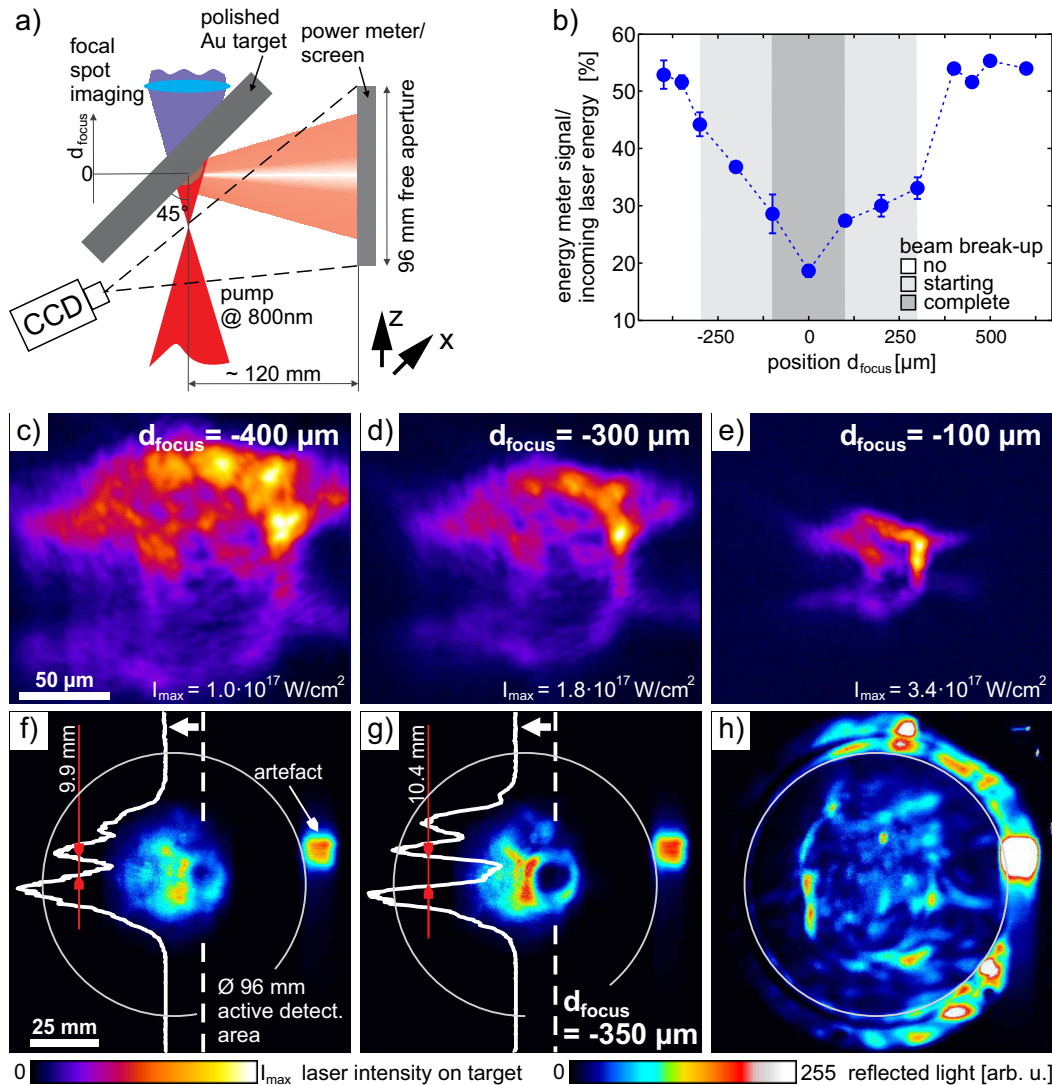


Figure 4.1.: Specular reflection of the pump laser pulse. a) Experimental setup at the Draco I laser system. The target is irradiated under an incidence angle of 45°. The specularly reflected beam is captured with a large-aperture energy meter, which measures the beam energy and serves as a screen for the beam profile. b) Data for the relative specularly reflected energy as a function of the longitudinal (i.e. z-) position of the focal spot. The zero position corresponds to the focusing on the target surface and positive positions to focusing behind the target (see coordinate axis d_{focus}). Specularly reflected light scattered due to beam break-up, which does not reach the detector, is not contained in the data. The degree of beam break-up for each position is qualified by the shaded areas. c-e) The spatial intensity distribution on the target surface for different longitudinal focusing positions is recorded using the focal spot imaging (Section 3.2). f-h) Images of the specularly reflected laser beam for the corresponding d_{focus} positions. All color scales are linear.

the spatial intensity distribution on the target surface for different longitudinal focusing positions are shown in Figure 4.1c - e. The peak intensity covered in the focus scan ranges from $1.0 \cdot 10^{17}$ W/cm² for $d_{focus} = -400$ μ m to $8.6 \cdot 10^{19}$ W/cm² for $d_{focus} = 0$ μ m. The ratio of laser energy specularly reflected onto the energy meter, divided by the incoming laser energy, is plotted in Figure 4.1b. This ratio, termed reflectivity in the following, ranges from 19% to 55%. The latter value is only reached for the lowest laser peak intensities applied ($\sim 10^{17}$ W/cm²).

Comparison with the representative beam profiles in Figure 4.1f - g shows that the decrease in signal on the energy meter coincides with a break-up of the specularly reflected beam¹. For the other data points in Figure 4.1b, the degree of beam break-up is qualitatively encoded in the shaded areas in the plot. Beam break-up here describes a strong increase in beam divergence for the specularly reflected beam as compared to the incoming laser beam. The effect is accompanied by a strong spatial modulation of the reflected beam and it can be caused by a corrugation of the critical density surface due to a radiation pressure driven Rayleigh-Taylor instability [66]. Beam break-up has also been reproduced in PIC simulations studying the far-field distribution of specularly reflected intense laser pulses impinging on a solid target [178].

The strong increase in beam divergence for higher peak intensities beyond the acceptance angle of the energy meter mainly determines the measured intensity-dependent decrease in signal on the energy meter (Figure 4.1b). A lower limit of the contribution of the divergence increase at the $d_{focus} = -100$ μ m position (Figure 4.1h) can be estimated based on the detector geometry: a homogeneous² distribution of reflected light covering the complete detector surface (including the non-sensitive outer ring) with a diameter of $d_d = 124$ mm (Figure 4.1a) is assumed. Since only an area with $d_a = 96$ mm diameter of the detector is active, only a fraction of $d_a^2/d_d^2 = 60\%$ of the beam are recorded as signal. Applying this correction to the measured 28.6% target reflectivity at $d_{focus} = -100$ μ m yields a reflectivity value of 48%. This is close to the on average measured 53% reflectivity for the lowest intensities. The estimation provides a limit for the contribution of absorptive processes at the target front surface to the decrease in reflectivity of $\approx 5\%$. A target reflectivity and hence absorption, which are practically independent from the laser intensity on target in the range from 10^{17} to 10^{19} W/cm², agree with results by Ping *et al.* and Streeter *et al.* in a similar laser parameter range [44, 182].

The measured value for the target reflectivity of $\approx 50\%$ and the intensity-dependence of the (apparent) decrease in reflectivity when approaching the focus (Figure 4.1b) are in very good agreement with results from a similar experiment [180] performed at the J-Karen laser system [184] by Pirozkhov *et al.*. They show that the intensity-dependent target reflectivity, as defined above, closely correlates with the temporal intensity contrast of the laser system. The J-Karen laser features an ASE contrast of $2 \cdot 10^{-9}$, which is indeed comparable to Draco I during the performance of the presented experiment [54].

Apart from the clearly detectable beam break-up, the non-modulated beam profiles in Figure 4.1f - g feature a hole signature on the right part of the profile. The position of the signature coincides with the intensity maximum in the incoming beam profile (Figure 4.1c - e). Regarding its spatial scale, the hole diameter is ≈ 10 mm on the detector screen. Taking into account the magnification of ≈ 400 on the screen, yields a feature size of ≈ 25 μ m in the plane of the target. The hole feature is consistently present in the

¹Note that the bright spot in the right part of the images is an artifact from the power meter frame.

²The assumption of a homogeneous light distribution over the whole detector surface is made for the sake of simplicity but cannot be tested based on the data, as the active area of the detector and the outer ring feature different surface properties. The brightness on both surfaces is hence not comparable.

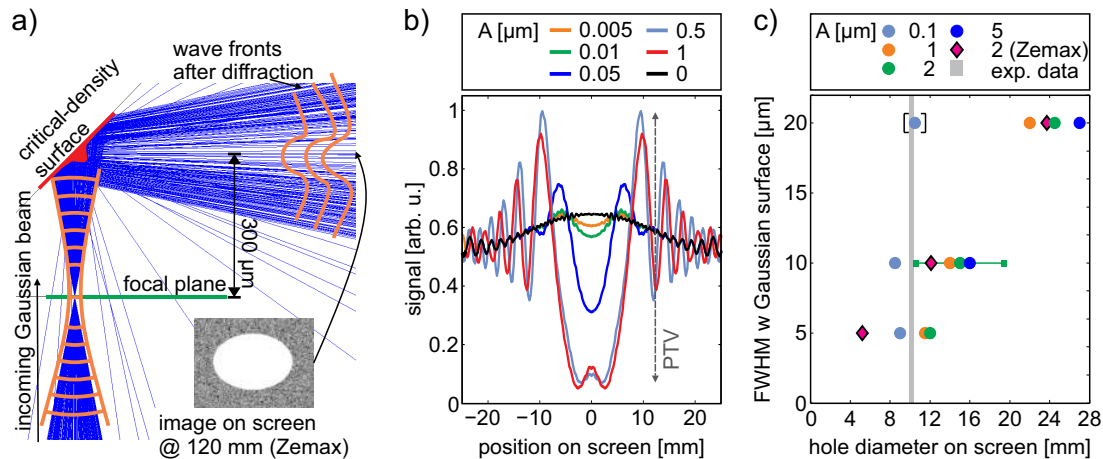


Figure 4.2.: Modeling of the pump pulse reflection. a) Simulation setup for the ray-tracing in Zemax. For the diffraction simulation, the Gaussian beam impinges normally onto the reflecting surface. b) Simulation result for the diffracted beam profiles on the screen for Gaussian parameters $A = 0-1 \mu\text{m}$ and $w = 10 \mu\text{m}$. The profiles have been smoothed. c) Data for the hole signature diameter (undistorted axis, perpendicular to the plane depicted in the setup sketch) for different A and w values from the ray-tracing and diffraction model. The data point for $A = 0.1 \mu\text{m}$ and $w = 20 \mu\text{m}$ is plotted in brackets as the hole signature has not yet fully developed in this case.

data points $d_{focus} = -300$ and $-200 \mu\text{m}$ but washed out when the beam breaks up more severely. It is however not observed when the focal spot is positioned behind the target, i.e. $d_{focus} \geq 0$ (Figure A.15).

Considering that the reflection of the laser pulse takes place at the critical density surface in the target front surface plasma, it is feasible to attribute this hole feature to a convex deformation in the critical surface due to the target expansion. Light reflected in the deformed region is expected to have a higher divergence and hence a dark zone is produced on the screen. Two geometric models, which connect the observed hole signature with the topology of the critical density surface, will be discussed in the following Section 4.2.2.

4.2.2. Modeling of the Experiment

In the geometric models, the critical density surface is set up as a flat, perfectly reflecting surface with a Gaussian-shaped deformation $z(x) = A \cdot \exp(-x^2/(w^2/4 \cdot \ln 2))$, where A is the amplitude and w the full width at half maximum (FWHM). The suitability of the Gaussian shape will be discussed in Section 4.4.2 based on PIC simulation results for a realistic front surface plasma distribution produced at Draco I.

For the simulation of the light propagation, two different approaches are compared. Firstly, based on the fact that the expansion amplitudes for the front surface plasma around the main pulse arrival are expected to be $A < 100 \text{ nm}$ in the laser parameter range studied [27], the diffraction of a Gaussian beam irradiating the deformed surface is modeled. Secondly, these data are compared to results from the ray-tracing program Zemax³. Zemax neglects wave-optical effects but allows for the integration of more complex optical setups, which will be needed for further studies (Section 4.4.2). The setup for the ray-tracing model is shown in Figure 4.2a. The incoming ray bundle (the pump laser beam) is adjusted to the experimental parameters with a beam diameter of 100 mm focused over a distance of 250 mm (Section 3.2) and the focal spot lying 300 μm in front of the reflecting surface. The

³Zemax LLC, Kirkland, Washington, USA

angular redistribution of rays caused by the surface deformation is visible in the reduced ray density in the central part of the reflected beam and then manifests itself in a clear hole signature in the beam profile on the screen at a distance of 120 mm (Figure 4.2a inset).

The wave-optical simulations are based on the Huygens-Fresnel principle, which treats the diffracting Gaussian surface as a secondary point source⁴. The Gaussian beam with $\lambda = 800$ nm and a wave front radius-of-curvature of 300 μm (resulting from the focus-surface distance of 300 μm) irradiates the deformed surface under normal incidence. The signal on a detector pixel at a distance of 120 mm is calculated by summing up the contributions from all point sources according to their intensity and relative phase. The size and spatial resolution of the diffracting surface and the detector surface are set to 200 μm and 80 mm (size) and 0.5 μm and 250 μm (resolution), respectively. It is verified that further refinement of the mesh does not influence the resulting data. In order to speed up the simulation time, only a line of detector pixels is simulated.

Simulation results for the diffracted beam profiles on the screen for different surface deformation parameters (FWHM of $w = 10$ μm , $A = 0.005 - 1$ μm) are plotted in Figure 4.2b. The data show that a shallow hole feature occurs on the screen even for the lowest deformation amplitude of only 5 nm ($\lambda/160$). As A is increased, the modulation depth (difference of the maximum and the minimum signal values of the profile, peak-to-valley) and the width of the hole feature both grow and saturate at $A \approx 0.5$ μm . Hence, the general feature from the ray-tracing model is recovered. In addition, the diffraction pattern contains details which are not included in the ray-tracing model, i.e. the interference pattern that surrounds the primary hole signature. As a reference, the diffraction/reflection on a flat surface ($A = 0$) is presented, which reproduces a magnified image of the beam profile on the detector screen.

Two central details can be derived from the amplitude scan: firstly, the scan proves that local surface deformations with amplitudes $A \sim 10$ nm can in principle be detected in the reflected and propagated beam profile, i.e. the beam's far field. The model calculations hence show the sensitivity of the probing method to deformations in the range expected in experimental settings. This fact supports the suggested interpretation of the experimental data. In comparison, the ray-tracing model predicts a much lower detection sensitivity in the order of micrometers. Secondly, the data also show that the deformation amplitude has an influence on the apparent hole size on the screen.

To connect the experimental and model data, Figure 4.2c summarizes results on the measured hole diameter on the screen for different deformation parameters A and w . The hole diameter is here defined as the width at 50% peak-to-valley (PTV) of the central dip in the profile. This definition agrees with the measurement in the experimental data (Figure 4.1f-g) but possesses a large uncertainty due to the finite slope of the signal flanks around the hole signature (Figure 4.2b). The uncertainty is illustrated by the data point $\{A = 2$ μm , $w = 10$ $\mu\text{m}\}$, in which the green line marks the range of measured hole sizes when using the 10% or 90% PTV width of the central dip, respectively. Consideration of the larger uncertainty also brings quantitative agreement between the ray-tracing (diamond-shaped data points for $A = 2$ μm) and the diffraction model data.

The experimentally observed hole diameter range is marked with a gray bar. It signifies that the signature's dependence on A and w of the Gaussian deformation only allows for an estimation of the experimental surface deformation conditions in the range of $w = 5 - 10$ μm . This size is in accordance with the spatial extend of the peak intensity regions

⁴Before applying, the code was verified using the diffraction by a 20 μm diameter circular aperture for which the near-field (Fresnel) and far-field (Fraunhofer) diffraction patterns were compared with available data.

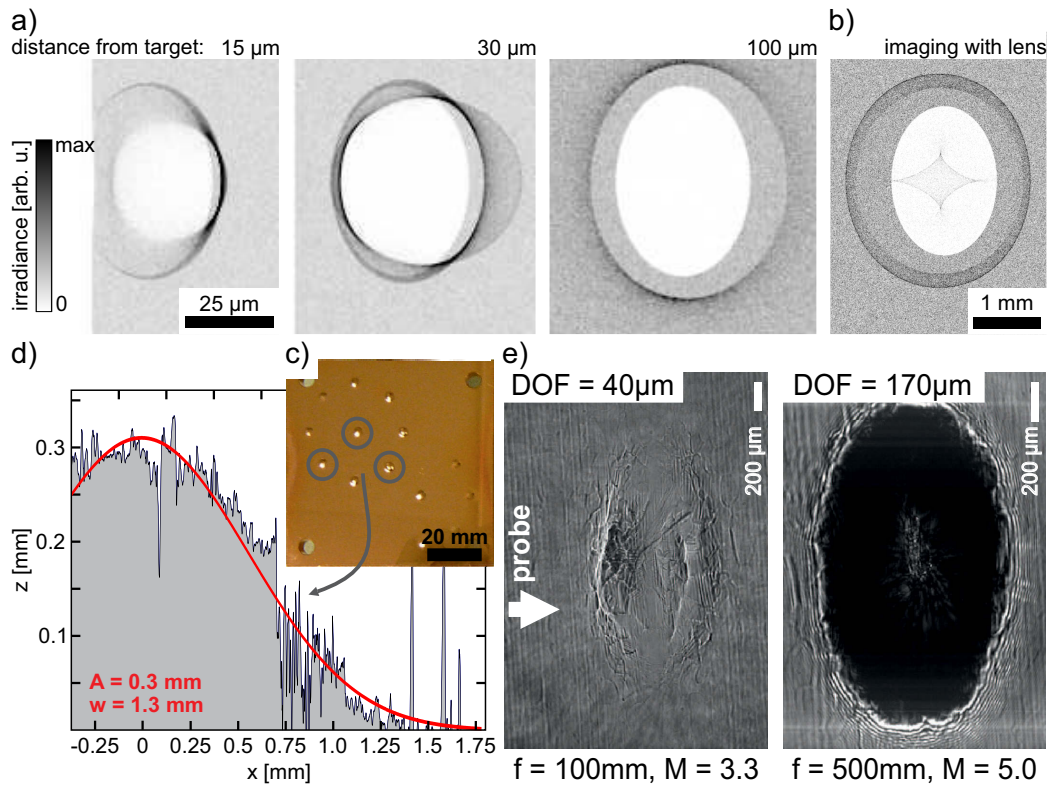


Figure 4.3.: The influence of surface imaging. a) Profiles of the reflected beam less than 100 μm behind a Gaussian deformed surface $\{A = 5 \mu\text{m}, w = 20 \mu\text{m}\}$ using the setup in Figure 4.2a with a collimated incoming beam. b) Surface imaging with a 50 mm diameter lens, $f = 100 \text{ mm}$, magnification $M \approx 40$ and a resulting depth-of-field (DOF) of 27 μm . c) Copper mirror with surface deformations (gray rings) for the experimental verification of the DOF effect. d) Profile of a model surface measured with a three-dimensional scanning microscope. The raw data are shown in gray, the red curve is a Gaussian fit to the data. e) Copper model surface illuminated with a continuous wave (cw) probing laser and imaged with two imaging systems featuring different depth-of-field (DOF) values.

in Figure 4.1c-d, which also supports the suggested link between plasma properties and the hole signature. A lower limit (neglecting e.g. amplified spontaneous emission) for the expansion amplitude A of the surface deformation can be estimated via the ion sound velocity c_s (Section 2.2.2) in the Au plasma created by the main laser pulse of a laser intensity of $\sim 10^{17} \text{ W/cm}^2$ and a pulse duration of $\tau_L = 30 \text{ fs}$. The assumption of a singly ionized Au plasma and an electron temperature of 200 keV [48] driving the expansion, results in a plasma scale length of $L_p = c_s \cdot \tau_L \approx 15 \text{ nm}$. This value is in the range of deformation amplitudes A discussed in the diffraction model.

The diffraction model and the experiment furthermore agree in this regard: if the focal spot of the incoming beam is placed behind the diffracting surface - equivalent to a change in sign for the radius of curvature of the wave front - the hole feature disappears (Figure A.15).

4.2.3. High Depth-of-Field Time-Resolved Microscopy

The above-presented experiment and the corresponding model used for the data interpretation show how the topography of the laser-produced critical density surface is imprinted into the specularly reflected laser beam and can hence be recorded by imaging the reflected

beam profile on a screen. This simple and *macroscopic* access to plasma parameters on the spatial scale of micrometers and below is an interesting tool for laser-plasma experiments. However, the current setup has several shortcomings. Firstly, the main pulse probes the plasma only during its pulse duration so that the dynamical process of the plasma evolution cannot be measured. Secondly, since the reflected light is recorded on a screen ~ 100 mm away from the ~ 10 μm source, small-scale details about the surface are washed out and only global information translating into larger reflection angles can be recorded. To overcome both shortcomings, the experimental setup is improved in two ways: First of all, in order to allow for temporal resolution, the pump pulse and the probe pulse are separated and a second low energy ultrashort pulse with variable delay is applied to the target. Furthermore, instead of letting the beam propagate to a screen, the target surface irradiated by the probe pulse is imaged with a lens to increase the spatial resolution. The second improvement constitutes a major change to the setup because whereas the screen captures an *angular* distribution far away from the surface, surface imaging provides *spatial* resolution of the surface.

To evaluate how the experiment can be performed when applying a lens for target imaging, the evolution of the reflected beam profile close to the surface of the target (≤ 100 μm) is simulated in Zemax using the setup in Figure 4.2a. In that case, the incoming beam is however collimated instead of being convergent and the Gaussian deformation parameters are set to $\{A = 5$ μm , $w = 20$ $\mu\text{m}\}$. The data in Figure 4.3a show that the hole signature already develops 15 μm behind the target surface (excluding the amplitude of the deformation) and undergoes further evolution with increasing distance from the target surface. This suggests that a lens with a sufficient depth-of-field should capture the hole signature even when imaging the target surface.

The surface imaging is also simulated in Zemax for a lens system matching the experimental demands for the imaging of small surface features. Hence, a short focal length of $f = 100$ mm and a large free aperture of 50 mm are applied to yield a high spatial resolution. The imaging system is set up to provide a magnification of $M \approx 40$ with a resulting depth-of-field (DOF) of 27 μm . Accordingly, the hole signature is clearly recorded in the image (Figure 4.3b). That demonstrates that the experimental approach of using the imaging of the target surface for the detection of the hole signature resulting from a critical density surface deformation is feasible. In detail, it shows that target surface imaging does not only allow for the spatial resolution of localized surface properties but that it can also capture global surface properties such as an overall deformation with a lateral size of ~ 10 μm . These result in an angular redistribution of the reflected light.

To verify and illustrate the effect of the DOF, a test experiment is performed in which pre-formed Gaussian-shaped deformations on a copper mirror are illuminated with a collimated beam from a continuous wave (cw) laser diode in an experimental setup otherwise similar to Figure 4.2a. The deformations are produced by drilling the rear of the mirror until the front surface forms a bulge. Variation of the drill diameter and the drilling depth yields a broad variety of parameters $\{A, w\}$ for the surface deformations ranging from ~ 100 μm to several millimeters. The choice of model surfaces which are larger than the expected plasma density deformations is made to allow for an accurate three-dimensional surface characterization via three-dimensional scanning microscopy. A sample copper mirror and the result of a surface characterization are presented in Figure 4.3c-d. Figure 4.3e compares the results of two surface imaging systems with DOFs of 40 μm and 170 μm , respectively. The model surface has parameters $A \leq 50$ μm and $w \leq 500$ μm . The data confirm that the hole signature caused by the the light reflection at the surface deformation is only captured in the case of the larger DOF. The considerable influence of the

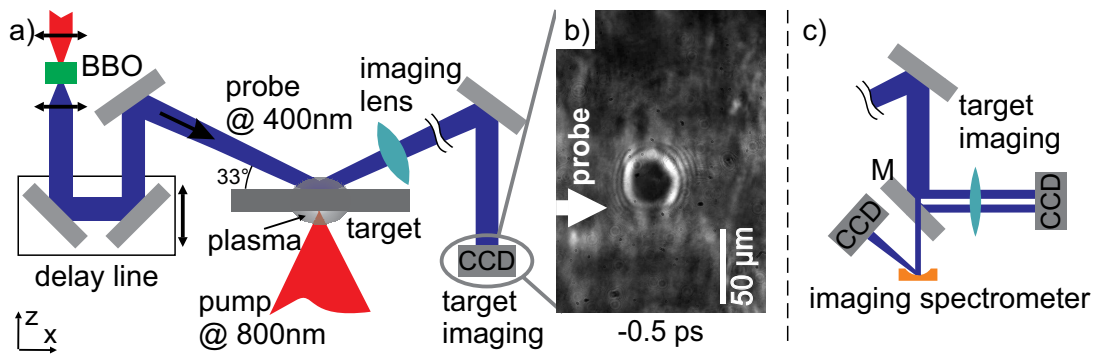


Figure 4.4.: Scheme of the pump-probe setup at the Draco I laser system. a) Interaction zone at the target including the nonlinear crystal and delay line for the probe pulse preparation and the target imaging setup for data recording. b) Representative data from the target rear surface imaging for a pump pulse energy of 84 mJ, yielding an approximate laser intensity of $1.4 \cdot 10^{19} \text{ W/cm}^2$ on target. c) Setup of the imaging spectrometer for spectrally resolved surface imaging along one spatial dimension. The mirror M has a slit through which light is transmitted into the spectrometer

DOF on the image formation indicates that modeling of the experiment must include the imaging system properties.

4.3. Setup of the Reflective Pump-Probe Experiments

The suggested experimental setup using a separate pulse to probe the plasma conditions at the target and to image the surface of the target is realized at the Draco I laser system. It is applied to investigate the temporal and spatial plasma evolution both at the target front and rear surfaces. Figure 4.4a shows the rear side plasma probing setup, which is also used for the front surface probing with only minor differences in the design parameters (summarized in Table 4.1). The presentation and discussion of the technical details will be made on the basis of the rear surface probing.

For the rear surface probing, the pump pulse with $(800 \pm 30) \text{ nm}$ wavelength and a pulse duration⁵ of either 30 fs or 80 fs irradiates the target front surface under normal incidence. The pulse energies on the target are varied between 36 mJ and 220 mJ, which results in peak intensities of $I_L^{\min} = 2 \cdot 10^{18} \text{ W/cm}^2$ to $I_L^{\max} = 4 \cdot 10^{19} \text{ W/cm}^2$. The probe pulse is derived from the pump pulse after pulse compression and it is frequency-doubled to provide for an improved discrimination from the pump pulse at 800 nm. Propagation through the optical elements for pulse preparation results in a probe pulse duration at the target of $\approx 500 \text{ fs}$. This is sufficiently short so as to resolve the picosecond plasma dynamics. The probe pulse energy on target amounts to $\approx 0.1\%$ of the pump energy. Focused to a spot size of $\approx 250 \mu\text{m}$ diameter, the probe intensity reached is $\approx 6 \cdot 10^{11} \text{ W/cm}^2$ (at 220 mJ pump laser energy) and it is therefore low enough to exclude severe target modification through the probe pulse.

The probe pulse illuminates the surface of the target under an angle of 33° . It is imaged onto a CCD camera with a magnification of 42 using an aberration-corrected long-distance (80 mm) microscope objective ($3 \mu\text{m}$ spatial resolution) with an aperture of 50 mm for a high light-collection efficiency. The depth-of-field is $27 \mu\text{m}$. In order to suppress stray and pump pulse light, the imaging system is set up with mirrors optimized for a wave-

⁵For some laser shots, the pump laser pulse was dispersively stretched to 80 fs starting from an almost Fourier-limited pulse of 30 fs.

length range between 345 - 470 nm (reflectivity > 95 %) and an additional short pass (Schott BG39) or band pass ($(400\text{nm} \pm 40)$ nm) filter positioned in front of the CCD camera. Alternatively, the target rear surface can be imaged onto mirror M (Figure 4.4c) using the same imaging system. At this mirror, a slice of the probe is transmitted into an imaging spectrometer resolving wavelengths from 390 - 440 nm in one axis and the positions on the slit in the other axis. The non-imaged axis is focused onto the spectrometer's entrance aperture (slit) using a cylinder lens. The setup is calibrated using diode lasers and different lamps (Ar, Hg (Ar), Kr). Mirror M is additionally relay-imaged onto a CCD camera in order to simultaneously obtain an image of the target surface. Moreover, the visible self-emission at the target front surface plasma is collected under 0° , which is the direction of the incoming pump beam.

| | front surface | rear surface |
|--------------------------------------|--|---|
| pump laser energy | 1 mJ | 36 – 220 mJ |
| pump pulse duration | 30 fs | 30 fs and 80 fs |
| pump intensity | $3 \cdot 10^{16}$ W/cm ² | $2 \cdot 10^{18}$ – $4 \cdot 10^{19}$ W/cm ² |
| probe pulse spot size | 130 μm \times 320 μm | 250 μm diameter |
| probe intensity | $4 \cdot 10^9$ W/cm ² | $6 \cdot 10^{11}$ W/cm ² |
| probe angle of incidence | 29° | 33° |
| surface imaging magnification | 30 | 42 |

Table 4.1.: Summary of the pump and probe pulse parameters for the front and rear surface probing. Note that the focal spot of the pump pulse was different in both setups, which is discussed in detail in Section 4.6.1. The surface imaging magnification is given for the uncompressed axis of the image, i.e. perpendicular to the x-z-plane shown in Figure 4.4a.

Probing Targetry

To provide a target surface of optical quality for the probe imaging, optically flat millimeter-range thick glass substrates are coated with an aluminum or gold layer by means of sputtering. Foils made of titanium or mylar with thickness in the range of micrometers prove to be too rough to provide sufficient resolution of the laser-induced surface effects.

For the target rear surface imaging, on the other hand, only foil targets are of interest. This is due to the fact that the energy transfer from the laser-heated front side of the target to the rear surface via electrons and hence the plasma evolution at the rear crucially depends on the target thickness [45, 174]. To achieve thin targets with optical quality, dedicated 2 μm thick membranes made of silicon wafers and small freestanding targets [32] of the same material are fabricated. The experiments show that the surface structures observable with probing at the rear surface are considerably smoother and larger than at the front surface. Hence, pure 2 μm thick titanium foils (Ti) are used as well and partially, they are spin-coated with a 0.8 μm thick layer of photo-resist (PR) at the rear side to improve the surface quality.

Temporal Synchronization

Conclusions about the plasma evolution on an absolute timescale can only be drawn when the absolute arrival time difference between the pump pulse and the probe pulse at the

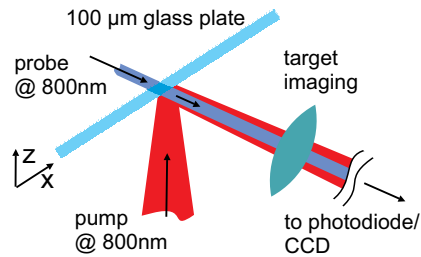


Figure 4.5.: Setup of the pump pulse and probe pulse arrival time synchronization at the interaction point.

interaction point is known. A common synchronization technique in laser-plasma experiments uses the sudden rise in reflectivity of the target for the probe pulse upon pump pulse arrival on a dielectric target [175]. The disadvantage of this method is its dependence on the plasma dynamics which are themselves under investigation in the experiment. At Draco I, the pump pulse and the probe pulse arrival at the target position are hence synchronized without plasma creation via the optical interference of both pulses at 800 nm wavelength. The synchronization setup around the interaction point is sketched in Figure 4.5. The probe pulse at 800 nm is provided by rotating the BBO nonlinear crystal out of its phase-matching position. A thin (100 μm) glass plate is used as a target, which is rotated to reflect the pump pulse into the beamline of the transmitted probe pulse. The spatial overlap of the pulses on the target is controlled via the imaging of the interaction point onto a CCD camera. The target position in focus/z-direction can be adjusted optically with an accuracy of 10 μm , which results in a deviation of ≈ 100 fs for the temporal overlap of pump and probe pulse. This is well below the probe pulse duration of ≈ 500 fs. A further precondition for synchronization via interference is that both pulses have a similar intensity on the target. The pump pulse intensity, which is a factor 10^3 higher than the probe pulse intensity, is therefore reduced by increasing the beam divergence with the deformable mirror (Section 3.2.1). Moreover, a circular aperture (10 mm diameter) is inserted in the beam path to diffract the beam and yield a larger and smoother spot on target. The pre-synchronization of both pulses to the level of ~ 100 ps is performed with a photodiode. To obtain the synchronization between the pump pulse at 800 nm and the probe pulse at 400 nm, the integrated difference in travel time for the probe pulse at 400 nm as compared to 800 nm in all optical components behind the BBO crystal has to be accounted for in addition to the delay in the glass plate used for synchronization. This gives an additional delay of (4.8 ± 0.2) ps and (6.2 ± 0.5) ps for the front and rear surface probing respectively. The given uncertainties stem from uncertainties in the optical material and thicknesses.

After synchronization, the pulse delay is varied using a motorized delay stage, which provides a temporal positioning accuracy below the probe pulse duration. Other factors influencing the timing error between consecutive laser shots are firstly, as mentioned above, the target positioning accuracy in focal direction. The alignment accuracy is limited to 10 μm and contributes an error of ≈ 100 fs. Moreover, the pointing of the probe pulse is subjected to jitter, which is visible in the fluctuations of the probe beam's position on the surface imaging CCD camera. The evaluation of data for 29 laser shots accumulated over a time of 17 minutes results in a diameter of 70 μm for the circle enclosing the probe beam positions of all shots. The analysis⁶ gives a timing difference of 5 fs, which is negligible.

⁶Using the ray-transfer matrix formalism to model the beamline elements, this jitter can be traced back to a corresponding pointing jitter at the entrance to the delay line. Based on this number, the difference

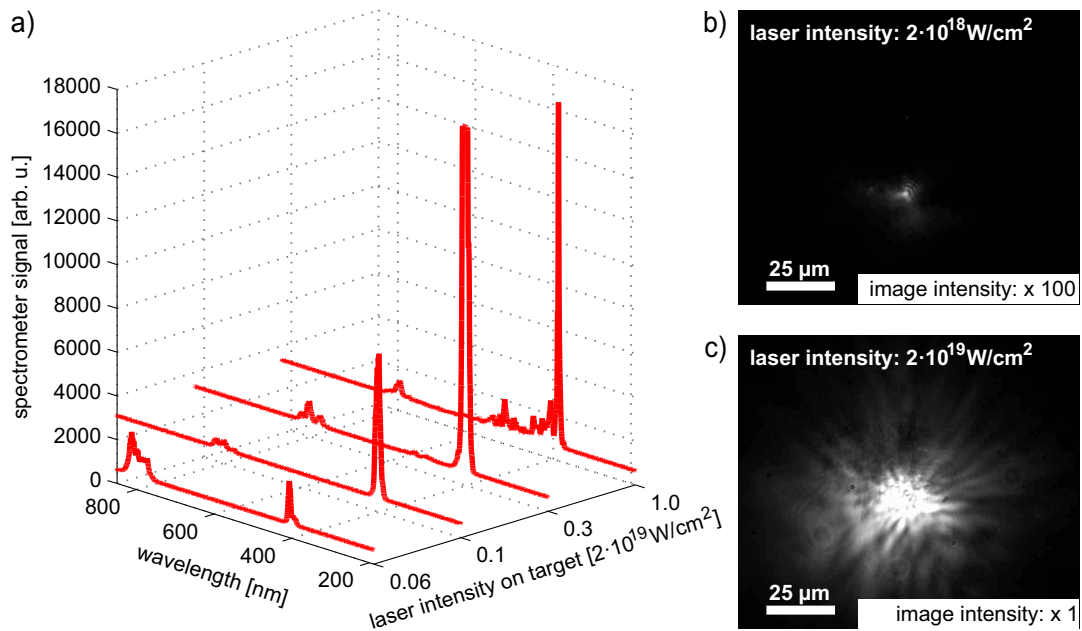


Figure 4.6.: Pump laser intensity-dependence of the plasma self-emission. a) Spectra of the plasma self-emission and reflected pump light generated during the interaction of the pump pulse with the target. The light is collected by the front surface imaging objective. The spectrometer is positioned at the end of the beamline for the reflected probe, so that the spectra represent the filter characteristics employed for the probe pulse imaging. b-c) Imaging of the plasma self-emission in the same setup. The image intensity in b) is scaled by a factor 100 compared to c).

Summing-up of all uncertainties results in a timing error of 600 fs and 700 fs for the probing of the front and rear surface, respectively. These numbers, that are both ≤ 1 ps, agree with the observation that data from consecutive experimental days with equal laser parameters, target parameters and temporal delay parameters are very comparable.

Plasma Self-Emission and the Influence on the Experiment

As presented in Table 4.1, the experiments are performed at laser intensities I_L^{max} which are a factor 10^1 (rear surface) to 10^4 (front surface) below the achievable intensities at the Draco I laser system (Section 3.2.1). Above I_L^{max} , strong light emission from the plasma triggered by the pump pulse is observed in the probe diagnostics. The light overexposes the CCD camera chip and consequentially prevents the probe pulse detection. The plasma self-emission and reflected pump light collected in the surface imaging optics is measured in the front surface probing setup by using both a spectrometer and a CCD camera. Representative data for different laser intensities on the target are summarized in Figure 4.6. The spectra (Figure 4.6a) confirm that the pump light at 800 nm is well filtered in the beamline set up with silver and UV range mirrors. With regards to the fluctuation of the spectrometer signal at 800 nm, note that the spectrometer does not measure the specular reflection of the pump pulse but only the radiation which is scattered into the probe beamline at an angle of 60° relative to the target's normal direction. A shot-to-shot fluctuation of the scattering properties of the front surface plasma under large angles is possible. The self-emission at 400 nm (probe wavelength) measurable in the diagnostics, however, in-

in optical path length of an optimally aligned axial ray versus a ray with a finite angle with respect to the optical axis is calculated.

creases for laser intensities above 10^{18} W/cm². Emission at the second harmonic is caused by the nonlinear response of the critical density plasma surface driven by the relativistic pump laser pulse [185]. For normal incidence and relativistic laser intensities, several mechanisms can be excluded, e.g. resonance absorption, the moving mirror model [48] and coherent wake emission [185]. Instead, the second harmonic generation is attributed to two other mechanisms: firstly, the oscillation of the critical density surface at twice the laser frequency and secondly the excitation of plasma waves by electron bunches accelerated by the $\mathbf{v} \times \mathbf{B}$ force (Section 2.5.1). An additional source of radiation at 400 nm is thermal emission from the target, which is however not a likely source in the presented experiment as the bandwidth of the emission at 400 nm is too small [186]. For a laser intensity of 10^{19} W/cm², additional plasma emission in the range of 400 - 600 nm is recorded (Figure 4.6a). It can likely be attributed to parametric instabilities [187, 183].

The CCD camera images in Figure 4.6b - c show the signature of plasma emission in the surface imaging. The data illustrate that the presence of self-emission prohibits the recording of probing data because the plasma emission masks the expected probing features with sizes in the order of 10 μm . Since the plasma emission at 400 nm strongly varies in intensity on a shot-to-shot basis, all measurements for the front surface probing are performed well below $I_L \sim 10^{18}$ W/cm².

On the rear and hence not laser-irradiated surface of the target, higher pump laser intensities can be applied before the plasma emission becomes stronger than the signal. According to Santos *et al.*, who performed experiments in a setup similar to the one applied in this thesis, the plasma emission at the second harmonic (400 nm) can be attributed to either coherent transition radiation (CTR) or thermal emission from the resistively heated target [186]. Coherent transition radiation is emitted when the electron current, which is generated by the $\mathbf{v} \times \mathbf{B}$ force and is hence longitudinally/temporally modulated, transverses the target-vacuum interface at the target rear (Section 2.5.1). However, since the (rear) surface probing is performed under an angle of 60° with respect to the target's normal direction, thermal emission is expected to dominate over CTR [188]. Besides CTR, the longitudinally modulated electron current can also drive plasma oscillations in the target rear surface plasma, which is another source of second harmonic radiation for thin foil targets [183].

In summary, probing at oblique angles is advantageous, because the contribution of directed emission driven by the normal incidence pump pulse is reduced. A further suppression of background radiation interfering with the surface imaging would require the conversion of the probe pulse to the third harmonic ($\lambda = 266.7$ nm) of the pump pulse.

4.4. Rear Surface Probing

4.4.1. Experimental Results

A collection of experimental data of the target rear side probing recorded for photo-resist (PR) coated Ti foils are presented in Figure 4.7a - f. The targets are irradiated with a pump pulse intensity of $1.4 \cdot 10^{19}$ W/cm² (laser energy of 84 mJ) at the target front surface. The images are taken for different time delays between probe and pump pulse, where negative delays correspond to a probe pulse arrival before the pump pulse. The direction of the probe in the images is, as marked, from top to bottom. Two distinct signatures can be observed in the data. Both only occurred when the pump pulse and the probe pulse were irradiating the target, confirming the signatures' origin in the pump-target interaction. Starting a few picoseconds before the pump pulse arrival (Figure 4.7a), a bright ring with

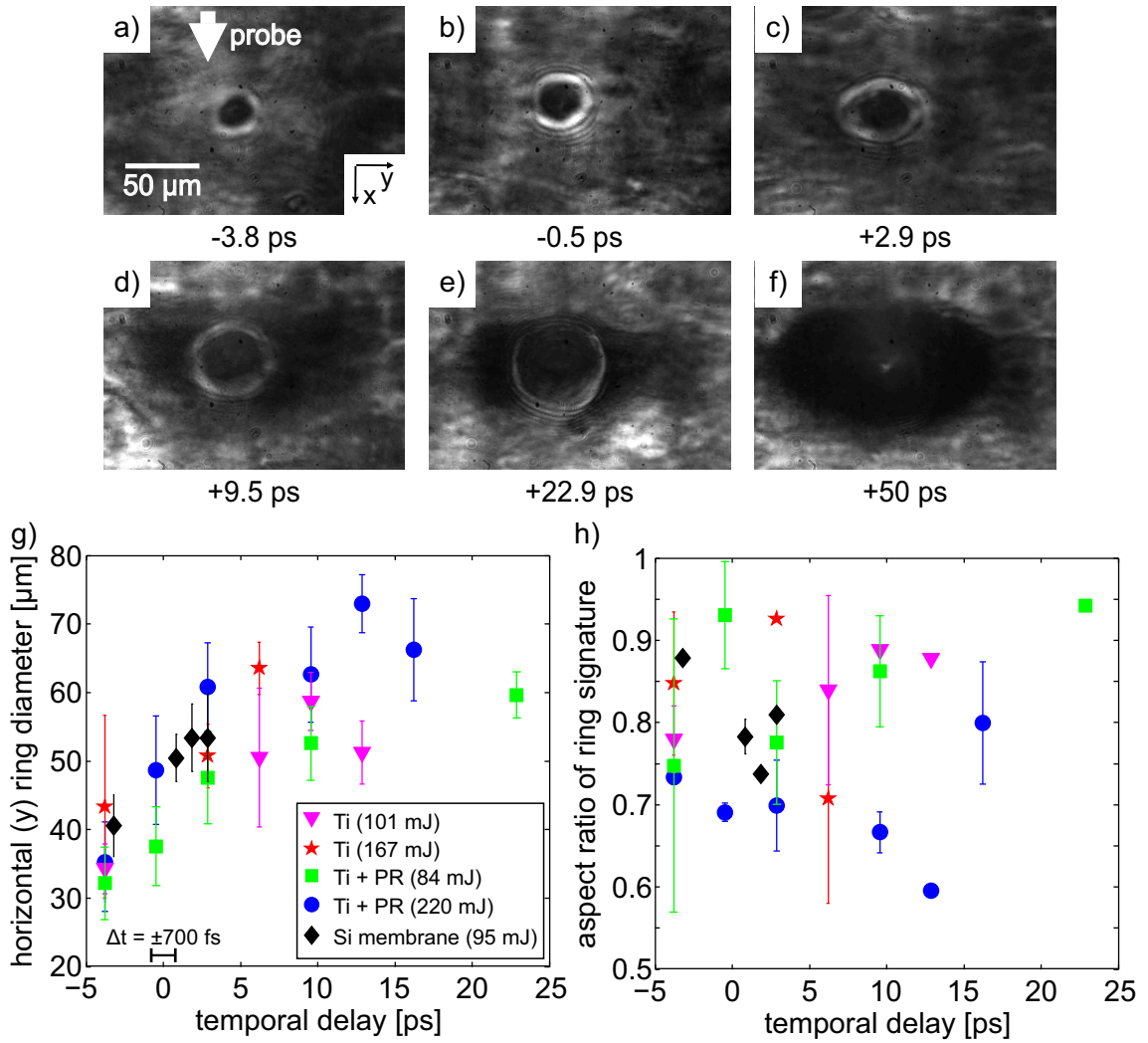


Figure 4.7.: Time-dependent rear side probing data for different targets and laser energies. a-f) Experimental data from the target imaging recorded with a pump pulse energy of 84 mJ. This gives an approximate laser intensity of $1.4 \cdot 10^{19}$ W/cm² at the target front surface. The images are recorded for different delays of the probe pulse and the pump pulse. Negative delays correspond to a probe arrival before the pump pulse arrival. The spatial scale is consistent for all images. g) Horizontal diameter, i.e. the axis orthogonal to the direction of probing, of the ring signature for different temporal delays between the probe and pump laser pulse. h) Aspect ratio (*AR*) of the ring signature, i.e. the ratio of the vertical to horizontal diameter.

a diameter in the order of several $10\ \mu\text{m}$ can be observed. The ring diameter is seen to increase when the delay between the probe and pump pulse are prolonged. For longer delays (Figure 4.7d), the ring fades, and is replaced by an extended dark spot which is elliptical with an aspect ratio of 0.5. This shape corresponds to the image distortion expected for the probe's angle of incidence ($\sin 33^\circ \approx 0.5$) and hence suggests that the feature resides directly on the target surface. It is attributed to a decrease of the target reflectivity caused by the heating of the target [174, 189, 190], a detailed discussion following in Section 4.4.3.

Evaluated data of the ring signature for three different target types ($2\ \mu\text{m}$ Ti foils, PR coated Ti foils and Si membranes) and at energies on the target ranging from 84 mJ to 220 mJ are presented in Figure 4.7g. The graph shows the time-dependence of the horizontal diameter of the ring signature, i.e. the axis perpendicular to the direction of probing. The given values are corrected for the magnification of the imaging system and the error bars include the average including all data points for the same delay, where available, and the uncertainty due to the ring FWHM with an average value of $(5 \pm 1)\ \mu\text{m}$. The ring feature appears at ≈ -3.8 ps before the peak intensity of the pump pulse reaches the target, which indicates the interaction of pre-main pulse light, e.g. prepulses, with the target (see Section 4.4.3). The feature size increases for all target types when the temporal delay is increased. A slight influence of the laser energy in the pump pulse can be detected, higher laser energies by trend corresponding to larger feature sizes. However, these data give no conclusive evidence about the influence of the material or the thickness of the target.

The ring feature's aspect ratio (AR) for the same data points is plotted in Figure 4.7h. AR here refers to the ratio of the vertical to the horizontal ring diameter. In accordance with the impression from the raw data in Figure 4.7, the AR is ≥ 0.6 for all data points and hence larger than the AR of 0.5 expected for the image distortion. This strongly suggests that the ring signature is not a direct image of a property of the target surface, particularly because the AR of the pump laser spot irradiating the target front surface was determined to be ≈ 1 .

4.4.2. Modeling of the Experiment

In the following, a link between the ring feature including its temporal evolution and the properties along with the dynamics of the probed target rear side plasma will be established. This link will ultimately allow for a quantitative access to central plasma parameters with the presented experimental setup. For the sake of brevity, details about the modeling are given in Appendix A.4.

Derivation of a Geometric Plasma Model

The properties of the laser-produced target rear side plasma relevant for modeling the propagation of the probe beam in the plasma are derived from 2D3V PICLS [153] particle-in-cell (PIC) simulation results. The simulation parameters closely match those typical for ion acceleration experiments at the Draco I laser system, which uses a laser pulse intensity of $10^{21}\ \text{W}/\text{cm}^2$ in a focal spot size of $5\ \mu\text{m}$. The laser pulse (45° incidence angle, see red arrow) irradiates a $1\ \mu\text{m}$ thick titanium foil covered with 30 nm of CH contaminant layer on the front and rear surface. The plasma expansion caused by laser light above the ionization threshold preceding the main pulse is accounted for by modeling a 3.5 ps long pedestal in addition to the 30 fs long main pulse [27]. The intensity level of the pedestal is stepwise increased from $10^{13}\ \text{W}/\text{cm}^2$ to the peak intensity. Figure 4.8a shows the electron density (n_e) iso-density lines for 9 normalized densities ranging from underdense ($n_e/n_c < 1$) to

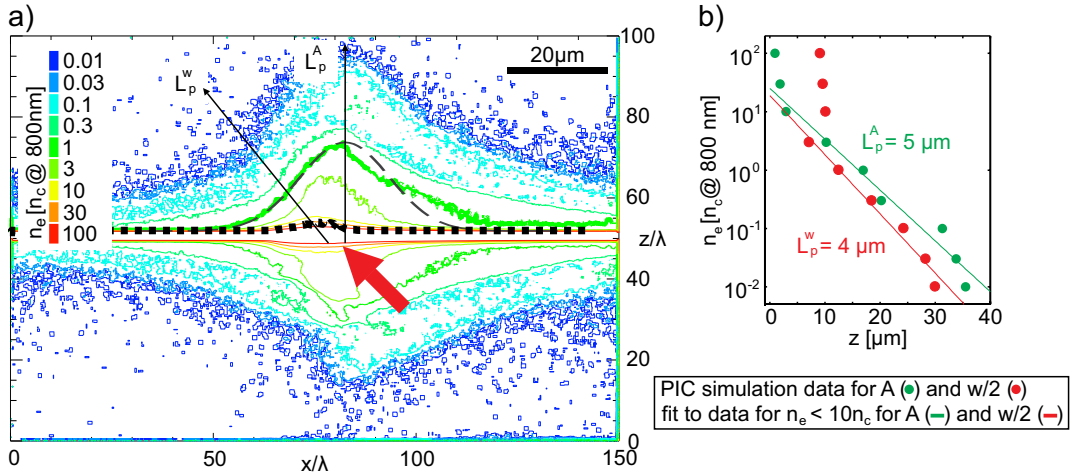


Figure 4.8.: Modeling of the experiment: PIC simulation results. a) Plasma density iso-density contours at the target’s surfaces 500 fs after main pulse arrival derived from 2D3V PICLS [153] particle-in-cell simulation results. The critical density surface for a wavelength of 800 nm 500 fs after the main pulse arrival is marked with a thicker green line and compared with a Gaussian curve shown in black, dashed. The black dotted line close to the target surface marks the position of the critical density surface at main pulse arrival. b) Density gradient at the target rear surface derived from the PIC simulation density map. The gradient L_p^A follows the amplitude and the gradient L_p^w follows the change in width w of the different iso-density contour lines. In the latter case, $w/2$ is plotted for different n_e/n_c values (vertical coordinate axis).

over-critical ($n_e/n_c > 1$) at 500 fs after the main pulse arrival. As the critical density surface n_c (solid green line) resides 20 μm outside of the target, the plasma has expanded considerably and a plasma gradient has formed at the target surface. On the other hand, at main pulse arrival, the critical density surface is located only $\approx 1 \mu\text{m}$ behind the target (black dotted line).

A probe beam with a low intensity sees a corresponding plasma density distribution as a graded-index material, i.e. a medium with a locally varying and wavelength-dependent index of refraction $n_r^\lambda(\vec{r})$, which is calculated from the local electron density via:

$$n_r^\lambda = \sqrt{1 - \frac{n_e^\lambda}{n_c^\lambda}} \quad \text{with} \quad n_c^\lambda = n_c^{800} \cdot \left(\frac{800 \text{ nm}}{\lambda}\right)^2. \quad (4.1)$$

n_e^λ and n_c^λ denote the (critical) electron density at an arbitrary wavelength λ , e.g. the spectral components of the probe beam. When propagating through the graded-index region of the plasma, the probe beam is refracted and then either reflected at the critical density plasma surface n_c^λ , at which the index of refraction n_r^λ becomes imaginary, or it suffers total internal reflection at an iso-density surface $n_e^\lambda < n_c^\lambda$. The discussion of nonlinear propagation effects of laser light in plasmas (Section 2.4.2) indicates that the assumption of linear probe pulse propagation is valid in the presented experiments, because the probe intensity is below 10^{12} W/cm^2 (Table 4.1).

For a geometrical model of the rear side plasma as a graded-index material, the spatial gradient in longitudinal (z -)direction can, as Figure 4.8b shows, be described by an exponential function $n_e = n_0 \cdot \exp(-z/L_p^A)$ with n_0 being the density of the target. It is characterized via its scale length $L_p^A = -\nabla n_e/n_e$ ⁷. The exponential fit to the data considers all density values $n_e < 10 n_c$, i.e. the range relevant for the probe propagation, since

⁷ L_p^A is the length over which the electron density has decreased to $1/e$ of the value of a reference density.

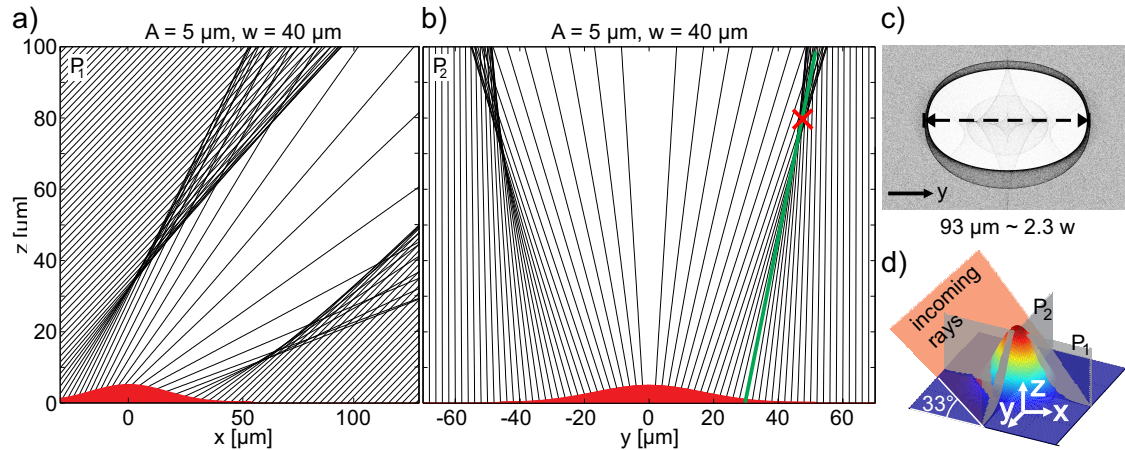


Figure 4.9.: Modeling of the experiment without preplasma. a - b) Ray-tracing of a collimated beam impinging from the left after reflection off a Gaussian-shaped surface (red area) with different A and w parameters, analyzed in two planes. The red cross marks the focus point of reflected rays. c) Surface imaging with a 50 mm diameter lens, $f = 100$ mm, magnification $M = 40$ and a resulting depth-of-field (DOF) of $27 \mu\text{m}$ simulated in Zemax. d) Sketch of the setup, clarifying the planes depicted in a) and b).

$n_r^{400} = 4 \cdot n_r^{800}$. It gives $L_p^A = 5 \mu\text{m}$.

The individual iso-density contours are reasonably approximated by Gaussian curves of the form $z(x) = A \cdot \exp(-x^2/(w^2/4 \cdot \ln 2))$ with the amplitude A and the full width at half maximum (FWHM) w . For comparison, the iso-density line for n_c is overlaid with a Gaussian curve (black dashed) in Figure 4.8a. Note that the asymmetry in the critical density surface is introduced by the oblique incidence of the laser and is not expected for normal incidence as applied in the setup for the pump-probe experiment. The values for $w/2$ of the individual iso-density surfaces also follow an exponential function $n_e = n_0 \cdot \exp(-w/2 \cdot L_p^w)$ and the fit to the data for $n_e < 10 n_c$ gives $L_p^w = 4 \mu\text{m}$ (Figure 4.8b).

It should also be noted that the experiment is performed at a lower laser intensity than the simulations. On the other hand, for probe delays of up to 50 ps, further expanded states of the plasma should be observable. Hence, the numerical values for $A \sim 1 - 10 \mu\text{m}$, $w \sim 10 \mu\text{m}$ and $L_p \sim 1 \mu\text{m}$ derived in the PIC simulation will be applied in the geometric plasma model to simulate the probe beam propagation, reflection and imaging.

Summary of the Modeling Results

Modeling Without Preplasma The basic geometric features of the probe beam reflection are investigated based on a model which neglects the preplasma gradient in front of the critical density surface. The critical density surface is hence set up as a flat, perfectly reflecting surface with a Gaussian-shaped deformation. The incoming ray bundle is collimated, with the angle of incidence matching the experimental setup. In contrast to the model presented in Section 4.2.2, here the pattern formation close to the reflecting surface, i.e. the near-field, is of interest. This region lies in the depth-of-field (DOF) of $27 \mu\text{m}$ of the imaging objective applied in the experiment.

First of all, the production of a hole feature and surrounding ring in the reflected beam - as observed in the experiment - is confirmed (Figure 4.9). The ring feature is caused by the concave flanks of the deformation, which have a focusing effect on the reflected rays. For the focus position (red cross in Figure 4.9b) holds approximately $F(A, w) \approx (1.19 \cdot w | w^2/4.02 \cdot A)$ as a function of the deformation parameters A and w . The ring diam-

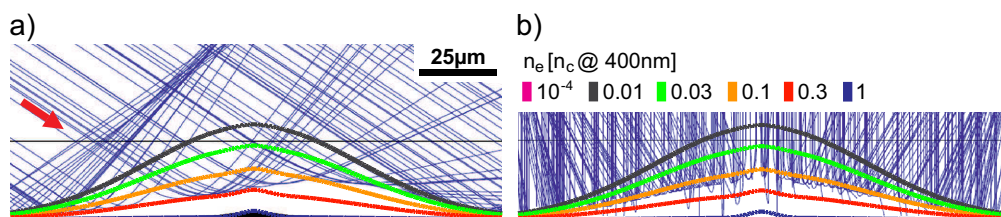


Figure 4.10.: The influence of underdense plasma. Incoming and reflected rays with preplasma in front of the reflecting surface. The plasma distribution is set up with the following parameters for the critical iso-density contour (at $\lambda = 400\text{ nm}$): $\{A = 2\ \mu\text{m}, w = 10\ \mu\text{m}\}$ and a longitudinal scale length of $L_p^A = 6.2\ \mu\text{m}$. The Gaussian-shaped lines indicate the iso-density contours within the plasma. a) Distribution in plane P_1 (see Figure 4.9d). b) Distribution in plane P_2 (see Figure 4.9d).

eter after surface imaging should hence scale as approximately $2.4 \cdot w$ with the FWHM of the Gaussian deformation, a result confirmed by Zemax simulations (Figure 4.9c).

This simple relation does however neglect the influence of the amplitude A , where an increase in A yields an increased diameter for the ring signature. The dependence on A arises because it is not only the focus of reflected rays but also parts of the region of overlapping rays that lie in the DOF of the lens and therefore contribute to the image. With increasing A , the focus F moves closer to the surface of the target and the region of overlapping rays hence acquires a flatter angle with respect to the target surface. In consequence, at a fixed position above the imaged surface, e.g. in the DOF, the region of overlapping rays lies further out for larger A and the ring feature in the image is larger in diameter (Figure A.16).

Test simulations including diffraction effects (Appendix A.4) show that the ray tracing model delivers accurate results regarding the qualitative properties of the hole feature as well as the deformation size-dependent hole diameter of $\approx 2.4 \cdot w$. Moreover, for the interpretation of pre-main pulse probing data, the wave-optical model confirms that the reflective probing technique presented is sensitive to deformations as small as $A \approx 200\text{ nm}$. In addition, the diffraction pattern contains details which are not included in the ray tracing model, i.e. the interference pattern that surrounds the primary ring signature. In a ray tracing image, this feature is attributed to the interference of overlapping reflected rays. It is visible in the experimental data, e.g. in Figure 4.7b.

Ray-Tracing Including Preplasma The full model of the pump-probe experiment including the plasma distribution as a graded-index material and the probe imaging beamline from the experimental setup is implemented in the ray-tracing software Zemax. Zemax accounts for refraction and total internal reflection in the graded-index material, as well as the image formation including depth-of-field effects.

The central aspect in the analysis is to determine the exact plasma iso-density surface which reflects the probe light and is hence characterized by the probing technique when total internal reflection in the preplasma is included. Of particular relevance for a quantitative evaluation is the plane perpendicular to the probe propagation (P_2 in Figure 4.9d). Here, the rays are reflected symmetrically on both sides of the distribution's peak at $\approx 0.1 n_c^{400}$ (Figure 4.10b). In that way, one specific iso-density surface is probed. Its density can be chosen via tuning of the incidence angle of the probe beam and e.g. a steeper incidence angle allowing for denser regions of the plasma to be probed.

Quantitative Analysis A correlation of the plasma surface properties A and w with the characteristic parameters of the ring feature is derived from a parameter scan of A and w performed in Zemax. Plasma setups with and without preplasma are considered (Appendix A.4) and the analysis is performed for the non-distorted plane (P_2 in Figure 4.9d), as motivated above.

The first important result of the analysis is the fact that the same correlation between the ring diameter and the deformation width w is fulfilled, independent from the presence of preplasma. The precondition is that the reflecting iso-density surface $0.1 n_c^{400}$ is evaluated in the preplasma case. Hence, the method in principle allows for the quantification of the reflecting surface parameters independent from the amount of preplasma present at the surface, which is mostly unknown for experimental data.

A second important point is the influence of the deformation amplitude A on the ring diameter for a given deformation width w . For small amplitudes $A \approx 5 \mu\text{m}$, the ring diameter increases as a function of w as $\sim 2.5 \cdot w$, in good agreement with the analytically determined value. The ratio increases to $\sim 3.1 \cdot w$ for larger amplitudes ($A = 20 - 40 \mu\text{m}$) and gives $\sim 2.8 \cdot w$ averaged over all amplitudes A . As a result, for an unknown A , as is generally the case for experimental data, the influence of the deformation amplitude on the horizontal ring diameter translates into an uncertainty for the determination of w from the measured ring data. The uncertainty can be quantified to $< 20\%$ (fig. A.19).

The probing method hence provides approximate values for the FWHM w of the plasma iso-density surface deformation derivable from the experimentally observed ring feature diameter D based on the relation $D = 2.8 \cdot w$ with an accuracy of $< \pm 20\%$. The deformation amplitude A can however not be inferred from the data due to the fact that the ring signature is generated at the flanks of the deformation at which an influence of A is present but not unambiguously quantifiable.

4.4.3. Data Analysis and Comparison with Plasma Simulations

Evaluation of the probing data (Section 4.4.1) based on the results of the quantitative analysis allows for the derivation of the temporal dynamics regarding the lateral extent (i.e. FWHM) of the reflecting plasma surface.

The probing diagnostics record the first signature of plasma expansion at a temporal delay of (-3.8 ± 0.7) ps (Figure 4.7). The focus of the analysis is on relating this experimentally observed plasma expansion preceding the main (pump) pulse (Figure 4.7g) to the temporal intensity contrast curve of the laser pulse (Figure 4.11c). It features four prepulses with an intensity of $\sim 10^{13} - 10^{14} \text{ W/cm}^2$, i.e. above the ionization threshold (Section 2.1.1). These prepulses have interacted with the target when the first signature of expansion is recorded in the diagnostics. The data are compared to plasma distributions derived from numerical simulations under consideration of the temporal intensity contrast of the Draco I laser system.

Data Analysis Based on the Geometric Model

Iso-Density Contour Size The experimentally observed values of the horizontal ring diameter cover the range of $32.2 - 72.9 \mu\text{m}$ (Figure 4.7g). The FWHM of the plasma surface deformation causing these ring signatures is derived based on the calibration factor of 2.8 (Figure A.19a), yielding $w_{exp} = 12 - 26 \mu\text{m}$ for early and later probing times. The respective results for PR-coated $2 \mu\text{m}$ Ti foil irradiated with pump pulses of two different laser energies and pulse durations on target (84 mJ, 80 fs and 220 mJ, 30 fs) are plotted in Figure 4.11a as a function of the temporal delay. The laser energies correspond to

pump laser intensities of $0.5 \cdot 10^{19}$ W/cm² and $4 \cdot 10^{19}$ W/cm². According to the ray-tracing results (Figure 4.10, Section 4.4.2), the surface probed in the experiment is the iso-density surface of $0.1 \cdot n_c^{400}$, or equivalently $0.4 \cdot n_c^{800}$, in the expanding plasma. The error bars in the plot are the scaled errors from the experimental data and include statistical errors and the contribution from the width of the ring. The uncertainty of the FWHM (w) values caused by the amplitude-dependence of the calibration amounts to ≈ 2.4 - 5.2 μm ($\pm 20\%$, Section 4.4.2, Figure A.19a). This uncertainty range is illustrated by exponentially fitting the data. Subsequently, the fitting curve is scaled to the case of small ($\sim 2.5 w$) and large ($\sim 3.1 w$) deformation amplitudes (dashed lines in Figure 4.11a). The calibration factor of 2.8 applied to calculate the FWHM values from the measured ring signature can hence be considered to underestimate the w value in the case of small amplitudes at early delay times and overestimate it for later times when the longitudinal expansion is large.

Expansion Velocity of the Plasma From the temporal scan of the ring signature, the expansion velocity of the probed plasma iso-density surface is derived. The data are approximated by exponential functions⁸ (Figure 4.11a), where the derivatives of the fit functions correspond to the temporally dependent rate of change for the size ($1/2 \cdot w$) of the plasma iso-density surface (Figure 4.11b). Both data sets feature expansion velocities in the range of 10^0 - 10^{-2} $\mu\text{m}/\text{ps}$, i.e. $\sim 10^{-2}$ - $10^{-4} c$, where c is the speed of light. The expansion velocity decreases by a factor of $1/e$ in ≈ 6 ps and ≈ 11 ps for the laser energy of 220 mJ and 84 mJ, respectively, which signifies the cooling of the expanding electron distribution.

Since the ring signature size is predominantly determined by the FWHM w of the plasma iso-density surface, the expansion velocity of the probed iso-density surface represents the plasma expansion in lateral direction, i.e. parallel to the target's surface (Section 4.4.2, Figure 4.8). The contribution from a plasma expansion in longitudinal direction (i.e. perpendicular to the target surface) is negligible because at early times the expansion velocity increases by only 10% when the case of small expansion amplitudes (see dashed lines for $A = 5$ μm in Figure 4.11a) is considered⁹

The plasma expansion parallel to the target surface can be described as a thermal diffusion process of electrons. In this process, the electron propagation distance l_d in the time interval τ_d is $l_d = v_{therm} \cdot \sqrt{\tau_d / \nu_{ei}}$ with the collision frequency ν_{ei} (Equation (2.8)) and the thermal electron velocity $v_{therm} = \sqrt{2 \cdot k_B T_e / m_e}$ [127]. For the effective diffusion velocity v_d then follows $v_d = v_{therm} / \sqrt{\tau_d \cdot \nu_{ei}}$. Assuming a singly ionized plasma at critical density at the target rear surface, an expansion velocity of $v_d \approx 1$ $\mu\text{m}/\text{ps}$ corresponds to an electron temperature of $k_B T_e \approx 80$ eV [59]. According to simulation results by Gibbon *et al.*, these electron temperatures can in principle be achieved by the ultrashort prepulses at an intensity of $I_{usp} \sim 10^{14}$ W/cm², which precede the peak of the pump pulse by several picoseconds. The dominating electron heating mechanism at I_{usp} for normal incidence however depends on the plasma conditions at the target front surface (surface shape, underdense plasma, etc.).

Data Comparison with Numerical Plasma Simulations

Simulation Setup The target rear surface plasma expansion caused by laser intensity preceding the ultrashort main pulse on the nano- and picosecond timescale is estimated based

⁸ $w_{220 \text{ mJ}}(t) = 24.9 \mu\text{m} - 6.44 \mu\text{m} \cdot \exp(-t/5.78 \text{ ps})$; $f_{84 \text{ mJ}}(t) = 22.27 \mu\text{m} - 7.79 \mu\text{m} \cdot \exp(-t/11.04 \text{ ps})$

⁹This value is the difference in slope for the exponential fit to the data and the exponential functions representing the small amplitude case.

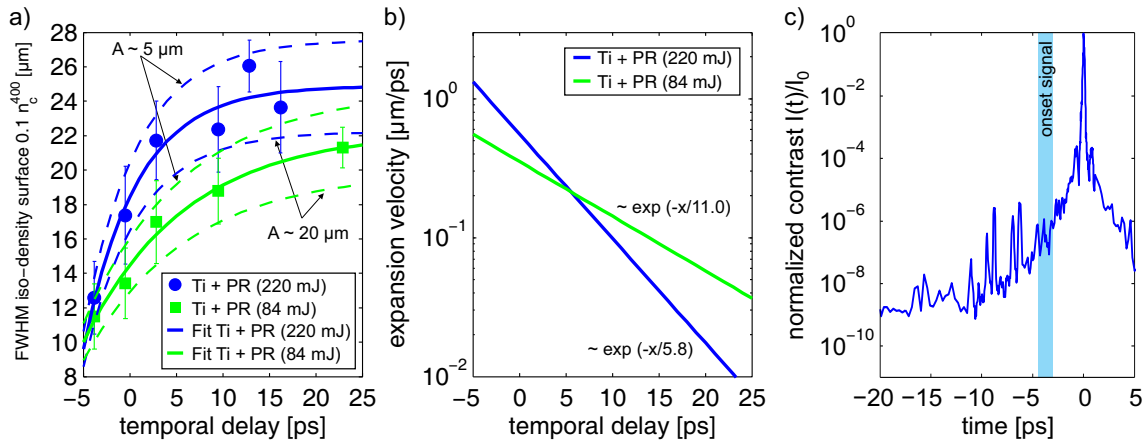


Figure 4.11.: Data analysis based on the geometric model and plasma expansion velocity. a) FWHM w of the iso-density surface of $0.1 \cdot n_c^{400}$ in the expanding plasma for the experimental data (PR coated $2 \mu\text{m}$ Ti foil) calculated as a function of the probe delay based on the quantitative analysis. The error bars only contain the scaled errors from experimental data, the influence of the amplitude A of the iso-density plasma surface on the FWHM is neglected. To give lower and upper boundaries for the influence of A , the data are fitted with an exponential function (solid lines), which is then scaled to the case of small ($5 \mu\text{m}$) and large ($\geq 20 \mu\text{m}$) expansion amplitudes (dashed lines). b) Temporal dependence of the plasma expansion velocity as derived from the exponential fit to the data. Plotted is the expansion of $1/2 \cdot w$, i.e. the radius of the Gaussian-shaped iso-density surface. c) The normalized temporal intensity contrast of the pump laser pulse as applied for the target rear surface probing.

on particle-in-cell (PIC) and hydrodynamic simulations. The PIC simulations are performed with the collisional 2D3V iPICLS code [153] using a simulation box of $12.5 \lambda \times 25 \lambda$ with 48 cells per laser wavelength $\lambda = 800 \text{ nm}$ and 48 time steps per laser period. The temporal profile of the p-polarized laser pulse is modeled after the measured temporal intensity contrast starting at -9.3 ps (Figure 4.11c), with the peak intensity ($I_L(t=0)$) being $4 \cdot 10^{19} \text{ W/cm}^2$. A detailed discussion of the temporal intensity contrast at Draco I can be found in Section 3.2.1. The spatial intensity profile of the laser pulse is defined as Gaussian with an FWHM of $3.5 \mu\text{m}$. A $2 \mu\text{m}$ thick Ti foil coated with $0.8 \mu\text{m}$ of PMMA¹⁰ at the rear surface is simulated as the target. The target front surface is covered with 10 nm of PMMA. The density of the target is set to $714 n_c$ (critical density) and the simulation is initialized with a cold, singly ionized target. Direct impact (collisional) and field ionization are included in the code.

The target's expansion potentially caused by the amplified spontaneous emission (ASE) background (Figure 3.3) is simulated with the hydrodynamic code MULTI [191]. The target is set up with $2 \mu\text{m}$ Ti at $\rho = 4.5 \text{ g/cm}^3$ with $0.8 \mu\text{m}$ of polystyrene at $\rho = 1.0 \text{ g/cm}^3$ at the target rear. The simulation box, containing the upper half of the target, which is simulated, is $20 \mu\text{m}$ wide. The target is irradiated on the Ti side at a constant intensity level of 10^8 , 10^9 and 10^{10} W/cm^2 . The spatial profile of the irradiating laser agrees with the setup as in the PIC simulations. Target irradiation starts at $t=0$ and lasts for several nanoseconds.

Simulation Results The PIC simulation results focus on the spatio-temporal evolution of the electron density both at the target front and rear surface (Figure 4.12). The target front surface starts to expand $\approx 6 \text{ ps}$ before the arrival of the main pulse and is triggered

¹⁰abbreviation for poly(methyl methacrylate)

by the picosecond prepulses (Figure 4.12c). Relevant for a direct comparison with the experimental data are the dynamics of the $0.1 n_c^{400}$ iso-density surfaces, which are fitted by Gaussian functions in Figure 4.12a-b. For the FWHM values of the Gaussian-shaped plasma iso-density contours holds $\text{FWHM} < 10 \mu\text{m}$, which is smaller than the values deduced from the experimental data ($\geq 12 \mu\text{m}$) even before main (pump) pulse arrival at the target. The expansion velocities in longitudinal (A) and lateral (FWHM, w) direction at the target front surface, however, agree with the experimentally observed velocity of $\sim 1 \mu\text{m}/\text{ps}$ around the arrival of the main pulse.

Regarding the target rear surface plasma dynamics, the simulations do not reproduce the experimentally observed onset of the ring signature at the target rear at (-3.8 ± 0.7) ps and the target rear surface only starts to expand beyond the level of ~ 100 nm after main pulse arrival. This indicates that the temporal intensity contrast of the laser pulses starting at -9.3 ps, as considered in the simulations, is not sufficient to explain the observed pre-main pulse plasma expansion.

A second source of preplasma is the amplified spontaneous emission background of the laser pulse, which precedes the main pulse for several nanoseconds at an intensity a factor $\lesssim 10^{-10}$ below the peak laser intensity (Section 3.2.1). According to the discussion on target ablation by ASE in Section 2.1.2, the ASE level in the present data is located around the ablation threshold, given the employed pump pulse peak intensity of $4 \cdot 10^{19} \text{ W}/\text{cm}^2$. The generation of preplasma at the target *front* surface due to ablation, as described by Wharton *et al.*, is hence feasible ([51], Section 2.1.2). McLean *et al.* present experimental data on the correlated (pre-)heating of the target *rear* surface of micrometer thick metal foils. In their data, heating of the target's rear surface is caused by target irradiation at an intensity level of $\sim 10^{12} \text{ W}/\text{cm}^2$ over several nanoseconds [192]. The predominant heating sources for the target rear are soft xrays and thermal conduction [192]. The derived temperatures of ~ 1 eV at the target rear surface causes surface expansion up to $\sim 10 \mu\text{m}$ during 1 ns for an expanding hydrogen plasma (Section 2.2.2). For the presented data, the ASE intensity is however a factor 10^2 - 10^3 lower, so that dedicated hydrodynamic simulations are performed to estimate the influence of ASE.

The respective results are summarized in Figure 4.12e, showing the density of the target after irradiation with three constant ASE intensity levels for 1 ns and 2 ns. The ASE intensity I_{ASE} in the experiment is estimated at $I_{ASE} \approx 4 \cdot 10^9 \text{ W}/\text{cm}^2$ and the ASE duration is > 2 ns. A local deformation (in contrast to a homogeneous expansion of the entire target) of the target rear surface sets in for $I_{ASE} = 10^{10} \text{ W}/\text{cm}^2$ after ~ 2 ns of irradiation. The expansion amplitude is ~ 200 nm and the width is $\approx 4 \mu\text{m}$ ($I_{ASE} = 10^{10} \text{ W}/\text{cm}^2$, $t = 2$ ns). ASE can hence be considered a source for pre-expansion of the target rear surface in the experimental setting in addition to the ultrashort prepulses. This can in principle explain the discrepancy between the PIC simulation and experimental results regarding the observed onset of plasma expansion at the target rear surface.

Effects Beyond the Limitations of the Geometric Model

The purely geometric plasma model applied for the data analysis can reproduce the core experimentally observed signatures. Lastly, aspects of the reflective probing experiment beyond the validity and limits of the geometrical model will be discussed.

Temporal Evolution of the Plasma Reflectivity In the geometric model, the reflecting plasma surface is treated as a perfectly reflecting mirror (i.e. homogeneous reflectivity of unity), while neglecting the spatio-temporal reflection properties of a laser-driven plasma.

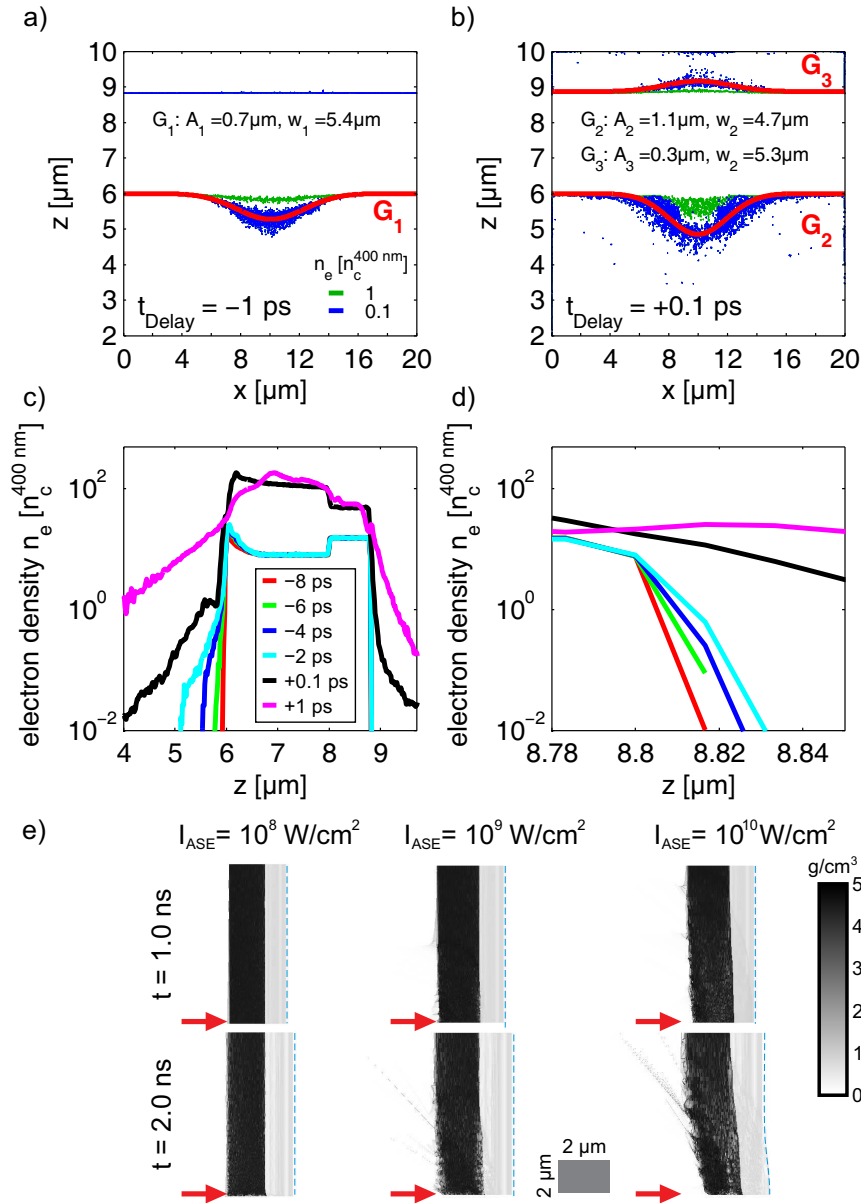


Figure 4.12.: PIC simulation analysis of the target rear surface plasma expansion. a-b) Spatial distribution of the electron density (iso-density contours of $n_e = 1/0.1 \cdot n_c$) for a $2 \mu\text{m}$ Ti target coated with $0.8 \mu\text{m}$ of photo-resist at the target rear before and after main pulse arrival. The simulation takes into account the temporal intensity contrast of the pump laser pulses starting at -9.3 ps (Figure 4.11c) with a peak intensity of $4 \cdot 10^{19} \text{ W/cm}^2$ for the pump pulse at $t = 0$. The laser irradiates the target ($z \approx 6 - 9 \mu\text{m}$) from the bottom. The electron iso-density contours $n_e = 0.1 \cdot n_c$ are fitted by Gaussian functions ($G_1 - G_3$, red lines). c) Temporal evolution of the electron density at $x = (10 \pm 0.4) \mu\text{m}$. d) Zoom into the target rear surface region. All densities are normalized to the critical density n_c at 400 nm and averaged over $2T$ (laser period). e) Target density distributions calculated with a hydrodynamic code as they result from irradiation with a constant laser intensity of 10^8 , 10^9 and 10^{10} W/cm^2 starting at $t = 0$. The laser irradiates the target, which consists of $2 \mu\text{m}$ of Ti and $0.8 \mu\text{m}$ of photo-resist, from the left on the Ti side (red arrows). Only the upper half of the targets is shown. The dashed line marks the position of the target rear surface, indicating the homogeneous and then localized target expansion.

With this assumption, the experimentally observed ring signature is well reproduced. However, the experimental data represented in Figure 4.7a-f additionally exhibit an elliptical extended dark spot for longer delay times (+ 2.9 ps), which persists up to the longest probing delay of + 50 ps after the arrival of the main pulse. The fact that the aspect ratio of the spots (i.e. the ratio of vertical and horizontal diameter) agrees with the image distortion of 0.5 of the imaging system strongly suggests that this feature resides on the target surface (see Section 4.4.1). In agreement with experimental observations, the feature is attributed to a decrease in reflectivity at the target. This effect is caused by ionization and heating of the target's surface [174, 189, 190]. In the published data, the dark spot develops immediately or at least shortly (~ 100 fs) [190] after the main pulse arrival and spreads laterally with an expansion speed of $\sim 10^7$ m/s, which decreases over time. A statement about the onset of the low reflectivity region cannot be derived from the experimental data presented in the thesis, because for earlier times and hence small feature sizes, the effect is potentially masked by the void zone of the ring signature. An increase of the feature sizes over time can however be confirmed. The growth of the dark spot far beyond the size of the focal spot is explained by diffusive electron transport along the target surface. The electrons reflux through the target and are confined close to the surface due to space charge or sheath fields. In summary, the slow decrease in target reflectivity has no direct influence on the geometry of the ring signature formation but can influence the visibility of the signature as it causes a change of the background brightness over time.

Aspect Ratio of the Ring Signature Whereas the ring signature resulting from the reflection of the probe beam off a deformed iso-density plasma surface is in general very well described in the geometric model, one discrepancy between experimental data and model persists. As shown in Figure 4.7h, the aspect ratio (AR) of the ring signature, i.e. the ratio of the (evaluated) horizontal diameter to the vertical diameter (probe beam direction), lies in the range of 0.6-0.94. For the simulated data, however, a mean value of 0.66 with an uncertainty of $\pm 5\%$ and a maximum AR value of 0.75 is calculated by averaging over 27 data sets of different A and w parameter pairs of the surface deformation. In addition to not explaining the AR values measured in the experiment, the simulated data also do not show a correlation between the geometry of the surface deformation and the resulting ring signature's AR .

This discrepancy can indicate that the assumption of a Gaussian deformation with cylindrical symmetry is not correct and hint at an asymmetry in the interaction and hence plasma conditions in the experimental case. For the case of normal incidence onto the target, such an asymmetry can be introduced either by a non-circular focal spot or the linear polarization (p-polarization) of the laser field.

The first option is ruled out by the analysis of focal spot imaging results, which results in a deviation of only 4% from unity for the ratio of the horizontal to vertical spot diameter. On the other hand, Seely *et al.* [193] have shown experimentally that for a linearly polarized laser pulse, the propagation of energetic electrons is stronger when it is parallel to the electric field than when it occurs in perpendicular direction. Applying this observation to the target rear surface plasma evolution, an enhanced (either stronger or faster) plasma expansion in laser polarization direction (direction of probing) than in the perpendicular direction (horizontal direction, used for evaluation) seems feasible. That in turn allows for the assumption of a plasma iso-density surface with a larger FWHM in polarization direction and leads to an increase in AR , as measured. This fundamental asymmetry cannot be resolved in interferometry experiments which rely on an Abel inversion and

hence the assumption of cylindrical symmetry to derive the plasma distribution from an interferogram [170].

4.5. Rear Surface Probing of Reduced-Mass Targets

The reflective probing method presented, enables the measurement of specific spatial properties of a chosen iso-density surface in the plasma and the mapping of the surface's temporal evolution. Whereas the analysis of the method and its limitations is performed based on experimental data from thin flat foils, the probing results from reduced-mass targets (RMT) will be discussed in this chapter. RMTs are targets which feature a finite transverse size and have been shown to lead to an increase in the maximum energy and yield of laser-accelerated protons [108, 32]. Moreover, regarding the proton acceleration performance, they are less sensitive to the temporal intensity contrast of the laser pulse [32]. These features, favorable for the generation of applicable proton distribution, are attributed to a time-averaged increased density, temperature, homogeneity and particle source size in the accelerating Debye sheath [108, 32]. Besides, proton distributions accelerated from RMTs exhibit strong spatial modulations attributed to particle emission from the target edges and its support structures [32].

The study presented in the following evaluates whether potential changes in the plasma evolution of RMTs due to their specific geometry can be detected with the reflective probing method applied to the target rear surface.

4.5.1. Analysis of the Experimental Data

The experiment is performed at the Draco I laser system with the setup presented in Section 4.3. A 2 μm thick silicon (Si) RMT target, as used in the experiment, is depicted in Figure 4.13i. The target itself has a transverse size of 100 μm and is kept in place by support stalks of 2/5/20/50 μm width, of which all but one (two in the case of 2 μm stalk width) are removed prior to target mounting. As a reference foil target, 2 μm thick Si membranes are applied. Whereas the foil targets are irradiated with a pump laser energy of 95 mJ, only 36 mJ pump laser energy can be applied to the RMTs without overexposing the surface imaging CCD camera with plasma emission (Section 4.3). The corresponding laser intensities are $6.3 \cdot 10^{18} \text{ W/cm}^2$ and $2.4 \cdot 10^{18} \text{ W/cm}^2$.

As diagnostic tools, the target surface imaging including the imaging spectrometer is applied (Section 4.3). Additionally, plasma emission in the optical range ($(400 \pm 40) \text{ nm}$) from the target front surface is recorded (Figure 3.4b). The light is recollimated by the off-axis parabolic mirror and is analyzed by imaging the leakage through mirror M2 onto a CCD camera (Figure 3.4b).

Raw data from the main diagnostic tool, i.e. the target surface imaging, are presented in Figure 4.13c-f. Note that the black stripe in the center of the images stems from the slit in the mirror M (Figure 4.4c) through which a part of the probe beam is transmitted into the imaging spectrometer.

Ring Signature Size

As the data of the ring diameter summarized in Figure 4.13a show, the RMTs yield an ≈ 1.7 times smaller ring signatures in comparison to the Si membrane targets. The influence of the difference in pump laser intensity (factor of 2.6) cannot be quantified. For the flat foil case (Ti with PR), data sets with different pump laser intensities (factor of 7) are discussed in Section 4.4.1, which indicate a ring diameter difference of ≈ 1.4 (Figure 4.7g).

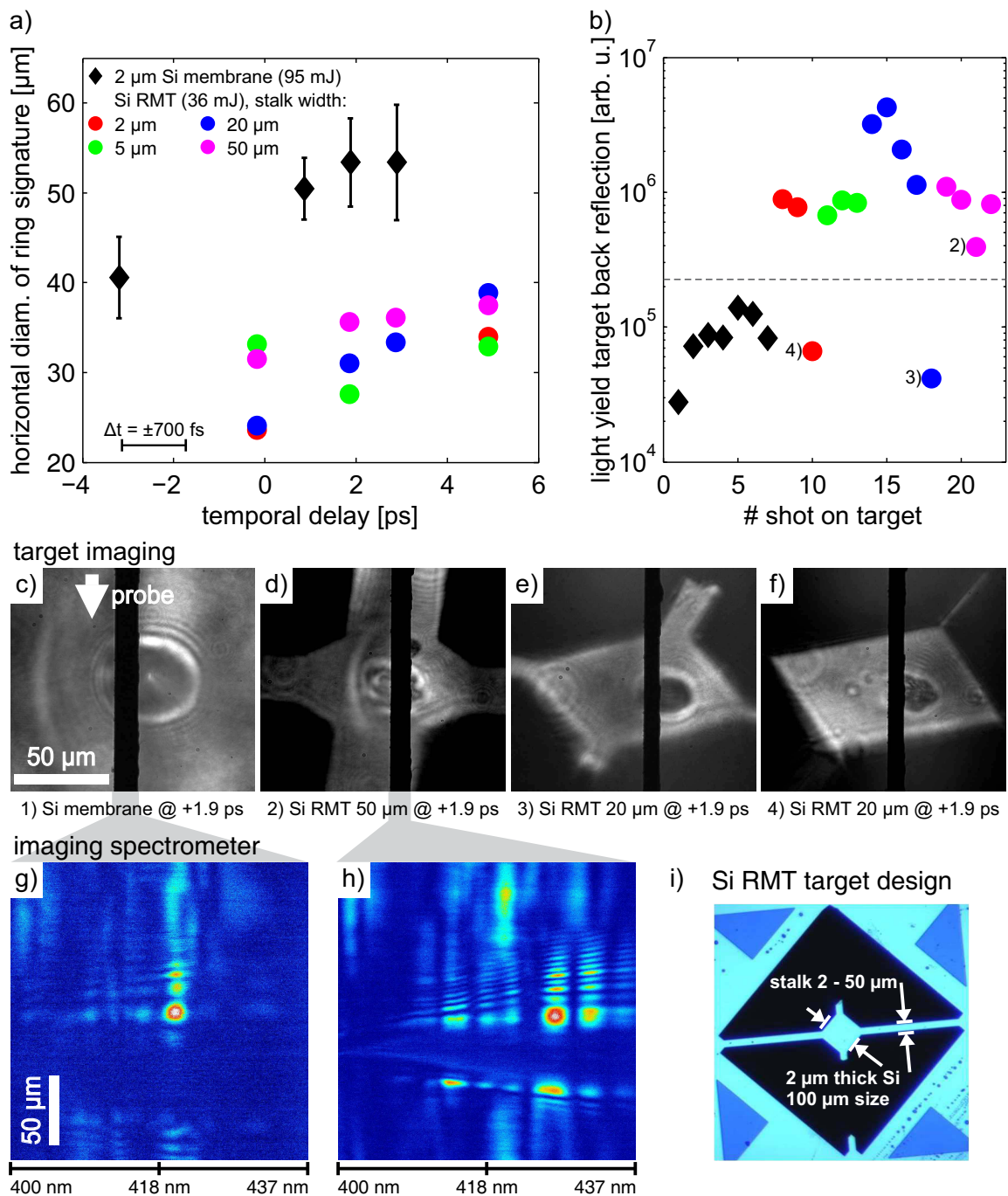


Figure 4.13.: Probing of reduced-mass targets. a) Evaluated data from the target imaging for the horizontal diameter of the ring signature as a function of the pump-probe delay. b) Light yield from the target front surface reflected back into the pump laser beamline and recorded in the wavelength range of (400 ± 40) nm for Si membrane targets and RMTs. c-f) Raw data from the target imaging for a Si membrane target and RMTs with different stalk sizes. The black stripes in the center of the images stem from the slit in the mirror through which a part of the probe beam is transmitted into the imaging spectrometer. g-h) Imaging spectrometer data for data c) and d). The vertical axis resolves the spatial axis along the probing direction. i) Geometry of the RMTs.

Crucial for the interpretation of these results is however the fact that the onset of the ring signature (delay of -3.8 ps) is detected for both intensities. This confirms that the initial ring size is the same within the error bars. Up to the pump pulse arrival, the higher intensity case then exhibits a faster growth of the ring diameter. For the RMTs and membrane targets, however, the data at the detection threshold are not available. Hence, it cannot be evaluated whether the two target types only feature a difference in expansion velocity or whether the RMTs feature a different shape and size of the probed plasma iso-density surface even at *initial* conditions.

Ring Signature Structure

Whereas the membrane targets feature a clear ring signature, for most of the RMT data (Figure 4.13d shows representative data), an additional structure within the outer ring occurs. The additional ring structure can in principle hint at several effects, e.g. firstly a more complex plasma iso-density surface than a single Gaussian deformation, which leads to a more complex reflection pattern of the probe beam. Secondly, the additional structure can stem from a locally varying plasma reflectivity for the probe beam at the target surface (see Section 4.6). Thirdly, since the surface imaging system has a finite transmission for light up to 600 nm wavelength (Section 4.3), the additional emission inside the outer ring can in principle stem from plasma self-emission (Section 4.3).

The data from the imaging spectrometer, which represent the probe beam's spectral range from 400 - 440 nm (Figure 4.13g - h), support the last hypothesis. The images for the RMT as well as membrane targets feature signal only in the upper and lower part of the image, where the signal surrounds an inner darker part. This pattern corresponds to the cross-section through a ring signature. A streak of plasma emission that the additional signal inside the outer ring structure is attributed to for the RMTs, is found in the left half of the image. The spectra of the plasma emission from the target rear over the entire spectral range are not available to definitely confirm the hypothesis. However, the plasma emission from the target front surface is recorded for each shot (Figure 4.13b), which confirms that the RMTs typically yield a considerably higher amount of plasma emission. Note that the two RMT data points with a signal comparable to the membrane targets (marked 3 and 4) also feature a clear ring signature without additional structure in the central part. Under the assumption that the plasma emission at the front and rear surface of the target is correlated with regards to its intensity, this observation strengthens the hypothesis that the additional ring signature structure is due to plasma emission.

Plasma Properties

Whereas the principle ring signature and central void zone is observed for both the membrane targets and the RMTs, the latter typically exhibit a wavelength-dependence for the void zone size in the imaging spectrometer data (Figure 4.13g - h). In particular, the size of the void zone decrease as the wavelength decreases. This effect is particularly visible in the upper right part of Figure 4.13h, where the horizontal structure in the signal curves. In the framework of the geometric model of the ring signature developed in this thesis, this effect can be attributed to the dispersion of the probe beam in the plasma¹¹. As

¹¹Note that since the measured ring diameter decreases for decreasing wavelength (i.e. $\partial w/\partial \lambda > 0$), the effect cannot be attributed to the temporal chirp of the probe pulse, which is dispersively stretched to ≈ 500 fs. For the stretched pulse holds $\partial \lambda/\partial t < 0$, i.e. shorter wavelengths follow later in time. Combined, it would follow $\partial w/\partial t < 0$, which corresponds to a decreasing feature size over time, which is in contradiction to the expected plasma expansion.

discussed in Section 4.4.2, the probe is reflected in the plasma distribution through total internal reflection in the presence of preplasma. The reflecting density of shorter wavelength is thereby higher (Equation (4.1)). Since higher densities are situated deeper in the plasma, their respective iso-density surfaces have a smaller size (A , w) than those lying further out. This effect, which is in principle always present, can manifest itself in the imaging spectrometer when the reflecting iso-density surfaces of different wavelength are to be separated in space. That is equivalent to the hypothesis that the RMTs feature a more expanded plasma gradient than the membrane targets. In the following, this effect will be quantified.

Estimation of the Plasma Gradient The normalized plasma distribution $n_e^\lambda/n_c^\lambda =: \tilde{n}^\lambda$ at the target surface (plasma gradient) is best modeled by an exponentially decreasing function $\tilde{n}^\lambda = \exp(-x/L_p)$ (Section 4.4.2). This relation is valid in transverse as well as longitudinal direction with different scale lengths L_p , i.e. parallel and normal to the target surface. Here, the transverse direction is considered since the reflecting probing technique mainly resolves the FWHM w of the density distribution. For the probe beam, the plasma distribution is a graded-index region (Equation (4.1)), in which the probe propagates up to an index of refraction n_r^{tir} of which the condition for total internal reflection $n_r^{tir} = \sin \alpha_{in}$ is fulfilled. α_{in} is the angle of incidence. The corresponding normalized densities at two wavelengths λ_1 and λ_2 (\tilde{n}_{tir}^λ) and the index of refraction n_r^{tir} are connected via Equation (4.1). When normalized to the critical density at λ_1 , the densities are referred to as $n_{tir}/n_c^{\lambda_1} =: \tilde{n}_{tir}^{\lambda_1}$ and for λ_2 holds $n_{tir}/n_c^{\lambda_1} \cdot (\lambda_1/\lambda_2)^2 =: \tilde{n}_{tir}^{\lambda_2}$ (Equation (4.1)).

The lateral spatial separation Δx of both normalized iso-density contours in the exponential density profile is calculated as $|\Delta x| = L_p \cdot \left| \ln(\lambda_1/\lambda_2)^2 \right| = 2L_p \cdot |\ln(\lambda_1/\lambda_2)|$. This relation allows for the derivation of the scale length L_p from the experimental data. Since it is independent from the probe beam's angle of incidence α_{in} , L_p can be determined from the experimentally measured data for Δx without further knowledge about the exact shape of the reflecting iso-density surfaces.

For the RMTs, 15 data sets from the imaging spectrometer (Figure 4.13h is representative) are analyzed by taking vertical profiles at three different wavelengths (408 - 434 nm). For those wavelengths, the distance of the peaks surrounding the inner void zone, i.e. the ring signature diameter, is measured. From the interpolated data at 410 nm and 425 nm, the ring signature diameter difference ΔD is determined, which covers a range from 3.8 - 14.1 μm with a mean value of $\overline{\Delta D} = (10.8 \pm 2.1) \mu\text{m}$. A correlation of ΔD either with the temporal delay between the pump pulse and the probe pulse or the RMT geometry cannot be detected in the data. Moreover, for the imaging spectrometer data of the membrane targets evaluated in the same manner, no wavelength-dependence for the ring signature diameter is found.

In order to arrive at the plasma scale length L_p as $L_p = \Delta x / 2 \cdot \ln(\lambda_1/\lambda_2)$ for $\lambda_1 = 410$ nm and $\lambda_2 = 425$ nm, the difference in ring signature diameter for λ_1 and λ_2 , ΔD , is calibrated to Δx . Δx is the spatial separation of the iso-density contours and the calculation gives $\overline{\Delta x} = (2.9 \pm 0.6) \mu\text{m}$. The calibration is based on the results presented in Figure A.19. It also takes into consideration that the imaging spectrometer data show the vertical instead of horizontal ring diameter (see P_1 and P_2 in Figure 4.9d), the latter being smaller by a factor of 0.66 (Section 4.4.3). The scale length then follows as $L_p \approx 40 \mu\text{m}$, where the calculated scale length value represents L_p^w (see Figure 4.8).

This value is an upper limit, since the derivation of L_p uses Δx (Figure 4.14). The common definition of the scale length L_p however refers to the plasma gradient orthogonal to the iso-density surfaces and hence corresponds to $\Delta \tilde{x}$. Δx and $\Delta \tilde{x}$ are related as $\Delta \tilde{x} = \Delta x \cdot \sin \alpha$,

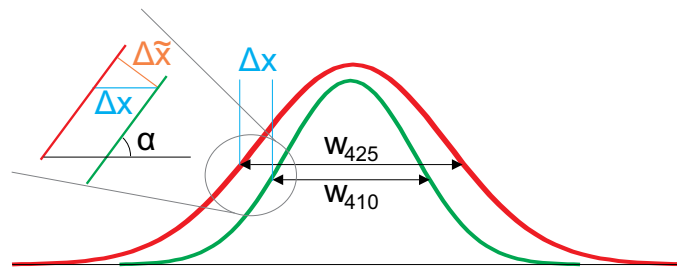


Figure 4.14.: Geometry for the estimation of L_p . Geometric correction factor for the spatial separation of the iso-density contours at 410 nm and 425 nm, Δx . For the corrected value, it holds: $\Delta \tilde{x} = \Delta x \cdot \sin \alpha$.

where α is the local slope of the surface. With amplitude-to-FWHM ratios of $A/w = 0.2 - 1$ for the iso-density surfaces, a correction factor of 0.3-0.8 is applied to L_p . L_p lies hence in the range of 12 - 32 μm .

4.5.2. Discussion

The analysis of the available RMT data in comparison to the data set for the Si membrane targets results in two hypotheses: firstly, the enhanced plasma emission of RMT targets and secondly a smoother gradient for the rear surface plasma. Both observations agree with the results of experimental and numerical studies on RMTs published in recent years [194, 188, 108, 150, 32].

Thermal plasma emission, i.e. emission from the cooling target recorded > 100 ps after the main pulse arrival in contrast to instantaneous emission (e.g. CTR [174]) is found to be enhanced when the target size is decreased [194, 188, 108]. This effect is attributed to an increased bulk target heating caused by electron confinement and refluxing through the target. When compared with the data of the visible emission recorded in the target imaging (Figure 4.13c-f), note that the time window for the CCD camera integration is ~ 100 μs around the pump pulse arrival. A separation of instantaneous and thermal emission is hence not possible for the data presented in this thesis.

Buffechoux, Kluge and Zeil *et al.* all report that electron refluxing in the target leads to a time-averaged more homogeneous electron sheath for RMTs as compared to flat foil targets. This results e.g. in a lower proton beam divergence [108, 150] and a reduced sensitivity to the target thickness for the proton acceleration performance [32]. A more homogeneous electron sheath is likely to occur in connection with a smoother plasma gradient, found as a signature in the experimental data presented.

In summary, the probing data of RMTs and membrane targets as reference show that the probing technique is able to resolve plasma properties related to the geometry of RMTs. The technique is hence potentially relevant in understanding the performance of this promising target type. Particularly a more detailed study of the plasma scale length properties for different target diameters or support stalk sizes could deliver relevant input to still open questions which can otherwise only be addressed in three-dimensional PIC simulations [32]. However, the technique needs to mature particularly with regards to the suppression of plasma emission. In that way, the pump pulse intensity can be increased to values applied in laser-driven proton acceleration and allow for a direct correlation of plasma properties and acceleration performance.

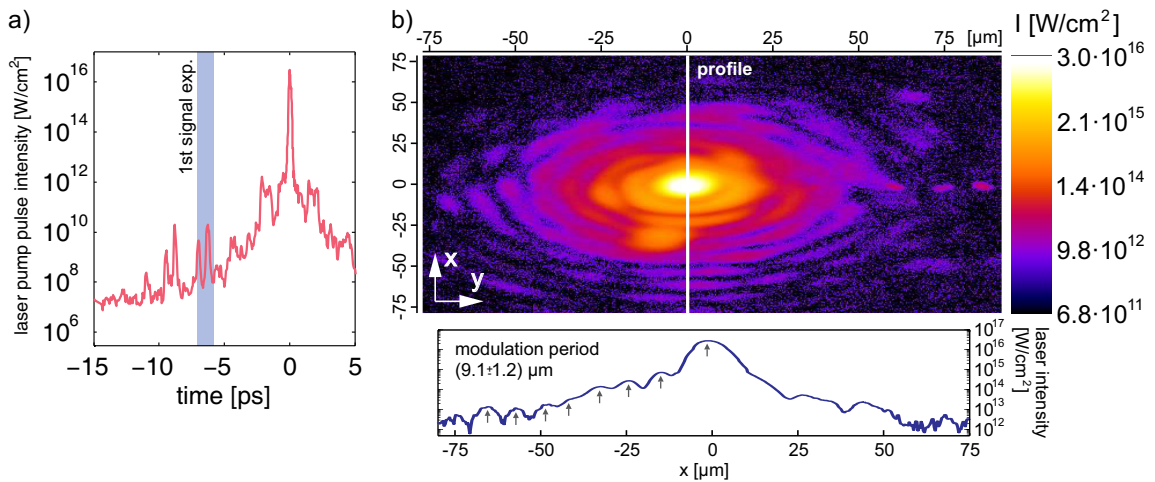


Figure 4.15.: Spatio-temporal pump laser intensity distribution of the front surface probing. a) The temporal intensity profile of the pump laser pulse. The onset of signal detection for the experimental data is marked. b) Spatial intensity distribution in the focal plane after laser beam diffraction at a 25 mm diameter aperture. The data are measured using the focal spot imaging system and a set of calibrated filters to yield images with different attenuation levels from which a montage is made to get the final image. This allows for the recording of the focal spot with a dynamic range beyond that of a CCD camera, so that the low intensity wings of the focal spot become visible.

4.6. Front Surface Probing

In the rear surface probing experiment, the depth-of-field (DOF) properties of the surface imaging system provide information about the *global* shape of a specific iso-density surface in the expanding plasma. On the other hand, the imaging of the target surface is also an approach to resolve *local* target or plasma conditions, e.g. the target's reflectivity. The technique is applied to the target front surface, the major goal of the study being the on-target verification of the spatio-temporal intensity contrast of the Draco I laser system. That includes the determination of when - relative to the main pulse arrival - the alteration of the target surface (e.g. ionization) sets in, a process potentially triggered by prepulses preceding the main pulse.

4.6.1. Experiment

Experimental Setup

The experiment is performed using the setup introduced in Section 4.3 but in this case, the probe pulse and surface imaging are applied to the target front surface. However, the common on-target laser intensity profile of a $3\ \mu\text{m}$ large focal spot with sharply decreasing slopes is found too small to provide the spatial resolution needed to study the spatial evolution of the ionization and target heating. Therefore, an iris with a 25 mm diameter aperture (8% transmission) is inserted into the full laser beam inside the target chamber, resulting in a defined pattern of evenly spaced diffraction rings in the focal plane (Figure 4.15b). The intensity varies over four orders of magnitude over $\approx 75\ \mu\text{m}$ in space. The color scale represents the laser intensities applied in the probing experiment, the peak intensity being $3 \cdot 10^{16}\ \text{W}/\text{cm}^2$ (Section 4.3). The profile plot of the focal spot exhibits up to 7 diffraction rings with an average peak-to-peak distance of $(9.1 \pm 1.2)\ \mu\text{m}$. The vertical image axis is compressed to represent the pump laser intensity profile as witnessed by the

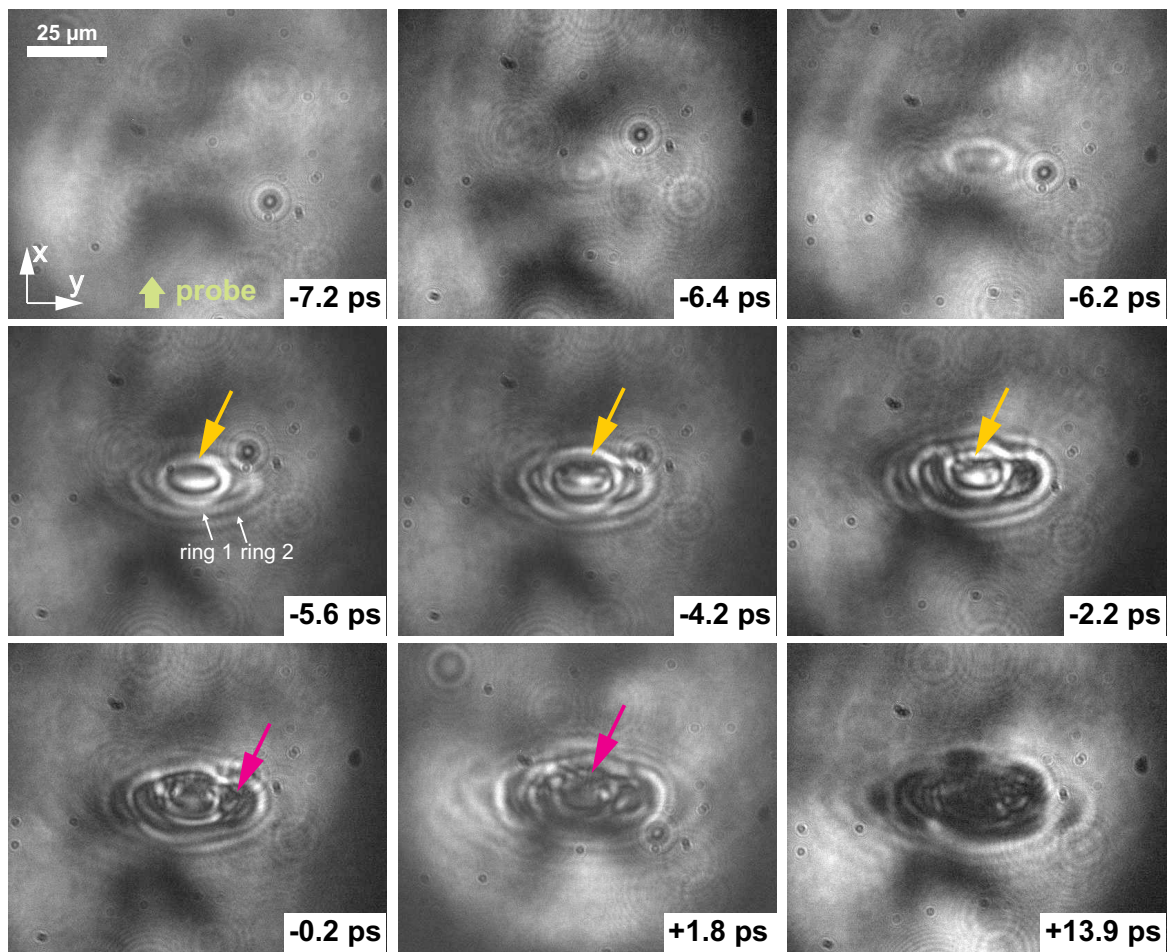


Figure 4.16.: Pump-probe delay scan for Al. Raw data from the front surface imaging for an Al target irradiated at a pump pulse peak intensity of $3 \cdot 10^{16} \text{ W/cm}^2$. Between consecutive data acquisitions, the target was moved to a fresh spot. The probe beam direction is from bottom to top, represented by the yellow arrow in the -7.2 ps image. A limiting factor for the pattern analysis in the data is the spatial inhomogeneity of the probe pulse (compare data at -7.2 ps). The color scale is individually optimized for each image to achieve the best visibility of the signatures. The arrows are explained in the text.

probe pulse, which impinges onto the target under a grazing angle of $\approx 30^\circ$. The temporal intensity contrast of the pump laser pulse is shown in Figure 4.15a.

Experimental Data

The pump pulse and the probe laser are applied to targets of optical quality, consisting of millimeter thick glass substrates sputtered with aluminum (Al) and gold (Au). The temporal delay between pump and probe pulse ranges from -7.2 to $+101.9 \text{ ps}$ with an uncertainty of $\pm 0.6 \text{ ps}$. Representative images are shown in Figure 4.16 for the Al sputtered target and the complete data sets for Al and Au are summarized in Appendix A.5. For a quantitative analysis, Figure 4.17 presents vertical profiles of selected temporal delays from Figure 4.16.

Local Surface Structure The raw data from the front surface imaging feature a complex pattern, which strongly resembles the intensity distribution of the focal spot (Figure 4.15b).

The data feature concentric rings, whose aspect ratio agrees with the image distortion expected for the viewing angle of the surface imaging. The signal is hence interpreted as residing on the target surface (hence *local* structure) and the image contrast as resulting from a local variation of the target or plasma reflectivity for the probe light.

The first signal is detected ≈ 6.4 ps before pump pulse arrival. Approaching pump pulse arrival, the signal size increases and a larger number of concentric rings becomes visible. This effect is confirmed by the profile plots in Figure 4.17, where the ratio of the side peak height (ring 1/2) normalized to the central peak height is found to increase from delay times -5.2 ps to -2.2 ps. Around main pulse arrival ((-0.2 ± 0.6) ps), the ring structure becomes more complex and develops small-scale structures (pink arrows). For delays longer than ≈ 10 ps, the reflectivity of the surface strongly decreases, starting in the central part of the signature. This effect agrees with the observations from the probing at the rear surface (Figure 4.7). In that case, it is attributed to the heating of the target and its ionization. The described signatures occur in the same way for the Au sputtered target and are reproduced on consecutive experimental days. This includes subtle details in the ring pattern. This supports the hypothesis that the pattern is predominantly determined by the intensity profile of the pump laser focal spot.

Moreover, the distance of neighboring rings (ring 1/2 in Figure 4.17) is in agreement with the average distance of the diffraction rings in the pump pulse focal spot (Figure 4.15b). The measurement of 11 ring distance data points gives an average value of (8.7 ± 1.0) μm . However, the comparison of the focal spot profile (Figure 4.15b) with the profiles from the surface imaging (Figure 4.17a) indicates that the two profiles do not match peak-to-peak. Moreover, the diameters of specific rings (ring 1/2) can change for different delay values, particularly during the transition from pre- to post-pump pulse probing delays. Both effects are not attributable to shot-to-shot fluctuations in the profiles because the surface imaging of consecutive shots at the same temporal delay delivers extremely comparable patterns of the surface rings.

Global Surface Structure Besides the ring structure being attributed to a local variation of the index of refraction at the surface, the pattern features an additional ring signature with an aspect ratio of 0.7-0.8 (yellow arrows in Figure 4.16) instead of 0.5. The latter value is the image distortion. This additional features indicates the global target/plasma surface deformation, as discussed and modeled for the case of the rear surface probing (Section 4.4). The corresponding peaks are marked by dashed vertical lines in Figure 4.17a, but no clear trend for the ring diameter as a function of delay can be found.

With regards to the ring signatures residing on the surface, a deformation of the reflecting surface might explain why the surface ring pattern and the focal spot intensity distribution cannot be matched.

4.6.2. Analysis of the Signal Formation

Similar to the findings of the rear surface probing (Section 4.4), the first signal indicating an alteration of the target front surface (probe reflectivity, target surface expansion) by the pump laser pulse is detected several picoseconds before the pump pulse peak reaches the target. The respective temporal delay is marked in Figure 4.15a, which shows the temporal intensity profile of the pump laser pulse with a peak intensity of $3 \cdot 10^{16}$ W/cm². This intensity is a factor of 10^3 lower than the pump pulse intensity applied in the target rear surface probing experiment. Hence, the short prepulses at a temporal delay of -10 ps to -5 ps (Figure 4.18) are below the threshold for tunneling or barrier-suppression ioniza-

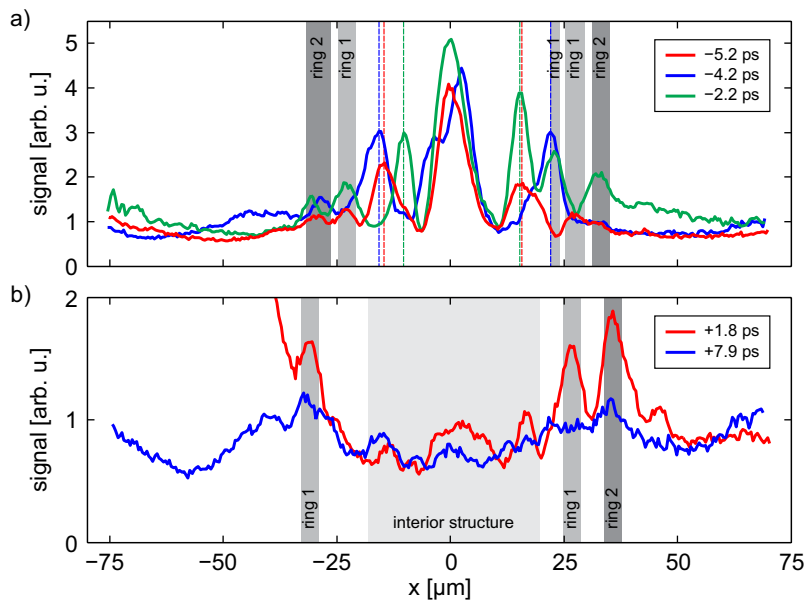


Figure 4.17.: Lineouts of the pump-probe delay scan for Al. Vertical profiles for selected temporal delays from Figure 4.16. The different markers are explained in the text.

tion (Section 2.1.1). PIC simulations, which only consider collisional and field ionization, therefore predict target ionization and heating only around main pulse arrival (Figure 4.18) for the temporal intensity profile in Figure 4.15a.

The alteration of the target by the ultrashort prepulses preceding the main pump pulse at ≈ -10 ps to -5 ps, e.g. via multi-photon ionization, and a potential contribution of the amplified spontaneous emission background will be discussed in the following.

The Contribution of Amplified Spontaneous Emission

The amplified spontaneous emission (ASE) precedes the ultrashort main or pump pulse for several nanoseconds at an intensity contrast of $\lesssim 10^{-10}$ at Draco I (Section 3.2.1). This results in an ASE intensity $I_{ASE} \sim 10^6$ W/cm² for the front surface probing. This intensity is below the ablation threshold for Al (Section 2.1.2) and, as it will be shown, the target heating via ASE is negligible as well.

The increase in temperature of the target surface due to ASE irradiation is estimated based on the one-dimensional thermal model for nanosecond laser pulse absorption in bulk targets presented in [195]. Absorption is assumed to occur in the skin layer [195] and to simplify the calculations, the target is assumed to be an Al bulk target instead of a Al-coated glass substrate. For the surface temperature at time t following irradiation by a constant ASE level at I_{ASE} starting at $t=0$ holds:

$$\Delta T(t) = 2 \cdot I_{ASE} \cdot (1 - R_p) \cdot \sqrt{\frac{t}{\pi \cdot c_{Al} \cdot \kappa_{Al} \cdot \rho}} \quad (4.2)$$

$R_p = 0.87$ is the target reflectivity for p-polarized light at 400 nm with an incidence angle of 60° onto the Al surface. The specific heat capacity for Al at room temperature is $c_{Al} = 0.897$ J/(g·K), the heat conductivity is $\kappa_{Al} = 2.37$ W/(cm·K) and the density is $\rho = 2.7$ g/cm³ [177].

ASE irradiation for 3 ns and 5 ns yields a change in surface temperature ΔT by 3.4 K and

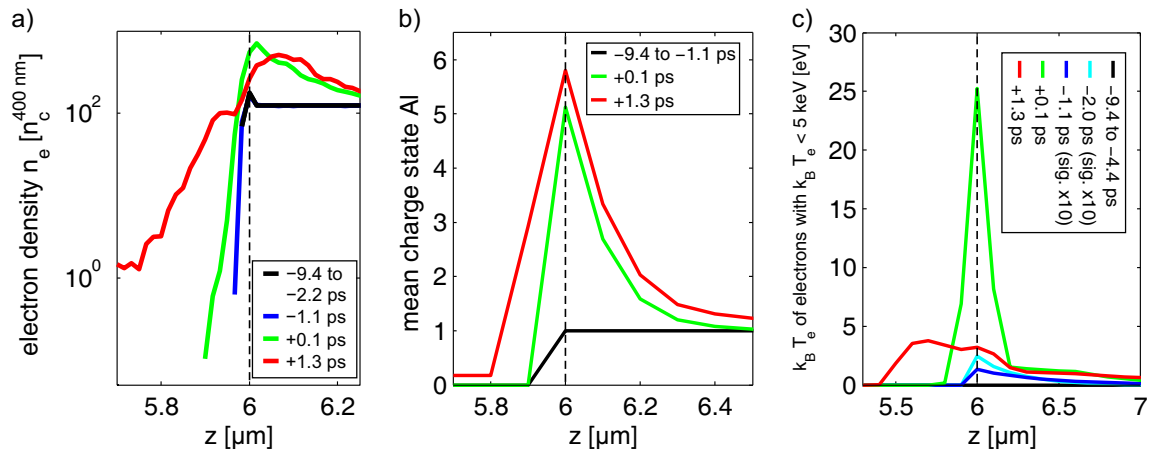


Figure 4.18.: PIC simulation analysis of the front surface probing data. The simulations are performed with the collisional 2D3V iPICLS code [153] and use a simulation box of a $12.5 \lambda \times 50 \lambda$ with 48 cells per laser wavelength $\lambda = 800$ nm and 48 time steps per laser period. The temporal intensity profile of the p-polarized laser pulse is modeled after Figure 4.15a starting at -9.3 ps. The experimentally employed spatial laser pulse profile (Figure 4.15b) is approximated by a multi-Gaussian distribution, interacting with a 4 μm thick Al bulk target, i.e. the target rear surface is connected to the simulation box boundary. All simulation box boundaries are thermal reflection boundaries for particles. The Al density is set to $404 n_c$ (critical density) and the simulation starts with a cold, singly ionized target. The target front surface is covered with 10 nm of PMMA. Direct impact (collisional) and field ionization are included in the code. a) Temporal evolution of the electron density. The density is averaged over $2T$ (laser period). b) Temporal evolution of the mean charge state of the Al bulk. c) Temporal evolution of the mean electron energy, averaged over electrons with $k_B T_e < 5$ keV. The dashed lines mark the cold target front surface position.

4.4 K, respectively, corresponding to $\Delta T \sim 10^{-4}$ eV in both cases¹².

The result firstly shows that the ASE does not contribute to the target heating considerably. Hence, an influence of ASE on the temperature-dependent index of refraction of the target, which would lead to a change in the reflectivity of the target, can be excluded.

The Contribution of ultrashort Prepulse on the Picosecond Timescale

The low peak intensity and hence ASE intensity chosen for the front surface probing allows for the isolated treatment of the target alteration caused by the ultrashort prepulses preceding the main pump pulse at -10 ps to -5 ps (Figure 4.15a). These pulses feature an intensity of $I_{usp} \sim 10^{10}$ W/cm² and a pulse duration comparable to the main pump pulse and are referred to as *ultrashort prepulses* in the following.

The correlation of the temporal intensity contrast (Figure 4.15a) with the temporal delay of the signal onset in the experimental data (Figure 4.16) confirms that the picosecond prepulses at ≈ -6 ps¹³ are real pulses, which alter the target properties, i.e. the reflectivity for the probe pulse. The presented experiment hence allows for the aspired on-target measurement of the temporal intensity contrast. To explain the exact mechanism causing the experimentally observed change in reflectivity is however beyond the capabilities of

¹² $\Delta T \sim 1$ K also justifies the assumption of c_{Al} , κ_{Al} and ρ as temperature-independent.

¹³The present experimental data cannot explain why the similarly intense prepulses at ≈ -9 ps do not lead to a signal in the front surface imaging. The fact that they do not alter the properties of the target surface can indicate that they are artifacts from the measurement of the temporal intensity of the laser pulse.

the presented experimental pump-probe setup, which is designed to capture a large class of processes altering the target properties (deformation, reflectivity) that can occur over a broad laser intensity range for different target materials. Potential mechanisms will be shortly evaluated in the following.

As for the ASE, ablation of the Al target surface by these ultrashort prepulses can be excluded because their fluence¹⁴ of $F_{usp} \sim 1 \text{ mJ/cm}^2$ is about a factor 10^{-3} to 10^{-2} below the ablation threshold for femtosecond pulses on metal surfaces [56].

The observed change in the target reflectivity is hence attributed to the ionization and the heating of the target. The ionization mechanisms relevant at the intensity level of the ultrashort prepulses are multi-photon ionization/multi-photon photoelectron emission and/or thermionic emission from the electron gas [196]. In order to get an approximate value for the degree of ionization within the target volume exposed to the peak fluence F_{usp} of the laser pulse, experimental data for the electron yield from Riffe *et al.* are applied [196]. The corresponding experimental setting is very comparable: A 100 fs long laser pulse at the fluence level of $\sim \text{mJ/cm}^2$ interacts with an Al surface, yielding $\sim 10^5$ electrons per laser pulse from the sample, which originate from a volume of $3 \cdot 10^{-11} \text{ cm}^3$. The volume is the focal spot size multiplied by the skin depth of $\sim 10 \text{ nm}$ [196] and contains $\sim 10^{12}$ atoms. The ionization ratio, i.e. the ratio of ionized to non-ionized atoms, in this regime is hence $\sim 10^{-7}$. This indicates that the target material has not yet turned into a plasma and that the observed changes in reflectivity are more likely ascribed to the heating of the target rather than its ionization.

In contrast to heating by the ASE, which is slow enough to assume the material in thermal equilibrium, the laser energy contained in the ultrashort prepulses is firstly coupled into the electronic system of the material. The electron temperature $k_B T_e$ in Al at the end of a 100 fs long laser pulse with a peak intensity of I_{usp} can be estimated to $\approx 0.2 \text{ eV}$ or $\approx 2000 \text{ }^\circ\text{C}$ [177], which is three times the melting temperature. Thermal equilibration with the lattice only occurs on the timescale of picoseconds and results in a lattice temperature of $k_B T_L \sim 1000 \text{ }^\circ\text{C}$, which is still above the melting temperature [177].

The transient states the material is potential undergoing are observed to lead to (partially transient) increases or decreases in the target reflectivity on the femto- to nanosecond timescale due to a number of physical processes such as solid-liquid phase transition [197], phonon excitation [177] or due to changes in the density of states around the Fermi level in the case of metals [198]. It should be noted that the latter mechanisms lead to reflectivity changes on the level of 10^{-3} or less and that the third mechanism depends on the material band structure and appropriate pump and probe wavelength/photon energies.

Regarding the experimental data, the similarity in signal for the Al and Au surface indicates a reflectivity-changing mechanism that is independent of the particular material band structure. The observed changes in the reflectivity are also on the order of a factor of 2 (see e.g. peak-to-valley ratio for ring 2 in Figure 4.17a) and not the per mill level as e.g. the case for transient phonon excitation [177]. Moreover, contributions from e.g. firstly the thickness of the sputtered metal layer on the glass substrate [199], secondly an oxide layer on the Al surface or thirdly changes in the angular reflection pattern due to micro-deformations of the surface cannot be excluded. A separation of the different potential distributions requires a dedicated experimental study, e.g. with a well-defined pump pulse providing a single/instantaneous excitation of the sample.

¹⁴The given intensity and fluence values are reached in the central part of the spatial intensity distribution (Figure 4.15b), which has a diameter of $\approx 10 \mu\text{m}$.

4.7. Conclusion

In this chapter, two experimental methods are presented and analyzed, which make it possible to optically infer information about the near-critical density region in an expanding, laser-driven plasma. This is the region which is most crucial in coupling laser energy into the target. In the first case, the specularly reflected pump pulse is analyzed, in the second case, the application of a separate probe pulse enables the measurement of the temporal plasma evolution. Both methods exploit the angular redistribution of light or rays in a beam reflected off a shaped plasma iso-density surface. The analysis of the experimental data shows that the probing technique termed *high depth-of-field time-resolved microscopy* makes it possible to temporally resolve the width of a specific near-critical iso-density surface in the plasma, which can be chosen via the probe wavelength and the probe's angle of incidence onto the target. Moreover, the reflectivity of the target or plasma surface is used as a signature for target alteration by ionization and heating.

In the context of this thesis, the probing technique is used to experimentally verify the temporal intensity contrast of the pump laser pulse interacting with the target, the focus being on target expansion temporally preceding the pump pulse peak arrival at the target. The application of the probing method at two different pump pulse intensities to the target front and rear surface respectively has confirmed the contribution of the amplified spontaneous emission and a series of ultrashort prepulses on pre-target expansion. These data are used as input for the filamentation study presented in Chapter 3. The comparison of the experimental data with simulation results has shown that only a combination of hydrodynamic and particle-in-cell simulations, the latter optimally including low intensity ionization effects such as multi-photon ionization, can reliably predict the preplasma conditions at main pulse arrival.

Moreover, the probing of the target rear surface of reduced-mass targets (RMT) in direct comparison with conventional flat foils has proven the method's potential in detecting the particular plasma distribution resulting from the RMT geometry. The geometry of RMTs is tightly connected to the target performance in laser-driven proton acceleration [108, 32].

Both presented fields of application for the probing technique will largely benefit when the pump pulse intensity can be increased to values applied in laser-driven proton acceleration ($I_L \sim 10^{21}$ W/cm²). This would allow for a direct correlation of plasma properties and the acceleration performance. In the experiments presented, the applied pump pulse intensity is limited by the pump pulse-dependent amount of plasma emission. Here, a probe pulse at $\lambda = 266$ nm, i.e. the third harmonic of the pump pulse, is expected to result in a considerable increase in the signal-to-noise ratio for the probe pulse detection.

The combination of the presented reflective probing technique with interferometry - similar to Fourier-domain interferometry (FDI) [200] or time-and-space-resolved-interferometry (TASRI) [169] - would enable the detection of the amplitude of the expanded plasma iso-density surface in addition to the width of the expanded surface. However, these techniques cannot distinguish whether a phase change in the probe beam is caused by underdense plasma or a spatial offset (i.e. expansion) of the critical/reflecting plasma surface and therefore rely on hydrodynamic simulations to estimate the latter. This shortcoming can be overcome by a combination of interferometry techniques with the presented probing technique of using pure surface imaging. The latter method is sensitive to small (~ 100 nm) plasma expansion amplitudes.

5. Summary and Outlook

In this thesis, the interaction of ultrashort, intense laser pulses with solid targets has been investigated experimentally in the target normal sheath acceleration (TNSA) regime. The focus was thereby on two aspects: Firstly, transverse modulations in laser-driven proton beams due to plasma instabilities were studied. Secondly, a reflective probing method termed *high depth-of-field time-resolved microscopy* was applied to characterize the plasma evolution at the solid target boundaries upon interaction with intense laser pulses. Both topics are relevant in further developing laser-driven ion sources (LDIS) for medical applications, which is the cooperative effort this thesis is embedded in.

In detail, the filamentation study investigated the transition from smooth to transversely modulated proton beam profiles, the transition occurring for increasing laser pulse energies applied to the target. The onset of proton beam modulations and the underlying physics was triggered by using a non-optimal temporal intensity profile for the laser pulse, i.e. a laser pulse featuring several prepulses on the picosecond timescale preceding the peak pulse. Numerical simulations for the laser-target interaction including ion acceleration indicated that plasma instabilities seeded at or close to the target front surface caused the filamentation of the laser-accelerated electron distribution. The resulting spatial pattern then translated into proton beam modulations during the acceleration process. In particular, a surface-ripple-seeded Rayleigh-Taylor or Weibel instability was observed in the simulations, their respective seeding being dependent on the initial plasma conditions at the target front surface. This supported the role of the laser's temporal intensity profile in the occurrence of spatially modulated proton distributions in the experiment. Numerical analysis of the experimental plasma conditions resulting from the temporal intensity profile implied the presence of preformed plasma at the target front surface, which agrees with the conditions for a Weibel instability. The study is considered the first observation of (regular) proton beam modulations for the TNSA regime using micrometer thick metal target foils irradiated with ultrashort laser pulses. The laser energy dependent onset of the effect indicates the potential relevance of plasma instabilities for the properties of laser-driven proton distributions produced with the upcoming generation of Petawatt (PW) power lasers.

Analysis of the plasma dynamics underlying the experimentally observed proton beam modulations relied on numerical simulations, in which certain plasma conditions at the target - including density, temperature, ionization, etc. - were preset to interact with the ultrashort laser pulse. Simulations in which the laser-target interaction is modeled entirely self-consistently by considering all parts of the laser pulse which can alter the target by e.g. heating, ablation or ionization are prohibited due to a lack of computing power as well as corresponding numerical codes. This emphasizes the requirement for experimental techniques, which allow for a correlation of specific temporal laser intensity profiles and the resulting plasma conditions at the target. These results can also serve to improve the available input parameter for numerical simulations.

With the reflective pump-probe experiments performed in the course of this thesis, the spatio-temporal evolution of the near-critical density plasma region at the front and rear surface of solid targets was investigated. For the target rear surface, the technique pro-

vided the lateral size of an expanding near-critical iso-density surface in the plasma. At the target front surface, the changes in reflectivity as a function of the pump-probe pulse delay indicated the onset of target heating by the laser pulse and its prepulses. Based on the comparison of the time-resolved experimental data and numerical simulations, which took into account the temporal intensity profile of the pulse over ≈ 10 ps preceding the peak pulse, the attempted correlation of laser pulse parameters and plasma formation was realized. The probing technique of high depth-of-field time-resolved microscopy was shown to be versatile, allowing for the simultaneous diagnostics of the local plasma properties, such as changes in the reflectivity due to target heating, ionization or plasma formation, as well as the global plasma shape resulting from plasma expansion.

In a larger context, both experiments presented in this thesis are pump-probe experiments, making use of proton acceleration and optical reflectivity to investigate the bulk and surface plasma dynamics resulting from the interaction of an ultrashort, intense laser pulses with a solid target. Regarding the optical probing, the technique will gain its full applicability once it is optimized for pump laser intensities at which simultaneous proton acceleration is possible. This has been prevented by plasma emission in the spectral range of the probe pulse so far. However, using the laser-driven protons to probe the target bulk dynamics of the hot electron distribution driving the proton acceleration constitutes a very indirect method.

The large potential of plasma probing for plasma-based accelerators is illustrated by recent experiments on laser-driven electron acceleration in gas targets [201, 202, 203]. Since dealing with underdense plasmas, the dynamics of the accelerating plasma wave structure have been visualized in real-time by optical probes, which considerably supports an understanding of the acceleration process (e.g. [204, 205, 206]).

For solid density targets, which are intransparent to optical but transparent to xray radiation, similar experimental opportunities open up with facilities combining high power optical or near-infrared lasers and xray free electron lasers (XFEL). Two facilities already in operation are LCLS¹ (2009) [207] and SACLA² (2011) [208]. The third facility, the European XFEL in Germany, will start the operation in 2017 [209]. XFEL facilities provide 10-100 fs long xray pulses containing $\sim 10^{12}$ photons in the energy range of kiloelectronvolts, which can be focused down to the micrometer scale [209]. The spatial and temporal characteristics of XFEL pulses match the necessary properties of a probe for solid density plasmas generated by an ultrashort laser pulse.

A proposed experiment directly related to the work presented in this thesis is small angle xray scattering (SAXS) from electron density modulations in overdense plasmas. Initiated by the simulation work for the filamentation study presented in this thesis, Kluge *et al.* proposed SAXS as an experimental diagnostic for plasma instabilities [155]. By using a scattering technique, the spatial resolution of xray probing is increased below the micrometer-scale focal spot size achievable with XFELs. Hence, the electron density modulations of ~ 100 nm spatial scale can be resolved. Particularly for a surface-ripple-seeded Rayleigh-Taylor or a Weibel instability - the two instabilities relevant for the experimental study in this thesis - the analysis of the respective scattering signals calculated from numerical electron density maps shows that SAXS potentially allows for a distinction of both instabilities. To name one further example for the experimental opportunities at XFELs regarding time- and space-resolved *in situ* probing of overdense plasma dynamics [210], XFEL probing using Faraday rotation of a polarized xray pulse can be applied to study

¹Stanford Linear Accelerator, Linac Coherent Light Source at California, USA

²SPring-8 Angstrom Compact Free Electron Laser, Japan

the hot electron transport in the target volume via the self-generated magnetic fields [211]. The investigation and understanding of the plasma dynamics resulting from specific laser-target/plasma interaction conditions and underlying e.g. TNSA, are necessary preconditions for an optimization of LDIS e.g. for medical applications.

An equally important task is the determination of interaction conditions which deliver particle distributions optimally suiting the intended application regarding particle number, spectral range or spatial distribution. Given the large parameter space of laser pulse as well as target properties, numerical simulations are the tool of choice. This point is not questioned even though a self-consistent modeling of the laser-target interaction, which might encompass nanoseconds of laser pulse background, cannot be realized. On the other hand, the experimental observation of proton beam modulations in the TNSA regime indicates that predictive simulations have to take into account plasma conditions as they result from an experimentally applied laser pulse intensity profile. Viable approaches are firstly a combination of systematic simulation and experimental pump-probe studies, which investigate the contribution of different sections of the temporal intensity profile³ to the plasma formation and resulting proton/ion distribution characteristics. The second step will then be to deduce minimal parameter sets (e.g. the spatial distribution of the plasma density, plasma temperature and charge states), which can replace the self-consistent modeling of specific sections of the temporal pulse profile without compromising the predictive power of the simulations. Such a treatment can support the definition of operation conditions for the upcoming PW lasers as drivers for LDIS with an applicable output of protons or ions.

³i.e. the amplified spontaneous emission background, single prepulses or the rising edge of the laser pulse

A. Appendix

A.1. Raw Data for the Laser Proton Beam Filamentation

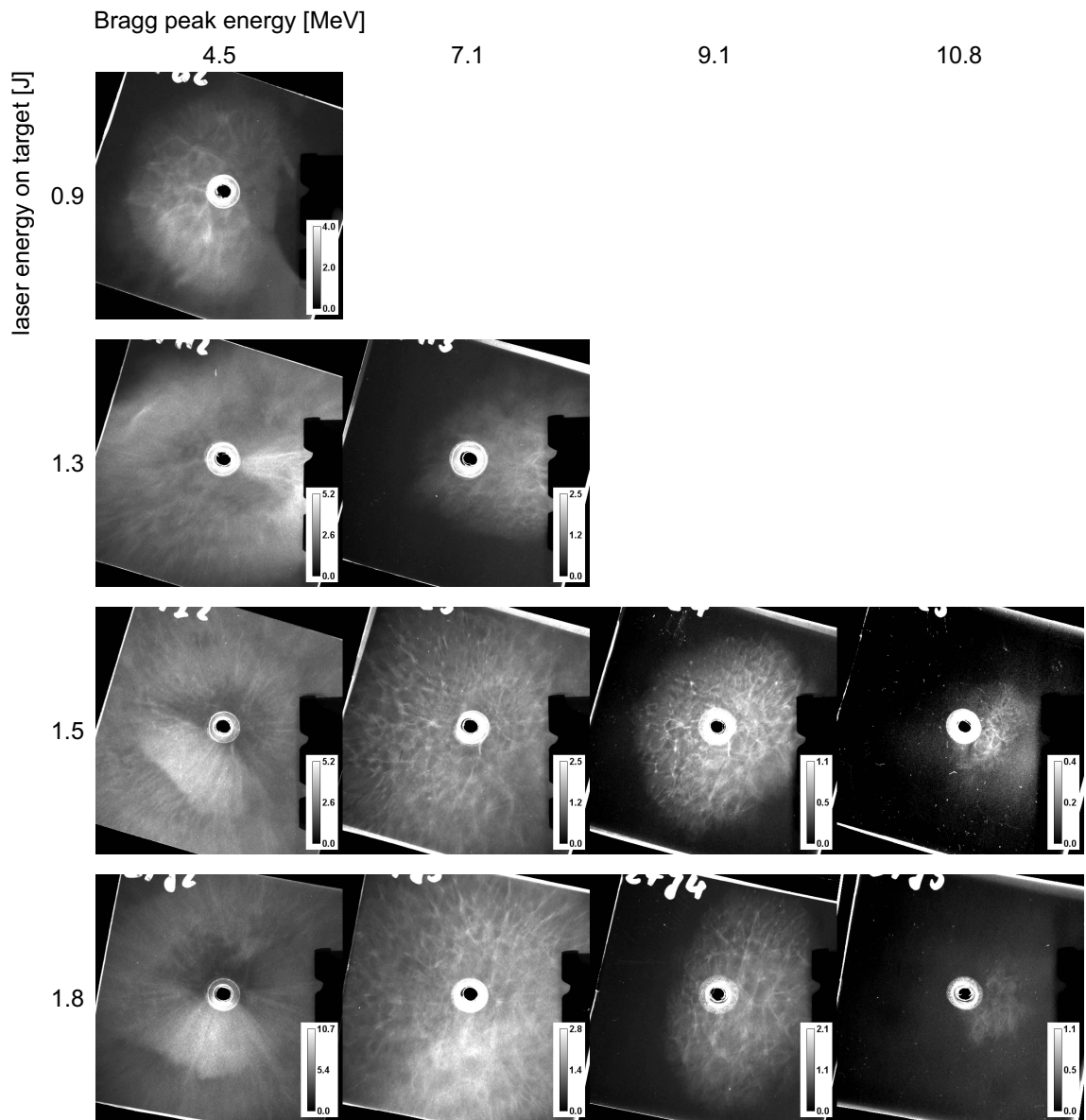


Figure A.1: 2 μm titanium target, laser energy on target $E_L = 0.9 - 1.8 \text{ J}$. Spatially resolved dose profiles measured with radiochromic film stacks for different laser energies on target. Each data set for a laser energy corresponds to a single laser shot. Each RCF layer represents protons with energies at or above the respective Bragg peak energy E_{BP} . The color bar represents the dose in each layer. The film layers have a size of $50 \times 50 \text{ mm}^2$.

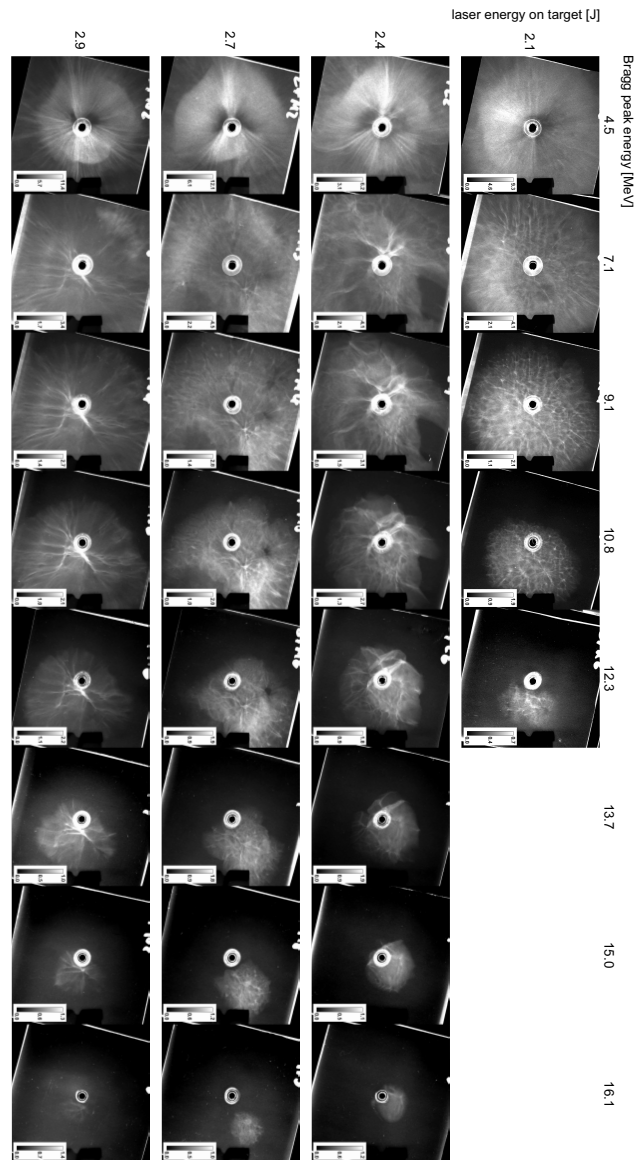


Figure A.2.: $2\ \mu\text{m}$ titanium target, laser energy on target $E_L = 2.1 - 2.9\ \text{J}$. Spatially resolved dose profiles measured with radiochromic film stacks for different laser energies on target. Each data set for a laser energy corresponds to a single laser shot. Each RCF layer represents protons with energies at or above the respective Bragg peak energy E_{BP} . The color bar represents the dose in each layer. The film layers have a size of $50 \times 50\ \text{mm}^2$.

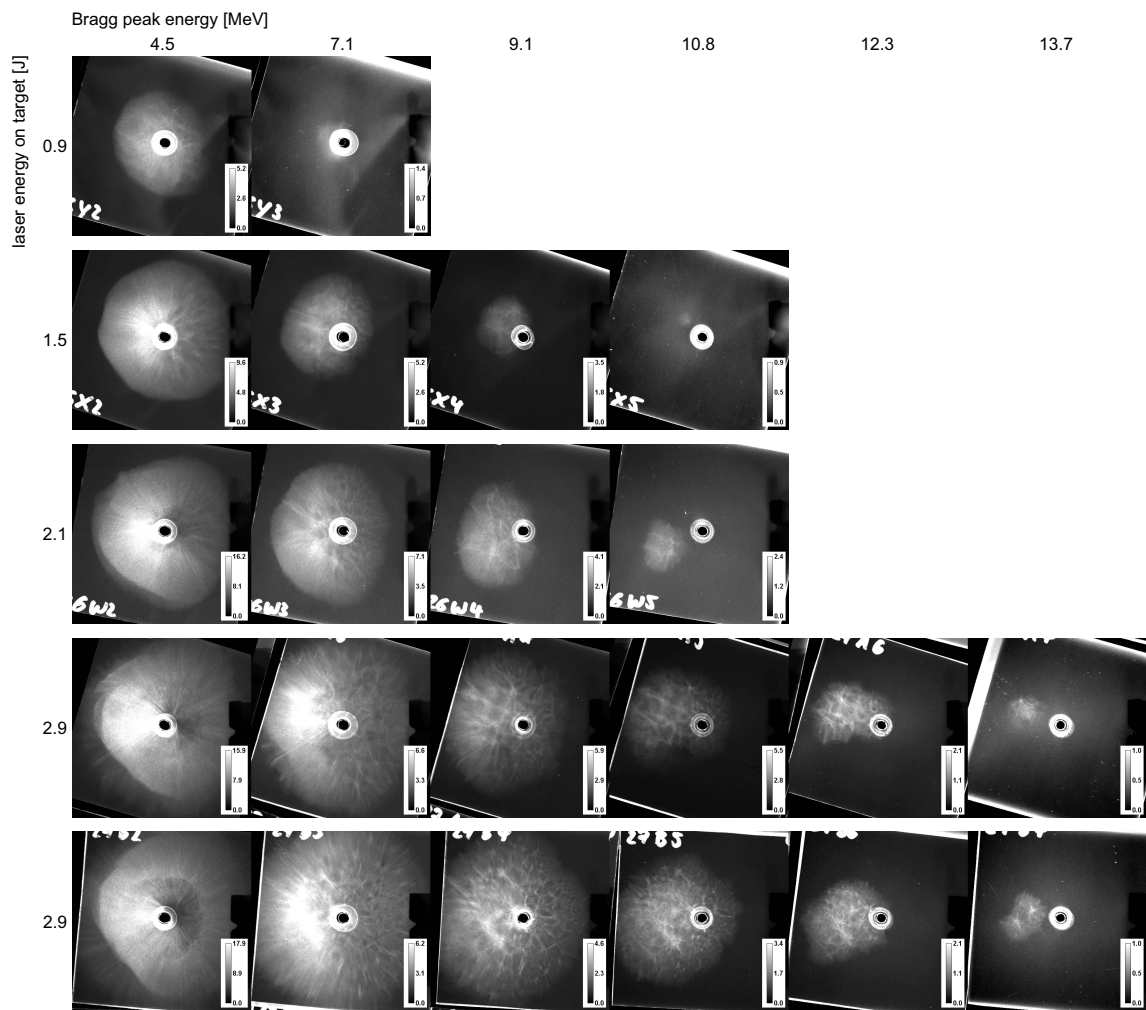


Figure A.3.: 3 μm titanium target, laser energy on target $E_L = 0.9 - 2.9$ J. Spatially resolved dose profiles measured with radiochromic film stacks for different laser energies on target. Each data set for a laser energy corresponds to a single laser shot. Each RCF layer represents protons with energies at or above the respective Bragg peak energy E_{BP} . The color bar represents the dose in each layer. The film layers have a size of 50×50 mm².

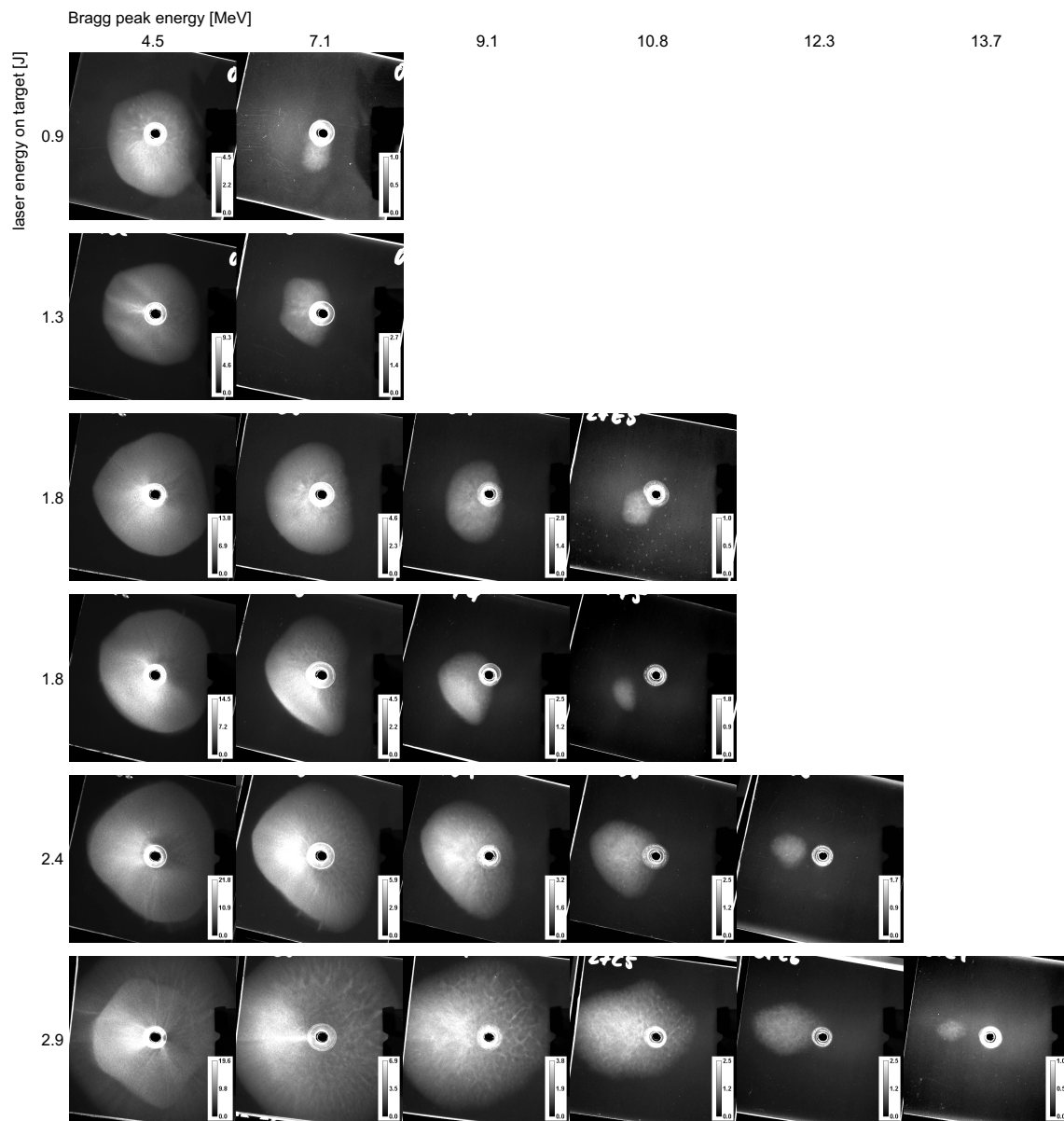


Figure A.4.: 2 μm titanium target with 0.8 μm of photo-resist, laser energy on target $E_L = 0.9 - 2.9$ J. Spatially resolved dose profiles measured with radiochromic film stacks for different laser energies on target. Each data set for a laser energy corresponds to a single laser shot. Each RCF layer represents protons with energies at or above the respective Bragg peak energy E_{BP} . The color bar represents the dose in each layer. The film layers have a size of 50×50 mm².

A.2. Online Detectors for Laser-Driven Proton Beams

In this chapter, two scintillator-based online detectors for laser-driven proton beams, developed as part of this thesis, are presented. Apart from the detector design and their characterization at conventional proton sources, the focus is on the detector application in an *in vitro* radiobiological study performed at the Draco I laser system with laser-driven protons [25, 26, 212]. That exemplifies the necessity of online detectors in laser-driven accelerator operation in addition to the established detection methods for laser-driven ion and proton beams.

Motivation

Radiobiological Studies with Laser-Driven Proton Beams

High repetition rate (~ 10 Hz), ~ 100 TW laser systems are currently opening opportunities for complex application experiments such as radiobiological studies with laser-accelerated protons [34, 25, 35, 36, 37, 26]. These studies mark a necessary step towards a medically applied laser-based accelerator since the properties of laser-accelerated proton pulses differ significantly from the radiation delivered by conventional proton sources (e.g. cyclotrons) regarding the pulse structure, peak current and spectrum [4]. Hence, an experimental comparison of the biological effectiveness of both radiation qualities is mandatory.

To that end, in the framework of the onCOOPTics project (Chapter 1), dose-controlled *in vitro* tumor cell irradiations with laser-accelerated protons were performed at the Draco I laser system [25, 24, 26]. A sketch of the experimental setup is shown in Figure A.5a. Protons with energies of up to 15 MeV are produced in an applicable quantity in the interaction of the Draco I laser pulse with a 2 μm thick titanium foil. After filtering, the protons exit the experimental chamber through a thin plastic window and enter the IDOCIS [24], which houses the in-air dosimetry unit and the cell-irradiation site. The beam filter is based on a non-focusing magnetic dipole, providing the energy dispersion of the protons and the suppression of parasitic charged particles [213]. The desired proton energy range is selected with an aperture in front of the IDOCIS. Figure A.5c summarizes the results of the study, i.e. the DNA double-strand breaks per cell as a function of the applied dose for both laser- as well as conventionally-accelerated protons. The data indicate that no significant difference in the biological effectiveness exists. Details on the experiment can be found in [26].

Regarding the performance of the laser-based accelerator, the key result is the achieved dose uncertainty $\Delta D/D$ below 10% averaged over all individual cell samples irradiated (Figure A.5c inset). This value is comparable to conventional irradiation data.

Basis for this achievement is firstly a dedicated dosimetry system, combining absolute and online relative dose measurements, both adapted to the properties of laser-accelerated proton pulses [24]. The second component is the high stability of the laser system and the laser-target interaction conditions [26]. Whereas the latter is best surveyed via the maximum proton energy and the particle yield, the spectral stability of the proton distribution is a crucial input for the dosimetry protocol [24]. That shows the relevance of online shot-to-shot control of the accelerated proton distribution, provided by appropriate instrumentation, as e.g. dedicated and compact scintillator-based online detectors. The following review of the established detectors for laser-driven protons and ions, exemplified by the Draco I experimental setup, will emphasize this point.

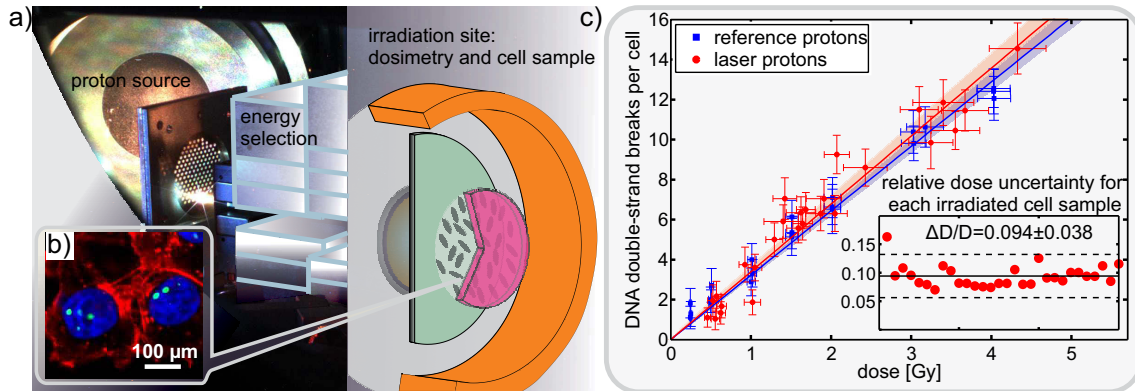


Figure A.5.: Dose-controlled tumor cell-irradiations with laser-driven protons at the Draco I laser facility. a) Experimental setup including the proton source, here shown as the focusing parabola and the target, the energy selection system and the IDOCIS [24] cell-irradiation and dosimetry site. b) Micrograph of immunostained DNA double-strand breaks in single-cell nuclei. c) Averaged number of DNA double-strand breaks as a function of the applied dose, comparing laser- and conventionally-accelerated protons. The error bars on the double-strand breaks include all systematic errors (e.g. automatic cell counting) as well as statistical errors. The data are fitted linearly in both cases. The figure is a combination of two plots published in [26].

Ion and Proton Detection at Draco

Using micrometer thick foils as interaction targets, TNSA (Section 2.6) is the prevalent acceleration mechanism for protons at the Draco I setup. That leads to a predominant particle emission from the non-irradiated target side into a solid angle of $\sim 40^\circ$ in the direction of laser propagation. As presented in Section 2.6, the proton pulses feature exponentially decreasing spectra with cut-off energies as high as 20 MeV [27] and co-occur with the emission of different charge states of all ions present in the target contaminant layer (carbon, oxygen) or the target material, and MeV electrons.

Combined Ion and Electron Spectrometer For the analysis of these multi-species pulses, a combined ion and electron spectrometer (SPIE [214]) is available 100 cm downstream from the target. The SPIE consists of a Thomson parabola spectrometer for ion detection with a parallel magnetic (560 mT) and electric (370 kV/m) field perpendicular to the particle propagation axis. This field configuration deflects ions on separate parabolic traces (according to their charge-to-mass ratio) and resolves their energy spectra along the parabolic trace. The particle signals are amplified and recorded at the spectrometer rear (ions) and side (electrons) exit using image-resolving microchannel plate (MCP) detectors. The MCPs are coupled to fluorescence screens that are read out with CCD cameras. This setup hence allows for the spectral real-time measurement of the particle distribution and particularly the cut-off energy of the proton spectrum as a characteristic observable for TNSA spectra. The relative energy resolution $\Delta E/E$ of the spectrometer with an entrance aperture of 100 μm diameter located 60 cm behind the target amounts to 4% and 7% for 10 MeV and 30 MeV protons, respectively. Together with the spatial (vertical) separation of the different ion trances on the detector, particularly for high particle energies, $\Delta E/E$ determines the precision for measurements of the proton cut-off energy. In order to optimize the resolution of the cut-off energy for different energy ranges, the spectrometer is mounted on a motorized stage. This allows for a flexible variation of the ion drift range in the field-free space in front of the detector, which influences both the energy resolution

and the ion trace separation [215, 214].

Radiochromic Film With the Thomson parabola spectrometer only covering a solid angle of $0.02 \mu\text{sr}$ out of the beam's solid angle of 0.4sr and the lack of reliable calibration protocols for MCP detectors [216], radiochromic films (RCF) are used as a complementary diagnostic tool. From RCF, the angular distribution and particle number of the accelerated proton pulse can be derived. Moreover, their high spatial resolution ($85 \mu\text{m}$ resolution per pixel when scanning with a 300 dpi resolution) make RCF an ideal tool to measure fine structures in proton beam profiles (Chapter 3). RCF is a self-developing film material consisting of a 100 - 200 μm thick plastic layer supporting an active layer with micro-crystalline monomers. These polymerize to dye molecules instantaneously under exposure to ionizing radiation. The optical density of the RCF correlates with the absorbed dose, allowing for particle number measurements after calibration [217, 218].

In the experimental setup, stacks of several RCF layers are placed 35 to 45 mm behind the non-irradiated target side to record the two-dimensional spatially resolved depth dose of the proton distribution, from which the spectrum can be deconvoluted numerically via the energy-range-correlation of protons in the film material [219, 99]. The energy resolution for RCF spectroscopy is limited by the thickness of the film material and amounts to $\leq 1 \text{MeV}$ above 15 MeV proton energy. To reliably extract the proton number covering a range of about two orders of magnitude over the exponential spectrum (e.g. [54]), the RCF stack is set up of an insensitive HD-810 film with a measurement range of up to 2 kGy (thin active layer of $6.5 \mu\text{m}$) at the front and EBT2/3 films (active layer $\approx 30 \mu\text{m}$) with a measurement range up to 40 Gy [220]. In that way, the dynamic range of the method is increased. In combination with the $13 \mu\text{m}$ thick aluminum cover for the stack, the HD-810 film also serves as an absorber for carbon and oxygen ions. The central part of the particle distribution propagates into the SPIE for diagnostics through a hole in the RCF stack. Using a motorized RCF holder and manipulator for up to 12 stacks, the venting cycle for the experimental chamber is considerably increased.

In summary a Thomson parabola spectrometer provides high resolution spectra for all ion species accelerated in the interaction at real-time but can only probe a fraction of the ion distribution due to the correlation of entrance aperture size and spectral resolution. This drawback is partly overcome by ion wide angle spectrometers by increasing the spectrometer's viewing angle from $\sim 100 \mu\text{rad}$ by a factor of 10^3 to 30° along the slit axis. That is however at the expense of an electric field, so that the separation of the proton and ion traces (C^{6+}) is only ensured through absorbers [221]. RCFs on the other hand provide spatially highly resolved and spectrally coarsely resolved spectra of the entire proton distribution but cannot be read out online.

In conclusion, neither of the two detector systems (Thomson parabola spectrometers and RCF) can provide the key parameters of the proton distribution, i.e the maximum proton energy, the spectral shape, the particle yield and the angular proton distribution, online for each single laser pulse interacting with the target.

Detector Development

As the basic detection principle for the development of online detectors for laser-accelerated protons, plastic scintillators combined with absorbers and read out by a CCD camera are chosen. Plastic scintillators feature ideal properties as detector material, as they are available in variable sizes, emit light in the visible range instantaneously after excitation through ionizing radiation and feature a linear response to particle flux (e.g. [222]).

The one-dimensional (1D) stack detector setup, published in [212], consists of a stack of 10 thin plastic scintillator layers with transverse signal readout along one spatial dimension. It features a spatial resolution of 1.3 mm and a spectral resolution better than 1.5 MeV for a maximum proton energy above 12 MeV in the current design. The detector design is optimized for the integration into the setup for cell-irradiations with laser-accelerated protons at Draco I [25, 26].

The two-dimensional (2D) pixel detector follows the approach by Green *et al.* [223] in using a scintillator screen to record the entire proton distribution in two dimension. The detector by Green *et al.* enables the simultaneous measurement of the proton pulse's angular profile at three different energies via a stack of three plastic scintillators with emission at different wavelength, the stack being imaged onto a color CCD camera from the rear side.

In order to increase the spectral resolution and resolvable energy ranges, the three different plastic scintillators are replaced by an aluminum absorber matrix, which is segmented into 60 pixels. Each pixel contains distinct holes with different material thicknesses as absorbers. The detector hence provides real-time information with a spatial resolution of $5.5 \text{ mm} \times 5.5 \text{ mm}$, the pixel size, and an energy resolution of $\sim 1 \text{ MeV}$ for proton energies above 8 MeV. Absolute calibration of the detector will facilitate the reconstruction of the proton distribution as performed in RCF spectroscopy [219, 99].

Scintillator-based 1D stack detector

Detector Setup and Principle

The scintillator-based online detector shown in Figure A.6 consists of two units, the scintillator unit itself and the CCD camera unit. The scintillator unit houses the central element for proton detection, which is a stack of 10 scintillator layers, each being 50 mm in width, 40 mm in height and 350 μm in thickness. The scintillation material is the polyvinyltoluene-based plastic scintillator BC418 from Bicorn with a central emission wavelength of 391 nm. Protons hitting the 10 mm high and 50 mm wide detection area of the detector pass through the scintillator stack and deposit energy in each layer until they stop in the stack depth that corresponds to their energy-dependent range. The energy deposited in each layer is converted into isotropically emitted scintillation photons which are, as in a light guide, guided through the 350 μm thick layers from the detection area towards the scintillator edges by total internal reflection (critical angle $\theta_c = 39.3^\circ$) at the polished scintillator surfaces. The light emitted at the upper scintillator edge is imaged onto the CCD camera that is looking from above, located in the camera unit. This design allows for a very slim scintillator unit that is only 15 mm thick and 76 mm wide, so that the detector can be applied close to the proton source or in tight experimental setups common for application experiments. The total height of the detector including the CCD camera housing is 310 mm and it has a footprint of 80 mm \times 80 mm.

In order to obtain a good spatial separation of the different scintillator layers in the imaging plane, the scintillator stack is set up as a fan with the layers being in contact in the detection area and separated by 300 μm thick spacers at the upper layer edges (see Figure A.6a). Crosstalk between different scintillator layers via the scintillator surfaces is avoided by covering each layer with 13 μm thick light-tight black plastic foil. Furthermore, the aluminum case of the scintillator unit is lined with black light-absorbing foil to avoid reflections and scattering inside the case. To avoid light scattering upon emission and hence signal distortion, the readout edge is polished. The other three scintillator edges are roughened to avoid that light is reflected back towards the readout edge, adding noise

to the image. A representative detector image measured with laser-accelerated protons is shown in Figure A.6b. The individual scintillator layers are well-resolved and the deepest layer showing signal corresponds to the maximum proton energy in the pulse. The resolution of the maximum proton energy is determined by the thickness of the scintillator layers, which is chosen to give a resolution below 1.5 MeV above a proton energy of 12 MeV, as summarized in the table in Figure A.6c. In lateral direction, the signal from each layer corresponds to the angular distribution of the proton distribution in horizontal direction (parallel to the scintillator edge) and integrated over the vertical dimension of the detection area. Usually positioned 50 mm behind the source, the detector captures a proton distribution with a divergence half-angle of up to 26° .

The camera model used for image acquisition is an AVT GUPPY PRO F-201B¹ that is selected first of all for its small foot print ($44.8 \times 29 \times 29 \text{ mm}^3$) and, secondly, the large chip size (1624×1234 pixel), small pixel size ($4.4 \mu\text{m}$) and high dynamic range (16 bit). The imaging is performed with a 12 mm focal length objective, which provides an image resolution of $48 \mu\text{m}$ per pixel or equivalently, images each of the $350 \mu\text{m}$ thick scintillator layer edges onto 7 pixels.

As shown in Figure A.6a, the readout unit housing the CCD camera is directly coupled to the scintillator unit to allow for efficient light collection. Furthermore, in combination with a light-tight cover at the detection area ($13 \mu\text{m}$ aluminum foil and $13 \mu\text{m}$ black plastic foil) direct coupling of scintillator and readout unit completely seals the detector against the strong stray light background that is commonly present in laser-plasma experiments [224]. The scintillator layers also have to be protected against the strong electron and x-ray background that can, in contrast to the proton signal, be collected in the detection as well as the light guiding area of the scintillator layers. For that reason, the front and rear surface of the scintillator unit above the detection area are covered with 2 mm thick lead foils. Additionally, the camera position chosen places the CCD chip parallel to the beam axis to minimize direct background radiation on the chip.

As the experiment chamber is evacuated during experiments, the camera housing contains a small air volume of about 0.5 l to allow for cooling of the camera. This camera set-up proved working in several experimental runs. Furthermore, proper grounding of the setup and the insulation of the cables with a metal wire shielding solved all problems connected to the electromagnetic pulse (EMP) produced in the laser-target interaction.

Application at a Laser-Based Accelerator

For a performance test at a laser-based accelerator, the 1D stack detector is integrated into the cell-irradiation setup (A.5a). A simplified sketch of the setup showing the detector placement is given in Figure A.7a.

The acceleration performance, and in particular the maximum proton energy, strongly depends on the laser intensity on target and is hence very responsive to the relative position of the laser focal plane with respect to the target foil. Routinely, the Thomson parabola spectrometer is used to optimize the performance of the proton acceleration before each experimental run, using the maximum proton energy as target variable. However, the complexity and size of the cell-irradiation equipment itself does not allow for the integration of the spectrometer into the experimental setup. Moreover, the spatial dispersion introduced by the energy filter [213] requires the maximum proton energy to be measured within a larger solid angle than covered by the Thomson parabola spectrometer.

To improve this shortcoming, the compact scintillator-based detector is integrated into

¹Allied Vision Technologies GmbH, Stadtroda, Germany

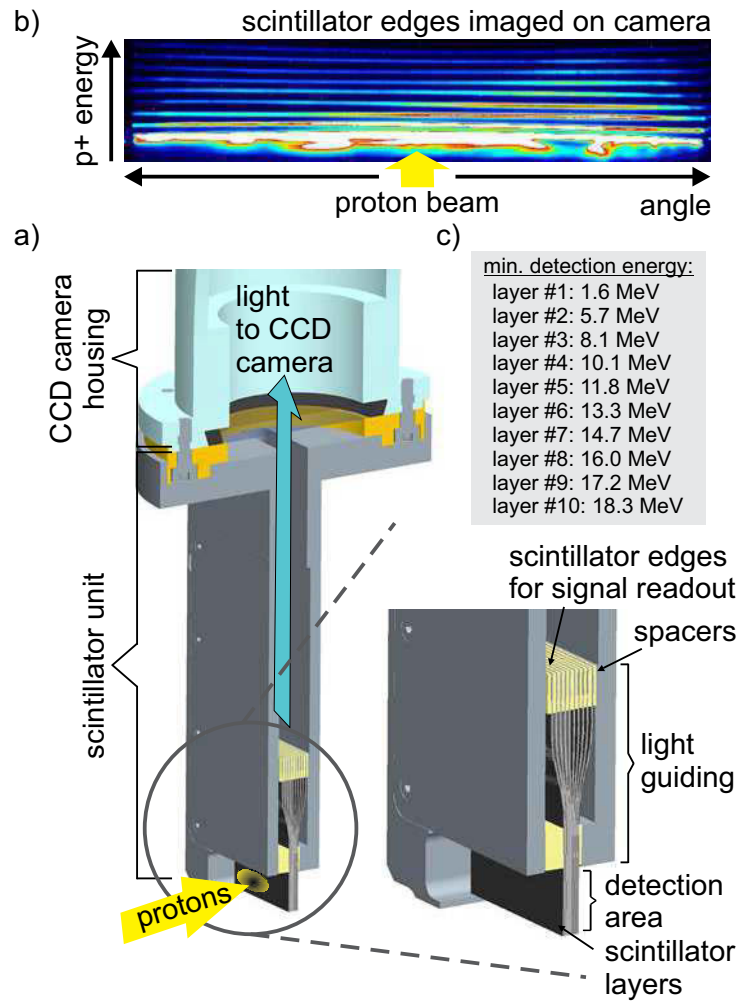


Figure A.6.: Setup of the scintillator-based 1D stack detector. a) Technical drawing of the detector. b) Exemplary raw data of the scintillator edges imaged onto the CCD camera. The light output of the scintillator layers as a measure for the deposited proton dose is encoded in a color table ranging from white to blue for decreasing signal intensity. c) Summary of the minimum initial energy a proton needs in order to reach a specific scintillator layer. The data is simulated with SRIM [225].

the setup in between the energy filter and the IDOCIS aperture. With the detection area sitting only 1 mm above the lower edge of the detector, the detector can be placed into an unused part of the proton beam, giving access to online information non-invasively for each laser shot. Figure A.7b summarizes the results of the experiment, showing the variation of the maximum proton energy when the distance between the focal plane and the target foil is changed. The maximum proton energy is sensitive to changes in distance of 25 μm , yielding differences of up to 5 MeV for the maximum proton energy in that particular case. This behavior is well-resolved with the detector. Once the optimal focus position is set, the scintillator-based detector serves as an online monitor for the acceleration performance and stability without interfering with the experiment itself. Indirectly, via the angularly resolved proton spectrum, the experimenter gets immediate feedback about the laser chain and setup stability and is enabled to react if performance changes occur. Moreover, the detector can be used to monitor the spectral stability of the accelerated proton pulses which is a crucial input for the dosimetry protocol [24].

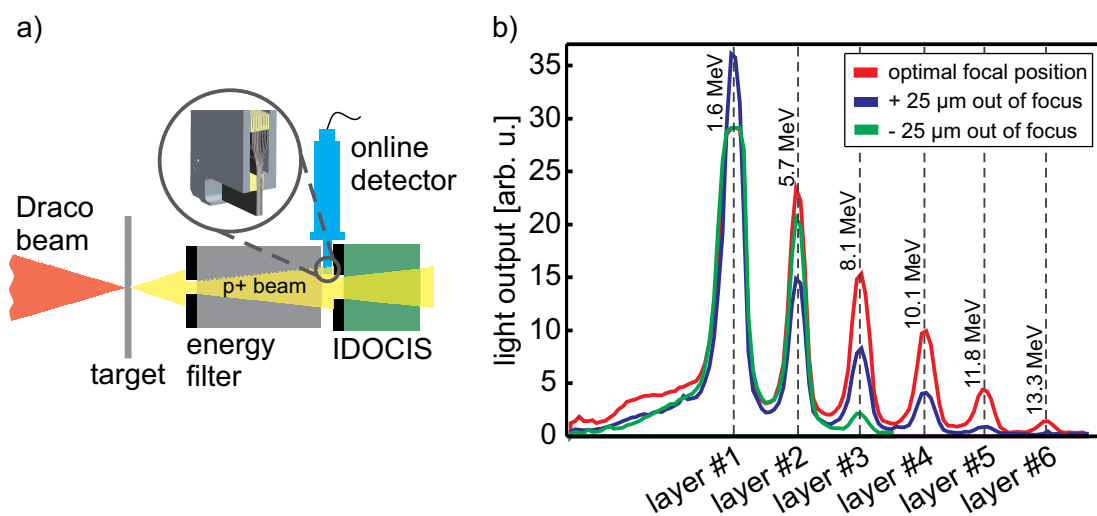


Figure A.7.: Detector application at the Draco I beam. a) Side view of the setup the detector is integrated in for a performance test. b) Sensitivity of the detector signal to a change of the focal depth position.

Imaging Properties

The requirement for the detector to spatially resolve proton beam spots with diameters in the order of 10 mm sets the necessary spatial resolution along the scintillator edge to below 2 mm. Figure A.8a, which shows the front side of a scintillator layer and the CCD camera entrance aperture, illustrates the design parameters, which determine the spatial resolution of the detector. In the first scenario (*pos.1*), energy deposition by a proton in the center of the detection area excites the scintillator and the isotropically emitted photons are guided towards the upper scintillator edge. All light within a cone of a half-angle smaller than the critical angle for total internal reflection (shaded area) is emitted at the upper scintillator edge, obviously illuminating the entire scintillator edge. Spatial resolution is only introduced through the imaging system because the entrance aperture of the camera objective limits the acceptance angle for light, as depicted by the detected light cones. For this detector setup, the entrance aperture of the objective with a diameter of 8.6 mm is positioned 182 mm above the detection area, reducing the acceptance angle to 1.8° , including the light refraction at the upper scintillator edge. The resulting spatial detector resolution is 1.3 mm, well agreeing with the requirements. Further improvement of the spatial resolution can be achieved either by increasing the distance between the upper scintillator edge and the camera aperture or by a smaller camera aperture. Both measures are at cost of the light collection efficiency and/or the detector size, but might be applied depending on the minimum proton beam spot size required to resolve.

If instead an excitation position off-center along the detection area is considered (*pos.2* in Figure A.8a), the detected light cone is tilted with respect to the normal direction, shifting the virtual position of the signal at the scintillator edge relative to the original position of energy deposition. The lateral shift increases with the distance from the detection area center but can be accounted for by a simple transformation.

Experimental testing of the inherent signal distortion was performed at a conventional proton source by covering the detection area of the detector with an aluminum plate with a regular mask pattern of 9 holes with a diameter of 2 mm during irradiation. In this was, localized dose deposition as sketched Figure A.8a is ensured. The measured profile normalized to the maximum light output value is shown in Figure A.8b. Comparison

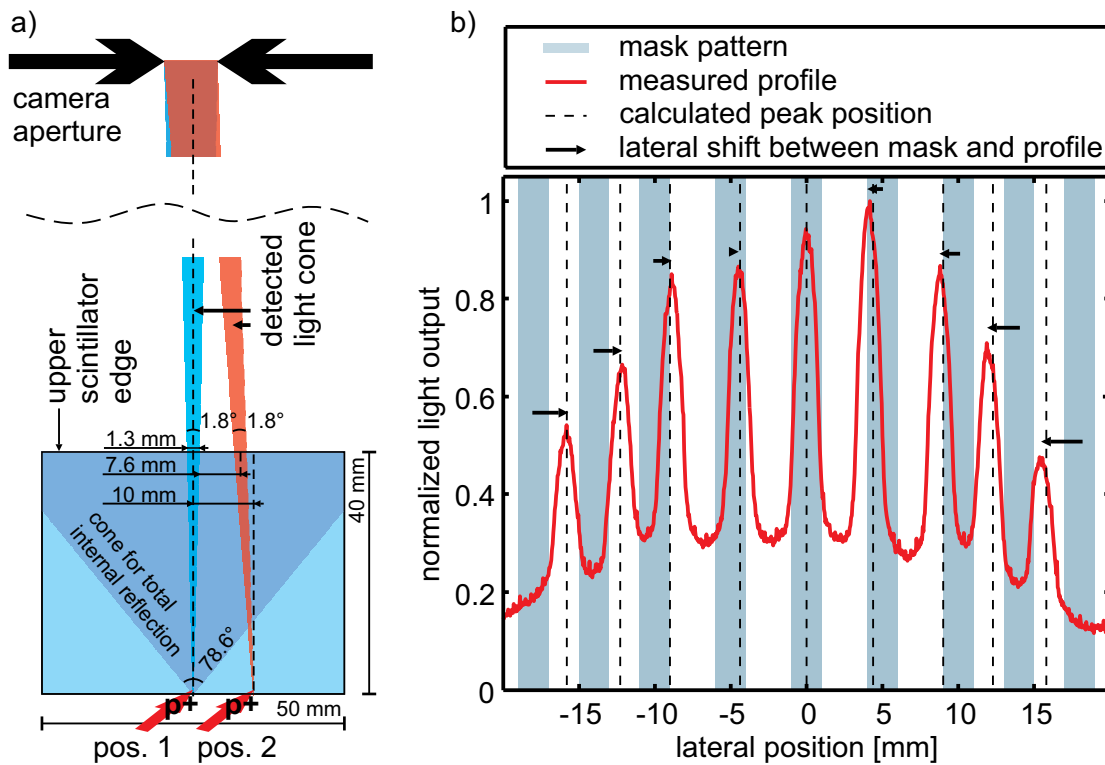


Figure A.8.: Imaging properties of the detector. a) Schematic front view of the detector with a scintillator layer at the bottom and the camera aperture at the top illustrating the imaging properties. b) Experimental validation of the imaging properties using a mask featuring a regular pattern of 2 mm diameter apertures. The shaded areas represent the mask patterns.

of the mask pattern printed as blue bars with the measured profile reveals that the peak positions in the measured profile are indeed shifted towards the center. The measured peak positions are in agreement with the positions calculated based on the geometry sketched in Figure A.8a.

Detector Characterization at a Conventional Proton Source

The sensitivity of the detector is characterized at the 6 MV Van de Graaff tandetron accelerator at the HZDR. Optimized for ion implantation, the tandetron accelerator delivers proton currents of up to $3 \mu\text{A}$ at a maximum energy of 11.8 MeV. In accordance with the high sensitivity of scintillators to ionizing radiation, the accelerator is however operated at currents of about 100 pA, corresponding to a dose rate of $\sim \text{Gy/s}$. The current reduction is achieved by beam defocusing and additional scanning over a large area. The final beam size for the irradiation is defined by an aluminum plate with an aperture of 10 mm placed at the entrance of the vacuum chamber in which the detector is installed. The beam current is controlled before and after each short series (every few minutes) using a Faraday cup with a diameter of 2.54 cm, hence capable to measure the complete proton beam. After the setting of the desired beam current, the dose applied to the detector is controlled via the irradiation time.

Aiming at a characterization of each scintillator layer in the final detector setup, the energy deposition profile in the scintillator stack of the 11.8 MeV proton beam is used for the measurement. Because the range of 11.8 MeV protons only allows to irradiate five of the 10 scintillator layers, the measurement is once performed for layers 1 to 5 and then, after

turning of the symmetrical scintillator case, for layers 10 to 6. During the measurement, the detector is exposed to a current of (86.7 ± 3.1) pA for layers 1 to 5 and (104.5 ± 1.6) pA for layers 6 to 10, respectively for a time duration of 0.5 s. The uncertainties for the current measurement correspond to the standard deviation of the mean value of the current measurement before and after the scintillator irradiation and also include errors of the device. An RCF placed around the sensitive area of the scintillation detector is used to determine the beam position and to deduce the proton number on the detector.

For post-processing of the images, the light output, corresponding to the integral CCD camera counts, is determined and corrected from background radiation for each scintillator layer. The results are summarized in Figure A.9, where the right axis shows, as a reference, the energy deposition profile dE/dx of an 11.8 MeV proton in the scintillator stack as calculated with SRIM [225]. On the left axis, the light output (i.e. the CCD camera counts) per proton per deposited energy for each scintillator layer normalized to the mean light output averaged over all 10 layers is plotted. The mean light output is (0.17 ± 0.06) CCD camera counts/proton/MeV.

Deviations from the mean light output of the individual scintillator layers can be attributed to different effects. Firstly, the reduced sensitivity in the case of layer 10 is attributed to an artifact of the imaging system and can be quantified and corrected for using a constant light source [226]. Moreover, the condition of the scintillator surfaces and edges for signal readout (e.g. scratches resulting from manual polishing) can influence the efficiency of the light guiding and emission [227], as observed in the case of layer 1. Thirdly, scintillating material inherently features a quenching effect resulting in a reduced light output with increasing energy deposition dE/dx ([227] and Equation (A.1)), which should affect most strongly layers 5 and 6, which are exposed to the Bragg peak during irradiation. Quenching describes non-radiative processes in the scintillator following excitation, which reduce the light output per absorbed or input energy. Measurements of the quenching behavior for a polyvinyltoluene-based scintillator predict a difference of 40% in the light output when plateau and Bragg peak region are compared [222]. However, the presented measurement does not allow for a distinction between the influence of quenching versus the contribution of the scintillator edge conditions so that the reduced performance of layer 6 cannot be definitely explained.

Scintillator-Based 2D Pixel Detector

Detector Setup and Principle

The setup of the scintillator-based 2D pixel detector is presented in Figure A.10a and it comprises, like the 1D stack detector, of a detector and a CCD camera unit. The central part of the detector unit is the $48 \text{ mm} \times 48 \text{ mm}$ large absorber matrix machined into a 2.5 mm thick aluminum plate. Designed for a location of about 50 mm behind the target, the detector's field of view has a half-angle of 26° with respect to the proton (point) source and can therefore record a two-dimensional imprint of the entire proton beam. To provide for spectral resolution, the absorber plate is segmented into 60 pixels, each containing a matrix of 3, 9 or 16 holes countersunk into the aluminum plate (Figure A.10b). That gives seven different absorber thicknesses in the range of $0 \text{ }\mu\text{m}$ to $800 \text{ }\mu\text{m}$ for the prototype design. Placed into the proton pulse, each detector pixel samples a specific part of the beam and resolves up to seven particle energy ranges. Protons energetic enough to pass a specific absorber hole, deposit energy in the $200 \text{ }\mu\text{m}$ thick layer of polyvinyltoluene-based plastic scintillator BC416 (Bicron) following directly behind the aluminum plate. The emission of scintillation photons at 434 nm is excited. The scintillator rear surface

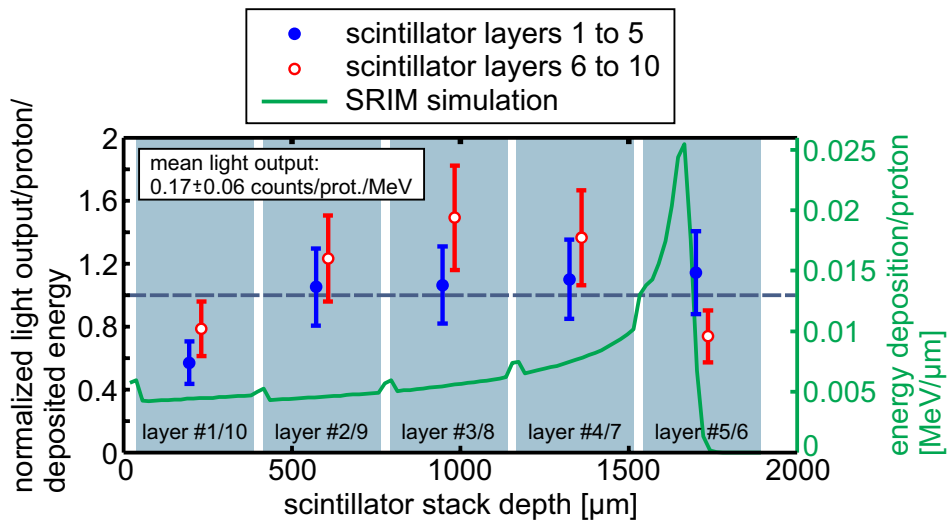


Figure A.9.: Light output characterization. The light output per proton per deposited MeV energy for each scintillator layers normalized to the average over all layers is shown in the left axis of the plot. The energy deposition of an 11.8 MeV proton beam in the scintillator stack, as used for the simultaneous characterization of five scintillator layers, is plotted in green. The shaded areas are the scintillator layers and the white area in between represents the plastic foil covering each layer.

is imaged onto a CCD camera, a representative raw data image taken at the HZDR tandemron accelerator being shown in Figure A.11. Each of the bright spots corresponds to an absorber hole and represent the signal from protons above a minimum kinetic energy given by the energy-range-correlation of protons for the specific absorber thickness. The detector hence provides spatial resolution in two dimensions as well as spectral resolution for the complete proton distribution in real-time. In this design, the spatial resolution is defined by the pixel size of $5.5 \text{ mm} \times 5.5 \text{ mm}$. It is strongly reduced compared to RCF for the benefit of spectral resolution, which can flexibly be chosen via the absorber thickness. The choice of the light material aluminum with a low stopping power for the absorber matrix allows to resolve the maximum proton energy with an accuracy of $\leq 1 \text{ MeV}$ for proton energies above 8 MeV by varying the absorber thickness by $\sim 100 \mu\text{m}$. The detector hence provides a better spectral resolution than RCF. The resolvable energy range can as well be tuned via the absorber design and is, in the case of this prototype, optimized for proton energies up to 12 MeV as provided by the HZDR tandemron accelerator.

Absorber Matrix Parameters After presenting the detector principle, a short discussion of the specific design considerations regarding the absorber matrix follows. Aiming at a setup manufacturable in-house, the basis of the absorber matrix is an aluminum plate with perpendicularly milled absorber holes, leaving their diameter and distance as design parameters. Optimization of both parameters is performed experimentally at the HZDR tandemron accelerator [228], resulting in an absorber hole diameter of 1 mm as the lower limit. For smaller hole diameters, despite being favorable in order to increase the spatial resolution of the detector, the scintillation signal is strongly reduced due to scattering of protons at the absorber hole walls. In order to compensate for the effect that absorber holes located off-center on the detector surface are irradiated under an angle and hence feature a reduced solid angle of detection, the hole diameter increases up to 1.8 mm in four steps towards the detector edges, as shown in Figure A.10b. In principle, the gracing

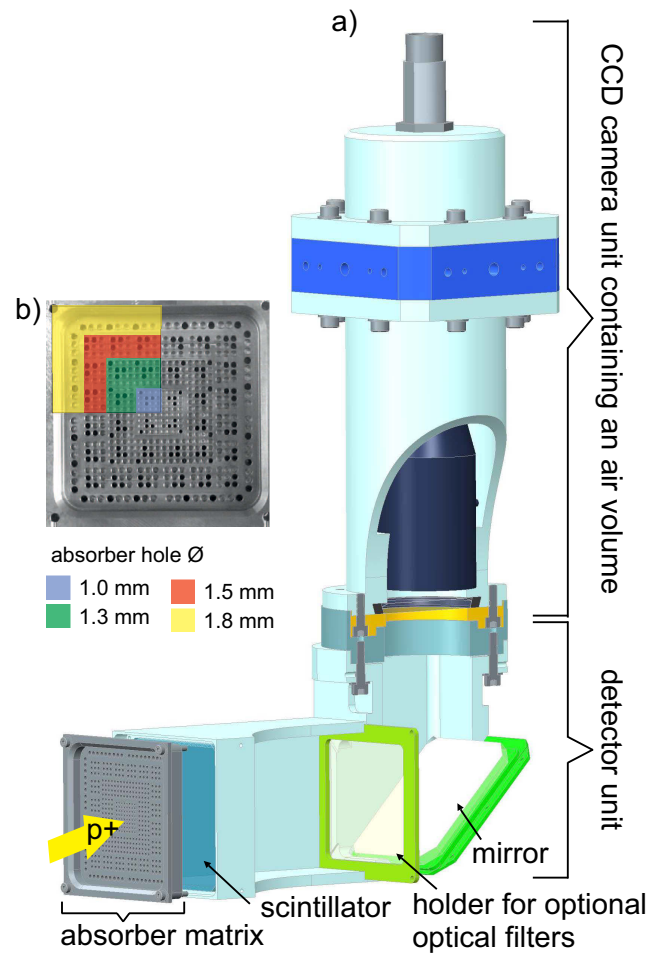


Figure A.10.: Setup of the 2D pixel detector. a) Technical drawing. b) Photograph of the absorber matrix. The different zones of absorber hole diameters are color-coded.

incidence under an angle α onto the absorber matrix at off-center positions also influences the spectral properties of the detector as protons then pass an increased absorber thickness $d/\cos \alpha$ with d being the nominal absorber thickness. Amounting to less than 10% in thickness gain, this effect can however be neglected for all practical purposes. For the distance of neighboring absorber holes, an optimum value is determined experimentally at $500 \mu\text{m}$, providing well-separated signal spots on the CCD camera. This is in good agreement with the fact that a localized energy deposition at the scintillator front surface is expected to result in a scintillation spot with a diameter of $330 \mu\text{m}$ at the rear surface of the $200 \mu\text{m}$ thick scintillator layer, which features a critical angle of $\theta_c = 39.3^\circ$ for total internal reflection. Hence, crosstalk between neighboring absorber holes should, apart from protons scattering in the material, be suppressed.

Regarding the camera unit including the camera model and the camera placement, i.e. horizontal orientation of the CCD chip to reduce background radiation, the setup of this detector equals the 1D stack detector setup. A mirror placed at an angle of 45° folds the optical beam path. The imaging is performed with a 25 mm focal length objective giving an image resolution of $41 \mu\text{m}$ per pixel. The total height of the detector including the CCD camera housing is 320 mm and it has a footprint of $60 \text{ mm} \times 160 \text{ mm}$.

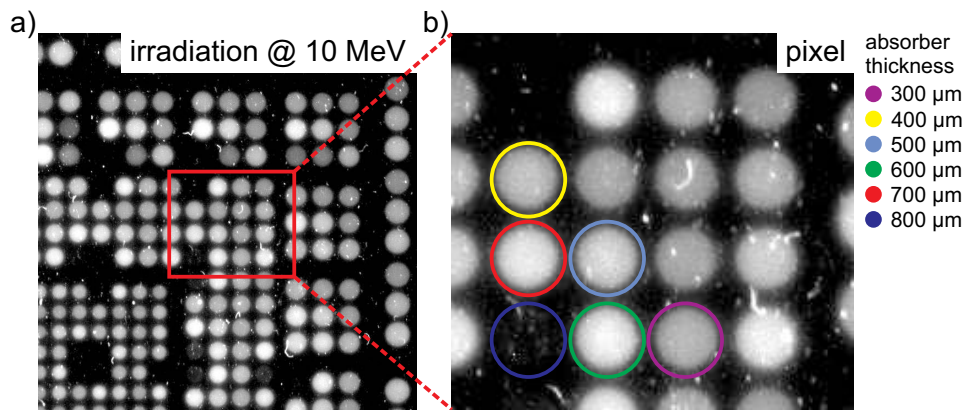


Figure A.11.: Raw data of the detector signal. a) Raw data for the detector irradiation with 10 MeV protons at the HZDR tandemtron accelerator. The absorber holes are well-separated, which simplifies the automatic readout for subsequent data analysis. b) Zoom into a pixel of the absorber, where the different absorber thicknesses are color-coded. In accordance with a range of $623\ \mu\text{m}$ [225] in aluminum for 10 MeV protons, the absorber hole for $800\ \mu\text{m}$ is dark whereas the maximum signal, corresponding to the Bragg peak, is recorded for an absorber thickness of $600\ \mu\text{m}$. The fact that the $700\ \mu\text{m}$ thick absorber features an equally bright signal indicates the necessity for a careful thickness characterization of the absorber plate in order to verify the nominal (manufacturing) parameters.

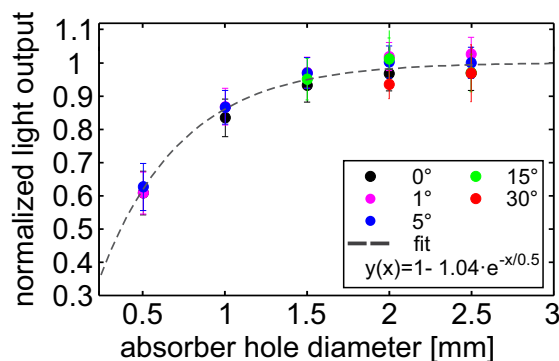


Figure A.12.: Geometric calibration. Relative light output as a function of the absorber hole diameter and the irradiation angle.

Detector Calibration

The calibration of the detector light output per proton as a function of the differential energy deposition dE/dx and regarding the influence of the detector geometry (i.e. absorber hole diameter and angle) is a necessary precondition for the reconstruction of the two-dimensional spectrally and spatially/angularly resolved proton distribution from the detector signal. According measurements are performed at the 6 MV HZDR tandemtron accelerator. For details of the setup see the according discussion for the 1D stack detector. The scintillator long-term performance under irradiation is characterized at the 14 MV Tandem accelerator at the Maier-Leibnitz-Laboratorium (MLL) in Garching.

Absorber Matrix Characterization Geometric factors such as the absorber hole diameter and the angle between the incoming proton beam and the absorber hole orientation are expected to influence the detector signal due to proton scattering in the absorber matrix (walls). The calibration of the geometric factors is performed using an absorber matrix

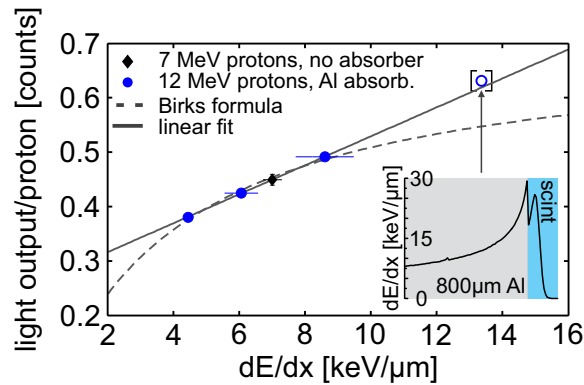


Figure A.13.: Light output calibration. Absolute light output calibration (\blacklozenge) and energy deposition calibration for the scintillator material including a linear and Birks fit for $dE/dx = 4$ - 8.6 keV/ μm . The inset shows the dE/dx curve for a proton stopping in the scintillator and refers to the case for the highest dE/dx data point. This data point is plotted in brackets due to its large dE/dx error bar (see inset) and because the light output has not been scaled to the reduced absorption length of 150 μm .

with hole diameters ranging from 0.5 - 2.5 mm and machined orientations of $0/1/5/15/30^\circ$ with respect to the absorber plate normal [228]. Note that the hole orientation of 30° is only tested for the large hole diameters as the sight through the hole is otherwise blocked. For post-processing, the detector signal is firstly corrected for inhomogeneities in the irradiation field and then averaged over a circular ROI with 50% of the nominal absorber hole diameter for each signal spot. Comparison of different ROI sizes shows that for a 50% ROI the mean signal deviates by less than 5% from the average over the signal spot center (25% ROI) for all hole diameters [228], rendering a 50% ROI standard for data evaluation. Each data point in Figure A.12 represents the average over 20 (10 for 30° orientation) absorber holes and the error bars include the standard deviation of the ROI as well as the sample mean. The results show that the light output is almost independent from the absorber hole diameter down to 1.5 mm and decreases by 14% for a diameter of 1.0 mm, which is the minimum hole size applied in the prototype detector. A further reduction of the absorber hole diameter e.g. down to 0.5 mm can according to the data not be recommended, since scattering leads to a strong signal reduction. The relative light output for an arbitrary absorber hole diameter can be calculated via the fitted exponential recovery function. The relative orientation between absorber hole and incoming proton beam has no influence on the signal for the chosen ROI size of 50% .

Light Output Calibration For the absolute calibration of the light output (i.e. the CCD camera signal) per proton passing through the scintillator, the absorber matrix shown in Figure A.10b is replaced by an aluminum plate with a 20 mm large aperture in the center, behind which a 13 μm thick light-tight plastic foil and the 200 μm thick scintillator are placed. The diameter of the proton beam is reduced to 10 mm in order to exclude the influence of proton scattering at the aluminum absorber plate on the measurement. The beam current is varied from 40 - 190 pA/ cm^2 to verify a linear response of the scintillator light output [228]. Performed at a proton energy of 7 MeV, the calibration results in (0.45 ± 0.01) counts for the light output per proton rescaled to a camera gain of 0 and corresponding to a differential energy deposition of $dE/dx = (7.0 \pm 0.3)$ keV/ μm (Figure A.13). In the case of the irradiation with protons or other highly ionizing ions (e.g. α particles), plastic scintillators show a nonlinear response of the light output per length dL/dx

as a function of the differential energy deposition of dE/dx , an effect termed ionization quenching [227]. The stopping power-dependent light output is a necessary input for the reconstruction of spatially/angularly resolved energy spectra from the detector raw data. That is due to the fact that protons contributing to the signal of an absorber hole can either stop in the scintillator behind or be energetic enough to just pass it, both cases corresponding to different dE/dx values.

The according calibration measurements are performed using aluminum absorbers with thicknesses ranging from 0-800 μm , which corresponds to dE/dx values between 4 keV/ μm and 13 keV/ μm for the 11.8 MeV protons available for irradiation. Due to the fact that the diameter of the absorber holes is only 1.5 mm, an influence of proton scattering on the signal cannot be excluded (Figure A.12). The raw data are therefore interpreted as a relative measurement and scaled to the light output at $dE/dx = 7 \text{ keV}/\mu\text{m}$ from the scattering-free calibration measurement. The results are summarized in Figure A.13. For practical purposes, i.e. as input data for the reconstruction of two-dimensional spectra from the detector signal, the light output as a function of dE/dx (for $dE/dx = 4 - 8.6 \text{ keV}/\mu\text{m}$) can well be approximated by a linear function with a slope of $0.03 \text{ counts} \cdot \mu\text{m}/\text{keV}$ and an intercept of 0.3 counts, the non-zero value for the intercept reflecting the nonlinear scintillator response. Birks [227] has proposed the formula

$$\frac{dL}{dx} = \frac{S \cdot \frac{dE}{dx}}{1 + kB \cdot \frac{dE}{dx}} \quad (\text{A.1})$$

to describe the saturation behavior of the light output per length dL/dx of organic scintillators with the fit parameters S for the scintillation efficiency and kB for the quenching efficiency. Regression analysis of the data for $dE/dx = 4 - 8.6 \text{ keV}/\mu\text{m}$ yields $S = 0.18 \text{ counts} \cdot \mu\text{m}/\text{keV}$ and $kB = 0.26 \mu\text{m}/\text{keV}$, in good agreement with the literature for a similar scintillator material [222]. Note however that the lack of data for low dE/dx values (restricted by the maximum available proton energy of 11.8 MeV) confine the presented fit parameters to the application for practical purposes and do not present a reliable saturation characterization for the BC416 scintillator material.

For both curve fittings, the highest dE/dx data point, which represents the average over the Bragg peak region in which dE/dx strongly varies (inset in Figure A.13), is omitted due to its large error bar. A reliable characterization measurement of the BC416 material would have to be performed with a considerably thinner scintillator layer in order to sample the proton dose depth curve with higher spatial and hence dE/dx resolution. The data point is however relevant for the detector application, because it gives the light output in the case of protons stopping in the scintillator layer. Note that the light output for $dE/dx = 13.4 \text{ MeV}$ is not been scaled to the absorption length of $\approx 150 \mu\text{m}$ in the scintillator.

Scintillator Long-Term Performance Under Irradiation Moreover, plastic scintillators can be subject to aging, which depends among other factors on the total accumulated irradiation dose ([227] and e.g. [229]). The result is a reduced light output. A first test experiment estimating the long-term performance degradation due to aging is performed at the 14 MV Tandem accelerator at the Maier-Leibnitz-Laboratorium (MLL) in Garching. All details of the experimental setup are summarized in the caption of Figure A.14. In agreement with the results of an extensive study on the luminescence degrading in a 50 μm thick polyvinyltoluene-based scintillators under proton irradiation up to megagray dose levels [229], no evidence for a signal reduction after irradiation with a total dose of 13 kGy is observed (Figure A.14).

Applied to a typical exponential spectrum from 5-14 MeV of laser-driven protons with

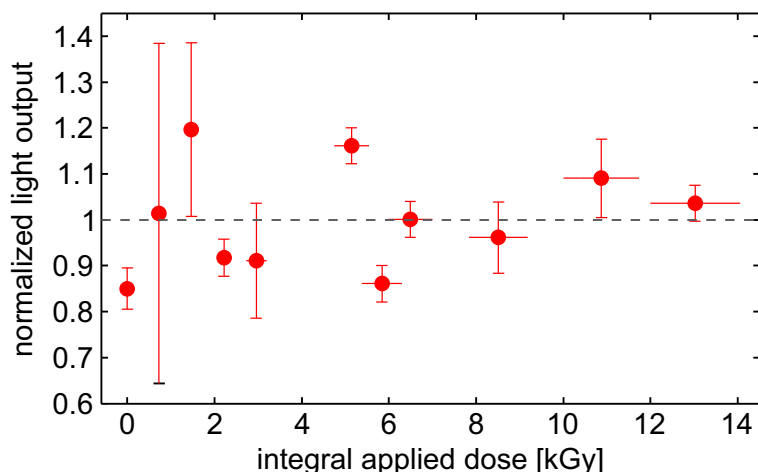


Figure A.14.: Scintillator long-term performance under irradiation. Characterization of a potential detector light output degradation due to material aging. The scintillator is irradiated with a total dose of 13 kGy on an area of 2.2 mm² in steps of ~ 1 -2 kGy. The light output after each irradiation step is probed via low-intensity irradiation at the dose level of ~ 1 Gy. These data are plotted. The error bars for the applied dose include the uncertainty for the differential energy deposition dE/dx as simulated with SRIM [225] and the error for the cross-calibration of RCF versus the ionization chamber. The vertical error bars correspond to the standard deviation of the evaluated ROI as well as the sample mean.

Experimental setup: The MML accelerator is operated in pulsed mode, delivering 3.5 ns pulses with $7.5 \cdot 10^4$ protons in an area of 5-10 mm² at an in-vacuum proton energy of 20 MeV. The experimental setup is placed in air, the proton beam leaving the beam tube through a 50 μ m thick Kapton window. A transmission ionization chamber cross-calibrated with RCF in front of the detector is used to measure the dose applied to the detector simultaneously to the irradiation. Including the absorber material covering the scintillator (1.5 mm of aluminum, 26 μ m of plastic), the differential energy deposition of the 20 MeV protons amounts to $dE/dx = (8.60 \pm 0.45)$ keV/ μ m in the scintillator.

fluxes of 10^9 - 10^{10} protons/MeV/sr (e.g. Figure 1b in [27]) and a detector setup in which the 6 MeV protons have their Bragg peak in the 200 μ m thick scintillator, more than 800 proton pulses can be recorded before accumulating a dose of 13 kGy. This estimation underlines that scintillator aging should not be a show-stopper for the application of scintillator-based detectors for laser-driven proton pulses.

Conclusion and Outlook

In conclusion, the two scintillator-based detectors systems provide in real-time angularly resolved spectra of the proton distribution for up to 10 different energy intervals in one and two dimensions, respectively. Their compact design and the optimization for the laser-plasma environment make them very versatile tools for the online optimization and the monitoring of key parameters in laser-proton acceleration experiments, such as maximum proton energy, particle yield and spectral stability. Such an on-shot correlation of laser and proton pulse properties, as enabled by online detectors, is valuable for experiments on laser-driven proton acceleration which aim at developing a reliable accelerator.

Regarding their area of application, both detectors cannot replace neither RCF nor Thomson parabola spectrometers but present very useful complements. In particular the combination with a Thomson parabola spectrometer, speedwise also matching the repetition rate capabilities of state-of-the-art ultrashort pulse laser systems, engenders an online diag-

nistic unit that features angularly resolved coarse spectral resolution for the entire proton distribution as well as high resolution spectroscopy of all ion species within a small solid angle. With such a detector unit, the uncertainties associated with Thomson parabola spectrometer measurements in the case of inhomogeneous proton distributions [53, 54, 27] about the representativeness of the spectra are avoided by the simultaneous sampling of the complete solid angle of the proton beam. In turn, the Thomson parabola spectrometer provides the discrimination of different ion species, which is beyond the capabilities of any scintillator-based detector relying on depth dose profiles in an absorber material for energy resolution.

The flexibility of plastic scintillators and the modularity of the detector setups presented allow for further developments of the design, particularly improving such shortcomings as the spatial/angular and spectral resolution. First of all, an improvement of the spectral resolution is for both detectors directly achieved through the choice of thinner scintillator and absorber layers. The high (1.3 mm) spatial resolution of the 1D stack detector can for instance be transferred to a 2D detector concept by increasing the detection area (Figure A.6a) in vertical direction and by reading out a vertical scintillator edge with a second CCD camera. The two-dimensional proton distribution is then reconstructed from the data using tomography techniques. An interesting extension of the 2D pixel detector is achieved when using a transparent absorber matrix sandwiched in between two plastic scintillator layers emitting at two different wavelength. Whereas the absorber and second scintillator function as in the original design, the first scintillator additionally provides a spatially highly resolved 2D profile of the proton distribution. Both signals are separated using a color CCD camera.

One additional limiting factor for scintillator-based detectors is their sensitivity to electrons and xrays. However, plastic scintillators are available with scintillation decay times in the nanosecond range, which can be exploited for time-of-flight applications. In combination with a gated camera, fast scintillators would allow for a separation of the fast electron and xray signal from the proton signal and hence a further improvement of the signal-to-noise ratio beyond the capabilities of pure passive shielding.

A.3. Additional Data for the Specularly Reflected Pump Pulse Probing

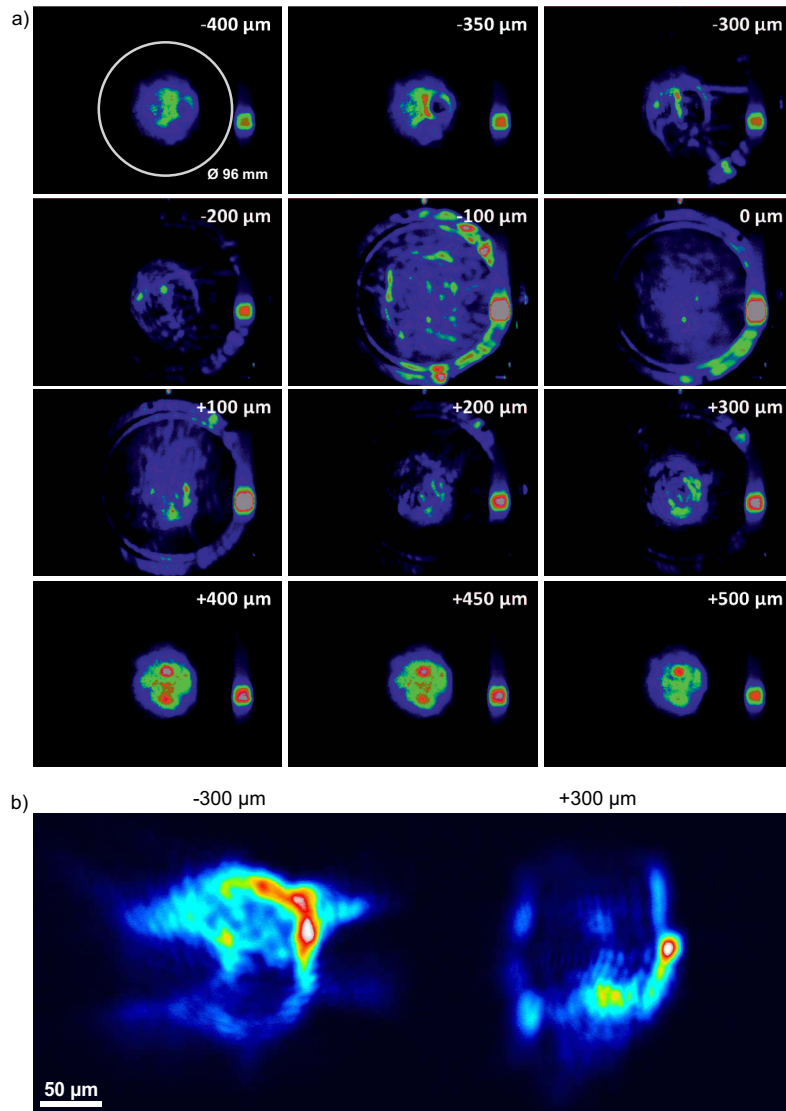


Figure A.15.: Specular reflection of the pump laser pulse. a) Images of the specularly reflected laser beam for different focal spot distances from the target surface. For negative and positive values, the focal spot lies in front of or behind the target surface, respectively. Only for negative focal spot positions, the hole feature in the reflected beam is observed. b) Spatial intensity distribution on the target surface for two longitudinal focusing positions. The data confirm that the spatial beam profiles feature a peak in intensity for both cases, i.e. the focal spot in front of and behind the target surface. For details see Section 4.2.

A.4. Modeling of the Reflective Pump-Probe Experiment

Appendix A.4 discusses the results of the analytic and numerical modeling of the pump-probe experiment. In Section 4.4.2, the key points of the analysis are presented.

Modeling Without Preplasma

Ray-Tracing Model

The basic geometric features of the probe beam reflection are firstly investigated based on a model, which neglects the preplasma gradient in front of the critical density surface. Hence, as in Section 4.2.2, the critical density surface is set up as a flat, perfectly reflecting surface with a Gaussian-shaped deformation. In contrast to the model for the specular pump pulse reflection recorded on a screen after ~ 100 mm of propagation, now the pattern formation close to the reflecting surface (i.e. the near-field) is of interest. That is due to the fact that the surface is imaged with a depth-of-field (DOF) of $27 \mu\text{m}$ in the experiment. The setup for the ray-tracing simulations is shown in Figure A.16. Matching the experiment, the incoming rays (not plotted) have an incidence angle of 33.4° , coming from the left. The beam is simulated as a collimated ray bundle. Tests have shown that the effects from focusing in the experiment, resulting in a beam cone with an opening angle below 2° , can be neglected. The distribution of reflected rays is analyzed in two specific planes through peak the of the Gaussian deformation, P_1 and P_2 , the first lying parallel to the incoming ray bundle, the latter being perpendicular (Figure A.16d).

Figure A.16a - c confirm the expected reflection out of the central part of the ray bundle, producing the hole feature as observed in the experiment (Figure 4.7). Moreover, the simulation of the near-field regions reveals that the concave flanks of the deformation have a focusing effect, forming a region around the focal spot in which the reflected rays overlap. This results in a ring feature framing the void zone, as visible in Figure A.16e - f, which show results of the surface imaging. Those images are strongly reminiscent of the experimental results presented in Figure 4.7a - d, indicating that the experimentally observed ring feature can indeed be a signature of the expanded plasma.

For an analytic and quantitative analysis of the focus position and hence the apparent ring feature diameter, the reflection patterns in plane P_2 are considered. In this plane, the angle of incidence relative to the y - z -plane can be neglected, reducing the problem to two dimensions. In this plane, the parallel ray bundle impinges onto the surface perpendicularly (Figure A.16b - c). In this scenario, the concave flanks of the Gaussian are optimally approximated by a parabolic curve (blue curves)

$$z(y) = p_1 \cdot (y - y_0)^2 + z_0 \quad \text{with} \quad f = \frac{1}{4 \cdot p_1} \quad , \quad (\text{A.2})$$

a parabola having the property to collect all parallel light into its focal point F with coordinates $(y_0 | f)$. To yield f as a function of A and w , Equation (A.2) is solved for p_1 . Thereby, the inflection point $y_{infl} = (w/\sqrt{8 \cdot \ln 2})$ of the Gaussian curve is set as y and $2.8 \cdot y_{infl}$ is set as the vertex y_0 of the parabola. The latter choice minimizes the deviation between the Gaussian curve and the fit independent from the deformation parameters A and w . The calculations yield a focal spot position $F(A, w) \approx (1.19 \cdot w | w^2/4.02 \cdot A)$, neglecting the small vertical offset z_0 . This result is in very good agreement with the ray tracing results in Figure A.16b - c, where calculated focus positions are marked with red crosses. From the lateral (y) position of the focal spot at $1.19 \cdot w$, it follows that the ring diameter after surface imaging should scale as approximately $2.4 \cdot w$ with the FWHM of the Gaussian

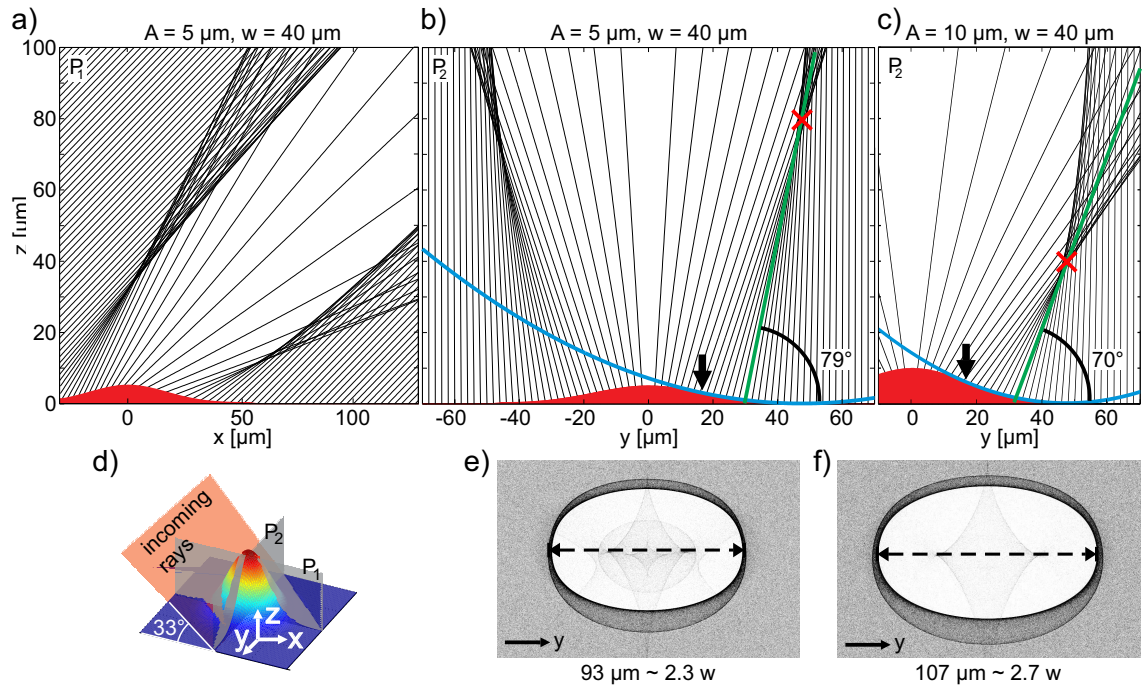


Figure A.16.: Modeling of the experiment without preplasma. a - c) Ray-tracing of a collimated beam impinging from the left after reflection off a Gaussian-shaped surfaces (red areas) with different A and w parameters, analyzed in two planes. The blue curves represent the fitted parabolic curve for the concave flanks of the Gaussian surfaces. The black arrow and red cross mark the inflection point and focus point, respectively. d) Simulation setup. e - f) Surface imaging with a 50 mm diameter lens, $f = 100$ mm, magnification $M = 40$ and a resulting depth-of-field (DOF) of $27 \mu\text{m}$.

deformation, which is confirmed in Figure A.16e. This simple relation however neglects the influence of the amplitude A . An increase in A yields an increased diameter for the ring signature (Figure A.16f). The dependence on A arises because it is not only the focal spot, but also parts of the region of overlapping rays that lie in the DOF of the lens and are therefore imaged. Then, since the focus F moves closer to the surface with increasing A , the region of overlapping rays acquires a flatter angle with respect to the horizontal plane (x - y -plane). In consequence, at a fixed position above the imaged surface (e.g. in the DOF), the region of overlapping rays lies further out for larger A and the ring feature on the image is larger in diameter.

In summary, the ray-tracing confirms that ring-like features similar to the experimental observation can indeed be produced when a collimated beam is reflected off a (Gaussian-)shaped surface.

Diffraction Model

The numerical simulations based on ray-tracing algorithms neglect wave-optical effects, such as diffraction. However, particularly when probing the plasma distribution at times before the main pulse arrival, the size of the iso-density surface deformation can be small and amount to only ~ 100 nm for the amplitude A (Section 4.2.2). Therefore, the role of diffraction effects in the pattern formation on the detector is evaluated.

In the setup, a plane light wave ($\lambda = 400$ nm) is impinging normally on a Gaussian-deformed surface. The diffracting surface and the detector diameter are set to 60 and $40 \mu\text{m}$, re-

spectively, with a spatial resolution of $\lambda/4 = 0.1 \mu\text{m}$. To keep the simulations simple, the contribution of underdense preplasma is neglected and in contrast to the ray-tracing simulation, the imaging lens is not considered.

Instead, the evolution of the diffraction pattern with increasing distance between the deformed surface and the detector is investigated (Figure A.17a). For that case, the surface deformation has an amplitude of $A = 0.2 \mu\text{m}$ and an FWHM of $w = 2 \mu\text{m}$. Whereas the diffraction pattern shows a central peak ($x = 0$) closest to the surface, a central hole feature and a surrounding area of higher intensity (a ring in 2D) develops $1 \mu\text{m}$ behind the surface. The width and depth of the hole feature increase as the detector distance is further increased. The range of distances sampled in the simulations lies within the DOF of $27 \mu\text{m}$ of the imaging lens used in the experiment. Hence, imaging of the surface should include the hole and ring signature of the diffraction pattern. This confirms that the inclusion of diffraction qualitatively yields results in agreement with the ray-tracing ansatz, even for deformations with sizes of $\{A, w\} \lesssim \lambda$. In addition, the diffraction pattern contains details which are not included in the ray tracing model, i.e. the interference pattern that surrounds the primary ring signature for the detector distances $10 \mu\text{m}$ and $20 \mu\text{m}$ (Figure A.17a). In a ray-tracing image, this feature is attributed to the interference of rays reflected outwards in the central part of the deformation with rays reflected far out on the flat flanks of the distribution. It is also visible in the experimental data, e.g. Figure 4.7b. In a second set of simulations, the amplitude of the surface deformation is varied in the range of $0.2 - 5 \mu\text{m}$ for a fixed FWHM of $10 \mu\text{m}$. The detector is placed $10 \mu\text{m}$ behind the surface, i.e. at $1/3$ of the DOF of the imaging lens used in the experiment. The results presented in Figure A.17b show that the hole signature starts to form within the DOF region of the imaging lens even for amplitudes below the wavelength. That confirms the sensitivity of the method to early stages of the plasma expansion. As with increasing detector distance, the hole feature's width and depth grows with increasing deformation amplitude. A quantitative analysis of the evolution of the ring diameter D shows that the values particularly for the two larger amplitudes A agree relatively well with the results for the ray-tracing model (Figure A.16e-f). Note however that a direct comparison of both data sets is not possible as only one includes the effects of the imaging lens which, through the DOF, averages over a larger depth above the surface than the results in Figure A.17b represent. Hence, for the largest deformation, a direct comparison with a Zemax ray-tracing simulation in the same setup as used from the diffraction model and for the same plane above the surface is performed. The results give excellent agreement for the ring diameter.

In summary, the test simulations including diffraction effects show that the ray-tracing model delivers accurate results, which can be used for quantitative analysis. Moreover, for the interpretation of pre-main pulse probing data, it is important to confirm that the reflective probing technique presented is also sensitive to deformations in the order of the wavelength of the probe beam.

Ray-Tracing Including Preplasma

The full model of the pump-probe experiment including the plasma distribution as a graded-index material, the imaging lens with focal length, entrance aperture and hence depth of field according to the experimental setup are implemented in the ray-tracing software Zemax². Zemax accounts for optical effects of the probe propagation in the graded-index material, such as refraction and total internal reflection, as well as the image

²Zemax LLC, Kirkland, Washington, USA

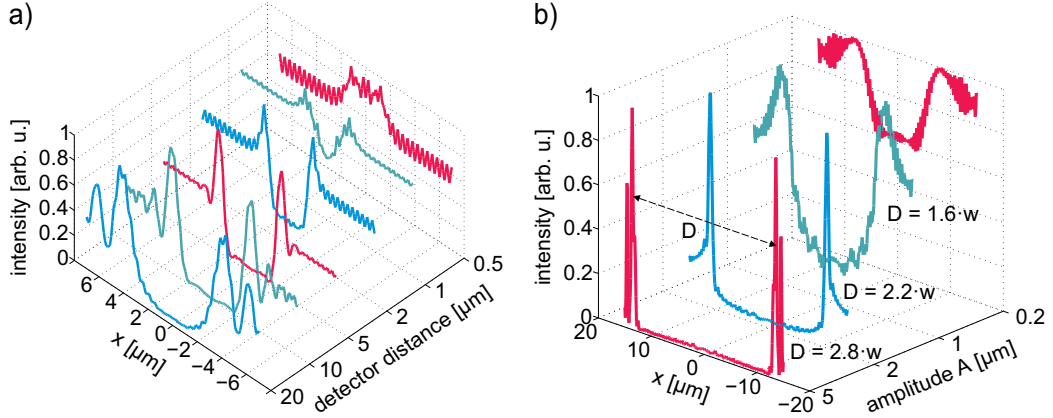


Figure A.17.: Fresnel diffraction at a surface deformation. Numerical simulation of the diffraction of a plane wave with normal incidence on a Gaussian-deformed surface using the Huygens-Fresnel principle. The plots show the intensity distribution of reflected and diffracted light on a line detector parallel to the surface. a) For deformation parameters $A = 0.2 \mu\text{m}$ and $w = 2 \mu\text{m}$, the distance surface-detector was varied between $0.5 \mu\text{m}$ and $20 \mu\text{m}$. b) Scan of the deformation amplitude for a fixed FWHM of $w = 10 \mu\text{m}$ and a surface-detector distance of $10 \mu\text{m}$. The distance of the two peaks in the distribution is given in units of the FWHM w of the Gaussian deformation.

formation including depth-of-field effects. The incoming probe beam is again simulated as a collimated beam.

Two representative plasma density distributions (S_1 , S_2) including the incoming and reflected rays and the simulation results for the surface imaging are presented in Figure A.18. The plasma distributions are set up by keeping the critical iso-density contour constant ($A = 2 \mu\text{m}$ and $w = 10 \mu\text{m}$) and varying the iso-density contour at $2.5 \times 10^{-3} n_c$ to yield different underdense distributions. The longitudinal scale length (Figure 4.8) is kept at $L_p^A = 6.2 \mu\text{m}$ for S_1 and S_2 . Note that all critical-density values refer to $\lambda = 400 \text{ nm}$.

The central aspect in the analysis including preplasma is to determine the exact plasma iso-density surface, which reflects the probe light and whose topography is hence imaged with the diagnostics. For both density distributions analyzed, the rays do not penetrate the plasma up to the critical density but are reflected through total internal reflection at lower densities. At the flanks of the plasma distribution facing the incoming rays (left sides in Figure A.18b), for example, reflection takes place at the iso-density contour $\sim 0.3 n_c^{400}$. This result is in agreement with a simple estimation: The index of refraction for the reflecting surface n_r^{refl} is calculated from Snell's law including the conditions for total internal reflection via $n_r^{refl} = \sin \alpha_{in}$, where α_{in} is the angle of incidence with respect to the local surface normal. In the given setup with a probe incidence angle of 33° measured with respect to the target surface, for α_{in} holds $\alpha_{in} \leq 57^\circ$ and hence $n_r^{refl} \leq 0.84$. Taking into account Equation (4.1) then yields $n_e^{400}/n_c^{400} \geq 0.3$ for the normalized density of the reflecting surface, in agreement with the simulation. On the opposite side of the plasma distribution, which faces away from the incoming rays (right sides in Figure A.18b), on the other hand, probe reflection takes place at lower-density surfaces due to larger incoming angles α_{in} . The reflecting surface is shifted to even lower densities when the amplitudes of the iso-density surfaces are in the order of their respective FWHM, creating a shadow area behind the peak of the plasma distribution (S_1 in Figure A.18b).

In the perpendicular plane P_2 , the rays are reflected symmetrically on both sides of the distribution's peak at $\sim 0.1 n_c^{400}$. Here $\alpha_{in} \geq 57^\circ$ holds and for instance for $\alpha_{in} = 62^\circ$ (i.e.

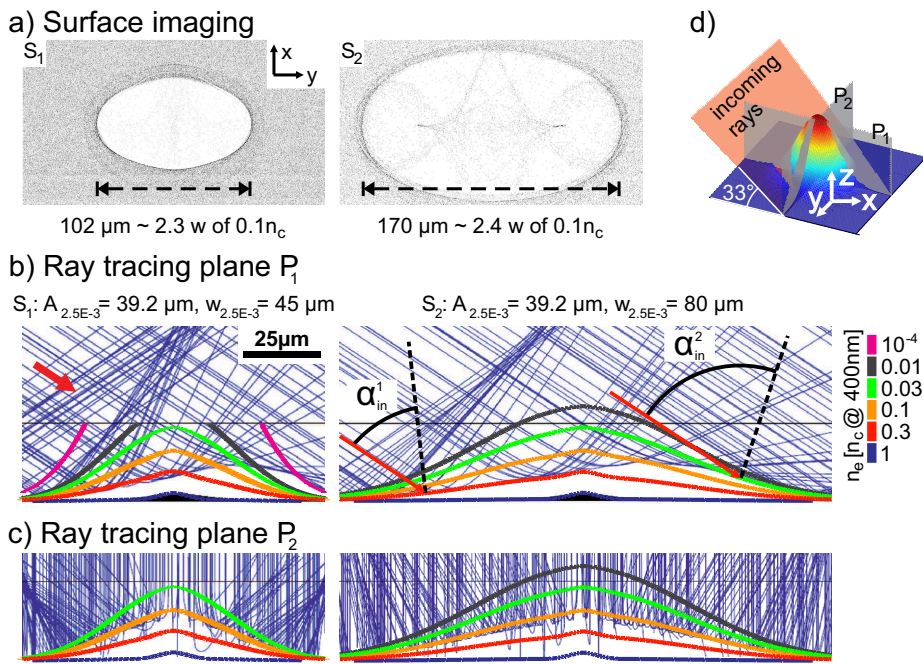


Figure A.18.: Influence of underdense plasma. a) Simulated surface imaging using the experimental parameters. b-c) Incoming and reflected rays under the consideration of preplasma in front of the reflecting surface. The Gaussian-shaped lines indicate the iso-density contour lines within the plasma. d) Simulation setup and illustration of the analyzed planes P_1 and P_2 .

considering an additional small contribution to the incidence angle from the slope of the plasma surface) follows $n_e^{400}/n_c^{400} \geq 0.22$ for the normalized density of the reflecting surface. Note that the probed surface can be chosen via the incidence angle of the probe beam. In particular, a steeper incidence angle allows to probe deeper regions of the plasma.

The fact that in plane P_2 one specific iso-density surface is probed, makes this plane optimal for quantitative evaluation. Comparison of the FWHM for the $0.1 n_c^{400}$ surfaces with the respective feature in the simulated target imaging, i.e. the major (horizontal) diameter of the void areas d_v in Figure A.18a, yields $d_v \approx 2.3 - 2.4 w_{0.1 n_c}$ for both S_1 and S_2 . That is in very good agreement with the estimation via the parabola fit presented in Figure A.16. As a last comment, the results in Figure A.18 illustrate that the position of the focal spot produced by the concave flanks of the plasma distribution within the DOF of the lens determines the ring width.

Quantitative Analysis

The presented ray-tracing studies show that the model of a (Gaussian-)deformed surface for the plasma, which reflects the probe light, can explain the ring pattern as observed in the experimental data. In order to calibrate the observed pattern, i.e. to correlate the plasma surface properties A and w with characteristic parameters of the ring feature, simulations for a variety of $\{A, w\}$ values with and without the consideration of preplasma are performed in Zemax. The results are summarized in Figure A.19a, where w is plotted on the vertical axis and A is color-coded. Open and filled circles represent data for ray-tracing without and with preplasma, respectively. The longitudinal preplasma scale length is $L_p = 3.8 \mu\text{m}$. On the x-axis, the horizontal ring diameter is plotted. According to the ray-tracing results including preplasma (Figure A.18), the horizontal ring diameter (P_2) originates from the probe beam reflection at the same iso-density surface on both sides

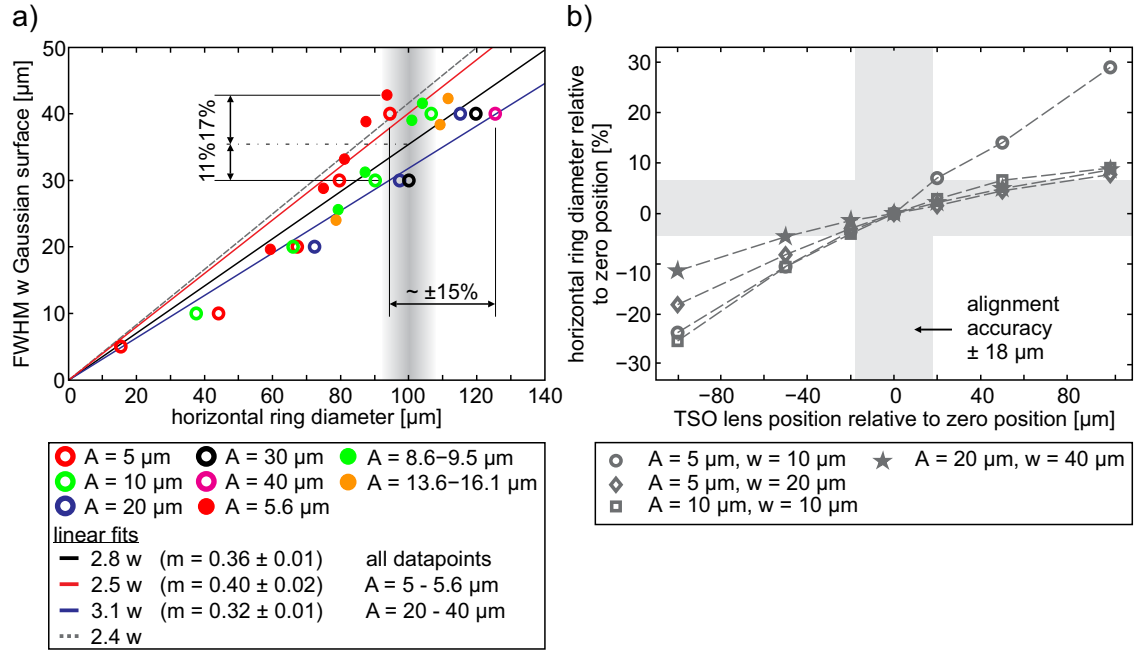


Figure A.19.: Quantitative analysis. a) Simulated data for the correlation of the horizontal ring diameter observed in the surface imaging and the FWHM w of the Gaussian deformed surface. The open and filled circles correspond to data for ray-tracing without and with preplasma, respectively. The upper dashed line represents the analytically determined value of $2.4 \cdot w$ for the horizontal ring diameter. The linear fit parameters for data points with arbitrary and selected values of A , respectively, are explained in the legend. b) Simulation of the influence of the lens position for the surface imaging on the apparent horizontal ring diameter in the data.

of the deformation and is hence suitable a for quantitative analysis. As a first important information, the data indicate the same correlation between the ring diameter and w independent from the presence of preplasma when the reflecting iso-density surface $0.1 n_c^{400}$ is evaluated in the preplasma case. Hence, the method in principle allows to quantify the reflecting surface parameters independent from the amount of preplasma present at the surface, which is mostly unknown for experimental data.

However, as already discussed in connection with the preplasma-free model, the ring diameter is mainly, but not only, influenced by the FWHM w of the surface deformation and the amplitude A plays a role as well. In order to quantify the influence, the resulting horizontal ring diameters for surface deformations with $w = 40 \mu\text{m}$ and A ranging from 5-40 μm are compared (Figure A.19a). A mean diameter of 112.3 μm and a deviation of -15% and +10% for small and large A values, respectively, is predicted. Consequentially, when A is unknown, as generally the case for experimental data, the influence of the deformation amplitude on the horizontal ring diameter translates into an uncertainty for the determination of w from the measured ring data. The uncertainty is estimated from the simulated data in Figure A.19a, assuming in this case a measured horizontal ring diameter of 100 μm with a full ring width (not FWHM) of $\pm 8 \mu\text{m}$. The latter value is derived from the experimental data (Section 4.4.1). The range of $(100 \pm 8) \mu\text{m}$ is marked in gray in the plot, showing that a number of $\{A, w\}$ combinations for the surface deformation yield horizontal ring diameter values within these limits (e.g. $\{A = 5 \mu\text{m}, w = 40 \mu\text{m}\}$ or $\{A = 30 \mu\text{m}, w = 30 \mu\text{m}\}$). Relative to the value of 36 μm for w , which follows from the fit to all simulated data points for a ring diameter of 100 μm (black line in Figure A.19a), the uncertainty for a derivation of w from the ring diameter is +17% and -11%.

The influence of the amplitude A is also quantified in the selective linear fits taking only amplitudes of $\approx 5 \mu\text{m}$ or $20\text{-}40 \mu\text{m}$ into consideration. Here, the linear fit for the small amplitude case agrees well with the analytically determined value of $2.4 \cdot w$ for the horizontal ring diameter, as expected from the discussion using the parabola model (Figure A.16). In summary, the probing method provides approximate values for the FWHM w of the deformation with an uncertainty of $< 20\%$, whereas its amplitude A cannot be inferred from the data.

Apart from the surface properties, the observed horizontal ring diameter is also sensitive to the position of the imaging lens with respect to the imaged surface. This point is relevant as the target position is reproduced for consecutive shots with an accuracy of (only) $\pm 10 \mu\text{m}$. That results in an uncertainty of $\pm 18 \mu\text{m}$ ($2/3$ of the DOF of the lens) for the distance of target surface and lens. A change of this distance firstly affects the magnification of the imaging system and secondly influences where the DOF of the lens is positioned with respect to the reflected light pattern. The latter effect is quantified in Zemax simulations for a set of surface deformations (Figure A.19b). The gray areas mark the range covered by the alignment accuracy, showing that the expected effect is $\approx \pm 5\%$ and hence much smaller than the uncertainty resulting from the geometric shape, as discussed above. The magnification changes by only 0.5% for a change in the surface-lens distance as large as $500 \mu\text{m}$, confirming that the in- or decrease in the horizontal ring diameter is mainly due to the change in which part of the reflected light is sampled in the DOF of the lens.

A.5. Raw Data from the Front Surface Probing

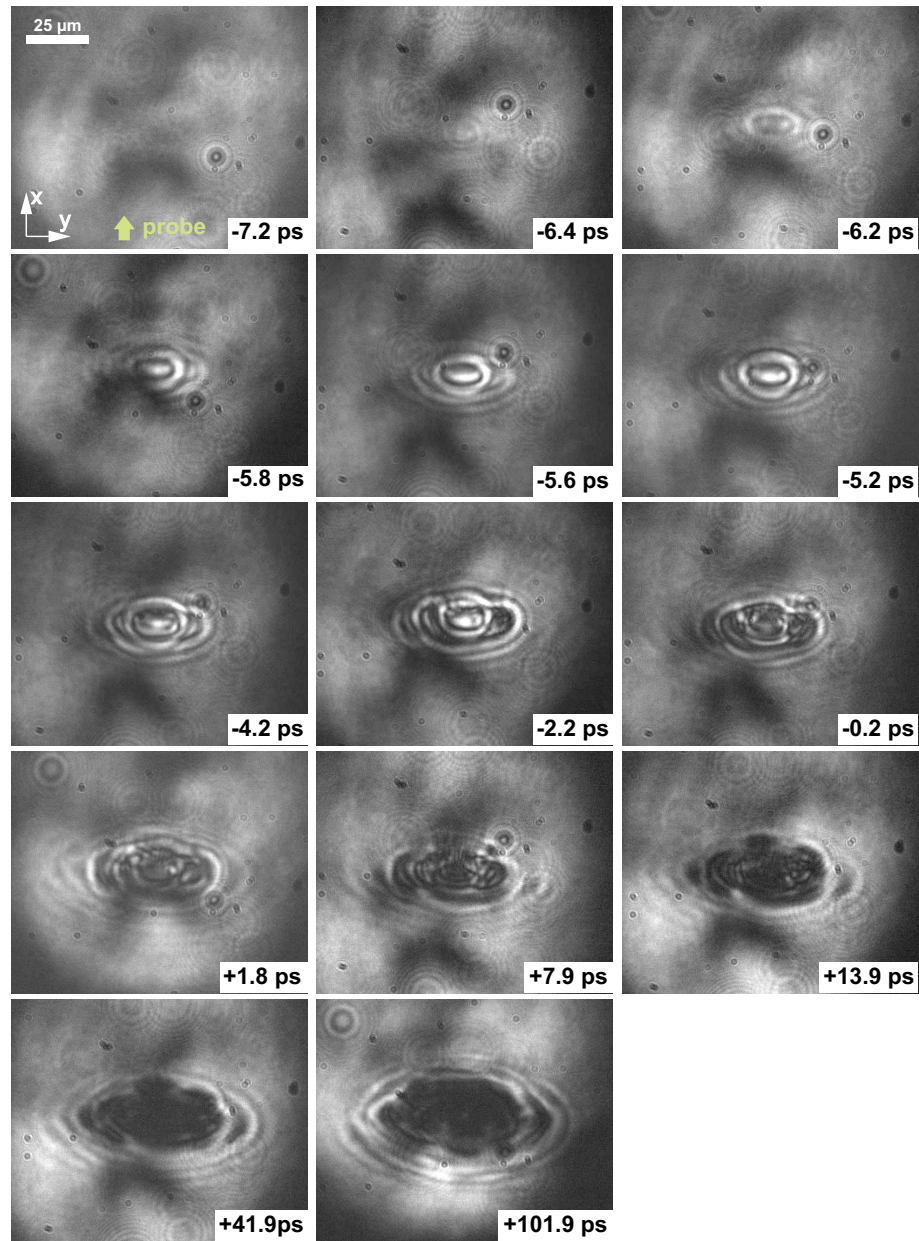


Figure A.20.: Pump-probe delay scan for Al. Raw data from the front surface imaging for an Al target irradiated at a pump pulse peak intensity of $3 \cdot 10^{16} \text{ W/cm}^2$. The probe beam direction is from bottom to top, represented by the yellow arrow in the -7.2 ps image. The color scale is individually optimized for each image to yield the best visibility of the signatures.

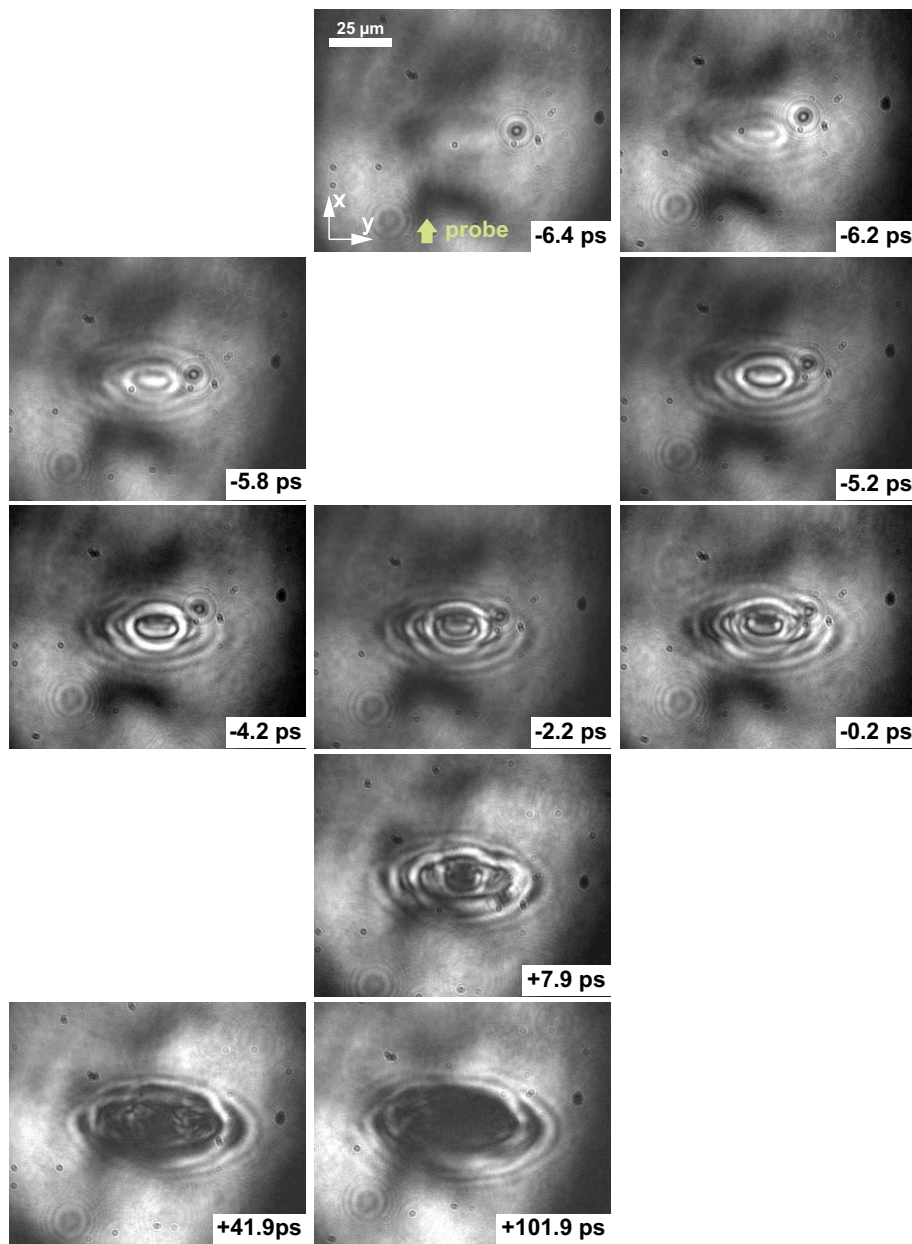


Figure A.21.: Pump-probe delay scan for Au. Raw data from the front surface imaging for an Au target irradiated at a pump pulse peak intensity of $3 \cdot 10^{16} \text{ W/cm}^2$. The probe beam direction is from bottom to top, represented by the yellow arrow in the -7.2 ps image. The color scale is individually optimized for each image to yield the best visibility of the signatures.

A.6. Modeling the Target Reflectivity Using Fresnel's Equations

For the case of a solid surface or a step-gradient interface between vacuum and an overdense plasma, the optical Fresnel equations [230] can be applied [48] to relate the reflectivity of a medium to its (complex) index of refraction n_r . To that end, the frequency-dependent (laser frequency ω) complex dielectric function

$$\epsilon(\omega) = 1 - \frac{\omega_p^2}{\omega(\omega + i\nu)} = 1 - \frac{\left(\frac{\omega_p}{\omega}\right)^2}{1 + \left(\frac{\nu}{\omega}\right)^2} + i \cdot \left(\frac{\nu}{\omega}\right) \cdot \frac{\left(\frac{\omega_p}{\omega}\right)^2}{1 + \left(\frac{\nu}{\omega}\right)^2} \quad (\text{A.3})$$

with the plasma frequency ω_p and the electron-ion/phonon collision frequency ν is expressed as [48]

$$\epsilon(\omega) = n_r^2 = (n_1 + i \cdot n_2)^2 = (n_1^2 - n_2^2) + i \cdot 2n_1n_2 =: n_R + i \cdot n_I \quad . \quad (\text{A.4})$$

For the Fresnel equation for the reflectivity of an s-polarized wave impinging onto a vacuum-solid interface under normal incidence then holds for instance [231]:

$$R_s = \frac{I_s^{refl}}{I_s^{in}} = \frac{(1 - \alpha)^2 + \beta^2}{(1 + \alpha)^2 + \beta^2} \quad \text{with} \quad \left\{ \begin{array}{l} \alpha \\ \beta \end{array} \right\} = \pm \frac{1}{\sqrt{2}} \sqrt{n_R \pm \sqrt{n_R^2 + n_I^2}} \quad . \quad (\text{A.5})$$

I_s^{in} and I_s^{refl} are the incoming and reflected light intensity, respectively. The dependence of the reflectivity on the target parameters electron density n_e , charge state Z (in the case of a plasma) and (electron) temperature T is indirectly given via the parameters $\omega_p = f(n_e)$ and $\nu = f(n_e, Z, T_e)$ (Equation (2.9) and Equation (2.8)).

Of particular interest is the temperature-dependence of the collision frequency ν . For a solid holds $\nu_{e-l} \propto T_{lat}^2$, the lattice temperature, because electrons are scattered by phonons [177]. In an ideal plasma, on the other hand, holds $\nu_{e-i} \propto T_e^{-3/2}$, representing collisions of electrons and ions in the plasma ([177], Section 2.2.1).

Figure A.22 summarizes angularly resolved values for the reflectivity of p- and s-polarized light, R_p and R_s , for Al and Au for different parameters ν . The reflectivity decreases with increasing collision frequency ν .

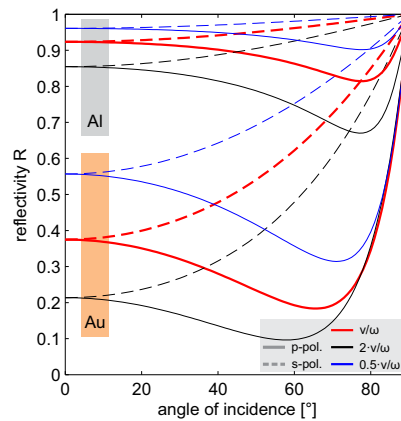


Figure A.22.: Fresnel reflectivity of Al and Au for s- and p-polarized light at $\lambda = 400$ nm. The reflectivity of Al and Au at $\lambda = 400$ nm ($\omega = 3.1$ eV) follows from Equation (A.4) with $\nu^{Al} = 0.59$ eV, $\omega_p^{Al} = 15.13$ eV and $\nu^{Au} = 8.50$ eV, $\omega_p^{Au} = 12.95$ eV [231, 232, 233]. Full and dashed lines represent values for R_p and R_s , respectively. Reflectivity values for different collision frequencies ν are color-coded.

Bibliography

- [1] M. Baumann, S. M. Bentzen, W. Doerr, M. C. Joiner, M. Saunders, I. F. Tannock, and H. D. Thames. The translational research chain: Is it delivering the goods? *International Journal of Radiation Oncology Biology Physics*, 49(2):345–351, 2001.
- [2] S. F. Keevil. Physics and medicine: A historical perspective. *The Lancet*, 379(9825):1517–1524, 2012.
- [3] R. Wilson. Radiological use of fast protons. *Radiology*, 47:487–491, 1946.
- [4] U. Linz and J. Alonso. What will it take for laser driven proton accelerators to be applied to tumor therapy? *Physical Review Special Topics - Accelerators and Beams*, 10:094801, 2007.
- [5] S. V. Bulanov and V. S. Khoroshkov. Feasibility of using laser ion accelerators in proton therapy. *Plasma Physics Reports*, 28(5):453–456, 2001.
- [6] S. V. Bulanov, T. Zh. Esirkepov, V. S. Khoroshkov, A. V. Kuznetsov, and F. Pegoraro. Oncological hadrontherapy with laser ion accelerators. *Physics Letters A*, 299:240–247, 2002.
- [7] E. Fourkal, J. S. Li, M. Ding, T. Tajima, and C. M. Ma. Particle selection for laser-accelerated proton therapy feasibility study. *Medical physics*, 30(7):1660–1670, 2003.
- [8] V. Malka, S. Fritzler, E. Lefebvre, E. D’Humières, R. Ferrand, G. Grillon, C. Albarete, S. Meyroneinc, J.-P. Chambaret, A. Antonetti, and D. Hulin. Practicability of protontherapy using compact laser systems. *Medical Physics*, 31(6):1587–1592, 2004.
- [9] C.-M. Ma, I. Veltchev, E. Fourkal, J.S. Li, W. Luo, J. Fan, T. Lin, and Pollack. Development of a laser-driven proton accelerator for cancer therapy. *Laser Physics*, 16:639–646, 2006.
- [10] K. W. D. Ledingham and W. Galster. Laser-driven particle and photon beams and some applications. *New Journal of Physics*, 12:045005, 2010.
- [11] S. P. Hatchett, C. G. Brown, T. E. Cowan, E. A. Henry, J. S. Johnson, M. H. Key, J. A. Koch, A. B. Langdon, B. F. Lasinski, R. W. Lee, A. J. Mackinnon, D. M. Pennington, M. D. Perry, T. W. Phillips, M. Roth, T. C. Sangster, M. S. Singh, R. A. Snavely, M. A. Stoyer, S. C. Wilks, and K. Yasuike. Electron, photon, and ion beams from the relativistic interaction of Petawatt laser pulses with solid targets. *Physics of Plasmas*, 7:2076, 2000.
- [12] R. A. Snavely, M. H. Key, S. P. Hatchett, T. E. Cowan, M. Roth, T. W. Phillips, M. A. Stoyer, E. A. Henry, T. C. Sangster, M. S. Singh, S. C. Wilks, A. MacKinnon, A. Offenberger, D. M. Pennington, K. Yasuike, A. B. Langdon, B. F. Lasinski,

- J. Johnson, M. D. Perry, and E. M. Campbell. Intense high-energy proton beams from Petawatt-laser irradiation of solids. *Physical Review Letters*, 85(14):2945–2948, 2000.
- [13] S. C. Wilks, A. B. Langdon, T. E. Cowan, M. Roth, M. Singh, S. Hatchett, M. H. Key, D. Pennington, A. MacKinnon, and R. A. Snavely. Energetic proton generation in ultra-intense laser-solid interactions. *Physics of Plasmas*, 8:542–549, 2001.
- [14] M. M. Murnane, H. C. Kapteyn, M. D. Rosen, and R. W. Falcone. Ultrafast x-ray pulses from laser-produced plasmas. *Science*, 251(4993):531–536, 1991.
- [15] T. E. Cowan, J. Fuchs, H. Ruhl, A. Kemp, P. Audebert, M. Roth, R. Stephens, I. Barton, A. Blazevic, E. Brambrink, J. Cobble, J. Fernandez, J. C. Gauthier, M. Geissel, M. Hegelich, J. Kaae, S. Karsch, G. P. Le Sage, S. Letzring, M. Manclossi, S. Meyroneinc, A. Newkirk, H. Pepin, and N. R. Legalloudec. Ultralow emittance, multi-MeV proton beams from a laser virtual-cathode plasma accelerator. *Physical Review Letters*, 92(20):204801, 2004.
- [16] H. Daido, M. Nishiuchi, and A. S. Pirozhkov. Review of laser-driven ion sources and their applications. *Reports on Progress in Physics*, 75(5):056401, 2012.
- [17] M. Borghesi, A. Schiavi, D. H. Campbell, M. G. Haines, O. Willi, A. J. MacKinnon, L. A. Gizzi, M. Galimberti, R. J. Clarke, and H. Ruhl. Proton imaging: a diagnostic for inertial confinement fusion/fast ignitor studies. *Plasma Physics and Controlled Fusion*, 43(12A):A267–A276, 2001.
- [18] K. L. Lancaster, S. Karsch, H. Habara, F. N. Beg, E. L. Clark, R. Freeman, M. H. Key, J. A. King, R. Kodama, K. Krushelnick, K. W. D. Ledingham, P. McKenna, C. D. Murphy, P. a. Norreys, R. Stephens, C. Stöckl, Y. Toyama, M. S. Wei, and M. Zepf. Characterization of ${}^7\text{Li}(p,n){}^7\text{Be}$ neutron yields from laser produced ion beams for fast neutron radiography. *Physics of Plasmas*, 11(7):3404, 2004.
- [19] M. Roth, T. E. Cowan, M. H. Key, S. P. Hatchett, C. Brown, W. Fountain, J. Johnson, D. M. Pennington, R. A. Snavely, S. C. Wilks, K. Yasuike, H. Ruhl, F. Pegoraro, S. V. Bulanov, E. M. Campbell, M. D. Perry, and H. Powell. Fast ignition by intense laser-accelerated proton beams. *Physical Review Letters*, 86(3):436–439, 2001.
- [20] S. Fritzler, V. Malka, G. Grillon, J. P. Rousseau, F. Burgy, E. Lefebvre, E. D’Humières, P. McKenna, and K. W. D. Ledingham. Proton beams generated with high-intensity lasers: Applications to medical isotope production. *Applied Physics Letters*, 83(15):3039–3041, 2003.
- [21] T. Burris-Mog, K. Harres, F. Nürnberg, S. Busold, M. Bussmann, O. Deppert, G. Hoffmeister, M. Joost, M. Sobiella, A. Tauschwitz, B. Zielbauer, V. Bagnoud, T. Herrmannsdoerfer, M. Roth, and T. E. Cowan. Laser accelerated protons captured and transported by a pulse power solenoid. *Physical Review Special Topics - Accelerators and Beams*, 14(12):7–13, 2011.
- [22] S. Busold, D. Schumacher, O. Deppert, C. Brabetz, S. Frydrych, F. Kroll, M. Joost, H. Al-Omari, A. Blažević, B. Zielbauer, I. Hofmann, V. Bagnoud, T. E. Cowan, and M. Roth. Focusing and transport of high-intensity multi-MeV proton bunches from a compact laser-driven source. *Physical Review Special Topics - Accelerators and Beams*, 16(10):1–6, 2013.

-
- [23] U. Masood, M. Bussmann, T. E. Cowan, W. Enghardt, L. Karsch, F. Kroll, U. Schramm, and J. Pawelke. A compact solution for ion beam therapy with laser accelerated protons. *Applied Physics B*, 117(1):41–52, 2014.
- [24] C. Richter, L. Karsch, Y. Dammene, S. D. Kraft, J. Metzkes, U. Schramm, M. Schürer, M. Sobiella, A. Weber, K. Zeil, and J. Pawelke. A dosimetric system for quantitative cell irradiation experiments with laser-accelerated protons. *Physics in Medicine and Biology*, 56(6):1529–1543, 2011.
- [25] S. D. Kraft, C. Richter, K. Zeil, M. Baumann, E. Beyreuther, S. Bock, M. Bussmann, T. E. Cowan, Y. Dammene, W. Enghardt, U. Helbig, L. Karsch, T. Kluge, L. Laschinsky, E. Lessmann, J. Metzkes, D. Naumburger, R. Sauerbrey, M. Schürer, M. Sobiella, J. Woithe, U. Schramm, and J. Pawelke. Dose-dependent biological damage of tumour cells by laser-accelerated proton beams. *New Journal of Physics*, 12(8):85003, 2010.
- [26] K. Zeil, M. Baumann, E. Beyreuther, T. Burris-Mog, T. E. Cowan, W. Enghardt, L. Karsch, S. D. Kraft, L. Laschinsky, J. Metzkes, D. Naumburger, M. Oppelt, C. Richter, R. Sauerbrey, M. Schürer, U. Schramm, and J. Pawelke. Dose-controlled irradiation of cancer cells with laser-accelerated proton pulses. *Applied Physics B*, 110(4):437–444, 2012.
- [27] K. Zeil, J. Metzkes, T. Kluge, M. Bussmann, T. E. Cowan, S. D. Kraft, R. Sauerbrey, and U. Schramm. Direct observation of prompt pre-thermal laser ion sheath acceleration. *Nature Communications*, 3:874, 2012.
- [28] K. Ogura, M. Nishiuchi, A. S. Pirozhkov, T. Tanimoto, A. Sagisaka, T. Zh. Esirkepov, M. Kando, T. Shizuma, T. Hayakawa, H. Kiriya, T. Shimomura, S. Kondo, S. Kanazawa, Y. Nakai, H. Sasao, F. Sasao, Y. Fukuda, H. Sakaki, M. Kanasaki, A. Yogo, S. V. Bulanov, P. R. Bolton, and K. Kondo. Proton acceleration to 40 MeV using a high intensity, high contrast optical parametric chirped-pulse amplification Ti:sapphire hybrid laser system. *Optics Letters*, 37(14):2868–2870, 2012.
- [29] A. Henig, D. Kiefer, K. Markey, D. C. Gautier, K. A. Flippo, S. Letzring, R. P. Johnson, T. Shimada, L. Yin, B. J. Albright, K. J. Bowers, J. C. Fernández, S. G. Rykovanov, H.-C. Wu, M. Zepf, D. Jung, V. Kh. Liechtenstein, J. Schreiber, D. Habs, and B. M. Hegelich. Enhanced Laser-Driven Ion Acceleration in the Relativistic Transparency Regime. *Physical Review Letters*, 103(4):45002, 2009.
- [30] S. A. Gaillard, T. Kluge, K. A. Flippo, M. Bussmann, B. Gall, T. Lockard, M. Geissel, D. T. Offermann, M. Schollmeier, Y. Sentoku, and T. E. Cowan. Increased laser-accelerated proton energies via direct laser-light-pressure acceleration of electrons in microcone targets. *Physics of Plasmas*, 18:056710, 2011.
- [31] T. Kluge, S. A. Gaillard, K. A. Flippo, T. Burris-Mog, W. Enghardt, B. Gall, M. Geissel, A. Helm, S. D. Kraft, T. Lockard, J. Metzkes, D. T. Offermann, M. Schollmeier, U. Schramm, K. Zeil, M. Bussmann, and T. E. Cowan. High proton energies from cone targets: Electron acceleration mechanisms. *New Journal of Physics*, 14:023038, 2012.
- [32] K. Zeil, J. Metzkes, T. Kluge, M. Bussmann, T. E. Cowan, S. D. Kraft, R. Sauerbrey, B. Schmidt, M. Zier, and U. Schramm. Robust energy enhancement of ultrashort

- pulse laser accelerated protons from reduced mass targets. *Plasma Physics and Controlled Fusion*, 56(8):084004, 2014.
- [33] A. Macchi, M. Borghesi, and M. Passoni. Ion acceleration by superintense laser-plasma interaction. *Reviews of Modern Physics*, 85(2):751–793, 2013.
- [34] A. Yogo, K. Sato, M. Nishikino, M. Mori, T. Teshima, H. Numasaki, M. Murakami, Y. Demizu, S. Akagi, S. Nagayama, K. Ogura, A. Sagisaka, S. Orimo, M. Nishiuchi, A. S. Pirozhkov, M. Ikegami, M. Tampo, H. Sakaki, M. Suzuki, I. Daito, Y. Oishi, H. Sugiyama, H. Kiriya, H. Okada, S. Kanazawa, S. Kondo, T. Shimomura, Y. Nakai, M. Tanoue, H. Sasao, D. Wakai, P. R. Bolton, and H. Daido. Application of laser-accelerated protons to the demonstration of DNA double-strand breaks in human cancer cells. *Applied Physics Letters*, 94(18):181502, 2009.
- [35] A. Yogo, T. Maeda, T. Hori, H. Sakaki, K. Ogura, M. Nishiuchi, A. Sagisaka, H. Kiriya, H. Okada, S. Kanazawa, T. Shimomura, Y. Nakai, M. Tanoue, F. Sasao, P. R. Bolton, M. Murakami, T. Nomura, S. Kawanishi, and K. Kondo. Measurement of relative biological effectiveness of protons in human cancer cells using a laser-driven quasimonoenergetic proton beamline. *Applied Physics Letters*, 98(5):053701, 2011.
- [36] F. Fiorini, D. Kirby, M. Borghesi, D. Doria, J. C. G. Jaynes, K. F. Kakolee, S. Kar, S. Kaur, K. J. Kirby, M. J. Merchant, and S. Green. Dosimetry and spectral analysis of a radiobiological experiment using laser-driven proton beams. *Physics in Medicine and Biology*, 56(21):6969–82, 2011.
- [37] D. Doria, K. F. Kakolee, S. Kar, S. K. Litt, F. Fiorini, H. Ahmed, S. Green, J. C. G. Jaynes, J. Kavanagh, D. Kirby, K. J. Kirkby, C. L. Lewis, M. J. Merchant, G. Nersisyan, R. Prasad, K. M. Prise, G. Schettino, M. Zepf, and M. Borghesi. Biological effectiveness on live cells of laser driven protons at dose rates exceeding 10^9 Gy/s. *AIP Advances*, 2(1):011209, 2012.
- [38] D. Strickland and G. Mourou. Compression of amplified chirped optical pulses. *Optics Communications*, 55(6):447–449, 1985.
- [39] T. M. Jeong and J. Lee. Femtosecond petawatt laser. *Annalen der Physik*, 526(3):157–172, 2014.
- [40] P. Mora. Plasma expansion into a vacuum. *Physical Review Letters*, 90(18):185002, 2003.
- [41] J. Schreiber, F. Bell, F. Grüner, U. Schramm, M. Geissler, M. Schnürer, S. Ter-Avetisyan, B. M. Hegelich, J. Cobble, E. Brambrink, J. Fuchs, P. Audebert, and D. Habs. Analytical model for ion acceleration by high-intensity laser pulses. *Physical Review Letters*, 97(4):45005, 2006.
- [42] J. Fuchs, P. Antici, E. D’Humières, E. Lefebvre, M. Borghesi, E. Brambrink, C. A. Cecchetti, M. Kaluza, V. Malka, M. Manclossi, S. Meyroneinc, P. Mora, J. Schreiber, T. Toncian, H. Pépin, and P. Audebert. Laser-driven proton scaling laws and new paths towards energy increase. *Nature Physics*, 2:48–54, 2006.
- [43] T. Kluge, T. E. Cowan, A. Debus, U. Schramm, K. Zeil, and M. Bussmann. Electron temperature scaling in laser interaction with solids. *Physical Review Letters*, 107:1–5, 2011.

-
- [44] Y. Ping, R. Shepherd, B. F. Lasinski, M. Tabak, H. Chen, H. K. Chung, K. B. Fournier, S. B. Hansen, A. Kemp, D. A. Liedahl, K. Widmann, S. C. Wilks, W. Rozmus, and M. Sherlock. Absorption of short laser pulses on solid targets in the ultra-relativistic regime. *Physical Review Letters*, 100(8):085004, 2008.
- [45] M. Kaluza, J. Schreiber, M. I. K. Santala, G. D. Tsakiris, K. Eidmann, J. Meyer-ter-Vehn, and K. J. Witte. Influence of the laser prepulse on proton acceleration in thin-foil experiments. *Physical Review Letters*, 93(4):45003, 2004.
- [46] J. Metzkes, T. Kluge, K. Zeil, M. Bussmann, S. D. Kraft, T. E. Cowan, and U. Schramm. Experimental observation of transverse modulations in laser-driven proton beams. *New Journal of Physics*, 16:023008, 2014.
- [47] M. Protopapas, C. H. Keitel, and P. L. Knight. Atomic physics with super-high intensity lasers. *Reports on Progress in Physics*, 60:389–486.
- [48] P. Gibbon. *Short pulse laser interactions with matter*. Imperial College Press, 2005.
- [49] G. Mainfray and C. Manus. Multiphoton ionization of atoms. *Reports on Progress in Physics*, 54(10):1333–1372, 1991.
- [50] T. Brabec and F. Krausz. Intense few-cycle laser fields : Frontiers of nonlinear optics. *Reviews of Modern Physics*, 72(2):545–591, 2000.
- [51] K. B. Wharton, C. D. Boley, A. M. Komashko, A. M. Rubenchik, J. Zweiback, J. Crane, G. Hays, T. E. Cowan, and T. Ditmire. Effects of nonionizing prepulses in high-intensity laser-solid interactions. *Physical Review E*, 64:025401(R), 2001.
- [52] F. Lindau, O. Lundh, A. Persson, P. McKenna, K. Osvay, D. Batani, and C. G. Wahlström. Laser-accelerated protons with energy-dependent beam direction. *Physical Review Letters*, 95:175002, 2005.
- [53] O. Lundh, F. Lindau, A. Persson, C. G. Wahlström, P. McKenna, and D. Batani. Influence of shock waves on laser-driven proton acceleration. *Physical Review E*, 76(2):26404, 2007.
- [54] K. Zeil, S. D. Kraft, S. Bock, M. Bussmann, T. E. Cowan, T. Kluge, J. Metzkes, T. Richter, R. Sauerbrey, and U. Schramm. The scaling of proton energies in ultrashort pulse laser plasma acceleration. *New Journal of Physics*, 12:045015, 2010.
- [55] B. N. Chichkov, C. Momma, S. Nolte, F. von Alvensleben, and A. Tünnermann. Femtosecond, picosecond and nanosecond laser ablation of solids. *Applied Physics A Materials Science & Processing*, 63:109–115, 1996.
- [56] E. G. Gamaly, A. V. Rode, B. Luther-Davies, and V. T. Tikhonchuk. Ablation of solids by femtosecond lasers: Ablation mechanism and ablation thresholds for metals and dielectrics. *Physics of Plasmas*, 9(3):949, 2002.
- [57] W. L. Kruer. *The physics of laser plasma interactions*. Westview Press, 2003.
- [58] F. Brunel. Not-so-resonant, resonant absorption. *Physical Review Letters*, 59(1):6–9, 1987.
- [59] P. Gibbon and A. R. Bell. Collisionless absorption in sharp-edged plasmas. *Physical Review Letters*, 68(10):1535–1538, 1992.

-
- [60] Y. Sentoku, T. E. Cowan, A. Kemp, and H. Ruhl. High energy proton acceleration in interaction of short laser pulse with dense plasma target. *Physics of Plasmas*, 10(5):2009, 2003.
- [61] S. Y. Chen, A. Maksimchuk, and D. Umstadter. Experimental observation of relativistic nonlinear Thomson scattering. *Nature*, 396:653–655, 1998.
- [62] S. Palaniyappan, B. M. Hegelich, H.-C. Wu, D. Jung, D. C. Gautier, L. Yin, B. J. Albright, R. P. Johnson, T. Shimada, S. Letzring, D. T. Offermann, J. Ren, C. Huang, R. Hörlein, B. Dromey, J. C. Fernandez, and R. C. Shah. Dynamics of relativistic transparency and optical shuttering in expanding overdense plasmas. *Nature Physics*, 8(10):763–769, 2012.
- [63] W. L. Kruer and Kent Estabrook. $J \times B$ heating by very intense laser light. *Physics of Fluids*, 28:430, 1985.
- [64] S. D. Baton, J. J. Santos, F. Amiranoff, H. Popescu, L. Gremillet, M. Koenig, E. Martinolli, O. Guilbaud, C. Rousseaux, M. Rabec Le Gloahec, T. Hall, D. Batani, E. Perelli, F. Scianitti, and T. E. Cowan. Evidence of ultrashort electron bunches in laser-plasma interactions at relativistic intensities. *Physical Review Letters*, 91(10):105001, 2003.
- [65] G. Malka and J. L. Miquel. Experimental confirmation of ponderomotive-force electrons produced by an ultrarelativistic laser pulse on a solid target. *Physical Review Letters*, 77:75–78, 1996.
- [66] S. C. Wilks, W. L. Kruer, M. Tabak, and A. B. Langdon. Absorption of ultra-intense laser pulses. *Physical Review Letters*, 69(9):1383–1386, 1992.
- [67] H. Chen, S. C. Wilks, W. L. Kruer, P. K. Patel, and R. Shepherd. Hot electron energy distributions from ultraintense laser solid interactions. *Physics of Plasmas*, 16:020705, 2009.
- [68] F. N. Beg, A. R. Bell, A. E. Dangor, C. N. Danson, A. P. Fews, M. E. Glinsky, B. A. Hammel, P. Lee, and M. Tatarakis. A study of picosecond laser – solid interactions up to 10^{19} W/cm². *Physics of Plasmas*, 4(2):447–457, 1997.
- [69] M. G. Haines, M. S. Wei, F. N. Beg, and R. B. Stephens. Hot-electron temperature and laser-light absorption in fast ignition. *Physical Review Letters*, 102:045008, 2009.
- [70] M. J. Berger, J. S. Coursey, M. A. Zucker, and J. Chang. ESTAR: Stopping-power and range tables for electrons. *NIST, Physical Measurement Laboratory*, 2015.
- [71] L. Volpe, D. Batani, G. Birindelli, A. Morace, P. Carpeggiani, M. H. Xu, F. Liu, Y. Zhang, Z. Zhang, X. X. Lin, F. Liu, S. J. Wang, P. F. Zhu, L. M. Meng, Z. H. Wang, Y. T. Li, Z. M. Sheng, Z. Y. Wei, J. Zhang, J. J. Santos, and C. Spindloe. Propagation of a short-pulse laser-driven electron beam in matter. *Physics of Plasmas*, 20:033105, 2013.
- [72] A. R. Bell, J. R. Davies, S. Guerin, and H. Ruhl. Fast-electron transport in high-intensity short-pulse laser - solid experiments. *Plasma Physics and Controlled Fusion*, 39(5):653–659, 1997.

-
- [73] J. Fuchs, T. E. Cowan, P. Audebert, H. Ruhl, L. Gremillet, A. Kemp, M. Allen, A. Blazevic, J. C. Gauthier, M. Geissel, M. Hegelich, S. Karsch, P. Parks, M. Roth, Y. Sentoku, R. Stephens, and E. M. Campbell. Spatial uniformity of laser-accelerated ultrahigh-current MeV electron propagation in metals and insulators. *Physical Review Letters*, 91(25):255002, 2003.
- [74] P. Norreys, D. Batani, S. Baton, F. N. Beg, R. Kodama, P. M. Nilson, P. Patel, F. Pérez, J. J. Santos, R. H. H. Scott, V. T. Tikhonchuk, M. Wei, and J. Zhang. Fast electron energy transport in solid density and compressed plasma. *Nuclear Fusion*, 54:054004, 2014.
- [75] A. R. Bell, J. R. Davies, and S. M. Guerin. Magnetic field in short-pulse high-intensity laser-solid experiments. *Phys. Rev. E*, 58(2):2471–2473, 1998.
- [76] Y. Sentoku, E. D’Humières, L. Romagnani, P. Audebert, and J. Fuchs. Dynamic control over mega-ampere electron currents in metals using ionization-driven resistive magnetic fields. *Physical Review Letters*, 107(13):135005, 2011.
- [77] Y. Sentoku, K. Mima, P. Kaw, and K. Nishikawa. Anomalous resistivity resulting from MeV-electron transport in overdense plasma. *Physical Review Letters*, 90:155001, 2003.
- [78] L. Yin, B. J. Albright, B. M. Hegelich, K. J. Bowers, K. A. Flippo, T. J. T. Kwan, and J. C. Fernández. Monoenergetic and GeV ion acceleration from the laser breakout afterburner using ultrathin targets. *Physics of Plasmas*, 14(5):056706, 2007.
- [79] B. J. Albright, L. Yin, K. J. Bowers, B. M. Hegelich, K. A. Flippo, T. J. T. Kwan, and J. C. Fernández. Relativistic Buneman instability in the laser breakout afterburner. *Physics of Plasmas*, 14:094502, 2007.
- [80] C. A. J. Palmer, J. Schreiber, S. R. Nagel, N. P. Dover, C. Bellei, F. N. Beg, S. Bott, R. J. Clarke, A. E. Dangor, S. M. Hassan, P. Hilz, D. Jung, S. Kneip, S. P. D. Mangles, K. L. Lancaster, A. Rehman, A. P. L. Robinson, C. Spindloe, J. Szerypo, M. Tatarakis, M. Yeung, M. Zepf, and Z. Najmudin. Rayleigh-taylor instability of an ultrathin foil accelerated by the radiation pressure of an intense laser. *Physical Review Letters*, 108:225002, 2012.
- [81] K. Quinn, L. Romagnani, B. Ramakrishna, G. Sarri, M. E. Dieckmann, P. A. Wilson, J. Fuchs, L. Lancia, A. Pipahl, T. Toncian, O. Willi, R. J. Clarke, M. Notley, A. Macchi, and M. Borghesi. Weibel-induced filamentation during an ultrafast laser-driven plasma expansion. *Physical Review Letters*, 108:135001, 2012.
- [82] D. an der Brügge, N. Kumar, A. Pukhov, and C. Rödel. Influence of surface waves on plasma high-order harmonic generation. *Physical Review Letters*, 108:125002, 2012.
- [83] F. F. Chen. *Introduction to Plasma Physics and Controlled Fusion*, volume 1: Plasma Physics. Springer US, 1984.
- [84] O. Buneman. Dissipation of currents in ionized media. *Physical Review*, 115(3):503–517, 1959.
- [85] E. S. Weibel. Spontaneously growing transverse waves in a plasma due to an anisotropic velocity distribution. *Physical Review Letters*, 2(3):83–84, 1959.

-
- [86] B. D. Fried. Mechanism for Instability of Transverse Plasma Waves. *Physics of Fluids*, 2(3):337, 1959.
- [87] A. Stockem. *Plasmainstabilitäten in anisotropen Gegenstromverteilungen*. PhD thesis, Ruhr-Universität Bochum, 2009.
- [88] A. Stockem, M. Lazar, P. K. Shukla, and A. Smolyakov. A comparative study of the filamentation and Weibel instabilities and their cumulative effect. II. Weakly relativistic beams. *Journal of Plasma Physics*, 75(4):529, 2009.
- [89] Y. Sentoku, K. Mima, Shin-ichi Kojima, and H. Ruhl. Magnetic instability by the relativistic laser pulses in overdense plasmas. *Physics of Plasmas*, 7(2):689, 2000.
- [90] M. Honda, J. Meyer-ter-Vehn, and A. Pukhov. Collective stopping and ion heating in relativistic-electron-beam transport for fast ignition. *Physical Review Letters*, 85(10):2128–2131, 2000.
- [91] L. Gremillet, F. Amiranoff, S. Baton, J.-C. Gauthier, M. Koenig, E. Martinolli, F. Pisani, G. Bonnaud, C. Lebourg, C. Rousseaux, C. Toupin, A. Antonicci, D. Batani, A. Bernardinello, T. Hall, D. Scott, P. Norreys, H. Bandulet, and H. Pépin. Time-resolved observation of ultrahigh intensity laser-produced electron jets propagating through transparent solid targets. *Physical Review Letters*, 83(24):5015–5018, 1999.
- [92] M. Tatarakis, F. N. Beg, E. L. Clark, A. E. Dangor, R. D. Edwards, R. G. Evans, T. J. Goldsack, K. W. D. Ledingham, P. A. Norreys, M. A. Sinclair, M.-S. Wei, M. Zepf, and K. Krushelnick. Propagation instabilities of high-intensity laser-produced electron beams. *Physical Review Letters*, 90:175001, 2003.
- [93] M. S. Wei, F. N. Beg, E. L. Clark, A. E. Dangor, R. G. Evans, A. Gopal, K. W. D. Ledingham, P. McKenna, P. A. Norreys, M. Tatarakis, M. Zepf, and K. Krushelnick. Observations of the filamentation of high-intensity laser-produced electron beams. *Physical Review E*, 70:056412, 2004.
- [94] R. Jung, J. Osterholz, K. Löwenbrück, S. Kiselev, G. Pretzler, A. Pukhov, O. Willi, S. Kar, M. Borghesi, W. Nazarov, S. Karsch, R. Clarke, and D. Neely. Study of electron-beam propagation through preionized dense foam plasmas. *Physical Review Letters*, 94:195001, 2005.
- [95] S. Mondal, V. Narayanan, W. J. Ding, A. D. Lad, B. Hao, S. Ahmad, W. M. Wang, Z. M. Sheng, S. Sengupta, P. Kaw, A. Das, and G. R. Kumar. Direct observation of turbulent magnetic fields in hot, dense laser produced plasmas. *Proceedings of the National Academy of Sciences*, 109(21):8011–8015, 2012.
- [96] M. Allen, P. K. Patel, A. Mackinnon, D. Price, S. Wilks, and E. Morse. Direct experimental evidence of back-surface ion acceleration from laser-irradiated gold foils. *Physical Review Letters*, 93:265004, 2004.
- [97] J. Fuchs, Y. Sentoku, S. Karsch, J. Cobble, P. Audebert, A. Kemp, A. Nikroo, P. Antici, E. Brambrink, A. Blazevic, E. M. Campbell, J. C. Fernández, J.-C. Gauthier, M. Geissel, M. Hegelich, H. Pépin, H. Popescu, N. Renard-LeGalloudec, M. Roth, J. Schreiber, R. Stephens, and T. E. Cowan. Comparison of laser ion acceleration from the front and rear surfaces of thin foils. *Physical Review Letters*, 94:045004, 2005.

-
- [98] M. Borghesi, J. Fuchs, S. V. Bulanov, A. J. MacKinnon, P. K. Patel, and M. Roth. Fast ion generation by high-intensity laser irradiation of solid targets and applications. *Fusion Science and Technology*, 49:412–439, 2006.
- [99] F. Nürnberg, M. Schollmeier, E. Brambrink, A. Blažević, D. C. Carroll, K. Flippo, D. C. Gautier, M. Geibel, K. Harres, B. M. Hegelich, O. Lundh, K. Markey, P. McKenna, D. Neely, J. Schreiber, and M. Roth. Radiochromic film imaging spectroscopy of laser-accelerated proton beams. *Review of Scientific Instruments*, 80:033301, 2009.
- [100] J. Schreiber, M. Kaluza, F. Grüner, U. Schramm, B. M. Hegelich, J. Cobble, M. Geissler, E. Brambrink, J. Fuchs, P. Audebert, D. Habs, and K. Witte. Source-size measurements and charge distributions of ions accelerated from thin foils irradiated by high-intensity laser pulses. *Applied Physics B*, 79(8):1041–1045, 2004.
- [101] C. Perego, A. Zani, D. Batani, and M. Passoni. Extensive comparison among Target Normal Sheath Acceleration theoretical models. *Nuclear Instruments and Methods in Physics Research, Section A: Accelerators, Spectrometers, Detectors and Associated Equipment*, 653(1):89–93, 2011.
- [102] A. Zani, A. Sgattoni, and M. Passoni. Parametric investigations of target normal sheath acceleration experiments. *Nuclear Instruments and Methods in Physics Research, Section A: Accelerators, Spectrometers, Detectors and Associated Equipment*, 653(1):94–97, 2011.
- [103] J. Schreiber. *Ion Acceleration driven by High-Intensity Laser Pulses*. PhD thesis, Ludwig-Maximilians-Universität München, 2006.
- [104] K. Zeil. *Efficient laser-driven proton acceleration in the ultra-short pulse regime*. PhD thesis, Technische Universität Dresden, 2013.
- [105] P. Mora. Thin-foil expansion into a vacuum. *Physical Review E*, 72(5):056401, 2005.
- [106] J. Fuchs, Y. Sentoku, E. D’Humières, T. E. Cowan, J. Cobble, P. Audebert, A. Kemp, A. Nikroo, P. Antici, E. Brambrink, A. Blazevic, E. M. Campbell, J. C. Fernandez, J.-C. Gauthier, M. Geissel, M. Hegelich, S. Karsch, H. Popescu, N. Renard-LeGalloudec, M. Roth, J. Schreiber, R. Stephens, and H. Pépin. Comparative spectra and efficiencies of ions laser-accelerated forward from the front and rear surfaces of thin solid foils. *Physics of Plasmas*, 14:053105, 2007.
- [107] P. McKenna, D. C. Carroll, O. Lundh, F. Nürnberg, K. Markey, S. Bandyopadhyay, D. Batani, R. G. Evans, R. Jafer, S. Kar, D. Neely, D. Pepler, M. N. Quinn, R. Redaelli, M. Roth, C. G. Wahlström, X. H. Yuan, and M. Zepf. Effects of front surface plasma expansion on proton acceleration in ultraintense laser irradiation of foil targets. *Laser and Particle Beams*, 26:591–596, 2008.
- [108] S. Buffechoux, J. Psikal, M. Nakatsutsumi, L. Romagnani, A. Andreev, K. Zeil, M. Amin, P. Antici, T. Burris-Mog, A. Compant-La-Fontaine, E. D’Humières, S. Fourmaux, S. Gaillard, F. Gobet, F. Hannachi, S. Kraft, A. Mancic, C. Plaisir, G. Sarri, M. Tarisien, T. Toncian, U. Schramm, M. Tampo, P. Audebert, O. Willi, T. E. Cowan, H. Pépin, V. Tikhonchuk, M. Borghesi, and J. Fuchs. Hot electrons transverse refluxing in ultraintense laser-solid interactions. *Physical Review Letters*, 105:15005, 2010.

-
- [109] J. S. Green, D. C. Carroll, C. Brenner, B. Dromey, P. S. Foster, S. Kar, Y. T. Li, K. Markey, P. McKenna, D. Neely, A. P. L. Robinson, M. J. V. Streeter, M. Tolley, C. G. Wahlström, M. H. Xu, and M. Zepf. Enhanced proton flux in the MeV range by defocused laser irradiation. *New Journal of Physics*, 12:085012, 2010.
- [110] K. Markey, P. McKenna, C. M. Brenner, D. C. Carroll, M. M. Günther, K. Harres, S. Kar, K. Lancaster, F. Nürnberg, M. N. Quinn, A. P. L. Robinson, M. Roth, M. Zepf, and D. Neely. Spectral enhancement in the double pulse regime of laser proton acceleration. *Physical Review Letters*, 105:195008, 2010.
- [111] C. M. Brenner, A. P. L. Robinson, K. Markey, R. H. H. Scott, R. J. Gray, M. Rosinski, O. Deppert, J. Badziak, D. Batani, J. R. Davies, S. M. Hassan, K. L. Lancaster, K. Li, I. O. Musgrave, P. A. Norreys, J. Pasley, M. Roth, H. P. Schlenvoigt, C. Spindloe, M. Tatarakis, T. Winstone, J. Wolowski, D. Wyatt, P. McKenna, and D. Neely. High energy conversion efficiency in laser-proton acceleration by controlling laser-energy deposition onto thin foil targets. *Applied Physics Letters*, 104:081123, 2014.
- [112] M. Hegelich, S. Karsch, G. Pretzler, D. Habs, K. Witte, W. Guenther, M. Allen, A. Blazevic, J. Fuchs, J. C. Gauthier, M. Geissel, P. Audebert, T. Cowan, and M. Roth. MeV ion jets from short-pulse-laser interaction with thin foils. *Physical Review Letters*, 89:85002, 2002.
- [113] D. C. Carroll, O. Tresca, R. Prasad, L. Romagnani, P. S. Foster, P. Gallegos, S. Ter-Avetisyan, J. S. Green, M. J. V. Streeter, N. Dover, C. A. J. Palmer, C. M. Brenner, F. H. Cameron, K. E. Quinn, J. Schreiber, A. P. L. Robinson, T. Baeva, M. N. Quinn, X. H. Yuan, Z. Najmudin, M. Zepf, D. Neely, M. Borghesi, and P. McKenna. Carbon ion acceleration from thin foil targets irradiated by ultrahigh-contrast, ultraintense laser pulses. *New Journal of Physics*, 12:045020, 2010.
- [114] P. K. Patel, A. J. Mackinnon, M. H. Key, T. E. Cowan, M. E. Foord, M. Allen, D. F. Price, H. Ruhl, P. T. Springer, and R. Stephens. Isochoric heating of solid-density matter with an ultrafast proton beam. *Physical Review Letters*, 91:125004, 2003.
- [115] S. Kar, K. Markey, P. T. Simpson, C. Bellei, J. S. Green, S. R. Nagel, S. Kneip, D. C. Carroll, B. Dromey, L. Willingale, E. L. Clark, P. McKenna, Z. Najmudin, K. Krushelnick, P. Norreys, R. J. Clarke, D. Neely, M. Borghesi, and M. Zepf. Dynamic control of laser-produced proton beams. *Physical Review Letters*, 100:105004, 2008.
- [116] T. Bartal, M. E. Foord, C. Bellei, M. H. Key, K. A. Flippo, S. A. Gaillard, D. T. Offermann, P. K. Patel, L. C. Jarrott, D. P. Higginson, M. Roth, A. Otten, D. Kraus, R. B. Stephens, H. S. McLean, E. M. Giraldez, M. S. Wei, D. C. Gautier, and F. N. Beg. Focusing of short-pulse high-intensity laser-accelerated proton beams. *Nature Physics*, 8(2):139–142, 2011.
- [117] S. Kar, K. Markey, M. Borghesi, D. C. Carroll, P. McKenna, D. Neely, M. N. Quinn, and M. Zepf. Ballistic focusing of polyenergetic protons driven by petawatt laser pulses. *Physical Review Letters*, 106:225003, 2011.
- [118] M. Nishiuchi, A. S. Pirozhkov, H. Sakaki, K. Ogura, T. Zh. Esirkepov, T. Tanimoto, M. Kanasaki, A. Yogo, T. Hori, A. Sagisaka, Y. Fukuda, Y. Matsumoto, S. Entani,

- S. Sakai, C. M. Brenner, D. Neely, T. Yamauchi, S. V. Bulanov, and K. Kondo. Quasi-monochromatic pencil beam of laser-driven protons generated using a conical cavity target holder. *Physics of Plasmas*, 19:030706, 2012.
- [119] J. S. Green, N. P. Dover, M. Borghesi, C. M. Brenner, F. H. Cameron, D. C. Carroll, P. S. Foster, P. Gallegos, G. Gregori, P. McKenna, C. D. Murphy, Z. Najmudin, C. A. J. Palmer, R. Prasad, L. Romagnani, K. E. Quinn, J. Schreiber, M. J. V. Streeter, S. Ter-Avetisyan, O. Tresca, M. Zepf, and D. Neely. Enhanced proton beam collimation in the ultra-intense short pulse regime. *Plasma Physics and Controlled Fusion*, 56:084001, 2014.
- [120] H. Schwoerer, S. Pfotenhauer, O. Jäckel, K. U. Amthor, B. Liesfeld, W. Ziegler, R. Sauerbrey, K. W. D. Ledingham, and T. Esirkepov. Laser-plasma acceleration of quasi-monoenergetic protons from microstructured targets. *Nature*, 439(7075):445–448, 2006.
- [121] B. M. Hegelich, B. J. Albright, J. Cobble, K. Flippo, S. Letzring, M. Paffett, H. Ruhl, J. Schreiber, R. K. Schulze, and J. C. Fernandez. Laser acceleration of quasi-monoenergetic MeV ion beams. *Nature*, 439(7075):441–444, 2006.
- [122] S. M. Pfotenhauer, O. Jäckel, A. Sachtleben, J. Polz, W. Ziegler, H.-P. Schlenvoigt, K.-U. Amthor, M. C. Kaluza, K. W. D. Ledingham, R. Sauerbrey, P. Gibbon, A. P. L. Robinson, and H. Schwoerer. Spectral shaping of laser generated proton beams. *New Journal of Physics*, 10:033034, 2008.
- [123] F. Dollar, T. Matsuoka, G. M. Petrov, A. G. R. Thomas, S. S. Bulanov, V. Chvykov, J. Davis, G. Kalinchenko, C. McGuffey, L. Willingale, V. Yanovsky, A. Maksimchuk, and K. Krushelnick. Control of energy spread and dark current in proton and ion beams generated in high-contrast laser solid interactions. *Physical Review Letters*, 107:065003, 2011.
- [124] S. Ter-Avetisyan, M. Schnürer, P. V. Nickles, M. Kalashnikov, E. Risse, T. Sokollik, W. Sandner, A. Andreev, and V. Tikhonchuk. Quasimonoenergetic deuteron bursts produced by ultraintense laser pulses. *Physical Review Letters*, 96:145006, 2006.
- [125] A. Henig, D. Kiefer, M. Geissler, S. Rykovanov, R. Ramis, R. Hörlein, J. Osterhoff, Zs. Major, L. Veisz, S. Karsch, F. Krausz, D. Habs, and J. Schreiber. Laser-driven shock acceleration of ion beams from spherical mass-limited targets. *Physical Review Letters*, 102:095002, 2009.
- [126] T. Sokollik, M. Schnürer, S. Steinke, P. Nickles, W. Sandner, M. Amin, T. Toncian, O. Willi, and A. Andreev. Directional laser-driven ion acceleration from microspheres. *Physical Review Letters*, 103:135003, 2009.
- [127] T. Sokollik, T. Paasch-Colberg, K. Gorling, U. Eichmann, M. Schnürer, S. Steinke, P. V. Nickles, A. Andreev, and W. Sandner. Laser-driven ion acceleration using isolated mass-limited spheres. *New Journal of Physics*, 12:113013, 2010.
- [128] T. Toncian, M. Swantusch, M. Toncian, O. Willi, A. A. Andreev, and K. Y. Platonov. Optimal proton acceleration from lateral limited foil sections and different laser pulse durations at relativistic intensity. *Physics of Plasmas*, 18:043105, 2011.

-
- [129] O. Tresca, D. C. Carroll, X. H. Yuan, B. Aurand, V. Bagnoud, C. M. Brenner, M. Coury, J. Fils, R. J. Gray, T. Kühl, C. Li, Y. T. Li, X. X. Lin, M. N. Quinn, R. G. Evans, B. Zielbauer, M. Roth, D. Neely, and P. McKenna. Controlling the properties of ultraintense laserproton sources using transverse refluxing of hot electrons in shaped mass-limited targets. *Plasma Physics and Controlled Fusion*, 53:105008, 2011.
- [130] S. M. Pfotenhauer, O. Jäckel, J. Polz, S. Steinke, H.-P. Schlenvoigt, J. Heymann, A. P. L. Robinson, and M. C. Kaluza. A cascaded laser acceleration scheme for the generation of spectrally controlled proton beams. *New Journal of Physics*, 12:103009, 2010.
- [131] M. Roth, A. Blazevic, M. Geissel, T. Schlegel, T. E. Cowan, M. Allen, J. C. Gauthier, P. Audebert, J. Fuchs, J. Meyer-ter-Vehn, M. Hegelich, S. Karsch, and A. Pukhov. Energetic ions generated by laser pulses: A detailed study on target properties. *Physical Review Special Topics - Accelerators and Beams*, 5:061301, 2002.
- [132] M. Manclossi, J. J. Santos, D. Batani, J. Faure, A. Debayle, V. T. Tikhonchuk, and V. Malka. Study of ultraintense laser-produced fast-electron propagation and filamentation in insulator and metal foil targets by optical emission diagnostics. *Physical Review Letters*, 96:125002, 2006.
- [133] P. Antici, P. Audebert, M. Borghesi, T. Cowan, L. Gremillet, Y. Sentoku, and J. Fuchs. Transport of hot electron currents in solid targets irradiated by high intensity short laser pulses. *Journal of Physics: Conference Series*, 244:022016, 2010.
- [134] L. A. Gizzi, S. Betti, E. Förster, D. Giulietti, S. Höfer, P. Köster, L. Labate, R. Löttsch, A. P. L. Robinson, and I. Uschmann. Role of resistivity gradient in laser-driven ion acceleration. *Physical Review Special Topics - Accelerators and Beams*, 14:011301, 2011.
- [135] P. McKenna, A. P. L. Robinson, D. Neely, M. P. Desjarlais, D. C. Carroll, M. N. Quinn, X. H. Yuan, C. M. Brenner, M. Burza, M. Coury, P. Gallegos, R. J. Gray, K. L. Lancaster, Y. T. Li, X. X. Lin, O. Tresca, and C.-G. Wahlström. Effect of lattice structure on energetic electron transport in solids irradiated by ultraintense laser pulses. *Physical Review Letters*, 106:185004, 2011.
- [136] P. Antici, J. Fuchs, E. D’Humières, E. Lefebvre, M. Borghesi, E. Brambrink, C. A. Cecchetti, S. Gaillard, L. Romagnani, Y. Sentoku, T. Toncian, O. Willi, P. Audebert, and H. Pépin. Energetic protons generated by ultrahigh contrast laser pulses interacting with ultrathin targets. *Physics of Plasmas*, 14:030701, 2007.
- [137] T. Dzelzainis, G. Nersisyan, D. Riley, L. Romagnani, H. Ahmed, A. Bigongiari, M. Borghesi, D. Doria, B. Dromey, M. Makita, S. White, S. Kar, D. Marlow, B. Ramakrishna, G. Sarri, M. Zaka-Ul-Islam, M. Zepf, and C. L. S. Lewis. The TARANIS laser: A multi-Terawatt system for laser-plasma investigations. *Laser and Particle Beams*, 28(3):451–461, 2010.
- [138] D. Neely, P. Foster, A. Robinson, F. Lindau, O. Lundh, A. Persson, C. G. Wahlström, and P. McKenna. Enhanced proton beams from ultrathin targets driven by high contrast laser pulses. *Applied Physics Letters*, 89(2):13–16, 2006.

- [139] T. Ceccotti, A. Lévy, H. Popescu, F. Réau, P. D'Oliveira, P. Monot, J. P. Geindre, E. Lefebvre, and Ph. Martin. Proton acceleration with high-intensity ultrahigh-contrast laser pulses. *Physical Review Letters*, 99(18):1–4, 2007.
- [140] J. Fuchs, C. A. Cecchetti, M. Borghesi, T. Grismayer, E. D'Humières, P. Antici, S. Atzeni, P. Mora, A. Pipahl, L. Romagnani, A. Schiavi, Y. Sentoku, T. Toncian, P. Audebert, and O. Willi. Laser-foil acceleration of high-energy protons in small-scale plasma gradients. *Physical Review Letters*, 99:015002, 2007.
- [141] L. Robson, P. T. Simpson, R. J. Clarke, K. W. D. Ledingham, F. Lindau, O. Lundh, T. McCanny, P. Mora, D. Neely, C. Wahlstrom, M. Zepf, and P. McKenna. Scaling of proton acceleration driven by petawatt-laser-plasma interactions. *Nature Physics*, 3:58–62, 2007.
- [142] J. R. Davies. Laser absorption by overdense plasmas in the relativistic regime. *Plasma Physics and Controlled Fusion*, 51:014006, 2008.
- [143] M. N. Quinn, D. C. Carroll, X. H. Yuan, M. Borghesi, R. J. Clarke, R. G. Evans, J. Fuchs, P. Gallegos, L. Lancia, K. Quinn, A. P. L. Robinson, L. Romagnani, G. Sarri, C. Spindloe, P. A. Wilson, D. Neely, and P. McKenna. On the investigation of fast electron beam filamentation in laser-irradiated solid targets using multi-MeV proton emission. *Plasma Physics and Controlled Fusion*, 53:124012, 2011.
- [144] C. Iaconis and I. A. Walmsley. Spectral phase interferometry for direct electric-field reconstruction of ultrashort optical pulses. *Optics Letters*, 23(10):792–794, 1998.
- [145] T. Oksenhendler, S. Coudreau, N. Forget, V. Crozatier, S. Grabielle, R. Herzog, O. Gobert, and D. Kaplan. Self-referenced spectral interferometry. *Applied Physics B*, 99:7–12, 2010.
- [146] A. Moulet, S. Grabielle, C. Cornaggia, N. Forget, and T. Oksenhendler. Single-shot, high-dynamic-range measurement of sub-15 fs pulses by self-referenced spectral interferometry. *Optics Letters*, 35:3856–3858, 2010.
- [147] X. Liu, R. Wagner, A. Maksimchuk, E. Goodman, J. Workman, D. Umstadter, and A. Migus. Nonlinear temporal diffraction and frequency shifts resulting from pulse shaping in chirped-pulse amplification systems. *Optics Letters*, 20(10):1163–1165, 1995.
- [148] N. V. Didenko, A. V. Konyashchenko, A. P. Lutsenko, and S. Yu. Tenyakov. Contrast degradation in a chirped-pulse amplifier due to generation of prepulses by postpulses. *Optics Express*, 16(5):3178–3190, 2008.
- [149] J. H. Bin, W. J. Ma, K. Allinger, H. Y. Wang, D. Kiefer, S. Reinhardt, P. Hilz, K. Khrennikov, S. Karsch, X. Q. Yan, F. Krausz, T. Tajima, D. Habs, and J. Schreiber. On the small divergence of laser-driven ion beams from nanometer thick foils. *Physics of Plasmas*, 20:073113, 2013.
- [150] T. Kluge, W. Enghardt, S. D. Kraft, U. Schramm, K. Zeil, T. E. Cowan, and M. Bussmann. Enhanced laser ion acceleration from mass-limited foils. *Physics of Plasmas*, 17:123103, 2010.

-
- [151] A. Link, R. R. Freeman, D. W. Schumacher, and L. D. van Woerkom. Effects of target charging and ion emission on the energy spectrum of emitted electrons. *Physics of Plasmas*, 18:053107, 2011.
- [152] A. Seidel. Kalibrierung eines Detektors für laserbeschleunigte Elektronen. Diploma thesis, Technische Universität Dresden, 2011.
- [153] Y. Sentoku and A. J. Kemp. Numerical methods for particle simulations at extreme densities and temperatures: Weighted particles, relativistic collisions and reduced currents. *Journal of Computational Physics*, 227(14):6846–6861, 2008.
- [154] A. Bigongiari, M. Raynaud, C. Riconda, A. Héron, and A. Macchi. Efficient laser-overdense plasma coupling via surface plasma waves and steady magnetic field generation. *Physics of Plasmas*, 18:102701, 2011.
- [155] T. Kluge, C. Gutt, L. G. Huang, J. Metzkes, U. Schramm, M. Bussmann, and T. E. Cowan. Using x-ray free-electron lasers for probing of complex interaction dynamics of ultra-intense lasers with solid matter. *Physics of Plasmas*, 21:033110, 2014.
- [156] T. Kluge, J. Metzkes, K. Zeil, M. Bussmann, U. Schramm, and T. E. Cowan. Two surface plasmon decay of plasma oscillations. *Physics of Plasmas*, 22:064502, 2015.
- [157] P. K. Kaw. Surface Waves on a Plasma Half-Space. *Physics of Fluids*, 13(7):1784, 1970.
- [158] A. Macchi, F. Cornolti, F. Pegoraro, T. V. Liseikina, H. Ruhl, and V. A. Vshivkov. Surface oscillations in overdense plasmas irradiated by ultrashort laser pulses. *Physical Review Letters*, 87:205004, 2001.
- [159] L. O. Silva, R. A. Fonseca, J. W. Tonge, W. B. Mori, and J. M. Dawson. On the role of the purely transverse weibel instability in fast ignitor scenarios. *Physics of Plasmas*, 9:2458, 2002.
- [160] V. M. Ovchinnikov, D. W. Schumacher, M. McMahon, E. A. Chowdhury, C. D. Chen, A. Morace, and R. R. Freeman. Effects of preplasma scale length and laser intensity on the divergence of laser-generated hot electrons. *Physical Review Letters*, 110:065007, 2013.
- [161] P. Leblanc and Y. Sentoku. Scaling of resistive guiding of laser-driven fast-electron currents in solid targets. *Physical Review E*, 89:023109, 2014.
- [162] J. C. Adam, A. Héron, and G. Laval. Dispersion and transport of energetic particles due to the interaction of intense laser pulses with overdense plasmas. *Physical Review Letters*, 97:205006, 2006.
- [163] A. Debayle, J. J. Honrubia, E. D’Humières, and V. T. Tikhonchuk. Divergence of laser-driven relativistic electron beams. *Physical Review E*, 82:036405, 2010.
- [164] H. Schmitz, R. Lloyd, and R. G. Evans. Collisional particle-in-cell modelling of the generation and control of relativistic electron beams produced by ultra-intense laser pulses. *Plasma Physics and Controlled Fusion*, 54:085016, 2012.

- [165] M. Storm, A. A. Solodov, J. F. Myatt, D. D. Meyerhofer, C. Stoeckl, C. Mileham, R. Betti, P. M. Nilson, T. C. Sangster, W. Theobald, and Chunlei Guo. High-current, relativistic electron-beam transport in metals and the role of magnetic collimation. *Physical Review Letters*, 102:235004, 2009.
- [166] D. Margarone, O. Klimo, I. J. Kim, J. Prokpek, J. Limpouch, T. M. Jeong, T. Mocek, J. Pkal, H. T. Kim, J. Proka, K. H. Nam, L. Tolcova, I. W. Choi, S. K. Lee, J. H. Sung, T. J. Yu, and G. Korn. Laser-driven proton acceleration enhancement by nanostructured foils. *Physical Review Letters*, 109:234801, 2012.
- [167] M. Passoni, A. Zani, A. Sgattoni, D. Dellasega, A. Macchi, I. Prencipe, V. Floquet, P. Martin, T. V. Liseykina, and T. Ceccotti. Energetic ions at moderate laser intensities using foam-based multi-layered targets. *Plasma Physics and Controlled Fusion*, 56:045001, 2014.
- [168] J. Bin, W. Ma, and H. Wang. Relativistic plasma optics enabled by near-critical density nanostructured material. *arXiv*, 1402.4301, 2014.
- [169] P. Antici, J. Fuchs, M. Borghesi, L. Gremillet, T. Grismayer, Y. Sentoku, E. D’Humieres, C. A. Cecchetti, A. Mancic, A. C. Pipahl, T. Toncian, O. Willi, P. Mora, and P. Audebert. Hot and cold electron dynamics following high-intensity laser matter interaction. *Physical Review Letters*, 101:105004, 2008.
- [170] O. Jackel, J. Polz, S. M. Pfotenhauer, H.-P. Schlenvoigt, H. Schwoerer, and M. C. Kaluza. All-optical measurement of the hot electron sheath driving laser ion acceleration from thin foils. *New Journal of Physics*, 12:103027, 2010.
- [171] Y. Ping, A. J. Kemp, L. Divol, M. H. Key, P. K. Patel, K. U. Akli, F. N. Beg, S. Chawla, C. D. Chen, R. R. Freeman, D. Hey, D. P. Higginson, L. C. Jarrott, G. E. Kemp, A. Link, H. S. McLean, H. Sawada, R. B. Stephens, D. Turnbull, B. Westover, and S. C. Wilks. Dynamics of Relativistic Laser-Plasma Interaction on Solid Targets. *Physical Review Letters*, 109:145006, 2012.
- [172] S. Mondal, Amit D. Lad, Saima Ahmed, V. Narayanan, J. Pasley, P. P. Rajeev, A. P. L. Robinson, and G. Ravindra Kumar. Doppler spectrometry for ultrafast temporal mapping of density dynamics in laser-induced plasmas. *Physical Review Letters*, 105:105002, 2010.
- [173] Gourab Chatterjee, Prashant Kumar Singh, Saima Ahmed, A. P. L. Robinson, Amit D. Lad, Sudipta Mondal, V. Narayanan, Iti Srivastava, Nikhil Koratkar, John Pasley, A. K. Sood, and G. Ravindra Kumar. Macroscopic transport of mega-ampere electron currents in aligned carbon-nanotube arrays. *Physical Review Letters*, 108:235005, 2012.
- [174] E. Martinolli, M. Koenig, F. Amiranoff, S. D. Baton, L. Gremillet, J. J. Santos, T. A. Hall, C. Rousseaux, and D. Batani. Fast electron heating of a solid target in ultrahigh-intensity laser pulse interaction. *Physical Review E*, 70:055402(R), 2004.
- [175] Prashant Kumar Singh, Y. Q. Cui, Gourab Chatterjee, Amitava Adak, W. M. Wang, Saima Ahmed, Amit D. Lad, Z. M. Sheng, and G. Ravindra Kumar. Direct observation of ultrafast surface transport of laser-driven fast electrons in a solid target. *Physics of Plasmas*, 20:110701, 2013.

- [176] M. Cerchez, R. Jung, J. Osterholz, T. Toncian, O. Willi, P. Mulser, and H. Ruhl. Absorption of ultrashort laser pulses in strongly overdense targets. *Physical Review Letters*, 100:245001, 2008.
- [177] E. G. Gamaly. The physics of ultra-short laser interaction with solids at non-relativistic intensities. *Physics Reports*, 508:91–243, 2011.
- [178] D. W. Schumacher, G. E. Kemp, A. Link, R. R. Freeman, and L. D. Van Woerkom. The shaped critical surface in high intensity laser plasma interactions. *Physics of Plasmas*, 18:013102, 2011.
- [179] M. A. Olmstead, N. M. Amer, and S. Kohn. Photothermal Displacement Spectroscopy: An Optical Probe for Solids and Surfaces. *Applied Physics A*, 32:141–154, 1983.
- [180] A. S. Pirozhkov, I. W. Choi, J. H. Sung, S. K. Lee, T. J. Yu, T. M. Jeong, I. J. Kim, N. Hafz, C. M. Kim, K. H. Pae, Y.-C. Noh, D.-K. Ko, J. Lee, A. P. L. Robinson, P. Foster, S. Hawkes, M. Streeter, C. Spindloe, P. McKenna, D. C. Carroll, C.-G. Wahlstrom, M. Zepf, D. Adams, B. Dromey, K. Markey, S. Kar, Y. T. Li, M. H. Xu, H. Nagatomo, M. Mori, A. Yogo, H. Kiriyaama, K. Ogura, A. Sagisaka, S. Orimo, M. Nishiuchi, H. Sugiyama, T. Zh. Esirkepov, H. Okada, S. Kondo, S. Kanazawa, Y. Nakai, A. Akutsu, T. Motomura, M. Tanoue, T. Shimomura, M. Ikegami, I. Daito, M. Kando, T. Kameshima, P. Bolton, S. V. Bulanov, H. Daido, and D. Neely. Diagnostic of laser contrast using target reflectivity. *Applied Physics Letters*, 94:241102, 2009.
- [181] G. E. Kemp, A. Link, Y. Ping, H. S. McLean, P. K. Patel, R. R. Freeman, D. W. Schumacher, H. F. Tiedje, Y. Y. Tsui, R. Ramis, and R. Fedosejevs. On specular reflectivity measurements in high and low-contrast relativistic laser-plasma interactions. *Physics of Plasmas*, 22:013110, 2015.
- [182] M. J. V. Streeter, P. S. Foster, F. H. Cameron, M. Borghesi, C. Brenner, D. C. Carroll, E. Divall, N. P. Dover, B. Dromey, P. Gallegos, J. S. Green, S. Hawkes, C. J. Hooker, S. Kar, P. McKenna, S. R. Nagel, Z. Najmudin, C. A. J. Palmer, R. Prasad, K. E. Quinn, P. P. Rajeev, A. P. L. Robinson, L. Romagnani, J. Schreiber, C. Spindloe, S. Ter-Avetisyan, O. Tresca, M. Zepf, and D. Neely. Relativistic plasma surfaces as an efficient second harmonic generator. *New Journal of Physics*, 13:023041, 2011.
- [183] U. Teubner and P. Gibbon. High-order harmonics from laser-irradiated plasma surfaces. *Reviews of Modern Physics*, 81:445–479, 2009.
- [184] H. Kiriyaama, M. Mori, Y. Nakai, T. Shimomura, M. Tanoue, A. Akutsu, H. Okada, T. Motomura, S. Kondo, S. Kanazawa, A. Sagisaka, J. Ma, I. Daito, H. Kotaki, H. Daido, S. Bulanov, T. Kimura, and T. Tajima. Generation of high-contrast and high-intensity laser pulses using an OPCPA preamplifier in a double CPA, Ti:sapphire laser system. *Optics Communications*, 282:625–628, 2009.
- [185] C. Thauray and F. Quéré. High-order harmonic and attosecond pulse generation on plasma mirrors: basic mechanisms. *Journal of Physics B: Atomic, Molecular and Optical Physics*, 43:213001, 2010.

- [186] J. J. Santos, A. Debayle, Ph. Nicolai, V. Tikhonchuk, M. Manclossi, D. Batani, A. Guemnie-Tafo, J. Faure, V. Malka, and J. J. Honrubia. Fast-electron transport and induced heating in aluminum foils. *Physics of Plasmas*, 14(10):103107, 2007.
- [187] L. Veisz, W. Theobald, T. Feurer, H. Schworer, I. Uschmann, O. Renner, and R. Sauerbrey. Three-halves harmonic emission from femtosecond laser produced plasmas with steep density gradients. *Physics of Plasmas*, 11(6):3311, 2004.
- [188] M. Nakatsutsumi, R. Kodama, Y. Aglitskiy, K. U. Akli, D. Batani, S. D. Baton, F. N. Beg, A. Benuzzi-Mounaix, S. N. Chen, D. Clark, J. R. Davies, R. R. Freeman, J. Fuchs, J. S. Green, C. D. Gregory, P. Guillou, H. Habara, R. Heathcote, D. S. Hey, K. Highbarger, P. Jaanimagi, M. H. Key, M. Koenig, K. Krushelnick, K. L. Lancaster, B. Loupias, T. Ma, A. Macphee, A. J. Mackinnon, K. Mima, A. Morace, H. Nakamura, P. A. Norryes, D. Piazza, C. Rousseaux, R. B. Stephans, M. Storm, M. Tampo, W. Theobald, L. van Woerkom, R. L. Weber, M. S. Wei, and N. C. Woolsey. Heating of solid target in electron refluxing dominated regime with ultra-intense laser. *Journal of Physics: Conference Series*, 112:022063, 2008.
- [189] B. T. Bowes, H. Langhoff, M. C. Downer, M. Wilcox, B. Hou, J. Nees, and G. Mourou. Femtosecond microscopy of radial energy transport in a micrometer-scale aluminum plasma excited at relativistic intensity. *Optics Letters*, 31(1):116, 2006.
- [190] H. Langhoff, B. T. Bowes, M. C. Downer, Bixue Hou, and J. A. Nees. Surface energy transport following relativistic laser-solid interaction. *Physics of Plasmas*, 16:072702, 2009.
- [191] R. Ramis, R. Schmalz, and J. Meyer-ter-Vehn. MULTI A computer code for one-dimensional multigroup radiation hydrodynamics. *Computer Physics Communications*, 49(3):475–505, 1988.
- [192] E. A. McLean, S. H. Gold, J. A. Stamper, R. R. Whitlock, H. R. Griem, S. P. Obenschain, B. H. Ripin, S. E. Bodner, M. J. Herbst, S. J. Gitomer, and M. K. Matzen. Preheat studies for foils accelerated by ablation due to laser irradiation. *Physical Review Letters*, 45(15):1246–1249, 1980.
- [193] J. F. Seely, C. I. Szabo, P. Audebert, E. Brambrink, E. Tabakhoff, and L. T. Hudson. Lateral propagation of MeV electrons generated by femtosecond laser irradiation. *Physics of Plasmas*, 17:023102, 2010.
- [194] S. D. Baton, M. Koenig, P. Guillou, A. Benuzzi-Mounaix, J. Fuchs, C. Rousseaux, L. Gremillet, D. Batani, A. Morace, and M. Nakatsutsumi. Relativistic electron transport and confinement within charge-insulated, mass-limited targets. *High Energy Density Physics*, 3:358–364, 2007.
- [195] J. M. Hicks, L. E. Urbach, E. W. Plummer, and H. L. Dai. Can pulsed laser excitation of surfaces be described by a thermal-model? *Physical Review Letters*, 61(22):2588–2591, 1988.
- [196] D. M. Riffe, X. Y. Wang, M. C. Downer, D. L. Fisher, T. Tajima, J. L. Erskine, and R. M. More. Femtosecond thermionic emission from metals in the space-charge-limited regime. *Journal of the Optical Society of America B*, 10(8):1424, 1993.

- [197] M. Kandyla, T. Shih, and E. Mazur. Femtosecond dynamics of the laser-induced solid-to-liquid phase transition in aluminum. *Physical Review B*, 75:214107, 2007.
- [198] G. L. Eesley. Generation of nonequilibrium electron and lattice temperatures in copper by picosecond laser pulses. *Physical Review B*, 33(4):2144–2151, 1986.
- [199] X. Sun, R. Hong, Ha. Hou, Z. Fan, and J. Shao. Thickness dependence of structure and optical properties of silver films deposited by magnetron sputtering. *Thin Solid Films*, 515(17):6962–6966, 2007.
- [200] J. P. Geindre, P. Audebert, A. Rousse, F. Fallies, and J. C. Gauthier. Frequency-domain interferometer for measuring the phase and amplitude of a femtosecond pulse probing a laser-produced plasma. *Optics Letters*, 19(23):1997–1999, 1994.
- [201] S. P. D. Mangles, C. D. Murphy, Z. Najmudin, A. G. R. Thomas, J. L. Collier, A. E. Dangor, E. J. Divall, P. S. Foster, J. G. Gallacher, C. J. Hooker, D. A. Jaroszynski, A. J. Langley, W. B. Mori, P. A. Norreys, F. S. Tsung, R. Viskup, B. R. Walton, and K. Krushelnick. Monoenergetic beams of relativistic electrons from intense laser-plasma interactions. *Nature*, 431(7008):535–538, 2004.
- [202] C. G. R. Geddes, Cs. Toth, J. van Tilborg, E. Esarey, C. B. Schroeder, D. Bruhwiler, C. Nieter, J. Cary, and W. P. Leemans. High-quality electron beams from a laser wakefield accelerator using plasma-channel guiding. *Nature*, 431(7008):538–541, 2004.
- [203] J. Faure, Y. Glinec, A. Pukhov, S. Kiselev, S. Gordienko, E. Lefebvre, J. P. Rousseau, F. Burgy, and V. Malka. A laser-plasma accelerator producing monoenergetic electron beams. *Nature*, 431(7008):541–544, 2004.
- [204] A. Buck, M. Nicolai, K. Schmid, C. M. S. Sears, A. Sävert, J. M. Mikhailova, F. Krausz, M. C. Kaluza, and L. Veisz. Real-time observation of laser-driven electron acceleration. *Nature Physics*, 7(7):543–548, 2011.
- [205] M. B. Schwab, A. Sävert, O. Jäckel, J. Polz, M. Schnell, T. Rinck, L. Veisz, M. Möller, P. Hansinger, G. G. Paulus, and M. C. Kaluza. Few-cycle optical probe-pulse for investigation of relativistic laser-plasma interactions. *Applied Physics Letters*, 103(19):2011–2016, 2013.
- [206] A. Sävert, S. P. D. Mangles, M. Schnell, E. Siminos, J. M. Cole, M. Leier, M. Reuter, M. B. Schwab, M. Möller, K. Poder, O. Jäckel, G. G. Paulus, C. Spielmann, S. Skupin, Z. Najmudin, and M. C. Kaluza. Direct observation of the injection dynamics of a laser wakefield accelerator using few-femtosecond shadowgraphy. *Physical Review Letters*, 115:055002, 2015.
- [207] P. Emma, R. Akre, J. Arthur, R. Bionta, C. Bostedt, J. Bozek, A. Brachmann, P. Bucksbaum, R. Coffee, F.-J. Decker, Y. Ding, D. Dowell, S. Edstrom, A. Fisher, J. Frisch, S. Gilevich, J. Hastings, G. Hays, Ph. Hering, Z. Huang, R. Iverson, H. Loos, M. Messerschmidt, A. Miahnahri, S. Moeller, H.-D. Nuhn, G. Pile, D. Ratner, J. Rzepiela, D. Schultz, T. Smith, P. Stefan, H. Tompkins, J. Turner, J. Welch, W. White, J. Wu, G. Yocky, and J. Galayda. First lasing and operation of an ångstrom-wavelength free-electron laser. *Nature Photonics*, 4(9):641–647, 2010.
- [208] D. Pile. X-rays: First light from SACLA. *Nature Photonics*, 5(8):456–457, 2011.

- [209] M. Altarelli, R. Brinkmann, M. Chergui, W. Decking, B. Dobson, S. Düsterer, G. Grübel, W. Graeff, H. Graafsma, J. Hajdu, J. Marangos, J. Pflüger, H. Redlin, D. Riley, I. Robinson, J. Rossbach, A. Schwarz, K. Tiedtke, T. Tschentscher, I. Vartanians, H. Wabnitz, H. Weise, R. Wichmann, K. Witte, A. Wolf, M. Wulff, and M. Yurkov. The Technical Design Report (TDR) of the European XFEL. Technical design report, 2007.
- [210] M. Nakatsutsumi and Th. Tschentscher. Scientific Instrument High Energy Density Physics (HED). Conceptual design report, 2013.
- [211] H.-P. Schlenvoigt. Measuring ultrafast dynamics of self-generated magnetic fields from laser-solid interaction by x-ray polarimetry. 2014.
- [212] J. Metzkes, L. Karsch, S. D. Kraft, J. Pawelke, C. Richter, M. Schürer, M. Sobbiella, N. Stiller, K. Zeil, and U. Schramm. A scintillator-based online detector for the angularly resolved measurement of laser-accelerated proton spectra. *Review of Scientific Instruments*, 83:123301, 2012.
- [213] J. Metzkes, T. E. Cowan, L. Karsch, S. D. Kraft, J. Pawelke, C. Richter, T. Richter, K. Zeil, and U. Schramm. Preparation of laser-accelerated proton beams for radiobiological applications. *Nuclear Instruments and Methods in Physics Research Section A: Accelerators, Spectrometers, Detectors and Associated Equipment*, 653:172–175, 2011.
- [214] J. Metzkes. Charakterisierung laserbeschleunigter Protonen und Elektronen. Diploma thesis, Martin-Luther-Universität Halle Wittenberg, 2009.
- [215] T. Richter. Entwicklung zweier Spektrometer für laserbeschleunigte Protonenstrahlen. Diploma thesis, Technische Universität Dresden, 2009.
- [216] O. Jäckel. *Characterization of ion acceleration with relativistic laser-plasma*. PhD thesis, Friedrich-Schiller-Universität Jena, 2009.
- [217] K. Zeil. Physikalisch–technische Vorbereitung von Zellbestrahlungen am intensiven Channeling–Röntgenstrahl der Strahlungsquelle ELBE. Diploma thesis, Humboldt-Universität zu Berlin, 2007.
- [218] C. Richter. *Dosimetrische Charakterisierung laserbeschleunigter Teilchenstrahlen für in vitro Zellbestrahlungen*. PhD thesis, Technische Universität Dresden, 2011.
- [219] E. Breschi, M. Borghesi, M. Galimberti, D. Giulietti, L. A. Gizzi, and L. Romagnani. A new algorithm for spectral and spatial reconstruction of proton beams from dosimetric measurements. *Nuclear Instruments and Methods in Physics Research, Section A: Accelerators, Spectrometers, Detectors and Associated Equipment*, 522:190–195, 2004.
- [220] International Specialty Products. Gafchromic EBT2 Specifications. Technical report.
- [221] D. Jung, R. Hörlein, D. C. Gautier, S. Letzring, D. Kiefer, K. Allinger, B. J. Albright, R. Shah, S. Palaniyappan, L. Yin, J. C. Fernandez, D. Habs, and B. M. Hegelich. A novel high resolution ion wide angle spectrometer. *Review of Scientific Instruments*, 82:043301, 2011.

- [222] L. Torrasi. Plastic scintillator investigations for relative dosimetry in proton-therapy. *Nuclear Instruments and Methods in Physics Research, Section B: Beam Interactions with Materials and Atoms*, 170:523–530, 2000.
- [223] J. S. Green, M. Borghesi, C. M. Brenner, D. C. Carroll, N. P. Dover, P. S. Foster, P. Gallegos, S. Green, D. Kirby, K. J. Kirkby, P. McKenna, M. J. Merchant, Z. Najmudin, C. A. J. Palmer, D. Parker, R. Prasad, K. E. Quinn, P. P. Rajeev, M. P. Read, L. Romagnani, J. Schreiber, M. J. V. Streeter, O. Tresca, C.-G. Wahlström, M. Zepf, and David Neely. Scintillator-based ion beam profiler for diagnosing laser-accelerated ion beams. *Proc. of SPIE*, 8079:807919, 2011.
- [224] B. Hidding, G. Pretzler, M. Clever, F. Brandl, F. Zamponi, A. Lübcke, T. Kämpfer, I. Uschmann, E. Förster, U. Schramm, R. Sauerbrey, E. Kroupp, L. Veisz, K. Schmid, S. Benavides, and S. Karsch. Novel method for characterizing relativistic electron beams in a harsh laser-plasma environment. *Review of Scientific Instruments*, 78:083301, 2007.
- [225] J. F. Ziegler. Srim - the stopping and range of ions in matter. <http://www.srim.org/>.
- [226] A. Buck, K. Zeil, A. Popp, K. Schmid, A. Jochmann, S. D. Kraft, B. Hidding, T. Kudyakov, C. M. S. Sears, L. Veisz, S. Karsch, J. Pawelke, R. Sauerbrey, T. Cowan, F. Krausz, and U. Schramm. Absolute charge calibration of scintillating screens for relativistic electron detection. *Review of Scientific Instruments*, 81:033301, 2010.
- [227] Birks, J. B. *Theory and Practice of Scintillation Counting*. Pergamon, New York, 1964.
- [228] N. Stiller. Entwicklung eines orts- und energieauflösenden Spektrometers für laserbeschleunigte Protonen. Diploma thesis, Technische Universität Dresden, 2012.
- [229] L. Torrasi. Luminescence degrading in polyvinyltoluene by ion beam irradiations. *Radiation Effects and Defects in Solids*, 154(2):89–98, 2001.
- [230] Born and Wolf. *Principles of Optics*. Pergamon Press, 4 edition, 1970.
- [231] M. Cerchez. *Ultrashort laser pulse interaction with overdense plasmas*. PhD thesis, Heinrich-Heine-Universität Düsseldorf, 2008.
- [232] H. Ehrenreich, H. R. Philipp, and B. Segall. Optical Properties of Aluminum. *Physical Review*, 132(5):1918, 1963.
- [233] M. Polyanskiy. Reflectivity data. <http://refractiveindex.info>, 2015.

Danksagung

An dieser Stelle möchte ich mich bei all denjenigen bedanken, die über die vergangenen Jahre zum Gelingen dieser Arbeit beigetragen haben!

An erster Stelle sind das die beiden Institutsdirektoren des Instituts für Strahlenphysik am HZDR, Ulrich Schramm und Tom Cowan. Bei Tom Cowan möchte ich mich zuerst für die Übernahme der Betreuung dieser Arbeit bedanken. Darüber hinaus hat seine Art, offen, enthusiastisch und anschaulich Ideen zu diskutieren und Verknüpfungen zu alten Messungen zu schaffen, an vielen Stellen neue Impulse für die Datenanalyse gegeben. Auch möchte ich mich für die Möglichkeit bedanken, an den von ihm initiierten externen Strahlzeiten in Los Alamos und am LCLS teilnehmen zu können.

Ulrich Schramm gilt mein Dank dafür, mir seit dem Beginn meiner Diplomarbeit die Arbeit in der damals noch *Projektgruppe Laser-Teilchenbeschleunigung* ermöglicht zu haben, sodass ich von Anfang an bei den Experimenten zur Laser-Ionenbeschleunigung am Draco dabei sein konnte. Den großen Freiraum, den er uns bei der Arbeit im Labor - von der Planung bis zur Durchführung der Experimente - gelassen hat, hat meine Entwicklung im Laufe der vergangenen Jahre maßgeblich beeinflusst. Darüber hinaus danke ich ihm für seine immer sehr konstruktive und zielgerichtete Unterstützung beim Schreiben von Publikationen und die Möglichkeit, meine Ergebnisse auf internationalen Konferenzen zu präsentieren.

An zweiter Stelle gilt mein Dank dem Ur-Ionen-Team Stephan Kraft und Karl Zeil, in das ich 2008 als Diplomandin aufgenommen wurde. Nicht denkbar wäre diese Arbeit ohne die Unterstützung von Karl Zeil gewesen, der das erste Experiment zur Laser-Ionenbeschleunigung an Draco aufgebaut und mich in die Geheimnisse der Off-Axis-Parabel-Justage und OWIS-Motoren-Steuerung usw. eingeweiht hat. Sein nimmermüder Elan, auch in verzwickten Situationen im Labor noch eine Idee zu entwickeln und diese auch zu später Stunde noch zu realisieren, waren ein sehr wichtiger Motor der Ionen-Experimente. Dank gilt Karl auch für die Unterstützung beim Interpretieren von manchmal etwas "hartnäckigen" Daten, bei der anschaulichen Darstellung von Ergebnissen in Vorträgen und beim Ausarbeiten von "Geschichten" oder "roten Fäden" für Publikationen. Von Stephan Kraft, dem Post-Doc der Gruppe, konnte ich in den vergangenen Jahren insbesondere lernen, auftretende Probleme - physikalischer oder technischer Natur - ganz unaufgeregt kritisch zu analysieren, bevor man mit Aktionismus zur Tat schreitet.

Mit ermöglicht hat die Experimente an Draco das Laser-Team mit Stefan Bock, Uwe Helbig und René Gebhardt, die Draco für viele Nächte am Laufen gehalten haben!

Experimente zur Laser-Ionenbeschleunigung haben den Nachteil, dass man nur schwer messen kann, was im Target passiert, und so geht ein großer Dank an den Ionen-Theoretiker der Gruppe, Thomas Kluge, dessen numerische Simulationen zur Plasmadynamik entscheidend für die Interpretation der Daten in dieser Arbeit waren. Besonders zu erwähnen sind hier die aufwändigen relativistischen Vorplasma-Simulationen!

Für alle Antworten auf Fragen zur Optik und den Umgang mit Zemax danke ich dem

Penelope-Team mit Mathias Siebold, Fabian Röser, Markus Löser und Daniel Albach. Viel Unterstützung habe ich im Laufe der Dissertation auch von studentischen Hilfskräften, Bachelor- und Diplomstudenten bekommen. Zu nennen sind Wiebke Jahr, die den Prototypen der Probe-Beamline aufgebaut hat, Nils Stiller, der am 2D-Pixeldetektor mitgearbeitet hat, Anne Seidel, die an der Auswertung der Elektronenspektren gearbeitet hat, Martin Rehwald, der die Modellmessungen zum Pump-Probe-Experiment durchgeführt hat, Roy König, der viele Semesterferien unter anderem beim Laboraufbau geholfen hat und Lotti Obst, die an der Kalibrierung von Elektronenspektrometern mitgearbeitet hat. Für spannende gemeinsame Zellbestrahlungsexperimente möchte ich mich beim Team um Jörg Pawelke vom OncoRay bedanken, insbesondere bei Leo Karsch, Christian Richter und Michael Schürer, mit denen zusammen auch die Idee für den 1D-Stack-Detektor entstanden ist.

Bedanken möchte ich mich auch bei Prof. G. Ravindra Kumar und Sudipta Mondal, mit denen die ersten Daten zum Probing mit dem spekularen Reflex des Pump-Pulses gemessen wurden. Diese haben den Anstoß für die folgenden Pump-Probe-Experimente gegeben.

Die Charakterisierung der Szintillationsdetektoren wurde in Messzeiten am Tandem-Beschleuniger am HZDR und am Maier-Leibnitz-Laboratorium (MLL) in Garching durchgeführt. Gedankt sei hier Herrn Dr. Shavkat Akhmadaliev und seinem Team am HZDR und Sabine Reinhardt und dem Team vom MLL für den reibungslosen Ablauf und die angenehme Arbeitsatmosphäre an beidem Maschinen.

Funktionieren kann so ein komplexes Experiment wie an Draco nur mit der Unterstützung vieler "Gewerke", sowohl beim Aufbau als auch bei der Analyse der Daten. Zu nennen ist hier zuerst Manfred Sobiella, der sich zum Beispiel bei der technischen Realisierung der Szintillationsdetektoren viel Zeit genommen hat, die anfänglichen Ideen in ein funktionierendes und formschönes Gerät zu verwandeln, das alle experimentellen Anforderungen erfüllt. Umgesetzt wurden seine Konstruktionen immer schnell und unkompliziert von Matthias Langer und seinem Team in der Werkstatt des Instituts für Strahlenphysik. Für die Unterstützung der Experimente bei allen elektrotechnischen Fragen und beim Neuaufbau des Labors danke ich Christoph Eisenmann und Simon Grams. Bei der Charakterisierung und Bearbeitung von Targets habe ich viel Hilfe im Ionenstrahlzentrum am HZDR bekommen, darunter von Herrn Dr. Lothar Bischoff und Frau Romy Aniol. Für die schnelle und konstruktive Hilfe bei allen administrativen Fragen wie Dienstreisen und Einkäufen danke ich Petra Neumann und Katrin Thiele.

Für die geteilten guten und manchmal auch zähen Zeiten - im Labor oder anderswo - möchte ich dem (ehemaligen) Doktoranden-Team mit Karl Zeil, Thomas Kluge, Alexander Debus, Axel Jochmann, Markus Löser, Jurjen Couperus und Florian Kroll danken! Raphael, dir danke ich für deine Entschlusskraft, die Koffer zu packen und nach Dresden zu kommen! Zu guter Letzt möchte ich mich bei meinen Eltern besonders dafür bedanken, dass sie seit so vielen Jahren ihre Kraft und Energie in unsere wunderbare Groß-Familie gesteckt haben, auf die man immer zählen kann!

Vesicherung

Hiermit versichere ich, Josefine Metzkes, geboren am 09.10.1983 in Berlin-Mitte, im Rahmen meines Promotionsverfahrens an der Fakultät Mathematik und Naturwissenschaften der Technischen Universität Dresden und an Eides statt, dass

1. ich die vorliegende Arbeit ohne unzulässige Hilfe Dritter und ohne Benutzung anderer als der angegebenen Hilfsmittel angefertigt habe; die aus fremden Quellen direkt oder indirekt übernommenen Gedanken sind als solche kenntlich gemacht. Die Arbeit wurde bisher weder im Inland noch im Ausland in gleicher oder ähnlicher Form einer anderen Prüfungsbehörde vorgelegt.
2. ich die vorliegende Arbeit am Helmholtz-Zentrum Dresden – Rossendorf am Institut für Strahlenphysik unter der wissenschaftlichen Betreuung von Prof. Thomas E. Cowan, PhD angefertigt habe.
3. mir die geltende Promotionsordnung (Stand 23.02.2011, Fakultät Mathematik und Naturwissenschaften der TU Dresden) bekannt ist und ich diese anerkenne.

Josefine Metzkes
Dresden, den 17.08.2015